BUILDING NEW TOOLS FOR GRAVITATIONAL WAVE ASTRONOMY

by

Kaze, Wang Kei, Wong

A dissertation submitted to The Johns Hopkins University in conformity with the requirements for the degree of Doctor of Philosophy.

Baltimore, Maryland

July, 2021

Abstract

There has been tremendous progress in gravitational-wave (GW) astronomy since 2015, including the first detection of a GW signal from a black hole binary, the first multi-messenger observation of a binary neutron star merger, and over 50 compact binary coalescence events in the current GW catalog. Next-generation detectors such as the Einstein Telescope (ET), Cosmic Explorer (CE) and the Laser Interferometer Space Antenna (LISA) should detect a wider variety of GW events at a hastening pace. It is important to think ahead and develop tools to address the challenges presented by the upcoming events. In the first half of this thesis we develop tools to compare the growing catalog of GW events against population synthesis simulations, and then we apply them to the current GW catalog to constrain physical processes in the formation of compact object binaries. In the second half we explore the detectability of various potential LISA sources, including black holes surrounded by ultralight boson clouds, exoplanets, single intermediate-mass black holes, and "multiband" events that may be observed by both LISA and ground-based interferometers.

ABSTRACT

Readers

Emanuele Berti (Primary Advisor)

Marc Kamionkowski

Jared Kaplan

Hans Lindblad

Yannick Sire

Acknowledgments

First and foremost I would like to thank Emanuele Berti for giving me guidance, resources and freedom to pursue my research throughout my PhD. In addition, a special thank you for tolerating my horrible grammar, we both know how insufferable that is. I will brag about having the coolest PhD supervisor for the rest of my life.

I was fortunate to have met an ample number of mentors who taught me plenty of practical skills and shaped my personality, including but not limited to Ely Kovetz, Davide Gerosa, Shirley Ho and Tjonnie G. F. Li. Thank you for being my role models, giving me clear directions to improve myself.

I am grateful to be a part of the Department of Physics and Astronomy and Johns Hopkins University. In particular, I would like to thank Marc Kamionkowski, Jared Kaplan and Brice Menard for giving me plenty of chances to discover new knowledge beyond my own domain of research.

I am blessed to have a group of supportive friends throughout this delightful but

sometimes dreadful journey. Specifically, I would like to thank Vishal Baibhav, Thomas Helfer, Felix Julie, Michael Busch, Cyril Creque-Sarbinowski, Utkarsh Sharma, Canon Sun, Carol Hung, Hsiang-Chih Hwang, Weichen Wang, Peter T. H. Pang, Ken K. Y. Ng and Wai Shing Tang. You have done a great deed for society by keeping me from turning into a psychopath.

Finally, I would like to thank my parents for their silent support.

致

還在堅持的你

Preface

The material included in this dissertation is part of my research work carried at the Department of Physics and Astronomy at Johns Hopkins University during the period between August 2017 and July 2021, under the supervision of Prof. Emanuele Berti. The chapters are meant to be read separately and they are based on different publications which I co-authored during this period, namely:

- Chapter 2 is based on:

  Machine-learning interpolation of population-synthesis simulations to interpret gravitational-wave observations: a case study

  Kaze W.K. Wong and Davide Gerosa

  Phys. Rev. D 100 083015 (2019)

- Chapter 3 is based on:

  Distinguishing double neutron star from neutron star-black hole binary populations with gravitational wave observations

  Margherita Fasano, Kaze W.K. Wong, Andrea Maselli, Emanuele Berti, Valeria Ferrari et al.

Phys. Rev. D 102 023025 (2020)

- Chapter 4 is based on:

  Gravitational wave population inference with deep flow-based generative network

  Kaze W.K. Wong, Gabriella Contardo, Shirley Ho

  Phys. Rev. D 101 123005 (2020)

- Chapter 5 is based on:

  Joint constraints on the field-cluster mixing fraction, common envelope efficiency, and globular cluster radii from a population of binary hole mergers via deep learning

  Kaze W.K. Wong, Katelyn Breivik, Kyle Kremer, Thomas Callister

  Phys. Rev. D 103 083021 (2021)

- Chapter 6 is based on:

  Constraining the primordial black hole scenario with Bayesian inference and machine learning: the GWTC-2 gravitational wave catalog

  Kaze W.K. Wong, Gabriele Franciolini, Valerio De Luca, Vishal Baibhav, Emanuele Berti et al.

  Phys. Rev. D 103 023026 (2021)

- Chapter 7 is based on:

  Probing the existence of ultralight bosons with a single gravitational-wave measurement

  Otto A. Hannuksela, Kaze W.K. Wong, Richard Brito, Emanuele Berti, Tjonnie G.F. Li

  Nature Astron. 3 447-451 (2019)

ACKNOWLEDGMENTS

- Chapter 8 is based on:

  On the possibility of detecting ultrashort period exoplanets with LISA

  Kaze W.K. Wong, Emanuele Berti, William E. Gabella, Kelly Holley-Bockelmann

  Mon. Not. Roy. Astron. Soc. 483 L33-L36 (2019)

- Chapter 9 is based on:

  Multiband gravitational-wave event rates and stellar physics

  Davide Gerosa, Sizheng Ma, Kaze W.K. Wong, Emanuele Berti, Richard O'Shaughnessy et al.

  Phys. Rev. D 99 103004 (2019)

- Chapter 10 is based on:

  Expanding the LISA Horizon from the Ground

  Kaze W.K. Wong, Ely D. Kovetz, Curt Cutler, Emanuele Berti

  Phys. Rev. Lett. 121 251102 (2018)

- Chapter 11 is based on:

  Binary radial velocity measurements with space-based gravitational-wave detectors

  Kaze W.K. Wong, Vishal Baibhav, Emanuele Berti

  Mon. Not. Roy. Astron. Soc. 488 5665-5670 (2019)

Contents

List of Tables

List of Figures

Chapter 1

The dawn and future of gravitational-wave astronomy

1.1 Executive summary

There are a number of excellent textbooks [16, 17, 18, 19, 20] where the reader can find detailed explanations to the question "What are gravitational waves?"

In this introductory Chapter, we instead briefly review the history and prospects of gravitational-wave (GW) astronomy to give a motivation for the theme of this thesis: preparing for the challenges that this research field faces in the coming decade. In section 1.2, we provide a brief review of recent discoveries in GW astronomy , followed by a discussion of future research directions in section 1.3. In section 1.4, we conclude with an outline and summary of this thesis.

1.2 The dawn of gravitational-wave astronomy

"Gravitational waves have opened a new window on the universe" is probably the most commonly used opening line for papers and presentations in the GW community since the very first detection of GWs from a binary black hole merger, GW150914 [21]. Six years have passed since that first detection, and detecting GWs is becoming routine as the sensitivity

of our detector network improves. Looking back at the history of astronomy, it is truly remarkable how much progress we have made in the past six years.

As perhaps the oldest subject among the natural sciences, astronomy played an important role in various ancient societies for many practical purposes, such as developing calendars and navigation tools [22]. Although people at the time built instruments such as Armillary spheres and observatories to quantitatively measure the relation between different celestial objects, the observations were limited to what is accessible to the naked eyes. As a result, our understanding of the universe was confined within the tiny window of optical astronomy for thousands of years.

The landscape of astronomy was permanently changed when Galileo Galilei pointed his telescope to the night sky in the 17th century. With the increased resolution and light collecting area of his modest-sized telescope, he discovered features of the Solar System that could not have been observed with the naked eye, such as Saturn's rings [23]. As technology improves, not only can we observe the universe with finer spatial detail and to dimmer corners, but we are also capable to observe a wider part of the electromagnetic spectrum with better resolution: at the high-energy end we have observations that led to the discovery of the most energetic events we have ever observed, gamma-ray bursts [24]; at the low-energy end, radio observations of the Cosmic Microwave Background provide the strongest evidence in favor of our current best model for the origin of the universe, the Big Bang theory [25, 26]. In less than five hundred years, we went from having an incomplete and incorrect picture of the Solar System, to a relatively accurate understanding of the very beginning of the universe.

All of this changed once again on September 14, 2015. While both LIGO detectors were still in engineering mode, they picked up a signal from a $36 - 29M_{\odot}$ binary black hole (BBH) merger at ~ 410Mpc [21] with a signal-to-noise ratio (SNR) of 24. The peak power of this event was estimated to be 3.6×10^{49} W, which is ~ 50 times greater than all stars combined in the observable universe. This crowned GW150914 as the most powerful event humankind has ever observed. Unlike previous breakthroughs in observational astronomy, the detection of GWs is not extending our reach within the realm of electromagnetic waves, but venturing into an entirely new territory of probing the universe. Since GWs only feebly interact with intervening matter, they are not affected by problems that we face in electromagnetic

observations, such as dust occlusion. This nice property of GWs enables us to understand the most dynamic and extreme parts of the universe without the need to worry about foreground contamination, leading to much better constraints on deviations from general relativity [27].

Two years after the first detection, another spectacular event further broadened our horizons. A $\sim$ 100 s signal from a binary neutron star (BNS) was observed by the LIGO-Virgo collaboration (LVC) on August 17, 2017 [28]. Before the public alert was sent by the LVC, the Fermi Gamma-ray Burst Monitor independently detected a gamma-ray burst (GRB 170817A) with a time delay of $\sim$ 1.7 s with respect to the BNS merger time [29]. In the following days, electromagnetic observations across all bands were reported by multiple independent groups for the same event. These multi-messenger observations provided crucial hints to the solution of many long-standing problems, confirming for example that GWs travel very close to the speed of light [30]. The cross-validation between electromagnetic and gravitational observations validated the capabilities of interferometric detectors, reassuring the community that the events are indeed astrophysical, and signaling the beginning of the era of multi-messenger astronomy.

The most recently announced catalog of GW events (GWTC-2) tallied up the total amount of GW events to 50 [31]. Out of those 50, 39 are coming from the first half of the third observational run (O3a), which has roughly the same observation time for coincidence analysis as the first two observational runs combined. The improved sensitivity not only brings us more events, we are also detecting more and more peculiar events, such as BBHs that are too massive to be explained by standard stellar evolution scenario [32] and a neutron star-black hole merger candidate [33]. As the network sensitivity increases we expect to add other sources, such as core-collapse supernovae and possibly primordial GWs, to the future catalog of GW observations.

In just six years, the perception of GWs by the broader astrophysics community has drastically changed. with new papers on the implications of the observed events appearing on the arXiv every day. However, the amazing pace of discovery of current detectors seems modest when compared to the potential of the next generation of detectors.

1.3 The high noon of gravitational-wave astronomy

If the late 2010s were the dawn of GW astronomy, the 2020s and 2030s will be the morning and high noon of the field. The fourth observational run (O4) of the ground-based detector network is expected to start some time around 2022. Aside from improvements in the sensitivity of the existing facilities, with the Japanese detector KAGRA [34] and LIGO India [35] joining the network, the duty cycle of the network as a whole will improve. These improvements should lead to an expected detection rate ranging from hundreds to thousands of events per year [36]. On top of the improved duty cycle, more detectors in the network also provide unique opportunities, such as better localization of the sources [37] and more stringent GW polarization tests [38].

Third-generation ground-based detectors such as the Einstein Telescope (ET) [39, 40, 41, 42] and Cosmic Explorer (CE) [43] are expected to start observations in the mid 2030s. While the low-frequency ($\sim$ 1 Hz) sensitivity of ET and CE may differ depending on design choices, both of them are at least one order of magnitude more sensitive compared to Advanced LIGO. A tenfold increase in sensitivity translates into a factor of 10^3 increase in detection rates, which scale with the observable volume. At design sensitivity, third-generation detectors are expected to deliver up to 10^6 GW detections per year [44]. The dramatic increase in the number of events will improve the precision of many measurements related to GW populations. For example, both BBHs and BNSs have been used to constrain the Hubble constant to a precision $\sim 10\%$ [45]. The majority of the constraining power comes from the first BNS event, GW170817, for which the electromagnetic counterpart measurements provide critical information on the redshift of the source. Even though BBHs are not generally expected to be accompanied by electromagnetic counterparts, there is still information in the signal that can be used to measure the Hubble constant statistically, i.e. they can be used as "standard sirens." By combining all the BBH events in GWTC-1, one gets a $\sim 4\%$ improvement in the measurement of the Hubble constant [45]. With more events, GW measurements of cosmological parameters are expected to become competitive with other current measurements [46]. The increase in search volume also means that we are more likely to observe rare and peculiar events, such as core-collapse supernovae [47] and lensed GW events [48].

In addition to the improvement in statistics, the quality of individual measurements will

also be improved dramatically. A GW150914-like event will have SNR $\rho \sim 2000$ in third-generation facilities. Since the uncertainty in parameter estimation is inversely proportional to the SNR, this high SNR translates into exceptionally precise measurements of the source parameters. One of the most notable improvements is in source localization. Detections from current facilities often come with rather large localization errors (> 100 deg^2) for sources in the local universe ($z \lesssim 0.7$). With third-generation facilities, most of the sources can be localized within 1 deg^2 up to $z \sim 3$ [49]. With this incredible localization precision, partners in electromagnetic follow-ups could find counterparts more easily than using the current facilities.

Approximately on the same timescale, the Laser Interferometer Space Antenna (LISA) [50], a space-based GW observatory, is expected to explore the low-frequency band ($10^{-4} - 1$ Hz) of the GW spectrum. As for electromagnetic observations, opening an additional window in the GW spectrum grants opportunities to observe new source classes. One of the most exciting primary targets for LISA is the merger of supermassive black holes (SMBHs). Due to the large amount of energy emitted by these mergers, they can be detected with SNR > 1000 out to cosmological distances [51]. Because of their very high SNR, SMBHs in LISA are perfect candidates for tests of general relativity [52, 53], and they can also be used as cosmological tracers to study the evolution of our universe [54]. Detecting SMBH mergers will shed light on the birth and evolution of these objects in the high-mass range, complementing the observations from ground-based detectors in the same era.

A large population of galactic binaries, primarily white dwarf binaries in the Milky Way, produces nearly monochromatic GWs at frequencies $\sim 10^{-3}$Hz. LISA is expected to detect $\sim 10^4$ such galactic binaries within the first year of operation [55], shedding light on the physics involved in the formation and evolution of these sources. Due to the nature of GWs, we can also observe these binaries beyond the Galactic Centre and in the Milky Way's halo without the need of worrying about dust obscuration. This means that galactic binaries may also probe the components and formation history of the Milky Way [56].

Perhaps the most exotic source class among LISA's primary targets are extreme mass ratio inspirals (EMRIs) [57]. Unlike SMBHs, which are expected to merge rather quickly, EMRIs are long-lasting signals, which could have $10^4 - 10^5$ cycles in band because of their extreme mass ratio. The large amount of GW cycles may allow us to measure the binary masses and

the dimensionless spin of the central black hole to exquisite precisions of order $\sim 10^{-6} - 10^{-3}$ [58]. Therefore, EMRIs will be excellent probes of the environment around massive black holes [59] or deviations from general relativity [60].

1.4 Outline of this thesis

The rest of this thesis consists of ten chapters. Chapters 2–6 focus on works related to analyzing a population of GW events with ground-based detectors and population-synthesis simulations. Chapters 7–11 focus on investigating the possibility of detecting a variety of sources in LISA.

As the number of GW events increases, our tools to analyze GW populations will become more and more inadequate. Population synthesis simulations are computationally expensive, so most studies before 2018 were limited to comparing the event rates predicted by simulations to the data. While it was possible to generate a sparse bank of simulations and interpolate their event rates, it was not trivial to generalize this interpolation to probability density functions (pdfs) of other observable quantities (such as the mass spectrum of the events) and to compare the resulting conditional pdf with the data. In the first half of the thesis we develop machine learning techniques to solve this interpolation problem, then apply these techniques to analyze various populations of GW events.

In Chapter 2 we analyze the first two observational runs of the LIGO/Virgo Collaboration (O1 and O2) using population synthesis together with a Gaussian process emulator. By employing a modest suite of simulations of isolated binary compact objects, we demonstrate that we can constrain the one-dimensional velocity dispersion of the black hole natal kicks.

In Chapter 3 we investigate whether it is possible to distinguish BNSs from neutron star-black hole binaries at the population level. Since black holes have zero tidal deformability, the effective tidal deformability of a BNS and of a neutron star-black hole binary are expected to be different. Although we cannot conclusively determine the nature of an event based on the effective tidal deformability, because our current detectors are not sensitive enough, the difference between the two source populations will become apparent as the number of detections increases. We found that even the currently operational network of GW detectors can separate the two source types given a reasonable number of events (~ 10), while more

events lead to improved statistical significance.

The Gaussian process emulator we employ in Chapters 2 and 3 can only handle simple models. To overcome this limitation, in Chapter 4 we develop a new emulator based on a deep learning technique called normalizing flow, and show that it can handle problems of a previously intractable complexity. This new technique enables us to employ more sophisticated models in analyzing the growing catalog of GW events. This emulator is the main tool behind the work described in Chapters 5 and 6.

In Chapter 5, we apply the emulator to study a mixture of two separate but consistent suites of population synthesis simulations: `COSMIC` for the isolated formation scenario, and `CMC` for dynamically formed BBHs. The origin of GW events has been a long standing question. By analyzing GWTC-2 with the emulator we find that, under certain assumptions, 80% of the entire population of GW events are dynamically formed. This is an important first step towards more complete comparisons of different astrophysical populations.

We end the first half of this thesis with an investigation of primordial black holes (PBHs) as one of the possible formation channels for the mergers observed by LIGO and Virgo. By analyzing the GWTC-2 dataset, we set an upper limit on the fraction of dark matter in the form of PBHs, and constrain the importance of accretion for the growth of their masses and spins.

In the second half of this thesis, we investigate the possibility of detecting a number of unusual GW source candidates. Unlike the main LISA targets, such as SMBHs, EMRIs or galactic binaries, these source candidates have not received much attention so far.

In Chapter 7 we study the possibility that LISA may detect and characterize ultra-light bosons, a dark matter candidate. If ultra-light bosons exist, spinning black holes in a suitable mass range will be surrounded by a boson cloud produced by superradiant instabilities. If one of the black holes in a GW-emitting binary is surrounded by such a cloud, the waveform of the GW signal will be modified. We show that EMRI observations by LISA could lead to the detection of ultra-light bosons in the mass range $[10^{-16.5}, 10^{-14}]$ eV, or exclude their existence in this mass range.

In Chapter 8 we examine the possibility of detecting GWs from exoplanets. Since only a binary where the exoplanet is very close to a star could emit significant GWs, GW

measurements could be used to study exoplanets in regions that are complementary to traditional electromagnetic surveys. We show that some known binary systems may be marginally detectable by LISA, and comment on the improvements that would be needed to detect this class of systems more efficiently.

In Chapters 9 and 10 we turn our attention to stellar-origin BBHs that can be detected in both ground-based detector networks and LISA, i.e. "multi-band" sources. While ground-based detectors observe roughly the last second of a stellar-origin BBH merger, space-based detectors could observe the earlier phase of the inspiral for months or years. These complementary measurements of the same event could yield strong tests of general relativity and constrain binary formation models. In Chapter 9 we compute event rates for multi-band events, and in Chapter 10 we propose a method to extract sub-threshold multi-band events from the LISA data stream by exploiting the coincident detection of their mergers with ground-based interferometers.

We conclude the thesis by asking whether we could detect intermediate mass black holes (IMBHs) using the radial velocity measurements of nearby GW-emitting binaries. While LISA can detect IMBH mergers up to cosmological distances, the IMBH merger rate is still largely unknown, since we have not detected any of them yet. On the other hand, there is some evidence that stellar clusters may host IMBHs at their center. In Chapter 11 we show that GW-emitting binaries orbiting around an IMBH have time-dependent Doppler shifts that may be measured by LISA. These Doppler modulations could be used to search for non-GW-emitting IMBHs.

Chapter 2

Machine-learning interpolation of population-synthesis simulations to interpret gravitational-wave observations: A case study

We report on advances to interpret current and future gravitational-wave events in light of astrophysical simulations. A machine-learning emulator is trained on numerical population-synthesis predictions and inserted into a Bayesian hierarchical framework. In this case study, a modest but state-of-the-art suite of simulations of isolated binary stars is interpolated across two event parameters and one population parameter. The validation process of our pipelines highlights how omitting some of the event parameters might cause errors in estimating selection effects, which propagates as systematics to the final population inference. Using LIGO/Virgo data from O1 and O2 we infer that black holes in binaries are most likely to receive natal kicks with one-dimensional velocity dispersion $\sigma = 105^{+44}_{-29}$ km/s. Our results showcase potential applications of machine-learning tools in conjunction with population-synthesis simulations and gravitational-wave data.

2.1 Introduction

The observed catalog of gravitational-wave (GW) detections is growing at a fast pace. Eleven [9] (or possibly more [61]) events have been announced so far and hundreds more are expected to be observed within a few years. This opens a unique possibility of inferring properties of the population of merging compact binaries in the Universe.

Current state-of-the-art analyses assume that the underlying population of GW sources is described by some phenomenological parametric expression (e.g. [62]). For instance, one can assume that the mass distribution of merging binary black holes (BHs) follows a power law, and use GW data to infer its spectral index.

As the size of the GW catalog grows, increasingly complex parametrizations and nonparametric tests (e.g. [63]) will allow us to capture finer and finer details of the observed population.

Astrophysical predictions of GW populations are typically computed using population-synthesis codes [64, 65, 66, 67, 68, 69] –collections of prescriptions that encode our understanding and ignorance of how compact binaries form and evolve from their stellar progenitors. The parameters needed to initialize a population-synthesis simulation are directly related to poorly understood astrophysical mechanisms ruling the lives of massive stars. These include, for instance, efficiency of the common-envelope phase (if any), strength of the supernova kicks, fallback material, mass-loss rates, stellar winds, etc.

A possible strategy to exploit future large GW catalogs is to bypass phenomenological models and compare data directly against population-synthesis simulations. A first step in this direction consists of estimating mixing fractions between two or more precomputed models [70, 71, 72, 73]. More ambitiously, one could use GW data to infer the set of code input flags that best matches the observations. This approach faces an immediate difficulty, namely that a new, computationally expensive population-synthesis simulation is required at each evaluation of the population likelihood.

Progress to overcome this limitation was recently presented by Taylor and Gerosa [74]. By combining Gaussian process regression (GPR), principal component analysis (PCA), space-filling algorithms, and a hierarchical Bayesian framework, they were able to efficiently

interpolate a precomputed bank of population-synthesis simulations and use the resulting emulator to infer the posterior distributions of the population parameters. Their method, however, was only applied to a few simple scenarios [74].

In this paper, we present a more realistic application: we train a GPR interpolant on a small, but state-of-the-art, set of population-synthesis predictions of BH binaries formed in isolation [75]. The resulting emulator slots into a hierarchical Bayesian analysis and is fed with BH binary data from LIGO/Virgo first (O1) and second (O2) observing runs. Under these astrophysical assumptions, we measure the natal kicks that BHs receive at birth.

This case study sheds light on some of the challenges one has to overcome to fully compare GW data and astrophysical simulations. In particular, we show that omitting a subset of the single-event parameters, either because they are not modeled in the simulations or simply because they make the inference problem computationally prohibitive, will cause a systematic bias on the final population inference.

This paper is organized as follows. In Sec. 2.2 we briefly review the procedure of Ref. [74] and present the current application. In Sec. 6.4 we show inference results using both mock datasets and real observations. Finally, in Sec. 11.4 we discuss some astrophysical implication of our findings and highlight future developments of this approach.

2.2 Methods

2.2.1 Hierarchical Bayesian inference

For each GW event, data d are routinely analyzed using Bayesian inference [9]. The chosen priors encode one's physical intuition of the underlying population and play an important role when interpreting the results [76]. A hierarchical analysis aims at parametrizing the choice of prior and using data to infer the resulting "hyperparameters." For clarity, in the following we will denote parameters describing single events (e.g. masses, redshifts) as "event parameters", and the hyperparameters describing the entire sample as "population parameters" (e.g. the strength of supernova kicks). Let us assume that a set of population

parameters λ predicts a distribution of event parameters θ

$$\frac{\mathrm{d}}{\mathrm{d}\theta} r(\lambda) = r(\lambda)\, p_{\rm pop}(\theta|\lambda)\,, \tag{2.1}$$

where $\int p_{\rm pop}(\theta|\lambda)\mathrm{d}\theta = 1$ and the total rate $r(\lambda)$ is typically measured in yr^{-1}. This function encodes our astrophysical assumptions on the underlying populations. It can be estimated using a parameterized model, a population-synthesis simulation, or, in our case, by evaluating a machine-learning emulator. The predicted number of events is $N(\lambda) = r(\lambda) \times T_{\rm obs}$ where $T_{\rm obs}$ is the duration of the observing run(s).

We wish to analyze a GW catalog containing $N_{\rm obs}$ entries. For simplicity, we assume that all the events present in the catalog are of astrophysical origin. A more complete analysis including triggers with larger false-alarm probabilities is left to future work (e.g. [77]). Single-event posterior $p(\theta|d)$ are computed using some default prior $\pi(\theta)$ which is chosen by issuers of the catalog. In practice, both prior and posterior are usually provided under the form of Monte Carlo samples [9].

Detector selection effect are encoded in a function $0 \leq p_{\rm det}(\theta) \leq 1$, indicating the likelihood that an event with parameters θ appears in the catalog. This is used to define the observable distribution

$$\frac{\mathrm{d}}{\mathrm{d}\theta} r_{\rm det}(\lambda) = r(\lambda)\, p_{\rm pop}(\theta|\lambda)\, p_{\rm det}(\theta) \tag{2.2}$$

and the expected number of observations $N_{\rm det}(\lambda) = r_{\rm det}(\lambda) \times T_{\rm obs}$. Here we follow a common approach and approximate $p_{\rm det}(\theta)$ using the single-detector semi-analytic approximation of Refs. [78, 79]) as implemented in Ref. [80] with a signal-to-noise ratio threshold equal to 8 and the waveform model of Ref. [81]. This was shown to be in good agreement with large-scale injection campaigns [62, 82].

All these ingredients enter the population likelihood, which has the standard expression of an inhomogeneous Poisson process (c.f. Refs. [74, 83, 84, 85] for detailed derivations). In particular, the population posterior reads

$$p(\lambda|d) \propto \pi(\lambda)\, e^{-N_{\rm det}(\lambda)} N(\lambda)^{N_{\rm obs}} \prod_{i=1}^{N_{\rm obs}} \int \frac{p_i(\theta|d)}{\pi_i(\theta)} p_{\rm pop}(\theta|\lambda)\mathrm{d}\theta\,, \tag{2.3}$$

where $\pi(\lambda)$ is some assumed population prior. If one wishes exclude rate information from

the inference, a marginalization over $N(\lambda)$ with prior $\propto 1/N(\lambda)$ yields [86]

$$p(\lambda|d) \propto \pi(\lambda) \prod_{i=1}^{N_{\rm obs}} \int \frac{p_i(\theta|d)}{\pi_i(\theta)} \frac{p_{\rm pop}(\theta|\lambda)}{\int p_{\rm pop}(\theta|\lambda) p_{\rm det}(\theta)} {\rm d}\theta \,. \tag{2.4}$$

2.2.2 Training simulations

In this paper we consider GW sources formed in isolation via a common-envelope phase –a leading formation channel for binary BHs (e.g. [87]). We use the set of predictions presented in Ref. [75, 88] (see references therein). The simulations are performed with the STARTRACK [67] and PRECESSION [89] codes (see also [90]). In particular, these runs employ the same set of assumptions used in model M10 of Ref. [91], except that BH natal kicks are not suppressed compared to neutron stars. Kicks are drawn from a Maxwellian distribution with one-dimensional velocity dispersion σ. We consider seven simulations with $\sigma = 0$, 25, 50, 70, 130, 200, and 265 km/s, the latter being the value inferred from pulsar proper motions [92].

Each event in our synthetic catalogs is described by masses, spins, redshift, as well as its contribution to the total merger rate ${\rm d}r/{\rm d}\theta$ [93]. In this paper, we restrict the event parameters used in our statistical inference to masses, redshifts, and rates (see below). Even though BH spins are not directly considered, assumptions on their distribution enter the waveform, hence the detection rates. Using the various spin models developed by Ref. [75], we verified that this indirect spin effect has a negligible impact on our final results. For concreteness, in the following we use the "time-uniform" model [75]. All binaries are assumed to reach the LIGO/Virgo band in quasicircular orbits.

Selection effects $p_{\rm det}(\theta)$ are computed using sensitivity curves for both LIGO in its design configuration and LIGO during O1/O2. In particular, we use the "Design Sensitivity" and the "Early High Sensitivity" from Ref. [94], respectively (cf. [62]).

2.2.3 Gaussian processing

Astrophysical simulations are used to train a Gaussian process interpolator to quickly evaluate the rates ${\rm d}r(\lambda)/{\rm d}\theta$. In particular, our problem has a single population parameter $\lambda = \{\sigma\}$. Our implementation closely follows that of Ref. [74]. We first assume a common

binning scheme across all simulations and convert the distribution using PCA.[1] The resulting features are then interpolated across the hyperparameter space with GPR.

The choice of event parameters used in the inference needs to be addressed with care. A trade-off is present between the size of the vector θ and the resulting GPR accuracy. A larger number of event parameters would increase the amount of astrophysical information captured by the analysis. However, this requires larger training banks to keep the interpolation error under control. This means, not surprisingly, that if we want to increase the amount of information used in the hyperparameters inference, we also need to feed in more training data to ensure the same accuracy.

We found that our set of 7 simulations allows us to accurately interpolate across source-frame chirp mass and redshift, i.e. $\theta = \{M_c, z\}$. For this (admittedly modest) training bank, inserting additional parameters, like mass ratio or effective spin, significantly degrades the performance of the interpolator. In particular, we use 40 equispaced bins in $M_c \in [5, 45]$ and $z \in [0, 1]$. GPR is implemented using SCIKIT-LEARN [95] with a squared exponential kernel as in Ref. [74]. The population posterior of Eq. (6.14) is sampled using EMCEE [96].

We validate our pipeline using a standard out-of-sample test. We train our regression machine using 6 simulations and validate results against the one that was left out. Figure 2.1 shows the predicted distributions of chirp mass M_c, redshift z, and rates r. Other than some small-scale differences, the interpolator accurately captures all the main features of the training set. For instance, we found a fractional difference in the intrinsic rate as small as $\Delta r/r \sim 6\%$

Reducing the number of event parameters implies that the quantities used in the inference differ from those needed to compute selection effects via $p_{\rm det}(\theta)$. Assumptions on other parameters beyond chirp mass and redshift such as mass ratio and spins will inevitably be necessary to compute waveforms. For this reason, one cannot simply interpolate $\mathrm{d}r(\lambda)/\mathrm{d}\theta$ across $\theta = \{M_c, z\}$ and compute $N_{\rm det}(\lambda)$ at each likelihood evaluation. We bypass the issue by computing the detectable rates from the training simulations (where mass ratios and spins are provided) and running a second GPR/PCA interpolation on $\mathrm{d}r_{\rm det}(\lambda)/\mathrm{d}\theta$ (cf. Fig. 2.1).

[1] PCA naturally allows reducing the size of the computational problem by filtering out unnecessary features [74]. In this case, we are only using 7 training simulations and are able to process the entire distributions without any compression.

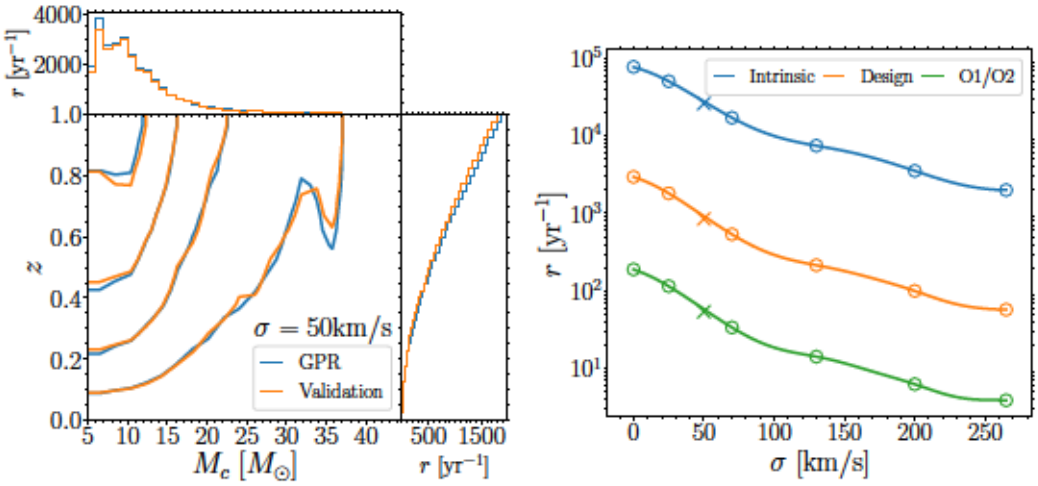

Figure 2.1: Out-of-sample test of our machine-learning interpolator. The simulation with $\sigma = 50$ km/s is excluded from the training dataset and used to validate results. The top panel shows the intrinsic distributions of chirp mass and redshift $\mathrm{d}r/\mathrm{d}\theta$. Blue curves show the interpolated result, while orange curves show the control set. Contours mark 30%, 50%, 70% and 90% confidence intervals; side histograms show the marginalized distributions. The bottom panel shows detection rates across the hyperparameter space. In particular, the blue line shows intrinsic rates r, while orange and green lines show observable rates $r_{\rm det}$ for LIGO at design sensitivity and during O1/O2, respectively. Circles mark the simulations used to train the interpolator; crosses mark the validating dataset.

This approach is tested in the next section.

2.3 Results

2.3.1 Mock data

We first apply our statistical pipeline to mock data. We assume that a population of BH binaries with true value $\bar{\sigma}$=100 km/s is observed by LIGO at design sensitivity. This is a location in parameter space where we have not performed a population-synthesis simulation. The observing time $T_{\rm obs}$ is chosen such that the predicted number of observation is $N_{\rm det}(\bar{\sigma}) = \{10, 100, 1000\}$. We assume the number of entries $N_{\rm obs}$ in our mock catalogs is Poisson-distributed with mean $N_{\rm det}(\bar{\sigma})$. Injections events $\theta = \{M_c, z\}$ are generated from the $\mathrm{d}r_{\rm det}/\mathrm{d}\theta$ emulator. For simplicity, we assume posterior $p_i(\theta|d)$ are bivariate Gaussians centered on those extracted values with standard deviations equal to 10%. We sample the posterior of Eq. (6.14) assuming a flat priors on M_c, z and σ.

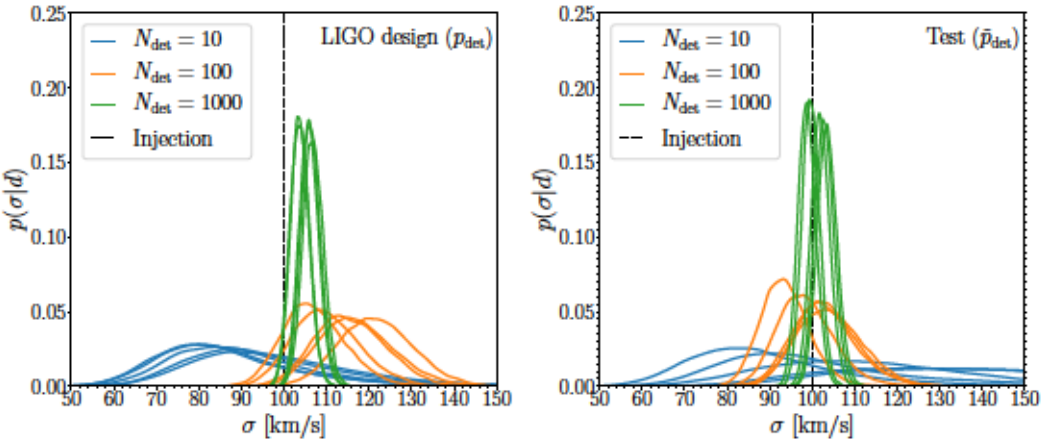

Figure 2.2: Injection-recovery test. The left panel considers LIGO at design sensitivity, where selection effects are included through $p_{\rm det}$. In this case, both $\mathrm{d}r/\mathrm{d}\theta$ and $\mathrm{d}r_{\rm det}/\mathrm{d}\theta$ are interpolated from population-synthesis simulations. The right panel shows a test run where we assume a fictitious LIGO detector described by $\tilde{p}_{\rm det}$ (see the description in the text), which allows us to only interpolate $\mathrm{d}r/\mathrm{d}\theta$. The injected value $\bar{\sigma}$= 100 km/s is marked by vertical dashed lines. Solid curves show posterior distributions of the strength of supernova kicks σ assuming the predicted number of observable sources is $N_{\rm det}(\bar{\sigma})$ =10 (blue), 100 (orange), and 1000 (green). A few realizations are reported for each of these cases.

Our injection-recovery results are shown in left panel of Fig. 2.2 for several catalog realizations. The injected value $\bar{\sigma} = 100$ km/s is well within the predicted posterior only for the case with $N_{\rm det} = 10$. As the number of detections grows, a systematic bias becomes more and more evident. For $N_{\rm det} = 1000$, the posteriors peak at ~ 105 km/s and the true values lies well outside the 90% confidence interval.

This bias is somewhat expected because we are neglecting some of the event parameters and only considering $\theta = \{M_c, z\}$. This forces us to interpolate $\mathrm{d}r(\lambda)/\mathrm{d}\theta$ and $\mathrm{d}r_{\rm det}(\lambda)/\mathrm{d}\theta$ separately. In normal circumstance these two distributions are related by a single detectability function, i.e. $\mathrm{d}r_{\rm det}(\lambda)/\mathrm{d}\theta = p_{\rm det}(\theta)\mathrm{d}r(\lambda)/\mathrm{d}\theta$. Our pipeline, however, violates this condition because the two interpolants have different interpolation errors occurring in each bin.

We test this interpretation by considering a fictitious detector where selection effects $\tilde{p}_{\rm det}$ depends only on M_c and z. This is constructed by assuming the same LIGO sensitivity curve which, however, responds to all binary BHs as if it they were equal mass and nonspinning, i.e. $\tilde{p}_{\rm det}(M_c, z) = p_{\rm det}(M_c, z, q = 1, \boldsymbol{\chi_1} = 0, \boldsymbol{\chi_2} = 0)$. In this case, we can interpolate only $\mathrm{d}r/\mathrm{d}\theta$ using population synthesis data. Injections are constructed extracting couples $\{M_c, z\}$

from $\mathrm{d}r/\mathrm{d}\theta$ and accepting/rejecting each draw according to $\tilde{p}_{\rm det}(\theta)$. The factor $e^{-N_{\rm det}(\lambda)}$ in Eq. (6.14) is estimated by integrating $\tilde{p}_{\rm det}(\theta) \times \mathrm{d}r/\mathrm{d}\theta$ at each likelihood evaluation. Results are shown in the right panel of Fig. 2.2. We recover a largely unbiased estimates of the population parameter.

As discussed above, the number of parameters we can confidently interpolate is limited by size of the training dataset. A larger set of simulations would allow us to model more event parameters, consequently reducing systematic uncertainties on the resulting inference. Figure 2.2 shows, however, that the present simulation set is appropriate for $\mathcal{O}(10)$ events, as in this case statistical uncertainties largely dominates over systematics. We thus proceed by analyzing the 10 BH binary events detected during O1 and O2.

2.3.2 Events from LIGO/Virgo O1 and O2

After removing data segments contaminated by significant noise sources, LIGO/Virgo O1 and O2 resulted in $T_{\rm obs} = 48.6$ and 118 days of coincident data, respectively [9, 97]. We make use of posterior and prior samples of 10 binary BH coalescences publicly released by the LIGO and Virgo collaborations [98]. In particular, they provide luminosity distance and detector-frame masses, which we convert to redshift and source-frame masses. A Gaussian kernel-density estimation is then employed to obtain $\pi(\theta)$ at the locations of the posterior samples, which allows approximating the integrals in Eqs. (6.14-6.15) as Monte Carlo sums.

The resulting inference is illustrated in Fig. 11.3, where we show the posterior distribution of the population parameter σ. This is our GW measurement of the kicks imparted to BHs at formation. Quoting median and 90% confidence interval, we find $\sigma = 105^{+44}_{-29}$ km/s. The information gain between prior and posterior, as quantified by the Kullback-Leibler divergence [99], is $D_{\rm KL} = 1.54$.

The posterior is skewed toward high values of σ. This is because the event rate r changes more (less) rapidly at low (high) values of σ (cf. Fig. 2.1). Consequently, data can more (less) easily accommodate kicks that are larger (smaller) than the inferred posterior maximum.

Our inference is largely driven by the integrated event rate $r(\lambda)$. For this set of simulations, the current GW catalog does not contain enough discriminating power to perform an informative analysis restricted to $p_{\rm pop}$. Repeating our study using the marginalized likelihood

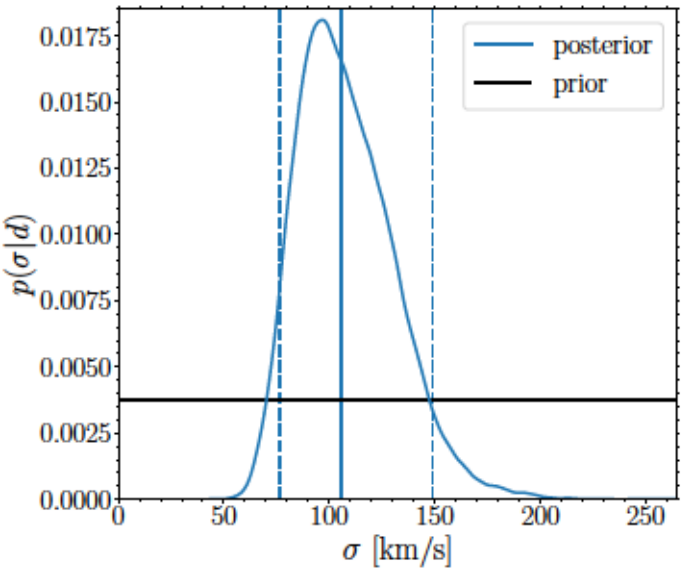

Figure 2.3: Constraints on the strength of BH natal kicks σ using 10 BH binary data from LIGO/Virgo O1 and O2. The blue curve shows our posterior distribution. Vertical blue lines show the corresponding median (solid) and 90% confidence interval (dashed). We assume a flat prior (horizontal black line).

of Eq. (6.15) returns a much lower information gain $D_{\rm KL} = 0.24$.

2.4 Discussion

By applying the statistical framework of Ref. [74], we analyzed current GW data using population-synthesis simulations of binary BHs formed in isolation. Simulations enter the training process of a machine-learning algorithm, in this case GPR. The resulting emulator is then used to evaluate the likelihood in the context of a standard hierarchical Bayesian analysis. The present case study puts this idea into practice using a modest set of 7 training simulations, allowing us to showcase both prospects and pitfalls of this approach. Overall, the pipeline returns posterior distributions of the input flags one needs to initialize and run population-synthesis simulations. These are related to poorly understood mechanisms in the lives of massive stars, like BH natal kicks, which are here measured directly from GW data.

We first tested our approach on mock catalogs and show the presence of a systematic bias that exceeds statistical uncertainties when the number of observations is $\gtrsim 100$. The

omission of some event parameters causes errors when modeling detector selection effects which in turn, propagate to the population inference. The test reported in Sec. 2.3.1 suggests that this issue can be alleviated with a larger set of training simulations, which will allow using a larger set of event parameters while keeping the interpolation error under control. The case where some parameters need to be omitted reflects a common situation. In this study, information on mass ratio and spins are available but limited number of simulations prevented us from carrying out a more complete analysis. A more damaging scenario occurs when some variables affecting the GW signal are not modeled at all in the astrophysical simulations. Our results show the importance of developing astrophysical models where all the observables (BH spins, eccentricity, etc) are taken into account.

We also applied our procedure to BH binary data from LIGO/Virgo O1 and O2. Our results suggest that binary BHs were imparted moderate kicks at formation ($\sigma \gtrsim 70\,\mathrm{km/s}$). This is in tentative agreement with position and proper-motion measurements in X-ray binaries [100, 101, 102], as well as GW measurements of BH-binary spin misalignment [103, 104]. Our findings are, however, in contrast with current supernova models which predict that BH natal kicks should be highly suppressed due to fallback material in the late stage of the explosion (e.g. [105]). The simulations used in this paper do not have a dedicated flag to tune the amount of fallback, which is instead controlled directly by the value of σ.

We stress that our result is model dependent. This is intentional: *we are interpreting GW events in light of a specific set of astrophysical assumptions*. Consequently, only those assumptions are put to test. Among the set of predictions explored here, current GW data prefer models where moderately large natal kicks are imparted onto BHs. It is natural to expect that a more complete set of training simulations might change this result qualitatively. Even assuming the same population-synthesis setup, a larger set of training simulations will allow (i) capturing degeneracies between different population parameters and (ii) efficiently interpolating across additional event parameters.

Prior assumptions are inevitably part of any statistical analysis. Instead of relying on parametrized distributions, our approach makes use of state-of-the-art simulations in a data-driven fashion. We believe our approach presents promising avenues to infer astrophysical formation and evolutionary processes of GW sources, thus making a step forward toward the goal of GW astronomy.

Chapter 3

Distinguishing double neutron star from neutron star-black hole binary populations with gravitational wave observations

Gravitational waves from the merger of two neutron stars cannot be easily distinguished from those produced by a comparable-mass mixed binary in which one of the companions is a black hole. Low-mass black holes are interesting because they could form in the aftermath of the coalescence of two neutron stars, from the collapse of massive stars, from matter overdensities in the primordial Universe, or as the outcome of the interaction between neutron stars and dark matter. Gravitational waves carry the imprint of the internal composition of neutron stars via the so-called tidal deformability parameter, which depends on the neutron star equation of state and is equal to zero for black holes. We present a new data analysis strategy powered by Bayesian inference and machine learning to identify mixed binaries, hence low-mass black holes, using the distribution of the tidal deformability parameter inferred from gravitational-wave observations.

3.1 Introduction

The past few years have seen remarkable advances in gravitational-wave (GW) astronomy. The ground-breaking discovery of merging binary black holes (BHs) [21, 106, 107, 108] was soon followed by the spectacular observation by the Laser Interferometer Gravitational-Wave Observatory (LIGO) [109] and Virgo [110] of the coalescence of binary neutron stars (BNSs) [28, 111], whose counterpart and afterglow was also witnessed in the entire electromagnetic spectrum by dozens of telescopes and detectors around the world and in space [29]. This latter observation has already shed light on a number of unsolved problems in physics and astronomy: it provided the first direct evidence that BNSs power the central engines of short gamma ray bursts [30], identified the merger debris of such systems as prolific sites of the formation of r-process elements [29, 112], and confirmed that GWs travel essentially at the speed of light [30]. Most importantly for our present purposes, the discovery of GW170817 has helped demonstrate that GW observations can infer the tidal deformability of neutron stars (NSs) [13, 111, 113, 114, 115] (but see [116] for caveats).

LIGO and Virgo observations have so far firmly confirmed GWs from two classes of ultra-compact binaries: binary BHs and BNSs. With the recent discovery of GW190425, they have potentially also observed the first example of a mixed system containing a BH and a NS (BHNS) [117], although GW190425 could well be a BNS merger [118]. When the masses of BHs in such systems are similar to those of NSs, how can one tell them apart?

The presence of NSs in a binary can leave behind relativistic ejecta that predominantly contain energetic neutrons, which source r-process heavy elements and kilonovae [119].Indeed several studies used electromagnetic information to understand whether the low-mass compact binary mergers detected so far are BHNS or BNS systems [120, 121, 122, 123, 124]. However, if the primary companion is a massive BH (where the precise mass threshold depends on the BH spin [14, 125, 126]) then no ejecta might be left behind, as tidal forces will be small. If instead the BH mass is comparable to the NS mass, the electromagnetic afterglow might be similar to that of BNS mergers. Simulations suggest that the disk mass in this case may be small, so that the electromagnetic counterpart may be hard to detect [125, 127].

Besides, not all binaries detected by LIGO and Virgo might be accessible for electromagnetic follow-ups for various reasons, including their large distance, the line-of-sight dependence

of the ejecta (see e.g. [128]), and large uncertainties in the sky position of the source as determined by LIGO and Virgo.

Even so, discriminating the BNS population from the BHNS population is an important science goal for GW detectors, as this could shed light on the origin of the two populations, testing astrophysical models of the formation and evolution of such systems. The presence of a NS in a binary can, in principle, be inferred by GW observations as the tidal field of the companion (BH or NS) can induce quadrupole deformation in the NS. This deformation is measured in terms of a dimensionless "tidal deformability" parameter Λ which is related to the quadrupolar $\ell = 2$ tidal Love number k_2 and the radius R and mass M of the NS via $\Lambda = (2/3)k_2(c^2R/GM)^5$ [129, 130, 131]. LIGO/Virgo GW observations have direct access to this parameter, as the quadrupole deformation of the star leads to a faster rate of inspiral of the orbit. This is captured in the observed waveform as a fifth post-Newtonian order (i.e., $\mathcal{O}(v/c)^{10}$) correction to the orbital phase evolution of the system. At this order the deformability parameters Λ_i $(i = 1, 2)$ do not appear separately, but as a dimensionless combination called the *effective tidal deformability*, which also depends on the mass ratio $q = M_2/M_1$ of the system:

$$\tilde{\Lambda} \equiv \frac{16}{13}\frac{(1+12q)\Lambda_1 + (q+12)q^4\Lambda_2}{(1+q)^5}. \tag{3.1}$$

While the primary goal behind measuring the tidal deformability is to determine the equation of state (EOS) of dense hadronic or quark matter in NS cores, in this paper we wish to exploit this measurement to distinguish BNS from BHNS systems. In particular, our goal is to develop a new statistic to discriminate between the two populations and measure a population hyperparameter that gives the fraction of BNS and BHNS systems in the observed population. To this end, we exploit the fact that according to our current understanding BHs have zero tidal deformability (see Refs. [131, 132, 133, 134] for further details), while NSs, depending on the stiffness of the EOS, could have a large tidal deformability [114, 129].

While it has long been known that mass measurements are not sufficient to distinguish between BNS and NSBH systems [135, 136], our work differs from similar recent proposals. Measurements of the tidal deformabilities Λ_1 and Λ_2 of the individual binary components could be consistent with a NSBH system even for large-SNR signals and large tidal effects if

at least one of the two tidal deformabilities is consistent with zero at the 50% confidence level [137], therefore it is hard to distinguish BNS from NSBH systems with GWs alone[1] if we assume that Λ_1 and Λ_2 are independent [138]. However, certain NS properties that can be measured via GWs can be expected to be similar for all NSs. This "universality" can be used to distinguish between the two classes of binaries, as described in Ref. [139]. The main caveat of this method is the requirement that the NS radius must be approximately constant for all NSs in binary systems, at least within statistical errors. This is reasonable when the EOS is hadronic, but it is not expected to hold if the EOS allows for phase transitions to quark matter [140, 141]. Conversely, the method we propose can be applied to any EOS model. We consider two "extreme" EOS models (see Sec. 3.2), one of which (the ALF2 EOS) indeed leads to hybrid stars. Previous work developed a method to distinguish BNSs and low-mass binary BHs solely from their GW signals, considering the imprint of the tidal deformability of the NSs on the GW signal for systems undergoing prompt BH formation after merger [142]. More recently, tidal heating of BH horizons has been suggested as a way of distinguishing BNS from BHNS systems [143].

The rest of this paper is organized as follows. In Sec. 3.2 we describe our assumptions on the mass distribution and the EOS, and their implications for the distribution of the effective tidal deformability parameter. In Sec. 3.3 we use hierarchical Bayesian inference to reconstruct the fraction of BHNS (BNS) systems from simulated observations. Finally, in Sec. 3.4 we discuss our results and point out possible directions for future work. Appendix 3.5 lists some of the proposed formation scenarios that could produce BHs in the mass range $\sim$ 1–3 $M_\odot$. Appendix 3.6 shows that EOS uncertainties can affect the inference in the worst-case scenario where we use the stiffest EOS to recover astrophysical systems that correspond to the softest EOS (or vice versa). Appendix 3.7 shows that our results are largely insensitive to the inclusion of tidal disruption effects in the waveform models.

3.2 The mass distribution of compact binaries

In this section we discuss and motivate our assumptions on the mass distribution of BNSs and BHNSs, which is an important ingredient to distinguish between the two families of

[1] Distinguishing low-mass binary BHs from BNSs is easier, as both tidal deformabilities vanish in the case of binary BHs.

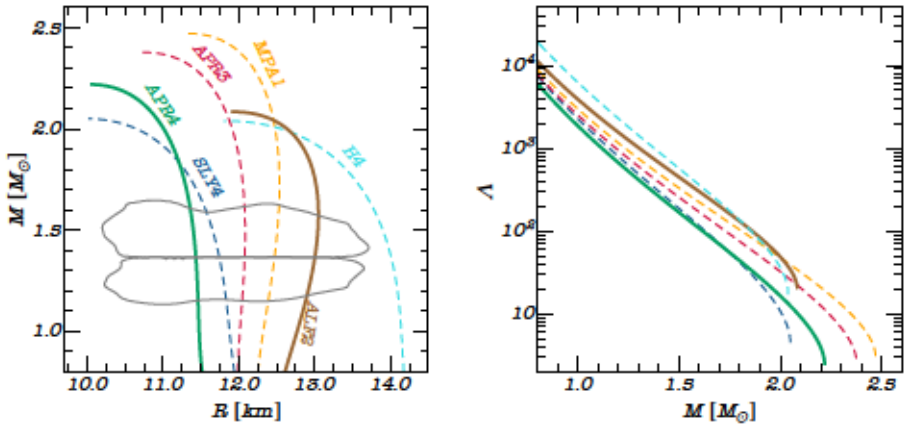

Figure 3.1: Left panel: Mass-radius relations for selected EOS models. Left to right: APR4 [1] (thick green), SLY4 [10] (dashed blue), APR3 [1] (dashed red), MPA1 [11] (dashed orange), ALF2 [2] (thick brown), and H4 [12] (dashed cyan). The gray lines represent the 90% confidence regions for the companion masses and their radii for the LIGO/Virgo event GW170817, assuming a parametrized EOS and imposing a lower limit on the maximum mass of $1.97\,M_\odot$ (cf. Fig. 3 of Ref. [13]). Right panel: Dimensionless tidal deformability Λ (on a log scale) as a function of the NS mass for the same EOS models considered in the left panel.

compact objects.

Stellar evolution theory suggests that the minimum mass of isolated, nonrotating NSs should be $\sim 1M_\odot$ (see e.g. [144, 145] and references therein), and there is a growing body of experimental and theoretical constraints on the upper end of the mass spectrum. The timing of radio pulsars recently established a new observational lower limit on the maximum mass of $\sim 2.14^{+0.20}_{-0.18}M_\odot$ at 95.4% confidence level [146]. Bayesian inference based on the electromagnetic observations of pulsars, nuclear physics calculations of the EOS and the recent observation of GW170817 together imply values of the maximum mass of stable NSs clustering around $\sim 2\,M_\odot$ [114, 147, 148, 149, 150, 151, 152, 153, 154, 155], although there are claimed observations of even more massive NSs [156], and theoretically the maximum mass can be as large as $\sim 3\,M_\odot$ [157]. In general, the mass spectrum of isolated BHs can span several orders of magnitude ranging from sub-solar mass objects to the supermassive BHs of mass $\gtrsim 10^6 M_\odot$ found in galactic centers. In this work we are interested in BHs with masses comparable to NSs, and therefore we will focus on the range $1M_\odot \lesssim M_{\rm BH} \lesssim 3M_\odot$.

3.2.1 Neutron star binaries

We consider two BNS mass distribution models.

The first model ("double Gaussian," henceforth `BNS-DG`) is based on the electromagnetic observations of Galactic radio pulsars, whose evolutionary path is described in Refs. [158, 159, 160]. In the standard isolated binary formation channel, the primary NS is spun up to $\sim$ 10–100 ms through accretion, whereas the secondary star spins down to a typical period of ~ 1 s after birth. A recent Bayesian analysis using a sample of 17 Galactic BNSs [161] indicates that the nonrecycled (secondary) NS mass is uniformly distributed within the range $M_{\rm NS} \in [1.14, 1.46] M_\odot$, while the recycled (primary) NS follows a double Gaussian distribution

$$G(m|\theta) = \frac{\alpha}{\sqrt{2\pi}\sigma_1} e^{\frac{(m-\mu_1)^2}{2\sigma_1^2}} + \frac{1-\alpha}{\sqrt{2\pi}\sigma_2} e^{\frac{(m-\mu_2)^2}{2\sigma_2^2}} , \tag{3.2}$$

where we introduced the four-dimensional parameter vector $\theta = (\mu_1, \mu_2, \sigma_1, \sigma_2)$ with $\mu_1 = 1.34\ M_\odot$, $\mu_2 = 1.47 M_\odot$, $\sigma_1 = 0.02 M_\odot$, $\sigma_2 = 0.15 M_\odot$, and the "mixing parameter" $\alpha = 0.68$. The `BNS-DG` prescription is completed by setting an EOS-dependent threshold $M_{\rm EOS}^{\rm max}$ for the maximum stellar mass (see Sec. 3.3). This model is based on observations of galactic NSs, and therefore it should be viewed with some caution if we consider third-generation (3G) interferometers such as the Einstein Telescope [40, 41, 42] or Cosmic Explorer [162], which are expected to detect binary systems out to large redshifts [43, 162].

In the second, more agnostic model (`BNS-U`), both NS masses are extracted from a uniform distribution with $M_{\rm NS} \in [1 M_\odot, M_{\rm EOS}^{\rm max}]$. This model is less physically motivated, but we use it to bracket uncertainties and to take into account the recent detection of GW190425 [117], which seems to suggest that the formation and evolution of the BNS population observed in GWs may be different from the Galactic population [163].

3.2.2 Black hole-neutron star binaries

The formation and evolution of BHNS binaries are arguably even more uncertain. "Low-mass" BHs can form from the gravitational collapse of stars of mass $\gtrsim 8\ M_\odot$ or from overdensities in the early Universe ("primordial BHs", henceforth PBHs [164, 165, 166, 167, 168, 169, 170, 171, 172, 173]). If the BH mass $m > M_{\rm EOS}^{\rm max}$ (where no stable NS configurations are

Table 3.1: Radius and dimensionless tidal deformability $\Lambda \equiv \lambda/m^5$ for a prototype $1.4M_\odot$ NS modelled with two examples of theoretical EOSs, namely APR4 [1] and ALF2 [2], which represent to cases of soft and stiff nuclear matter, respectively.

EOS	$R_{\rm NS}$ [km]	Λ	$M_{\rm EOS}^{\rm max}$ $[M_\odot]$
APR4	11.43	260.35	2.21
ALF2	13.02	666.23	2.08

allowed) the BH could have either primordial or stellar origin [174]. There are several (more or less exotic) formation scenarios that could produce BHs in the mass range $\sim$ 1–3 $M_\odot$. To improve readability, we briefly review them in the Appendix 3.5.

There are large uncertainties in current estimates of BNS and stellar BHNS merger rates (see e.g. [44]) and in key parameters of some of the more "exotic" formation scenarios, such as the fraction of dark matter in PBHs $f_{\rm PBH}$ (see e.g. [175, 176, 177, 178, 179, 180]), but it is reasonable to expect that BNS merger rates should be larger than BHNS merger rates in the mass range of interest here. LIGO-Virgo observations have measured a 90% credible rate (to the nearest significant figure) of 100–4000 $\rm yr^{-1}\,Gpc^{-3}$ for BNS mergers, while the upper limit (in the absence of any candidates) on BHNS binaries is 600 $\rm yr^{-1}\,Gpc^{-3}$ [181, 182]. However, we will be agnostic and allow for the possibility that BHNS rates may dominate over BNS rates. We adopt a flat distribution for the BH mass $M_{\rm BH}$ in the range $[1,3]M_\odot$, and (just as we did for BNSs) we consider either the double Gaussian distribution of Eq. (3.2) or a uniform NS mass distribution in the range $M_{\rm NS} \in [1, M_{\rm EOS}^{\rm max}]M_\odot$. In the following we will refer to these models as `BHNS-DG` and `BHNS-U`, respectively.

3.2.3 Choice of EOS

In our analysis we consider two EOS models, APR4 [1] and ALF2 [2], as prototypes for "soft" and "stiff" nuclear matter. Soft and stiff EOSs lead to more and less compact stellar configurations, respectively. The APR4 EOS is computed from a nonrelativistic model which includes relativistic boost corrections to the two- and three-nucleon interactions using variational methods [1]. The ALF2 EOS is a nuclear and quark matter EOS based on the so called MIT bag model, with a phase transition from nucleons to deconfined quarks at density $\rho \sim 8 \cdot 10^{14}$ g $\cdot$ cm^{-3} [2]. As shown in Table 3.1, for a given mass (here chosen to be the "canonical" $M = 1.4M_\odot$) the APR4 EOS yields a NS with smaller radius and tidal deformability than the ALF2 EOS.

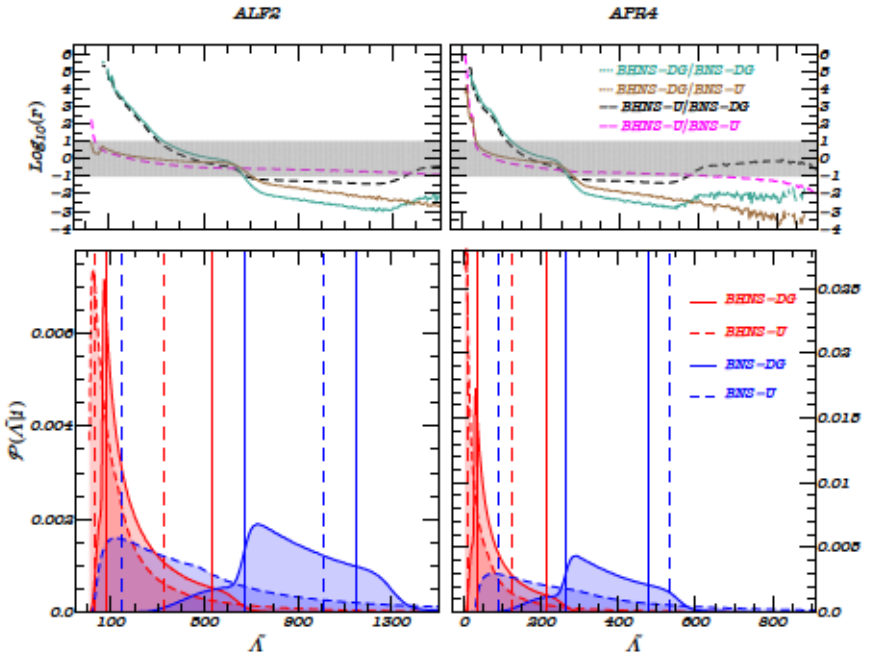

Figure 3.2: Bottom: Conditional probability distributions $\mathcal{P}(\tilde{\Lambda}|i)$, where $i =$ `BHNS-DG` (solid red), `BHNS-U` (dashed red), `BNS-DG` (solid blue) or `BNS-U` (dashed blue), for EOS ALF2 (left panel) and APR4 (right panel). Vertical lines identify the 68% confidence intervals for the three distributions (cf. Table 3.1). Top: $\log_{10}(r)$, where r is the probability ratio defined in Eq. (3.3) for different combinations of mass distribution models, as indicated in the legend. When this ratio is above the shaded region the binary is likely to be a BHNS. Below the shaded region it is likely to be a BNS. In the grey shaded region, the binary's origin is uncertain.

Both of these models are compatible with the LIGO/Virgo events GW170817 [13, 111, 113] and GW190425 [117] and with recent electromagnetic observations [183, 184, 185, 186, 187]. Furthermore, as shown in the left panel of Fig. 3.1, APR4 and ALF2 span a wide range of mass-radius configurations. The difference in stiffness between the two models has a large impact on the tidal deformability parameter Λ, which differs by a factor $\gtrsim 2$ between the two models for a given mass. In the right panel of Fig. 3.1 we plot the tidal deformability as a function of mass for the same equations of state. The soft EOS APR4 yields smaller values of Λ than the stiff EOS ALF2 for all NS masses. This is important for our purposes, because large values of Λ enhance matter effects in the signal, and, therefore, lead to tighter constraints [188].

3.2.4 Tidal deformability probability distribution

We populate the models `BNS-DG`, `BNS-U`, `BHNS-DG` and `BHNS-U` with $n \sim 8 \cdot 10^6$ samples, each representing a binary with component masses randomly selected according to the criteria described in Sec. 3.2. For each system (BNS and BHNS), we compute the NS tidal deformability by solving the relativistic stellar structure equations for a given EOS [129], while the tidal deformability of the BH is assumed to be zero [132, 133, 133, 189]. From these data sets we compute the dimensionless tidal deformability $\widetilde{\Lambda}$ defined in Eq. (3.1), and the corresponding conditional probability distributions $\mathcal{P}(\widetilde{\Lambda}|\mathrm{BNS})$ and $\mathcal{P}(\widetilde{\Lambda}|\mathrm{BHNS})$.

The blue and red histograms in Fig. 3.2 show the probability distributions $\mathcal{P}(\widetilde{\Lambda}|\mathrm{BHNS})$ (red) and $\mathcal{P}(\widetilde{\Lambda}|\mathrm{BNS})$ (blue) for EOS ALF2 (left panel) and APR4 (right panel). Within each panel, solid (dashed) lines correspond to a double Gaussian (uniform) mass distribution for NSs. The EOS has a small effect on the qualitative shape of the probability functions for both BNS and BHNS systems. However, the stiffness of the EOS does change the median and the 68% confidence intervals, as shown in Table 3.2. To guide the eye, in Fig. 3.2 we mark all 68% confidence intervals by vertical lines.

Compare for example the probability functions $\mathcal{P}(\widetilde{\Lambda}|\mathrm{BHNS\text{-}DG})$ and $\mathcal{P}(\widetilde{\Lambda}|\mathrm{BNS\text{-}DG})$. The left panel of Fig. 3.2 shows that they have some overlap when $300 \lesssim \widetilde{\Lambda} \lesssim 700$ for ALF2, while the right panel implies that they overlap for $100 \lesssim \widetilde{\Lambda} \lesssim 300$ for APR4. However, for both EOS models the 68% confidence levels of the two distributions are disjoint. These qualitative considerations provide a first visual indication that it may indeed be possible

Table 3.2: Median and 68% confidence intervals of the tidal deformability $\widetilde{\Lambda}$ (cf. Fig. 3.2.)

model	EOS	
	ALF2	APR4
BHNS-U	100^{+225}_{-70}	30^{+90}_{-24}
BHNS-DG	160^{+380}_{-78}	60^{+150}_{-31}
BNS-U	410^{+600}_{-260}	230^{+300}_{-140}
BNS-DG	870^{+280}_{-200}	350^{+130}_{-87}

to disentangle the nature of low-mass binaries from these probability distributions, with small and large values of $\widetilde{\Lambda}$ corresponding to BHNS and BNS systems, respectively, while intermediate values would suggest a mixture of the two populations.

The mass function of NSs does not significantly affect $\mathcal{P}(\widetilde{\Lambda}|\text{BHNS})$, which remains sharply peaked at small values of $\widetilde{\Lambda}$, but it does change the qualitative behavior of $\mathcal{P}(\widetilde{\Lambda}|\text{BNS})$. Table 3.2 shows that the median value of $\widetilde{\Lambda}$ is significantly lower for $\mathcal{P}(\widetilde{\Lambda}|\text{BNS-U})$ than for $\mathcal{P}(\widetilde{\Lambda}|\text{BNS-DG})$, so the region in which the tidal deformability of BHNS and of BNS overlap increases significantly, and we can expect that our ability to distinguish BHNSs from BNSs will degrade significantly. Note that this is a blessing and a curse: reconstructing the form of the probability distributions with future GW observations may allow us to reconstruct the mass distribution and the formation scenarios of BNS components.

The distributions of the tidal deformability shown in the bottom panels of Fig. 3.2 can be exploited to identify the specific type of binary. Let us introduce the ratio

$$r(\widetilde{\Lambda}) \equiv \frac{\mathcal{P}(\widetilde{\Lambda}|\text{BHNS})}{\mathcal{P}(\widetilde{\Lambda}|\text{BNS})}\,. \tag{3.3}$$

Large (small) values of $r(\widetilde{\Lambda})$ indicate that $\widetilde{\Lambda}$ is more likely to come from a BHNS (BNS, respectively). In the top panels of Fig. 3.2 we plot $r(\widetilde{\Lambda})$ for the four possible combinations of EOS models (either ALF2 or APR4) and NS mass distributions (either double Gaussian or uniform). When this ratio is above the shaded region, the binary is likely to be a BHNS. Below the shaded region, it is likely to be a BNS. In the grey shaded region, the binary's origin is uncertain.

The range of $\widetilde{\Lambda}$ corresponding to an uncertain binary origin (i.e., to the ratio r being in the shaded region) depends sensitively on the mass distribution of NSs in BNS systems, being

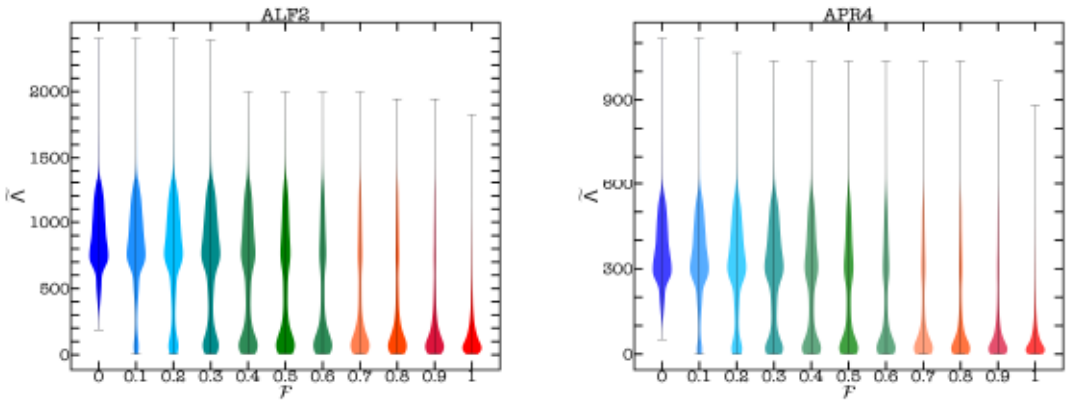

Figure 3.3: Violin plot showing the probability distribution of $\mathcal{P}(\widetilde{\Lambda})$ defined in Eq. (3.4) for the ALF2 (left) and APR4 (right) EOS and for selected values of $\mathcal{F} = [0, 0.1, 0.2, \ldots 1]$. The population is dominated by BNSs when $\mathcal{F} \to 0$, and by BHNSs when $\mathcal{F} \to 1$.

large when the mass distribution is flat. In general, the mixing fraction between BHNS and BNS systems will be hard to measure when the tidal deformability distributions for BNSs and BHNSs have a large overlap, i.e. when r is in the shaded region over a broad range of values of Λ.

3.3 Bayesian inference

The previous qualitative considerations can be put on a more solid footing by a Bayesian analysis. First of all, we can combine the probability distributions of the two compact binary families to obtain the observable probability distribution of $\widetilde{\Lambda}$:

$$\begin{aligned}\mathcal{P}(\widetilde{\Lambda}) = \mathcal{P}(\widetilde{\Lambda}|\mathrm{BHNS})\mathcal{P}^{\mathrm{obs}}(\mathrm{BHNS}) \\ + \mathcal{P}(\widetilde{\Lambda}|\mathrm{BNS})\mathcal{P}^{\mathrm{obs}}(\mathrm{BNS})\ ,\end{aligned} \tag{3.4}$$

where $\mathcal{P}^{\mathrm{obs}}(\mathrm{BNS})$ and $\mathcal{P}^{\mathrm{obs}}(\mathrm{BHNS})$ are the probabilities to observe a BNS and a BHNS system, respectively.

Equation (3.4) can be used to infer the relative abundance of BNSs and BHNSs as follows. We define a "mixing fraction" parameter $\mathcal{F} = \mathcal{P}^{\mathrm{obs}}(\mathrm{BHNS})$ such that $0 \leq \mathcal{F} \leq 1$ and

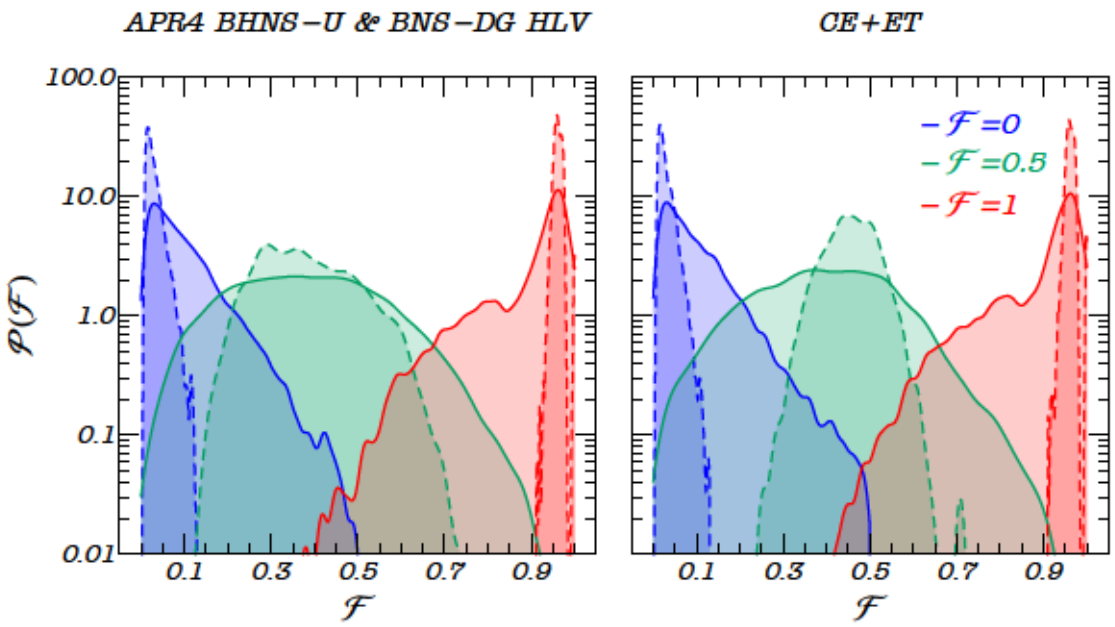

Figure 3.4: Reconstructed probability density functions of the parameter $\mathcal{F}$ assuming $N_{\rm obs} = 10$ observations (solid lines) or $N_{\rm obs} = 60$ observations (dashed lines). The left panel refers to a second-generation detector network (HLV), and the right panel to a third-generation network composed of two CEs and ET. We focus on three extreme cases: a pure BNS population ($\mathcal{F} = 0$, blue), a "perfectly mixed" population ($\mathcal{F} = 0.5$, green), and a pure BHNS population ($\mathcal{F} = 1$, red). For concreteness here we focus on EOS APR4 and we compare the mass distribution models `BHNS-U` and `BNS-DG`, but results are qualitatively similar for other EOS models and mass distributions.

$\mathcal{P}^{\rm obs}({\rm BNS}) = 1 - \mathcal{F}$. Then Eq. (3.4) reads

$$\mathcal{P}(\widetilde{\Lambda}) = \mathcal{P}(\widetilde{\Lambda}|{\rm BHNS})\mathcal{F} + \mathcal{P}(\widetilde{\Lambda}|{\rm BNS})(1-\mathcal{F}) \ . \tag{3.5}$$

For simplicity, in the following we will compare the `BHNS-U` and `BNS-DG` models only. In Fig. 3.3 we show how the shape of $\mathcal{P}(\widetilde{\Lambda})$ changes with $\mathcal{F}$. The left panel refers to the ALF2 EOS, and the right panel to the APR4 EOS. The two plots are qualitatively similar, although the range of possible values for $\widetilde{\Lambda}$ is very different. When $\mathcal{F}$ is close to unity most binaries are BHNSs, and $\mathcal{P}(\widetilde{\Lambda})$ has a single peak at values of $\widetilde{\Lambda} \lesssim 300(200)$ for ALF2 (APR4). As $\mathcal{F}$ decreases below $\simeq 0.7$ the distribution becomes bimodal, with a second broad peak between $300 \lesssim \widetilde{\Lambda} \lesssim 1400$ ($100 \lesssim \widetilde{\Lambda} \lesssim 600$) for ALF2 (APR4). This second peak becomes more and more dominant in the limit $\mathcal{F} \to 0$, when BNSs dominate the observed population.

Table 3.3: Median and 68% confidence intervals of $\mathcal{F}$ for the two EOS models ALF2 and APR4, a number of observations $N_{\rm obs} = 10$ or $N_{\rm obs} = 60$, and two detector networks: (i) a second-generation HLV network and (ii) a third-generation network composed of two CEs and ET. We focus on three extreme cases: a pure BNS population ($\mathcal{F} = 0$), a "perfectly mixed" population ($\mathcal{F} = 0.5$), and a pure BHNS population ($\mathcal{F} = 1$).

EOS	HLV		CE+ET	
	$N_{\rm obs} = 10$	$N_{\rm obs} = 60$	$N_{\rm obs} = 10$	$N_{\rm obs} = 60$
		$\mathcal{F} = 0$		
ALF2	$0.074^{+0.097}_{-0.046}$	$0.024^{+0.022}_{-0.010}$	$0.072^{+0.094}_{-0.045}$	$0.023^{+0.022}_{-0.0093}$
APR4	$0.075^{+0.110}_{-0.053}$	$0.024^{+0.032}_{-0.014}$	$0.075^{+0.100}_{-0.050}$	$0.023^{+0.023}_{-0.0096}$
		$\mathcal{F} = 0.5$		
ALF2	$0.53^{+0.13}_{-0.16}$	$0.54^{+0.062}_{-0.062}$	$0.53^{+0.13}_{-0.16}$	$0.54^{+0.059}_{-0.059}$
APR4	$0.38^{+0.18}_{-0.17}$	$0.37^{+0.130}_{-0.091}$	$0.40^{+0.15}_{-0.16}$	$0.46^{+0.054}_{-0.059}$
		$\mathcal{F} = 1$		
ALF2	$0.94^{+0.031}_{-0.15}$	$0.96^{+0.011}_{-0.008}$	$0.94^{+0.03}_{-0.15}$	$0.962^{+0.0096}_{-0.0078}$
APR4	$0.89^{+0.078}_{-0.15}$	$0.96^{+0.015}_{-0.009}$	$0.89^{+0.08}_{-0.15}$	$0.961^{+0.0103}_{-0.0080}$

We sample the probability distribution of the hyperparameter $\mathcal{F}$ using a machine-learning emulator trained on numerical predictions and inserted into a Bayesian hierarchical framework [190, 191, 192]. We train a Gaussian process regression interpolant on 100 values of $\mathcal{F} \in [0, 1]$. The resulting emulator slots into a hierarchical Bayesian analysis and is fed with simulated data from observations with second- and third-generation interferometer networks, providing different constraints on $\mathcal{F}$. We consider two detector configurations: (i) a network consisting of LIGO Hanford, LIGO Livingston [109] and Virgo [110] (HLV), all operating at design sensitivity [193], and (ii) a third-generation network [194] composed of two Cosmic Explorer (CE) detectors [43, 162] and one Einstein Telescope (ET) [40, 42].

The observations injected within the code are simulated using the publicly available code `BILBY`, a Bayesian inference library for GW astronomy [195, 196, 197]. For each binary injected in the data analysis pipeline, we randomly draw the component masses according to the specific model[2], while the luminosity distance d_L is sampled from a uniform distribution between 10 and 120 Mpc.

[2] `BILBY` cannot handle very small (and rare) values of $\tilde{\Lambda}$. Therefore we discard the lowest values of $\tilde{\Lambda}$, and this effectively sets the upper mass limit for BHs in our catalogs at $2M_\odot$.

For the GW signal we use the `IMRPhenomPv2_NRTidal` model [198, 199]. Numerical relativity simulations have shown that tidal disruption may occur in BHNS mergers, affecting the merger dynamics and introducing a characteristic frequency cutoff in the waveform. In general, the occurrence of tidal disruption and the waveform morphology are sensitive to the BH spin, the binary mass ratio and the EOS [14, 200, 201, 202, 203]. We focus (conservatively) on systems where tidal disruption does not occur, because the frequency cutoff due to tidal disruption makes BHNS binaries easier to tell apart from BNS binaries [204, 205]. We also verified by an explicit calculation that using PhenomNSBH [203], a waveform model which includes tidal disruption, would not affect our conclusions (see Appendix 3.7).

We assume an isotropic source position and orientation in the sky. We neglect the spins of both NSs (in which case the dimensionless spin parameter is expected to be $\lesssim 0.3$ [206]) and BHs (see e.g. [207, 208]). Although BHs, in principle, can have large spin, this should not significantly affect our results, because tidal deformability effects are expected to be dominant over spin effects at the relevant post-Newtonian order [209]. Moreover, we are focusing on black hole masses up to 2 $M_\odot$. These may involve BHs of primordial origin or dark matter cores (see Appendix 3.5), and theoretical calculation in these scenarios suggest that BH spins should be negligible [208, 210, 211].

For each posterior distribution of $\mathcal{F}$ we run three independent chains of $\sim 10^4$ samples, discarding the first ~ 10 % points as burn in. The convergence of the Markov Chain Monte Carlo simulations is determined by cross-checking the chains through a standard Rubin test [212].

We compute $\mathcal{P}(\widetilde{\Lambda})$, as defined in Eq. (3.5), for 100 values of $\mathcal{F} \in [0, 1]$. We have checked that the Gaussian process regression interpolant emulator reconstructs the probability distributions $\mathcal{P}(\widetilde{\Lambda})$ shown in Fig. 3.3 with accuracy better than 10% for any value of $\mathcal{F}$.

We choose a subset of binaries such that the inferred $\mathcal{P}(\widetilde{\Lambda})$ lies within the regions where we can correctly distinguish BNSs from BHNSs for both EOS models. For BHNSs (BNSs) we consider $\widetilde{\Lambda}$ in the range $\sim [50, 200]$ ($[300, 600]$) for APR4 and $[120, 500]$ ($[400, 1200]$) for ALF2. We inject these values into the machine learning emulator and reconstruct $\mathcal{P}(\mathcal{F})$.

Figure 3.4 shows the results of 10 and 60 simulated BNS and BHNS events assuming the ALF2 EOS in the HLV network (left panel) and for the the third-generation network of two

CEs and one ET (right panel). We reconstruct $\mathcal{P}(\mathcal{F})$ through a hierarchical Bayesian analysis under three assumptions: a "pure BNS" population ($\mathcal{F} = 0$), a "pure BHNS" population ($\mathcal{F} = 1$) and a "perfectly mixed" population ($\mathcal{F} = 0.5$). For the third-generation networks (right panel) the tidal deformability errors are roughly one order of magnitude smaller than for the second-generation network (left panel). This leads to slightly narrower probability distributions, but our results indicate that (quite remarkably) present detectors are sufficient to discriminate between the two populations, as long as the number of observations is large enough. The median and the 68% confidence intervals of the distributions are listed in Table 3.3. Note that the comparison in Fig. 3.4 (where we fix the number of observations) is somewhat unfair, because the higher sensitivity of third-generation detectors implies that event rates must increase with the cube of the sensitivity enhancement. As the number of events and detectors improve, the reconstruction of $\mathcal{P}(\mathcal{F})$ and our ability to determine $\mathcal{F}$ will get sensibly better.

This is one of the main conclusions of this work: current interferometers should already be able to determine the nature of low-mass compact binaries by measuring the tidal deformability distribution. Roughly $\mathcal{O}(10)$ GW observations in the low-mass range can identify whether $\mathcal{F}$ favors double NSs or mixed binaries when one of the two families dominates the population, and a few tens of observations are sufficient to measure $\mathcal{F}$ with an accuracy ~ 0.1 even if both families contribute to the overall observed population.

3.4 Conclusions

A new era in astronomy has begun with the observation of compact binary coalescences by the LIGO and Virgo GW detectors. This complementary window to observe the Universe can inform our knowledge of fundamental physics and astrophysics. In particular, we can address the long-standing problem of how compact object binaries form and evolve by measuring their fundamental properties, such as the distribution of their masses and spins and their cosmological merger rates.

In this paper we have addressed how GW observations could be exploited to measure another key property of the population, namely the relative abundance of BNSs and BHNSs when the BHs masses are similar to those of NSs. Delayed supernovae, the coalescence of NSs,

certain models of dark matter and physical processes in the primordial Universe might produce such BHs. It is, therefore, critical to discriminate the two populations to test the different formation scenarios of BHs.

A crucial difference between BNS and BHNS systems arises because the dimensionless tidal deformability of NSs is $\Lambda \sim \text{few} \times 100$, while it is predicted to be zero for BHs. Consequently, the effective tidal deformability $\widetilde{\Lambda}$ of a binary defined in Eq. (3.1), which depends on the tidal deformability of the binary components and their mass ratio, is significantly larger for BNSs ($\widetilde{\Lambda}_{\rm BNS} \sim 400$–$1200$ for the stiffer EOS, and ~ 300–600 for the softer EOS considered in this paper) than it is for BHNSs ($\widetilde{\Lambda}_{\rm BHNS} \sim 120$–$500$ for the stiffer EOS, and ~ 50–200 for the softer EOS). We exploit this asymmetry in the distribution of $\widetilde{\Lambda}$ to differentiate between the two populations.

To this end, we introduced a population hyperparameter $\mathcal{F}$ measuring the fraction of BHNS population relative to BNS population in the observed catalog of sources. We have shown that it is possible to infer the hyperparameter $\mathcal{F}$ from the measured distribution of $\widetilde{\Lambda}$. The distribution peaks at large (small) values of $\widetilde{\Lambda}$ if the population contains no BHNS (BNS) systems and $\mathcal{F} = 0$ ($\mathcal{F} = 1$), while it will be bimodal if the population contains a significant population of BHNS systems, say $0.2 < \mathcal{F} < 0.8$.

The highlight of this investigation is that the network of GW detectors that are currently operational (LIGO Hanford, LIGO Livingston and Virgo) can constrain $\mathcal{F}$ at 68% confidence level to the range $[0, 0.2], [0.7, 1]$ and $[0.3, 0.7]$ with only 10 detections if the population is dominated by BNSs or BHNSs or an equal admixture of both, respectively. A larger number of observations, with 60 events, would increase our ability to reconstruct $\mathcal{F}$, pinning down the confidence intervals to $[0, 0.05], [0.9, 1]$ and $[0.4, 0.6]$, for the same populations.

Our results are largely insensitive to the EOS of dense matter although stiffer equations of state do allow for a moderately better constraint on $\mathcal{F}$. On the other hand, the mass ratio of the companion stars spreads the range of possible values of effective tidal deformability, limiting the accuracy with which the hyperparameter $\mathcal{F}$ can be inferred. If NS masses are confined to a narrower range than is assumed in this paper, then it will be possible to measure the relative fraction of BNSs and BHNSs more accurately. This is where CE and ET could make an impact: they will be able to provide us with a very precise distribution of NS masses by accurately measuring the masses of thousands of NSs.

We thank Omar Benhar, Stefania Marassi, Raffaella Schneider, Luca Graziani and Lucas Tonetto for useful discussions and advice on the methods used in this work and Nathan Johnson-McDaniel and Wolfgang Kastaun for comments on the manuscript. E.B. and K.W. are supported by NSF Grants No. PHY-1912550 and AST-1841358, NASA ATP Grants No. 17-ATP17-0225 and 19-ATP19-0051, and NSF-XSEDE Grant No. PHY-090003 and B.S.S. in part by NSF Grant No. PHY-1836779, AST-1716394 and AST-1708146. This research was conducted using computational resources at the Maryland Advanced Research Computing Center (MARCC). The authors would like to acknowledge networking support by the GWverse COST Action CA16104, "Black holes, gravitational waves and fundamental physics." We acknowledge support from the Amaldi Research Center funded by the MIUR program "Dipartimento di Eccellenza" (CUP: B81I18001170001).

3.5 Low-mass black hole formation scenarios

In this appendix we present a short overview of formation scenarios that could produce BHs in the mass range $\sim [1-3]\ M_\odot$.

Supernovae. One possibility to produce low-mass BHs is through supernova explosion. If the explosion is driven by rapidly growing instabilities with timescale of $10-20$ ms, it is expected to form BHs with masses $> 5\ M_\odot$. However, instabilities may develop over a longer (> 200 ms) timescales and lead to lower mass remnants [213]. In both cases, gravitational collapse could produce BHs compatible with the mass range considered in this paper.

Accretion-induced collapse. A second possibility is that NSs may gain mass through accretion and collapse to low-mass BHs [214, 215, 216, 217]. Given current uncertainties on the maximum NS mass, it is not clear how to distinguish low-mass BHs formed in accretion-induced collapse from those formed in other channels.

Hierarchical mergers. The hierarchical merger of BHs in dense environments is a possible channel to form the heaviest BHs observed by LIGO and Virgo [218, 219, 220]. Similarly, the remnant BHs produced by a BNS merger should often have masses below $3\ M_\odot$ and they could merge again in dense stellar environments, forming BHNS binaries with low-mass BHs via dynamical interactions [221] (cf. [222] for caveats on the rates). An alternative scenario involves 2+2 quadruple systems, i.e. wide binary systems in which each component

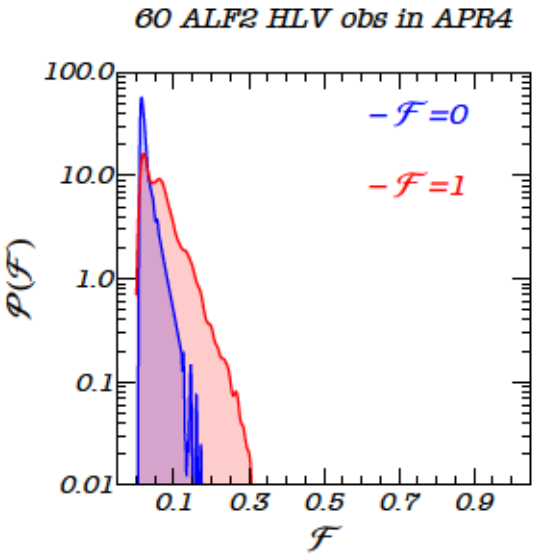

Figure 3.5: Reconstructed probability density functions of the parameter $\mathcal{F}$ assuming $N_{\rm obs} = 60$ observations with a second-generation detector network (HLV). Here we look at the most pessimistic scenario where we inject an ALF2 population into a Bayesian framework trained with the APR4 EOS, and we focus on the two extreme cases: a pure `BNS-DG` population ($\mathcal{F} = 0$, blue) and a pure `BHNS-U` population ($\mathcal{F} = 1$, red).

is itself a binary [223].

PBHs. Current observational constraints on the PBH abundance from microlensing indicate that their mass fraction compared to dark matter may be as large as $f_{\rm PBH} \lesssim 10\%$ [180]. If this bound is saturated, and we assume that the cross section for the dynamical capture of a NS and a BH of similar mass are comparable (this is reasonable, since the process is dominated by GW emission [224]), then the merger rate of BHNSs may be even larger than the merger rate of dynamically formed BNSs [138].

PBH captures. Another possibility is that NSs, white dwarfs or even main sequence stars could capture mini PBHs with $M_{\rm BH} \ll 1 M_\odot$. Efficient accretion from the star could then increase the PBH mass up to $\sim 1 - 3\ M_\odot$ [225, 226]. However, it is still not clear which fraction of NSs could survive this process to form a bound BHNS system [225].

Dark matter cores. It has been speculated that asymmetric dark matter could accumulate within the NS cores through nucleon scattering, and eventually form a BH seed [227, 228, 229], providing yet another possibility for converting a NS to a BH of similar mass.

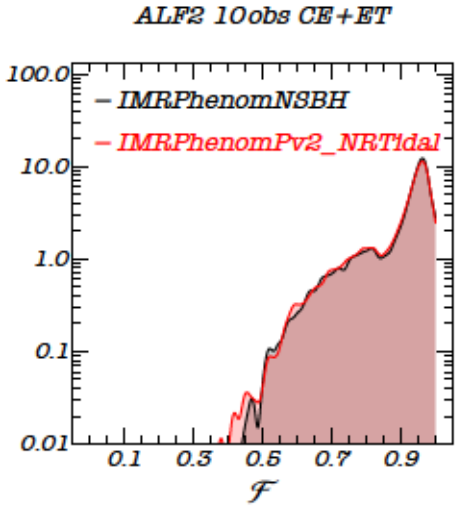

Figure 3.6: Probability distribution of $\mathcal{F}$ obtained by injecting 10 observations where tidal disruption occurs, as determined by imposing $q < Q_D(\mathcal{C}, \chi)$ (cf. Eq. (2) of Ref. [14]). We simulate our binaries using either the `IMRPhenomPv2_NRTidal` (red) or the `PhenomNSBH` (black) waveform models, using the ALF2 EOS and the CE+ET detector network. Allowing for tidal disruption does not significantly change the distributions inferred in the right panel of Fig. 3.4.

3.6 EOS systematics

Uncertainties in the NS EOS can affect our ability to distinguish BHNS from BNS systems. In this appendix we focus on the most pessimistic scenario compatible with current observations, and we analyze 60 detections with the HLV network to estimate the worst-case impact of EOS uncertainties on our results.

We inject GW observations of binaries modelled with the ALF2 EOS and different values of the mixing parameter $\mathcal{F}$ into the Bayesian framework trained with APR4. When we inject purely BNS binaries (blue curve in Fig. 3.5) we correctly recover the expected fraction of BNS/BHNS, i.e. $\mathcal{F} = 0$. On the other hand, when we inject purely BHNS systems (red distribution in Fig. 3.5) we obtain inconsistent results, i.e. the posterior probability of $\mathcal{F}$ peaks around the wrong estimate. This is because the ALF2 EOS yields large values of the tidal deformability $\widetilde{\Lambda}$ relative to APR4, and therefore the observed events are misinterpreted as BNSs when they would be interpreted as BHNS with the "correct" assumption on the EOS.

Vice versa, we can inject observations of binaries modelled with APR4 into a Bayesian framework trained with ALF2. In this case, when we inject a pure-BHNS population we can correctly recover it as such, because APR4 yields values of $\widetilde{\Lambda}$ which are generally smaller than those derived using ALF2. However, when we inject BNS systems the approach leads to the wrong reconstruction.

In summary, EOS uncertainties can dramatically affect the inference in the worst-case scenario where we use the stiffest EOS to recover astrophysical systems that correspond to the softest EOS, or vice versa. We expect the uncertainty in the EOS to reduce significantly through electromagnetic and GW observations well before third-generation detectors become operational. A more realistic Bayesian analysis should reconstruct the EOS and the population fraction simultaneously. We plan to address this problem in future work.

3.7 Tidal disruption

Tidal disruption can affect the merger dynamics. Investigations of BHNS mergers in numerical relativity have shown that the occurrence and nature of tidal disruption depends, in general, on the binary parameters, and in particular on the BH spin, the adopted EOS model, and the binary mass ratio (cf. [14, 202]). Tidal disruption is a characteristic signature of the presence of a BH in the binary, because it typically produces a sharp frequency cutoff in the GW signal [230]. From the presence of such a cutoff (if detectable) we can conclude that one of the merging objects is a BH [204, 205].

In most of our work we have focused on systems where tidal disruption does not occur in the sensitive frequency band of the detectors. This is a conservative choice, in the sense that our method does not rely on the additional information provided by tidal disruption. To check that tidal-disruption effects would not significantly affect our conclusions, we have computed the posterior probability distribution of $\mathcal{F}$ obtained using injections in which disruptive mergers can occur. Using the criterion in Eq. (2) of [14], this corresponds to binaries with $q < Q_D(\mathcal{C}, \chi)$, where $q = M_{\rm BH}/M_{\rm NS}$ is the binary mass ratio, $\mathcal{C} = M_{\rm NS}/R_{\rm NS}$ is the NS compactness, and χ is the dimensionless BH spin. In Fig. 3.6 we compare results obtained using the `IMRPhenomNSBH` model [203] (black line), which allows for tidal disruption, against

the results in right panel of Fig. 3.4 (red line). Our main conclusions are clearly unaffected.

Chapter 4

Gravitational wave population inference with deep flow-based generative network

We combine hierarchical Bayesian modeling with a flow-based deep generative network, in order to demonstrate that one can efficiently constraint numerical gravitational wave (GW) population models at a previously intractable complexity. Existing techniques for comparing data to simulation, such as discrete model selection and Gaussian process regression, can only be applied efficiently to moderate-dimension data. This limits the number of observable (e.g. chirp mass, spins.) and hyper-parameters (e.g. common envelope efficiency) one can use in a population inference. In this study, we train a network to emulate a phenomenological model with 6 observables and 4 hyper-parameters, use it to infer the properties of a simulated catalogue and compare the results to using a phenomenological model. We find that a 10-layer network can emulate the phenomenological model accurately and efficiently. Our machine enables simulation-based GW population inferences to take on data at a new complexity level.

4.1 Introduction

Since the discovery of gravitational waves (GWs) [21], GW events are being detected routinely at an accelerating pace. By the end of the third observational run (O3) of the ground-based GW detector network, which will end on 31 April 2020, one can anticipate ~ 60 detected events in total. The Laser Interferometer Gravitational-Wave Observatory (LIGO) is expected to operate at its design sensitivity in late 2021, which will detect ~ 100 events per year [37]. And with the planned A+ upgrade, we will detect hundreds to a thousand events per year [231]. With the growing GW catalogue, the focus of gravitational wave astrophysics will rapidly shift toward studying the population of GW events [181, 232]. The population of GW events offers a unique window into a plethora of physics, including fundamental physics such as modifications to general relativity (GR) [233], the expansion rate of the universe [45], and astrophysics related to the progenitor of the binaries [234, 235, 236, 237]. The growing catalogue of stellar-mass compact binary systems detected by GWs offers burgeoning insights to the physics governing their evolution. At the same time, its increasing complexity demands more sophisticated modeling and data analysis techniques.

Current state-of-the-art GW analyses employ phenomenological parametric models to describe the GW population [238, 239, 240, 241, 242]. This is advantageous for its simplicity and agnostic to physical assumptions. On the other hand, it cannot provide much physical insight directly precisely because of the same reason. Alternatively, there are simulations which create synthetic populations of GW events based on some physical assumptions which are characterized by a set of parameters, such as the metallicity of the environment [243] or the escape speed of the stellar cluster in which the GW-emitting binary resides [244]. One can in principle compare the simulation results to the data and obtain direct constraints on these physical parameters. This is often done by calculating the Bayes factor between models with different parameters under the same parameterization [245, 246, 247]. In practice, the simulation-based approach has an obvious disadvantage—simulations are often computationally heavy. Obtaining constraints on the physical parameters requires good sampling in the parameter space of interest, which in turn would require a simulation on each sample point, and the heavy computational load of each simulation basically renders this thorough sampling impractical.

There are recent developments in circumventing this technical difficulty by creating an

emulator of the simulations with machine learning techniques [190, 191]. They emulate the output of the simulations with Gaussian process regression (GPR) and principal component analysis (PCA) without going through the sophisticated simulations, hence gaining enough speed up so that the emulator can be used in the population inference. Despite the novelty demonstrated in previous studies, this existing method has a few limitations:

i. Data with high complexity, such as simulations parameterized by a large number of hyper-parameters, will require a decent number of training simulations to reach a given accuracy. Since the machine is running Gaussian processes on every principal component (PC) that characterize the entire set of simulations, which the number scales roughly linearly with the number of simulations, the GPR-PCA machine becomes progressively inefficient in emulating simulations as the complexity of the set of simulations increases[1]. Also, PCA is used to compress the dimension of the training data in order to reduce the computational load, which means there is an inevitable loss of information.

ii. As mentioned in the first point, the computational load of a GPR-PCA machine scales linearly with the number of PCs after the compression. If one wants to maintain the same speed of the machine, more PCs need to be discarded, which degrades the quality of the interpolation and potentially introduces bias into the final result. Another issue is that the existing machines use histograms to estimate the probability density function of their observable space, which means their estimate of the probability density is binning-dependent.

iii. Moreover, the memory requirement for a histogram increases geometrically with the dimension of the problem. For example, we want to have 6 observables in our problem, and we choose to bin our observables into 30 bins in each observable axis. Assuming we use FLOAT32 to store the histograms which we use to train the machine, and we have 1000 simulations, then the size of the training data to be loaded in memory will be ~ 2.5 TB, which is not available on most computer cluster. Therefore the existing machine cannot be easily generalized to higher-dimensional problems.

In this work, we demonstrate the technique of normalizing flows (a type of flow-based generative model) can overcome these difficulties, hence improving the efficiency and accuracy of simulation-based GW population inference. More specifically, we use a normalizing flow

[1]The more complex the simulations are, the harder it is to compress the entire set of simulations to the same number of principal components.

network to emulate the likelihood in a Hierarchical Bayesian Analysis (HBA) framework. The field of deep learning is growing exponentially due to advancements in various fields: innovations on the topic of neural networks [248, 249], increasingly powerful hardware [250, 251], development of open source general purpose deep learning libraries [252, 253], etc. These advancements lower the barrier to apply deep learning techniques to problems in other fields. In particular, the astronomy and astrophysics community has applied deep learning techniques in various aspects, including signal detection [254, 255, 256, 257, 258], inference [259, 260, 261, 262] and simulations [263]. Deep learning techniques often offer more flexible and much faster solutions compared to traditional methods. Normalizing-flows models rely on using a series of simple invertible transformations to map a complicated distribution (usually the data observed) to a simple one (e.g. a multivariate Gaussian). This specific formulation can provide an estimate of the log-probability for a given data-point in the original distribution. They can therefore be used for density estimation, see for instance [264].

This paper is structured as follow: In section 4.2,e describe the specific problem of GW population inference and review the HBA framework. In section 4.3, we review the basics of normalizing flows, layout the architecture of our network. In section 4.4, we present our data and results. In section 4.5, we discuss prospects of this work.

4.2 Hierarchical Bayesian inference

In this section, we summarize the salient points of Hierarchical Bayesian inference and clarify our objective. We refer interested readers to more detailed explanations in the literature [77, 265, 266]. GW data is usually given as a time series with some characteristic waveform. In order to extract physical quantities from the time series, such as masses and spins of a GW-emitting binary, one often adopts a parameter estimation process with Bayesian inference [85]. Given some data $\boldsymbol{d}$, the posterior probability of the signal being an astrophysical source with parameters $\boldsymbol{\theta}$ is given by $p(\boldsymbol{\theta}|\boldsymbol{d}) \propto p(\boldsymbol{d}|\boldsymbol{\theta})p(\boldsymbol{\theta})$, where $p(\boldsymbol{d}|\boldsymbol{\theta})$ is the likelihood of observing the data given our model of the astrophysical signal and detector, and $p(\boldsymbol{\theta})$ is the prior we assume on the source parameters. The prior encodes our intuition on the underlying physics (for example, mass should not be negative), and plays an important role in interpreting the result [267, 268].

A hierarchical analysis parameterizes the prior used in parameter estimation of a GW event with some *hyper-parameters* $\boldsymbol{\lambda}$, so that we can infer the true hyper-parameters by marginalising over the event parameters,

$$p(\boldsymbol{\lambda}|\boldsymbol{d}) = \frac{p(\boldsymbol{\lambda}) \int p(\boldsymbol{d}|\boldsymbol{\theta}) p(\boldsymbol{\theta}|\boldsymbol{\lambda}) d\boldsymbol{\theta}}{p(\boldsymbol{d})}. \tag{4.1}$$

The term $p(\boldsymbol{d}|\boldsymbol{\theta})$ is the single event likelihood, whereas $p(\boldsymbol{\lambda})$ is now a prior on the hyper-parameter. $p(\boldsymbol{\theta}|\boldsymbol{\lambda})$ is the *population likelihood*. For clarity, we denote the parameters which describe the individual GW event properties as *event parameters*, $\boldsymbol{\theta}$, and the parameters which describe the entire set of events as *population parameters*, $\boldsymbol{\lambda}$. As an example, in studies which take the route of employing phenomenological models, $p(\boldsymbol{\theta}|\boldsymbol{\lambda})$ could be a power law in mass, where the spectral index α is the population parameter and the mass m is the event parameter, i.e. $p(m|\alpha) \sim m^{\alpha}$. In contrast, a simulation-based model often provides a synthetic catalogue of GW event, instead of an analytical expression of the population likelihood. The objective of this study is to find an efficient way to construct an emulator of the population likelihood $p(\boldsymbol{\theta}|\boldsymbol{\lambda})$ given a set of GW catalogue generated by numerical simulations, so we can then use the emulator in eq. (6.11) to compute the population posterior.

For a set of events which are drawn independently from the same underlying population, and if the parameter estimation of different astrophysical events is not correlated (i.e. the signal are not overlapping), the likelihood of observing that particular set of events can be factorized into the product of the individual event likelihoods,

$$p(\boldsymbol{d}|\boldsymbol{\lambda}) = \int p(\boldsymbol{d}|\{\boldsymbol{\theta}\}) p(\{\boldsymbol{\theta}\}|\boldsymbol{\lambda}) d\{\boldsymbol{\theta}\} \tag{4.2}$$

$$= \prod_{i=1}^{N_{\rm obs}} \int p(\boldsymbol{d}_i|\boldsymbol{\theta}_i) p(\boldsymbol{\theta}_i|\boldsymbol{\lambda}) d\boldsymbol{\theta}_i. \tag{4.3}$$

Note that $\boldsymbol{d}$ in Eq.(4.2) is the entire time series observed by LIGO, while $\boldsymbol{d}_i$ is Eq. (4.3) refers to the segment which contains the event characterized by $\boldsymbol{\theta}_i$. The term $p(\boldsymbol{d}_i|\boldsymbol{\theta}_i)$ is usually rewritten as $p(\boldsymbol{\theta}_i|\boldsymbol{d})p(\boldsymbol{d}_i)/p(\boldsymbol{\theta}_i)$ using Bayes' theorem. Combining Eq. (6.11) and

Eq. (4.3), we obtain the population posterior,

$$p(\boldsymbol{\lambda}|\boldsymbol{d}) = p(\boldsymbol{\lambda}) \prod_{i=1}^{N_{\rm obs}} \int \frac{p(\boldsymbol{\theta}_i|\boldsymbol{d}) p(\boldsymbol{\theta}_i|\boldsymbol{\lambda})}{p(\boldsymbol{\theta}_i)} d\boldsymbol{\theta}_i. \tag{4.4}$$

The event posterior PDF $p(\boldsymbol{\theta}_i|\boldsymbol{d})$ is often given in the form of S discrete samples by a parameter estimation process [197, 269]. We can now make use of the posterior samples produced by a separate parameter estimation pipeline, thus avoiding unnecessary re-computation of estimating $p(\boldsymbol{d}|\boldsymbol{\theta})$ and reducing the computation load for each population inference run significantly. The integral in Eq. (4.4) is essentially the expectation value of the prior-reweighted population likelihood, which can be turned into a discrete sum over the event posterior PDF samples:

$$p(\boldsymbol{\lambda}|\boldsymbol{d}) = p(\boldsymbol{\lambda}) \prod_{i=1}^{N_{\rm obs}} \frac{1}{S_i} \sum_{j=1}^{S_i} \frac{p({}^j\boldsymbol{\theta}_i|\boldsymbol{\lambda})}{p({}^j\boldsymbol{\theta}_i)}, \tag{4.5}$$

where j labels the $j-$th sample of the $i-$th event. Our models in this work do not predict the event rate, so we also leave the rate out in deriving Eq (6.17). Since the event rate is integrated over all the event's parameters, it is solely a function of the hyper-parameters, so traditional interpolation methods can handle the rate, and it can be incorporated into the inference machine trivially.

Parameter estimation of GW events comes with its own systematics [270, 271, 272] and the computation is often quite time consuming. In the limit of high signal-to-noise ratio (SNR), measurement uncertainties are negligible and the inferred parameters of an event will be distributed as a Gaussian around the true value [273], with standard deviation inversely proportional to the SNR. To avoid complication and unnecessary use of computational resources, in this study we take the high-SNR limit and treat the measured events as if they had no measurement systematics and statistical uncertainties on the event parameters, i.e. $p(\boldsymbol{\theta}_i|\boldsymbol{d}) = \delta(\boldsymbol{\theta}_{i,\rm true} - \boldsymbol{\theta}_i)$. Then the integration in Eq.(4.4) will simply pick out the correct value, therefore the posterior can be written as

$$p(\boldsymbol{\lambda}|\boldsymbol{d}) = p(\boldsymbol{\lambda}) \prod_{i=1}^{N_{\rm obs}} p(\boldsymbol{\theta}_i|\boldsymbol{\lambda}). \tag{4.6}$$

In the high-SNR limit, the prior on event parameters is irrelevant [273] and can be treated as a constant. Uncertainties in the selection biases will propagate through the analysis pipeline, resulting in an additional systematic error in the result when analysing real data [274, 275]. In this paper, our goal is to demonstrate that this deep learning technique can enable the use of more sophisticated simulations in population inference, and we are generating simulated data for this purpose. Leaving the selection biases out avoids the confusion between systematic from the deep learning method and inaccuracy in the selection biases. We focus here on the ability of the model to recover the hyper-parameters $\boldsymbol{\lambda}$ without considering the effect of selection biases, so any systematics will be due to the inaccuracy in the interpolation.

In reality, the uncertainties and systematic biases in event parameter estimation will propagate to the population inference result, smoothing out the population posterior and adding biases to the inferred population parameters. This means that systematic biases induced by the inaccuracy of our interpolation method will become less significant when we include measurement uncertainties and biases in our analysis, so the results we present in this work are conservative.

4.3 Normalizing flows

As posed in section 4.2, the central problem we are trying to tackle in this paper is: Given a set of simulated catalogues of GW events, with each event characterized by a vector of event parameters $\boldsymbol{\theta}$ and each catalogue labelled by a vector of hyper-parameters $\boldsymbol{\lambda}$, can we construct a function that can approximate $p(\boldsymbol{\theta}|\boldsymbol{\lambda})$ with satisfying accuracy, and at the same time can be evaluated fast enough to be used as the population likelihood in a hierarchical Bayesian analysis?

We approach this question using a conditional neural density estimator, in particular a flow-based generative (often referred as normalizing flow) model. Flow-based generative models have been recently developed and explored in the machine-learning community [264, 276, 277, 278, 279, 280]. This family of models has a unique perk compared to other neural generative models. In addition to being able to perform good data generation, they also provide an estimate of the probability density function of the data. This makes this

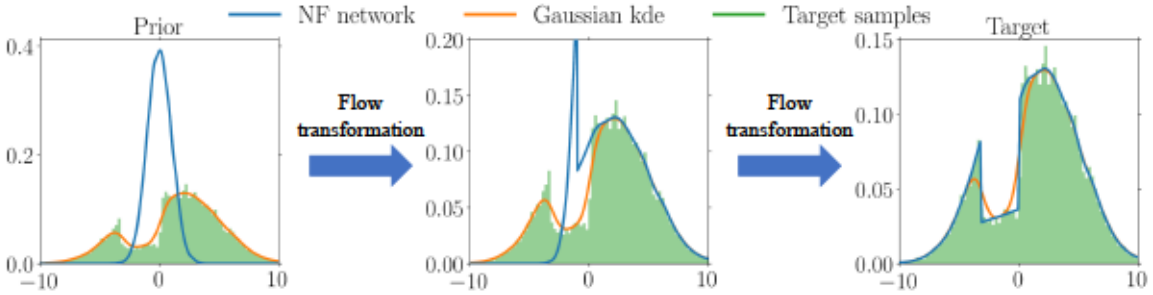

Figure 4.1: An illustration of the working principle of normalizing flow. Given the target samples (histogram in green), whose pdf we want to estimate , we apply a series of transformations to wrap a Gaussian to fit the target sample. Since the probability density of the Gaussian can be obtained trivially, the pdf of the target (shown in blue) can also be computed as long as the transformations are known. In the case of a neural network, the transformation is a set of parameterized functions, whose parameters are obtained during the training of the neural network. For comparison, we also use a Gaussian kde to estimate the pdf given the target samples. While the Gaussian kde can capture the bimodality of the target, it misses the sharp edges of the distribution. On the other hand, the normalizing flow framework reproduce the distribution with excellent accuracy.

family of model a perfect fit for our task. In this section, we present the general principles behind the model we employ.

Normalizing flow propose to transform a simple density (e.g. a Gaussian) $z \sim p_z$ into a target, complex, density (the data) $x \sim p_x$. Building a model to learn a mapping g from z to x is a common idea in generative models, and several methods have been proposed, e.g. using discriminator networks (Generative Adversarial Networks, [249]), or approximate inference (Variational Auto Encoders [281]). However, these approaches don't allow to evaluate p_x, but can only generate new data that mimics p_x. On the other hand, normalizing flow [276, 282] propose to use a mapping function $g : \mathbb{R}^d \to \mathbb{R}^d$ that is invertible (bijective), with a tractable Jacobian. This will allow to learn the mapping using directly the maximum likelihood, through a change of variable, with which we can compute the normalized probability density $p_x(x)$ from $p_z(z)$ when we use an invertible function:

$$p(\boldsymbol{x}) = p_z(\boldsymbol{z}) \left| \det \left(\frac{\partial g(z)}{\partial \boldsymbol{z}^T} \right) \right|^{-1}. \tag{4.7}$$

Eq. (4.7) is tractable as long as g is easily invertible and the determinant of its Jacobian is

easy to compute, hence normalizing flow only require a careful design of g. Interestingly, if two functions g_1 and g_2 are bothinvertible and have a tractable Jacobian, the composition $g_1 \circ g_2$ also has these properties. Additionally, generating new data x can be done by drawing a sample $z \sim p_z$ and computing the value of x through the set of transforms in the normalizing flow network, $x = f^{-1}(z) = g(z)$. As written above, the density on a given data point x can be computed as the density of its image $f(x)$ multiplied by the determinant of the corresponding Jacobian.

Instead of choosing one complicated transform which maps our prior to the target density distribution, we can restrict the network to use a series of K simple transforms $g_k, k = 1, \ldots, K$, which are invertible and whose Jacobians can be easily calculated. We can then apply Eq. (4.7) repeatedly to obtain arbitrarily complex probability density distributions, given enough number of transforms. With the series of transform, the target random variable and its probability density distribution are given by

$$\boldsymbol{z_k} = g_k \circ \cdots \circ g_1(\boldsymbol{z_0}), \tag{4.8}$$

$$p(\boldsymbol{x}) = p(\boldsymbol{z}_K) = p_{z_0}(\boldsymbol{z_0}) \prod_{k=1}^{K} \left| \det \left(\frac{\partial g_k}{\partial \boldsymbol{z}_k} \right) \right|^{-1}. \tag{4.9}$$

As an example, we can now estimate the probability density in a relatively simple distribution such as a multivariate Gaussian, then apply Eq.(4.9) to obtain the probability in the target distribution. Given the transformation, we can also generate new samples from the distribution by applying the transforms to a set of samples from the prior as well.

Figure 11.1 illustrates the essence of normalizing flow. Given the target samples, we apply multiple transforms to a one-dimensional Gaussian distribution to fit the target[2]. After two transformations, the Gaussian prior is wrapped to fit the target sample. We also included a Gaussian kernel density estimation (kde) result for comparison. While the Gaussian kde is missing the sharp edges of the target distribution, normalizing flow can capture these features.

Choosing the correct transformation is crucial to designing an efficient network for our specific problem. Because our target is $p(\boldsymbol{\theta}|\boldsymbol{\lambda})$, it is essential that our network is capable to model conditional probabilities. A specifically designed autoregressive model known as Masked

[2]We used planar flow described in [283] for the illustration.

Autoregressive Flow (MAF) [264] trivially incorporates the ability to model conditional probability. Therefore, we adopt MAF as the "flow" in the flow-based generative model. Autoregressive models [284, 285] expand the joint density of a set of random variables $p(x)$ as a product of one-dimensional conditionals $p(\boldsymbol{x}) = \prod_i p(x_i|\boldsymbol{x}_{1:i-1})$. Assuming a specific order of those random variables $\boldsymbol{x} = \{x_1...x_D\}$, the $i-th$ conditional probabilities only depend on the random variables appearing prior to x_i, i.e. $p(x_i) = p(x_i|x_{<i})$, which $x_{<i} = \{x_1...x_{i-1}\}$. From the definition of an autoregressive model, we can understand why it naturally extends to conditional probability modeling. As long as the conditional variable $\boldsymbol{y}$ comes before other random variables, we can write the conditional probability of observing $\boldsymbol{x}$ given $\boldsymbol{y}$ as

$$p(\boldsymbol{x}|\boldsymbol{y}) = \prod_i p(x_i|\boldsymbol{x}_{1:i-1}, \boldsymbol{y}), \tag{4.10}$$

which is similar to the definition of an autoregressive model. The main drawback of this approach is its sensitivity to the order of the variables x_i. Refs. [264, 286] show that specific autoregressive models can be interpreted as normalizing flow (i.e. they have tractable Jacobian and are invertible). Using an autoregressive model as normalizing flow allows to increase the flexibility of the model while retaining a tractable Jacobian, but also to make the model more resilient to the ordering of variables. More specifically, in the MAF framework, a Conditional-MAF simply stacks MADEs functions that have been made *conditionals* by adding the condition $\boldsymbol{\lambda}$ as an additional input for each layer. We can train a conditional-MAF network to emulate a given set of training GWs catalogue. Once the network is trained, it can be used as the population likelihood in Eq. (6.11).

The only difference between the model described in [264] and the model implemented in this paper are the size of input layer and network-related hyper-parameters (such as the number of hidden units in a hidden layer). Therefore, we refer interested readers to Refs. [264] and [287] for more elaborated description of the model. We use 1024 hidden units in each layer, and we explore two variations of this model, one using 5 flow layers and the other one using 10 layers. We find the accuracy of a 10-layers network to be sufficient for our purpose.

4.4 Validating against a phenomenological model

To demonstrate the robustness of our deep learning interpolation method, we cross check the performance of our machine against a phenomenological model, for which we can write down an analytic expression for $p(\boldsymbol{\theta}|\boldsymbol{\lambda})$, thus we can use the model directly in the population inference process and validate the results from the nerual network. We generate our training data from the analytical model and train a network to interpolate the model. We use the trained network to emulate $p(\boldsymbol{\theta}|\boldsymbol{\lambda})$ in a population inference analysis, then compare the inference result using the network with the result using the analytical model.

We generate our population according to the prescriptions described in [232]. The most general model family described in [232] includes 7 event parameters and 16 hyper-parameters. In order to facilitate the speed of the training and inference process, we choose 6 event parameters and 4 hyper-parameters as our phenomenological models. Our model includes the primary mass m_1, mass ratio q, the spin magnitude of each binary $a_i, i \in (1, 2)$ and the tilt angles t_i between each BH spin and the orbital angular momentum.

For simplicity, we parameterized our mass model as two independent power laws in the primary mass and mass ratio,

$$P(m_1) \propto \begin{cases} {m_1}^{\alpha_m} & \text{if } m_1 \in [5, 50] \\ 0 & \text{otherwise,} \end{cases} \tag{4.11}$$

$$P(q) \propto q^{\beta_m} \qquad q \in (0, 1], \tag{4.12}$$

where α_m and β_m are the spectral indices of the two power laws. We choose the lower mass cutoff to be 5 $M_\odot$ and the upper mass cutoff at 50 $M_\odot$. Both are assumed to be sharp. The range of sampling in α_m and β_m are chosen to be $[-3, -1]$ and $[1, 3]$, respectively. More sophisticate models [238, 241, 242, 288] were discussed in [232], which add more free parameters into the model to capture more features in the data. However, there is no strong evidence favouring one model over another, therefore we pick a simple model in this studies.

We assume that both BH spins magnitudes are drawn from a common beta distribution

[239]:

$$P(a_i|\alpha_a,\beta_a) \propto \frac{{a_i}^{\alpha_a-1}(1-a_i)^{\beta_a-1}}{B(\alpha_a,\beta_a)}, \tag{4.13}$$

where $B(\alpha_a,\beta_a)$ is the beta function. Following the choice presented in [232], we choose to model the moments of the beta distribution using the mean ($\mathbb{E}[a]$) and variance ($\mathrm{Var}[a]$), given by

$$\mathbb{E}[a] = \frac{\alpha_a}{\alpha_a+\beta_a}, \tag{4.14}$$

$$\mathrm{Var}[a] = \frac{\alpha_a\beta_a}{(\alpha_a+\beta_a)^2(\alpha_a+\beta_a+1)}. \tag{4.15}$$

The pdf of a beta distribution can change quite drastically depending on the parameters characterizing the distribution, which means we will need more data and a more complex network to capture the features which represent the change in the pdf as a function of distribution parameters. For simplicity, we fix the mean and variance to be $\mathbb{E}[a] = 0.5$ and $\mathrm{Var}[a] = 0.05$. Note that even though this choice means we do not include the change of the beta distribution as a function of the distribution parameter in the training of our model, the network still needs to fit for the beta distribution we have chosen. This resembles a practical scenario that the model one tries to interpolate has some discrete flags which affect the event parameters distribution, yet there is no need to interpolate over those discrete flags.

Finally, we follow Ref. [241] to simulate the spin orientation. We assume that the tilt angles between each BH spin and the orbital angular momentum are drawn from a mixture of two distributions: an isotropic component and a preferentially aligned component, represented by a truncated Gaussian distribution in $\cos t_i$ peaked at $\cos t_i = 1$

$$p(\cos t_1, \cos t_2|\sigma_1,\sigma_2,\xi) = \frac{(1-\xi)}{4} \tag{4.16}$$

$$+\frac{2\xi}{\pi}\prod_{i\in 1,2}\frac{e^{-(1-\cos t_i)^2/2{\sigma_i}^2}}{\sigma_i \mathrm{erf}(\sqrt{2}/\sigma_i)}. \tag{4.17}$$

The distribution is parameterized by three parameters, σ_1, σ_2, ξ, which are the standard deviation of the two Gaussian and the mixing fraction between the two components. A value of $\xi = 1$ implies that all the BBH spins are preferentially aligned with the orbital angular

Table 4.1: Event parameters and hyper-parameters used in this work

Event parameters $\boldsymbol{\theta}$	
m_1	Primary mass in the binary
q	Mass ratio of the binary
a_1, a_2	Spin magnitudes of the binary
$\cos t_1, \cos t_2$	Tilt angles between each BH spin and the orbital angular momentum.
Hyper-parameters $\boldsymbol{\lambda}$	
α_m	Spectral index of m_1
β_m	Spectral index of q
σ_1, σ_2	Width of the preferentially aligned component of the BH spin orientation

momentum, while $\xi = 0$ implies that the spin orientations are distributed isotropically. The two components represents the two most prominent formation channels of BBH mergers: isolated and cluster formation. We fix the mixing fraction to be $\xi = 0.5$, and include σ_1 and σ_2 in our training. The range of σ_1 and σ_2 are both $[0, 2]$. The parameters and hyper-parameters used in our phenomenological models are summarized in Table 8.1.

Given the analytical model, we train and evaluate the performance of our machine as described below. We create the training set by sampling 100 points in the hyper-parameter space with Latin hyper-cube sampling [289]. For each point in the hyper-parameter space, we create a catalogue of 10^5 BBH events, each characterized by the 6 event parameters, following the distribution parameterized by the 4 hyper-parameters. This means the entire training set contains 10^7 training samples. We also create a smaller validation set, which follows the same method as creating the training set but with only 10 points in the hyper-parameter space. Note that the locations of the points in hyper-parameter space in the validation set is different from the training dataset. We take the state of the network for which the validation loss is minimum as our best-trained model, and use it in the inference process. The entire process of training and validating the 10 layers model takes ~ 10 hours on a Tesla k80 gpu.

Figure 4.2 shows the interpolation result of $p(\boldsymbol{\theta}|\boldsymbol{\lambda})$ for a specific $\boldsymbol{\lambda} = (-2, 2, 0.5, 0.7)$, which is a test point in the hyper-parameter which we have not included in both the training set and validation set. Despite the small scale difference, mainly originating from individual

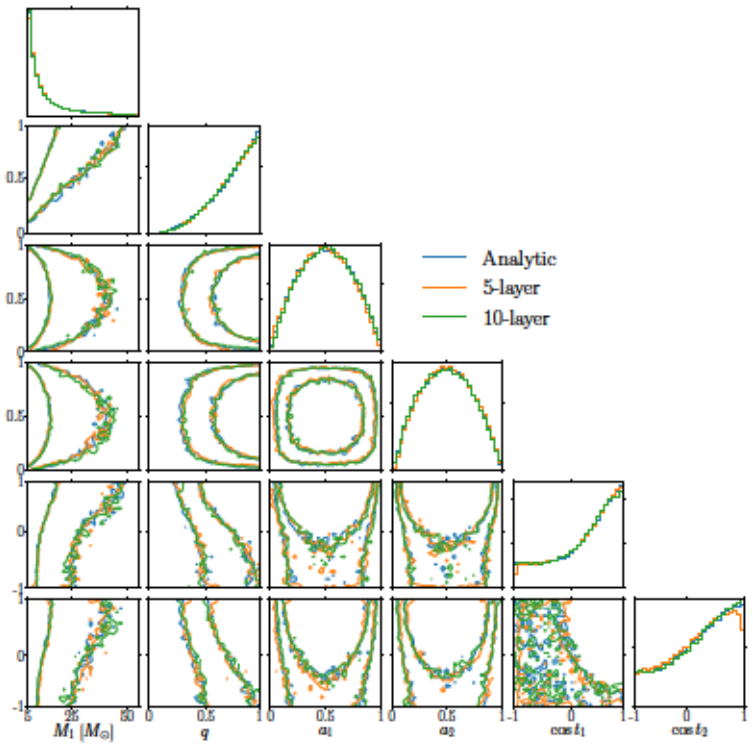

Figure 4.2: The joint probability distribution of the 6 event parameters in the phenomenological model, given the hyper-parameters $\boldsymbol{\lambda} = (-2, 2, 0.5, 0.7)$. The two contour represent the 68% and 95% confidence interval of the sampled distribution. The analytical (blue) line represents the true answer. The 5-layer (orange) and 10-layer (green) lines are the output of the network with the corresponding number of flow layers. Each contour are created from 100000 samples, either drawn from the analytical distribution or generated by the network. The 5-layer model fits the analytical answer fairly well on large scale yet having some inaccuracy near the edge of $\cos t_1$ and $\cos t_2$. We find the accuracy of 10-layer model to be sufficient for our purpose.

sampling fluctuations, both 5-layer and 10-layer models fit the large-scale behaviour of the distribution quite well. In particular, the 10-layer model is performing better than the 5-layer model at the edge of $\cos t_1$ and $\cos t_2$. This is expected since a model with more layers is applying more transforms to the prior distribution, which means it is more flexible in terms of modeling a target distribution, therefore it should be able to capture more features such as the edge of a distribution.

Next, we inspect the performance of the network on a population level. The population posterior produced by a well trained network should be similar to the posterior produced by the analytical model. To test this, we compare the population posterior inferred from

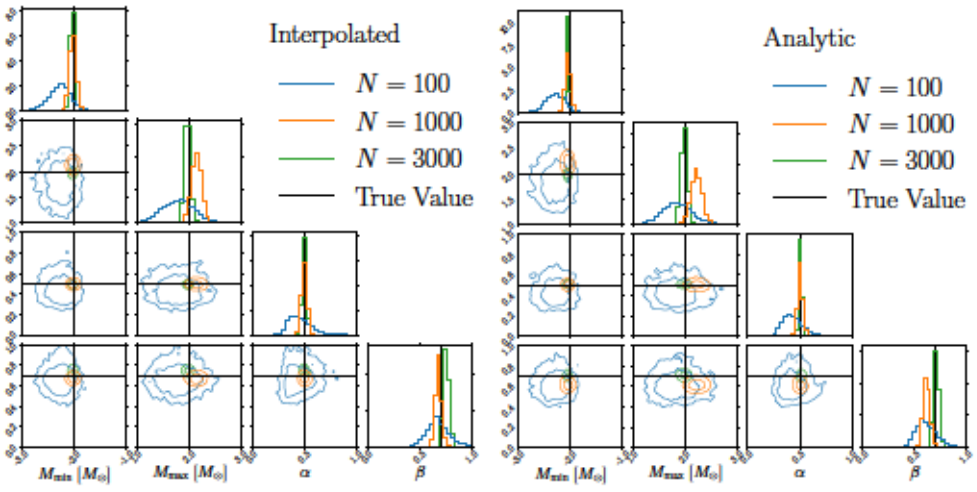

Figure 4.3: *Left*: The population posterior recovered by the neural network emulator as the population likelihood. The injected hyper-parameters are $\boldsymbol{\lambda} = (-2, 2, 0.5, 0.7)$, which is marked by the black lines. The contours are the 68% and 95% confidence intervals. The blue, orange and green line mark the case of having 100, 1000 and 3000 events, respectively. *Right*: The population posterior recovered by the analytical distribution stated in section 4.4. The only difference between the right panel and the left panel is the population likelihood, all other factors are the same.

three simulated "injection" BBH catalogues using the network-output to the results inferred using the analytical model. We create the injection catalogues by sampling events from the distribution characterized by the vector of hyper-parameters $\boldsymbol{\lambda} = (-2, 2, 0.5, 0.7)$. We consider the events in each catalogues to be perfectly measured, which means the measured values are the true value with infinite precision. The main difference between the injection sets are the number of events, which are 100, 1000 and 3000, respectively. These numbers are chosen to be approximately the number of detected events one can anticipated in early-, mid- and late-2020s [44]. Even though the network can in principle extrapolate to regions outside the trained hyper-parameters space, the accuracy is expect to drop, hence the result we obtain will become less credible. Therefore, we choose the range of population prior to be the same as the range where training data are sampled from. We use EMCEE [96] to sample the population posterior (Eq.4.6).

As shown in Fig 4.3, the inference results using a network agree well with the analytical model. Not only the posterior agrees with the injected hyper-parameters within the 95% confidence interval, the shape and the location of the confidence interval produced by the

network is also similar to the analytical result. There are some minor discrepancies in the case which we consider 3000 events, which can be overcame by increasing the number of layers in the network and training. Considering we are not including other sources of error in this analysis, the minor discrepancies shown in Figure 4.3 are unlikely to be the dominant source of systematic error.

We have focused on the accuracy aspect of the machine so far. A equally important aspect of this machine is the speed at which a population inference run is done. With 3000 events and each event with 100 posterior samples in a six dimensional event parameters space, one evaluation of the posterior function described in (4.4) takes ~ 0.1 second if we are using the normalizing flow network. On the other hand, we tried using the simulation and the GAUSSIAN_KDE function from SCIPY to evalute the same posterior function, which each evaluation would take more than ~ 20 minutes. Note that the simulations used here are relatively simple and fast, which can be generated in a minute. In this case, most of the computational cost comes from estimating the probability of a point in the event parameter-hyper parameter space. A typical inference runs requires $\sim 10^3$ to few 10^4 point to ensure convergence of the results. This means the gaussian kernel density estimation method would require months to years to produce one population inference run, while our network requires only a few hours. More sophisticated simulations will need more time to be produced, which can take days or even weeks on a computer cluster, rendering a direct estimate of $p(\theta|\lambda)$ from simulation impossible.

4.5 Discussion

We have incorporated a flow-based deep generative network into a hierarchical Bayesian analysis, and showed that the neural network we have integrated in this study is capable to handle data and simulations which are too complicated for previous machines. While previous studies [190, 191] have shown how population-synthesis simulations and machine learning can be used in GW population inference, they are severely limited in various aspects, especially in terms of scalability, thus cannot be used to explore the increasingly complex GW dataset and simulations in practice. We have demonstrated that a normalizing flow network can be used as a highly accurate, efficient, and most importantly scalable machine in GW population inference. There are up to 15 standard event parameters per BBH

event in GR, among them there are 8 intrinsic parameters (1 mass and 3 spins per black hole), which are particularly important to astrophysical theories. Many population-synthesis models predict features in at least 4 of these intrinsic parameters, very often in 6 or more intrinsic parameters. Previous approaches can only function accurately and efficiently up to 2 event parameters. When one tries to use the previous machine for 3 or more event parameters, the performance in terms of speed and accuracy drops significantly, and the memory usage starts to become unmanageable. As shown in Section 4.4, our network can reproduce the analytical answer very accurately in a reasonable time even with 6 event parameters. Given the high fidelity of our results and the fact that we will have ~ 1000 compact binary coalescence events in late 2020 [44], our method is a promising way forward for simulation-based population inference.

Equipped with this machine, our next step will be testing different state-of-the-art models [290, 291, 292, 293] with the upcoming LVC O3 catalogue. An interesting application is that we are now able to compare different family of model directly. Each of the simulations has their own set of hyper-parameters. After we obtain the population posterior for each of them, we can marginalize it to obtain the evidence and compare between models. The Bayes factor between one model and another will indicate which model is favored by the data. Furthermore, one can compare these simulation-based models to the evidence from a phenomenological model. In this way we can investigate whether a model contains redundant parameters or not. Being able to compare entire families of models means not only we can use the data to constrain the model, we can also gauge the importance of individual components in a simulation, hence gaining insight on how to improve the simulation.

The simulations used in this work are relatively simple compared to the state-of-the-art models. We also neglected event uncertainties and selection bias, which are crucial when applying this method to real data. The precise effect of the interplay between all these uncertainties and systematics will depend on the properties of the data and simulations. We will follow up with a case study which employs our method and state-of-the-art simulations on O3 data in the soon future, with uncertainties and selection bias taken into account.

We only trained a relatively small network with relatively small amount of data, as compared to other deep neural network trained for the same purpose[262, 294]. This means we still have not reached the limit of the network capability. The purpose of this paper is to demonstrate

the robustness and efficiency of our method, yet we have not exactly quantified the precise uncertainty from the network as a function of the size of the training data, simulation complexity and architecture of the network. A study of the precise scaling behavior of the method, which will shed light on the reason why neural networks perform well in this particular type of problem, will be carried out in the future.

This study is specifically dedicated to the GW community, therefore we discussed the BBH case. But the machine can be applied to more general problems such as other GW sources, or even other inference problems that are not related to GWs. As examples, while keeping the vast differences between detector design and potential sources of systematic error in mind, the same machinery can be applied to understanding the population of gamma-ray burst [295], fast radio burst [296] and exoplanets [297], especially when the data is noisy and Bayesian statistics is necessary to characterize the data.

Because of its capability to solve problems with much greater efficiency and accuracy in many settings, deep learning is revolutionizing many different aspects of our society. By integrating the existing tools from deep learning to GW population inference, we enable the possibility of constraining state-of-the-art models with upcoming data at a complexity which was previously intractable. On the other hand, the traditional tools we use to understand physical models and data offer very interpretable checks, which we can use to gauge the performance of our deep learning model and improve it. GW data analysis is known to be in the extremely noise dominated regime, which is where deep learning often encounter trouble in. We hope that the progressively frequent cross talk between the deep learning and GW communities can be mutually beneficial to both fields.

Chapter 5

Joint constraints on the field-cluster mixing fraction, common envelope efficiency, and globular cluster radii from a population of binary hole mergers via deep learning

The recent release of the second Gravitational-Wave Transient Catalog (GWTC-2) has increased significantly the number of known GW events, enabling unprecedented constraints on formation models of compact binaries. One pressing question is to understand the fraction of binaries originating from different formation channels, such as isolated field formation versus dynamical formation in dense stellar clusters. In this paper, we combine the `COSMIC` binary population synthesis suite and the `CMC` code for globular cluster evolution to create a mixture model for black hole binary formation under both formation scenarios. For the first time, these code bodies are combined self-consistently, with `CMC` itself employing

COSMIC to track stellar evolution. We then use a deep-learning enhanced hierarchical Bayesian analysis to continuously sample over and constrain the common envelope efficiency α assumed in COSMIC, the initial cluster virial radius r_v adopted in CMC, and the intrinsic mixture fraction f between each channel. Under specific assumptions about other uncertain aspects of isolated binary and globular cluster evolution, we report the median and 90% confidence interval of three physical parameters for the intrinsic population $(f, \alpha, r_v) = (0.20^{+0.32}_{-0.18}, 2.26^{+2.65}_{-1.84}, 2.71^{+0.83}_{-1.17})$. This simultaneous constraint agrees with observed properties of globular clusters in the Milky Way and is an important first step in the pathway toward learning the astrophysics of compact binary formation through GW observations.

5.1 Introduction

The number of gravitational-wave (GW) detections is growing at an accelerating pace since the first detection [21]. The LIGO-Virgo-KAGRA Collaboration (LVKC) recently released the second Gravitational-Wave Transient Catalog (GWTC-2), which includes 39 events from the first half of of the third observational run (O3) [31]. The number of GW events in this new catalogue (50) is ~ 4 times the number of events from the first two observational runs combined [181], allowing for the increasingly sensitive exploration of their mass, spin and merger redshift distributions [15]. As the statistical uncertainties in these distributions continue to drop with the growing number of detections, the population of GW events provides a unique, and increasingly powerful, avenue to probe a wide range of topics, including fundamental physics [298], cosmology [45, 299], and astrophysics [300, 301, 302].

One of the most pressing questions in GW population analyses is which binary formation channels generate the observed GW events. In particular, it is expected that compact binary mergers may arise via isolated binary evolution in the stellar field or dynamical assembly in dense clusters, although a variety of other channels have also been theorized [303, 304, 305]. In the isolated field scenario, compact binary mergers are the end result of stellar binary evolution [306, 307]. On the other hand, events from dynamical formation scenarios are formed through multi-body encounters in dense environments, such as globular clusters, young stellar clusters, or galactic nuclear clusters [308, 309]. While the precise distributions of compact binaries originating from each scenario are not known, field and cluster channels generally differ in their predictions regarding spin, eccentricity, and component

mass distributions of binary mergers. Due to mass transfer and tidal alignment, binaries resulting from the isolated formation tend to have component spins aligned with their orbital angular momenta, whereas dynamically formed binaries are believed to have an isotropic distribution of spins [235, 310, 311, 312]. Also, hierarchical mergers are likely only possible in a dynamical-formation scenario [236, 244, 313, 314], which could result in black holes with masses in the theorized pair-instability supernova (PISN) gap (commonly known as the "upper mass gap") [315, 316].

Some studies have already sought to use the observed masses and spins of compact binary mergers to infer the mixing fraction between the two formation channels [15, 317, 318]. Such studies, however, generally adopt heuristic models for expected spin distributions, or ignore possible variation within individual channels that may be correlated with the inferred mixing fractions. Moreover, although the mixing fraction itself is an important question, understanding the mixing fraction alone yields little insight on the physics of each underlying formation channel. Thus, it is important to infer the mixing fraction and channel-specific parameters *jointly*. In this study, we create a mixture model of merging binary black holes (BBHs) from isolated binary evolution using the binary population synthesis code `COSMIC` and from globular clusters (GCs) using the GC evolution code `CMC`. We infer the properties of this mixture model by applying a deep learning enhanced hierarchical Bayesian modeling framework on the GWTC-2 BBH catalogue.

The paper is structured as follows: In section 6.2, we describe the library of `COSMIC` and `CMC` simulations used in this study. In section 6.3, we review our data analysis pipeline that applies deep-learning to emulate and interpolate between our library, allowing for hierarchical inference of parameters governing binary formation. In section 11.3, we present results obtained by applying our pipeline to public data released in support of GWTC-2. Finally, in section 11.4, we discuss implications of this work.

5.2 Simulation

5.2.1 Isolated binary evolution with `COSMIC`

We generate a cosmological population of BBH mergers originating from isolated binary evolution using `COSMIC`[319], which is based on an updated version of `BSE` [320]. See [319]

for a comprehensive summary of all upgrades currently employed in `COSMIC` and [321] for a detailed discussion of the prescriptions which most heavily impact compact-object formation in biaries. We assume that massive stars are initially distributed with masses following a power law with index $\alpha = -2.3$ [322] and 70% of them have companions with mass ratios distributed uniformly [323]. We distribute initial orbital periods with a power law in log orbital period with index $\pi = -0.55$ and log $(P_{\rm orb}/{\rm day}) \in [0.15, 5]$ following the assumptions of [323, 324] and initial eccentricities with a power law with index $\xi = -0.45$ for $e \in [0.001, 0.9]$ [323].

One of the largest uncertainties in binary evolution is the amount a binary's orbital separation shrinks as a result of common envelope evolution [325]. `COSMIC` employs the $\alpha\lambda$ prescription to parameterize how efficiently orbital energy is used in unbinding the stellar envelope, where λ is the envelope binding energy and is calculated following Appendix A of [326] assuming no contributions from ionizing energy. Previous studies suggest a wide range of ejection efficiencies varying from $\alpha = 0.25 - 5$ for a wide variety of stellar masses [327, 328, 329]. To capture this uncertainty, we ran 8 separate models ($\alpha = 0.25, 0.5, 0.75, 1, 2, 3, 4, 5$) each with 16 metallicity bins spaced logarithmically between $Z_\odot/200$ and $2Z_\odot$, where $Z_\odot = 0.017$ [330]. The binary evolution model, except for the variation of envelope ejection efficiency, is identical to that of [321] which consistently produces local ($z < 0.01$) merger rates consistent within a factor of 2 to the 90% credible interval of the observed rates from the GWTC-1 catalog for $\alpha = 1, 5$. For a discussion of the local comoving merger rates for our simulated populations, see Sec. 11.4.

To generate a cosmological population of merging BBHs, we use the redshift-dependent star formation history and metallicity evolution of [331] and assume *Planck 2015* cosmological parameters: $H_0 = 68$ km s^{-1} Mpc^{-1}, $\Omega_m = 0.31$ and $\Omega_\Lambda = 0.69$ [332] as implemented in `astropy` [333, 334]. Similar to [321], we assume a truncated log-normal distribution of metallicities with $\sigma = 0.5\,{\rm dex}$ following [312]. We break the star formation into 100 linearly spaced redshift bins between 0 and 14 and calculate the number of BBHs formed, weighted by their metallicity, by normalizing the total mass of stars from our simulated population to the total amount of star formation in each redshift bin. We then record the lookback time and the redshift of each BBH merger to create a catalog of all merging BBHs for redshifts $z < 15$.

5.2.2 Globular cluster evolution with CMC

We use N-body simulations presented in the `CMC Cluster Catalog` [335] to simulate GC evolution. These simulations were computed using `CMC` (for `Cluster Monte Carlo`) [336, 337], a Hénon-type Monte Carlo code which includes various processes relevant to BH binary formation including two-body relaxation [336], three-body binary formation [338], direct integration of small-N resonate encounters [339, 340], and stellar/binary evolution. For the latter, `CMC` uses updated versions of `SSE` and `BSE` [320, 341], identical to those used in `COSMIC`, only varying in choices of binary evolution prescriptions. In `CMC`, we assume a 5% percent primordial binary fraction (uniform across all primary masses which in turn are drawn from a Kroupa [342] initial mass function over the range $0.08 - 150\,M_{\odot}$). We assume mass ratios are drawn from a uniform distribution in range $[0.1 - 1]$. Binary orbital periods are drawn from a distribution flat in log-scale, with the orbital separations ranging from near contact ($a \geq 5(R_1 + R_2)$, where R_1 and R_2 are the stellar radii) to the hard/soft boundary of the cluster (reflecting the fact that soft binaries are expected to be broken quickly through dynamical encounters). Additionally, we assume initial eccentricities are drawn from a thermal distribution [343].

In the `CMC Cluster Catalog`, four key cluster parameters are varied between the different simulations: initial number of stars per cluster ($N/10^5 = 2, 4, 8, 16$), initial virial radius ($r_v/\mathrm{pc} = 0.5, 1, 2, 4$), metallicity ($Z/Z_{\odot} = 0.01, 0.1, 1$), and radial position within a (Milky-Way-like) galactic potential ($R_{\rm gc}$/kpc=2,8,20). Collectively, this simulation suite covers the full parameter space of the Milky Way GCs and captures the formation of a variety of astrophysical objects including GW sources, X-ray binaries, millisecond pulsars, and blue stragglers.

By coupling a cluster age distribution model from [344] with the BBH merger delay time distributions gathered from the `CMC` models, a realistic distribution of dynamical BBH merger times can be assembled. In [335], this method was used to estimate a BBH merger rate of roughly $20\,\mathrm{Gpc}^{-3}\,\mathrm{yr}^{-1}$ in the local universe (assuming all N, r_v, Z, and $R_{\rm gc}$ values are equally weighted), consistent with similar rate estimates from other recent studies [345, 346, 347].

While `COSMIC` can produce nearly arbitrarily large catalogs of compact binary mergers, the output of `CMC` is limited by the relatively high computational costs associated with dynamical N-body simulations [337]. As a result, the total number of GW events from our set of `CMC`

models is of order 10^4 compared to several million from each COSMIC model. To mitigate the presence of small-scale fluctuations due to finite sampling, which may inadvertently be learned and reproduced by our emulator, we smooth the binary mass distributions given by each CMC simulation with a gaussian kernel using `scipy.stats.gaussian_kde`. The smoothing preserves physical features in the mass functions, such as high-mass "bumps" due to repeated mergers, while smoothing out small unwanted scale fluctuations.

5.2.3 Mixture model

In an ideal scenario, a single model would be used to simultaneously predict both the observable properties and the merger rates of compact binaries across all different formation channels. In this case, the mixing fraction between channels would be a direct prediction of the model, requiring no additional free parameters. In practice, the compact binary merger rates given by both COSMIC and CMC are highly uncertain and possibly subject to severe systematic bias. Therefore, when combining simulations to create a mixture model between field and cluster populations, we deliberately introduce a free parameter f controlling the mixing fraction:

$$\begin{aligned} p(m_1, m_2, z|\alpha, r_v, f) = f p_{\rm cosmic}(m_1, m_2, z|\alpha) \\ + (1-f) p_{\rm CMC}(m_1, m_2, z|r_v), \end{aligned} \tag{5.1}$$

where $p_{\rm cosmic}(m_1, m_2, z)$ and $p_{\rm CMC}(m_1, m_2, z)$ are the probability densities on the primary mass m_1, secondary mass $m_2 \leq m_1$, and redshift z of BBH mergers predicted by COSMIC and CMC, respectively. This choice of mixture model ensures that our conclusions are physically informed by the *shapes* of the observed mass and redshift distributions, and not on the *rates* of binary mergers. The parameters of the mixture model are summarized in table 8.1.

Each combination of hyper-parameters generically yields a different distribution of primary masses and mass ratios ($q = m_2/m_1$). Several different examples are shown in Fig. 5.1, varying the common envelope efficiency α in COSMIC (left-hand side) and the initial cluster virial radius r_v in CMC (right-hand side). Larger common envelope efficiencies, for instance, produce relatviely lower primary masses, while clusters with larger r_v retain more massive BHs at late times and thus exhibit the high-mass peak around 80 $M_\odot$ due to repeated BH mergers.

Table 5.1: Event parameters and hyper-parameters used in this work.

Event parameters $\boldsymbol{\theta}$	
$m_1 \in [2.5, 100]\ M_\odot$	Source-frame primary mass of the binary
$m_2 \in [2.5, 100]\ M_\odot$	Source-frame secondary mass of the binary
$z \in [0, 1.2]$	Redshift of the binary
Hyper-parameters $\boldsymbol{\lambda}$	
$\alpha \in [0.25, 5]$	Common envelope efficiency
$r_v \in [0.5, 4]$ pc	Initial cluster virial radius
$f \in [0, 1]$	Fraction of binaries from field-formation channel

The shift towards lower primary masses with increasing common envelope ejection efficiency is a result of increased rates of mergers during the common envelope phase, before a BBH forms. `COSMIC` assumes that BH mass is directly correlated with progenitor mass, thus lower mass BHs will have lower mass stellar progenitors which enter common envelopes in closer orbits relative to higher mass BHs and progenitors. Since the delay times for merging BBHs in all of our models which originate from post-common-envelope binaries are short enough for the majority of the population to merge within a few Gyr at most (even with $\alpha = 5$), the mergers of progenitors which would form lower mass BHs is the dominant effect which shapes the black hole primary mass spectrum. We note that Fig. 5.1 shows the probability distribution in primary mass, thus direct comparisons of histogram height do not reflect the absolute contributions of model to the overall rate of merging BBHs.

In the `CMC` models, the BH mass spectrum features three prominent peaks: the first at roughly $10 - 20\,M_\odot$ due to the assumptions concerning mass fallback during core collapse [348], the second at roughly $40\,M_\odot$ due to the assumptions concerning the pair-instability [349], and the third at roughly $70 - 80\,M_\odot$ due to first-generation-BH-merger products retained in their host cluster post-merger [244]. The first two peaks are similarly found in the `COSMIC` models (as expected, given these peaks are features of single star evolution assumptions), while the third peak is unique to the dynamical cluster environment. The shift toward higher primary masses at higher r_v is a consequence of the effect of r_v on BH cluster dynamics. Primarily due to mass segregation arguments, the most massive BHs in a cluster will, on average, be the first to be ejected from their host cluster and merge [335, 338]. The lower-mass ($\approx 10 - 15\,M_\odot$) BHs become dynamically active only after the most massive BHs have been ejected. For smaller initial r_v, high-mass BHs are dynamically processed and ejected early on. Therefore, in these clusters, high-mass ($M \gtrsim 40 M_\odot$) BHs,

including the second-generation BHs with masses in the pair-instability gap, typically merge at high redshift leaving only the least massive BHs in any significant quantity at late times (low redshift). Meanwhile, for high-r_v clusters, the initial relaxation time is longer [350], so many high-mass BHs still remain and may merge at late times. Thus, BBH mergers tend to have higher component masses for higher r_v clusters, as shown in Fig. 5.1.

The most significant difference between the two formation channels is the existence or absence of black holes in the upper mass gap, with $m_1 \gtrsim 45\,M_\odot$. All stars in our simulations, including those formed in GCs, are subject to PISNe which results in a sharp mass cutoff near $m_1 \approx 45\ M_\odot$ for all first generation BBH mergers. We note that the assumptions for neutrino mass loss in our `COSMIC` and `CMC` models differ slightly such that the maximum mass for a first generation BBH component is $44.5\,\mathrm{M}_\odot$ in `COSMIC` and $40.5\,\mathrm{M}_\odot$ in `CMC`. This difference arises in the choice for neutrino mass loss to carry away a fixed $0.5\,\mathrm{M}_\odot$ or 10% of the compact object mass at formation. Only hierarchical mergers, which do not occur in our isolated binary simulations, can result in BBHs with masses polluting the upper mass gap. This fact serves as the primary means of disentangling formation channels and measuring their mixing fraction f. Figure 5.2, for example, shows the *total* m_1 and q distributions resulting from combining field and cluster channels, assuming $alpha = 1$ and $r_v = 1$ for several different mixing fractions f, the exact value of which sensitively controls the prevalence of high-mass systems. Thus the relative numbers of high- and low-mass binaries among GWTC-2 serves as a sensitive probe of the true value of f.

5.3 Method

In this section, we give a brief summary of the hierarchical inference and deep learning methods used in this work. We refer the readers to the comprehensive descriptions in e.g. Refs [191, 192, 265] for additional details.

Given data $\boldsymbol{d}$ spanning a number N_{obs} of gravitational-wave detections, we wish to infer the posterior $p(\boldsymbol{\lambda}|\boldsymbol{d})$ on the hyperparameters $\boldsymbol{\lambda}$ governing their population. Assuming that the population is described as an inhomogenous Poisson process, the posterior takes the form [265, 351]

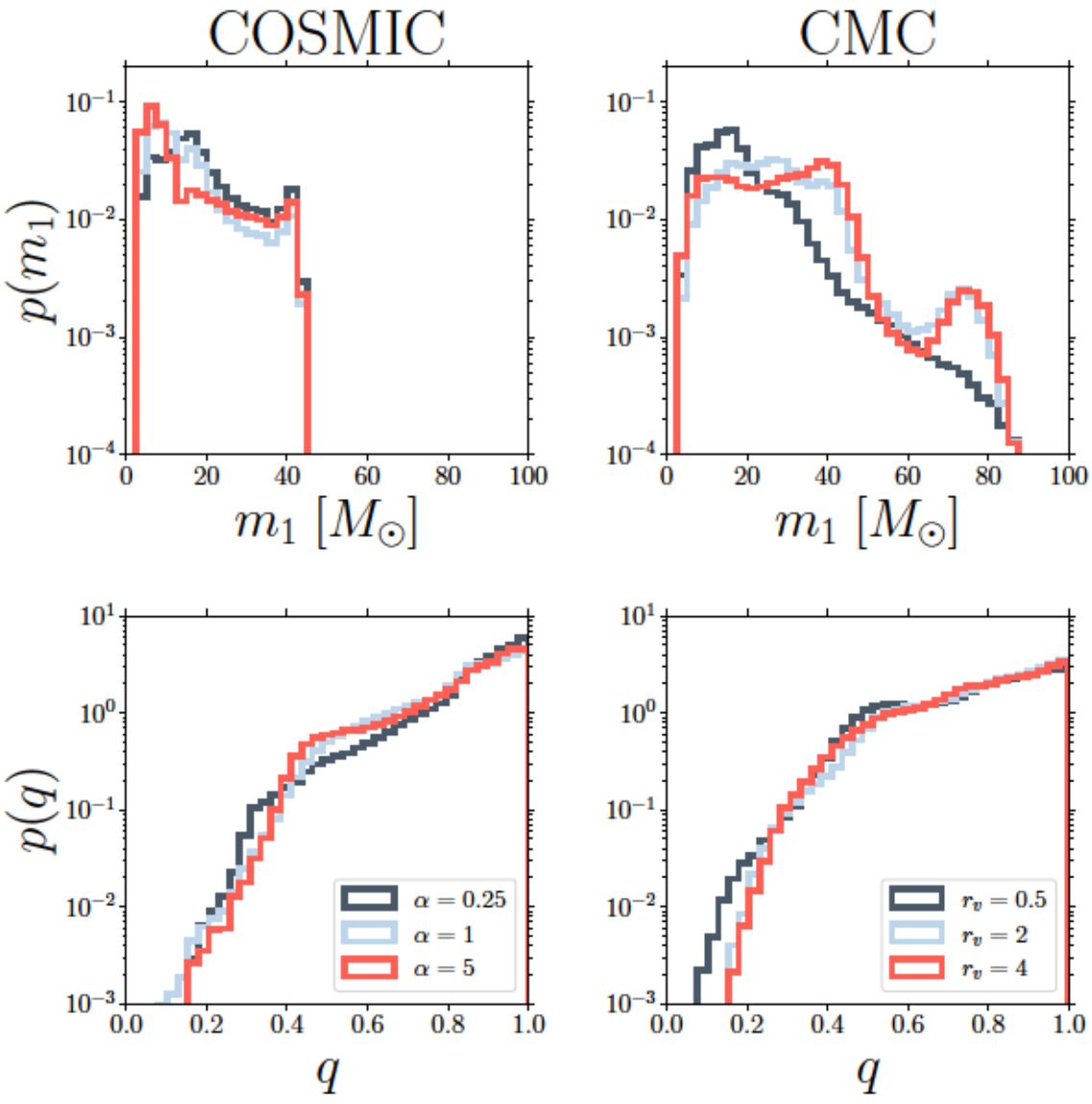

Figure 5.1: Distributions of source-frame primary mass and mass ratio for all merging BBHs from the `COSMIC` and `CMC` models. The left column shows the distributions for different common envelope efficiencies and merging BBHs from `COSMIC` only, and the right column shows the distributions for different initial virial radii when we only consider BBH mergers from `CMC`.

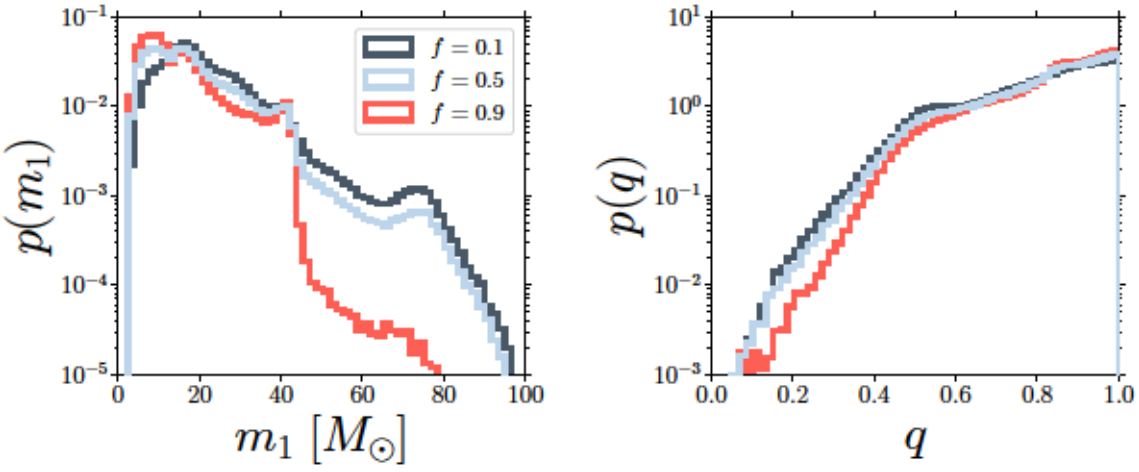

Figure 5.2: The source-frame primary mass and mass ratio distribution for all merging BBHs in the mixture model. We fixed $\alpha = 1$ and $r_v = 1$ then mix the distributions with three values of the mixing fraction $f = [0.1, 0.5, 0.9]$

$$p(\boldsymbol{\lambda}|\boldsymbol{d}) \propto \pi(\boldsymbol{\lambda})\, e^{-\alpha(\boldsymbol{\lambda})N(\boldsymbol{\lambda})} N(\boldsymbol{\lambda})^{N_{\rm obs}} \times \prod_{i=1}^{N_{\rm obs}} \int \frac{p(\boldsymbol{d}|\boldsymbol{\theta}_i)\, p_{\rm pop}(\boldsymbol{\theta}_i|\boldsymbol{\lambda})}{\alpha(\boldsymbol{\theta}_i)} {\rm d}\boldsymbol{\theta}_i\,, \tag{5.2}$$

where $N(\boldsymbol{\lambda})$ is the intrinsic volume-integrated event rate predicted by the model, and $N_{\rm obs}$ is the number of observed event in the data. $p(\boldsymbol{d}|\boldsymbol{\theta}_i)$ is the likelihood of the i-th event in the observed catalogue and $\pi(\boldsymbol{\lambda})$ is the prior on our hyperparameters. Meanwhile, $p_{\rm pop}(\boldsymbol{\theta}_i|\boldsymbol{\lambda})$ is the probability density function for the event-level parameters $\boldsymbol{\theta}_i$; this function will be computed using a normalizing flow emulator.

The term $\alpha(\boldsymbol{\lambda})$ is known as the selection bias, and gives the fraction of events one expects to detect:

$$\alpha(\boldsymbol{\lambda}) = \int p_{\rm pop}(\boldsymbol{\theta}'|\boldsymbol{\lambda}) P_{\rm det}(\boldsymbol{\theta}') d\boldsymbol{\theta}'. \tag{5.3}$$

where $P_{\rm det}(\boldsymbol{\theta}')$ is the probability that an event with specific parameters $\boldsymbol{\theta}'$ is successfully detected. In principle, one needs to inject a large amount of signals and recover them with a search pipeline to estimate the selection bias, which is very computationally expensive. In

practice, we follow the procedure described in [15, 352], reweighting an injection campaign done by the LVKC to compute the selection bias for the O12 + O3a catalog. We interpolate $N(\boldsymbol{\lambda})$ and $\alpha(\boldsymbol{\lambda})$ and use the interpolated function during the inference to maximize computational efficiency.

As discussed above, the absolute merger rates predicted by the `COSMIC` and `CMC` simulations are likely subject to unknown systematic uncertainties. We therefore marginalize the posterior shown in Eq.(6.14) over the intrinsic merger rate, using a prior $\pi(N) \propto 1/N$. Additionally, we do not know the underlying likelihood $p(\boldsymbol{d}|\boldsymbol{\theta}_i)$ for each catalog event, but only the *posterior* $p(\boldsymbol{\theta}_i|\boldsymbol{d})$ obtained under some default prior $\pi(\boldsymbol{\theta}_i)$ adopted by the LVKC during parameter estimation. Under both of these conditions, Eq. (6.14) can be written as [86]

$$p(\boldsymbol{\lambda}|\boldsymbol{d}) \propto \pi(\boldsymbol{\lambda}) \prod_{i=1}^{N_{\rm obs}} \int \frac{p(\boldsymbol{\theta}_i|\boldsymbol{d})}{\pi(\boldsymbol{\theta}_i)} \frac{p_{\rm pop}(\boldsymbol{\theta}_i|\boldsymbol{\lambda})}{\alpha(\boldsymbol{\lambda})} \mathrm{d}\boldsymbol{\theta}_i \,. \tag{5.4}$$

Specifically, the LVKC releases their event posterior in the form of discrete samples produced by their parameter estimation pipeline. Given these samples, the integral in Eq. (6.15) can be evaluated by using importance sampling, which turns the integral into a discrete sum over the event posterior PDF samples

$$p(\boldsymbol{\lambda}|\boldsymbol{d}) \propto \pi(\boldsymbol{\lambda}) \prod_{i=1}^{N_{\rm obs}} \frac{1}{S_i} \sum_{j=1}^{S_i} \frac{p_{\rm pop}({}^j\boldsymbol{\theta}_i|\boldsymbol{\lambda})}{\pi({}^j\boldsymbol{\theta}_i)\alpha(\boldsymbol{\lambda})}. \tag{5.5}$$

where j labels the posterior samples of the i-th event and S_i is the total number of samples per event. The default prior used in the LVKC `LALInference` software [353] is uniform in *detector-frame* masses and quadratic in luminosity distance, whereas we wish to model the distributions of source-frame masses and redshifts. In terms of these desired coordinates, the `LALInference` prior takes the form

$$\pi(m_1, m_2, z) \propto (1+z)^2 D_L^2(z) \left(D_c(z) + \frac{c(1+z)}{H(z)} \right). \tag{5.6}$$

To evaluate Eq. (6.17), we make use of the posterior samples presented in Refs. [181] and [31] and released through the Gravitational-Wave Open Science Center [354]. In particular, we use the "`PublicationSamples`" dataset associated with each event, and restrict to the 44 events with false alarm rates $< 1\,\mathrm{yr}^{-1}$ following Ref. [15].

The final term we need for evaluating Eq. (6.17) is the distribution of observables predicted by our simulation $p_{\rm pop}(\boldsymbol{\theta}|\boldsymbol{\lambda})$, which we obtain through training a deep learning emulator on the simulations. Here we give the network-related hyperparameters for reproducing our result. A detailed discussion of the architecture of the neural network and of the training procedure can be found in Refs. [191, 192]. We train a masked autoregressive flow network [264] with 10 hidden layers, each layer having 1024 units with ReLU activation. We include 3 observables $\{m_1, m_2, z\}$ and 3 hyper-parameters $\{f, \alpha, r_v\}$ in our training, as tabulated in Table 8.1. The training set contains 160 simulations with different combinations of 8 values of $\alpha \in [0.25, 5]$, 4 values of $r_v \in [0.5, 4]$ and 5 values of $f \in [0, 1]$. Each simulation has 10^5 events, of which 80% are randomly chosen our training set and 10% for both validation and test sets. Note that we follow the LVKC convention to enforce $m_1 > m_2$. We train the network for 100 epoch on a Nvidia K80 GPU to ensure convergence. The code for the neural network is written in python with PYTORCH [253]. Eq. (6.17) is then sampled using the MCMC package `emcee` [96] to produce the results shown in this work.

5.4 Result

We infer the hyper-parameters of Eq. (5.1) using the posterior samples publicly released in support of GWTC-1 [181, 355] and GWTC-2 [31, 356], restricting to the 44 events with false alarm rates $< 1\,\mathrm{yr}^{-1}$. Our main results are shown in Fig. 5.3. As shown in Fig. 5.1, a component mass larger than $\sim 45\ M_\odot$ is a signature of GC-formed BBHs within our two-channel model. In GWTC-1, only GW170729 has a source-frame primary mass estimate with a median larger than $45\ M_\odot$. With only 10 events in GWTC-1, the mixing fraction is therefore rather unconstrained, and the data show a preference for a near-equal mixing of the two populations instead of one dominating the other (grey $1-$D histograms). This is not the case for GWTC-2. There are 8 events with median source-frame primary masses $> 45\ M_\odot$. Together with the events from GWTC-1, 9 out of 44 events pass the PISN mass gap. This boost in number of high mass events significantly shifts the preferred value of the mixing fraction toward the cluster formation scenario. For comparison, if we ignore the 9 events in the PISN mass gap, the inferred mixing fraction becomes $0.5^{+0.4}_{-0.28}$. Despite this preference for cluster formation, the field formation scenario can still contribute significantly to the entire observed population. Our 90% credible upper bound on the mixing fraction is

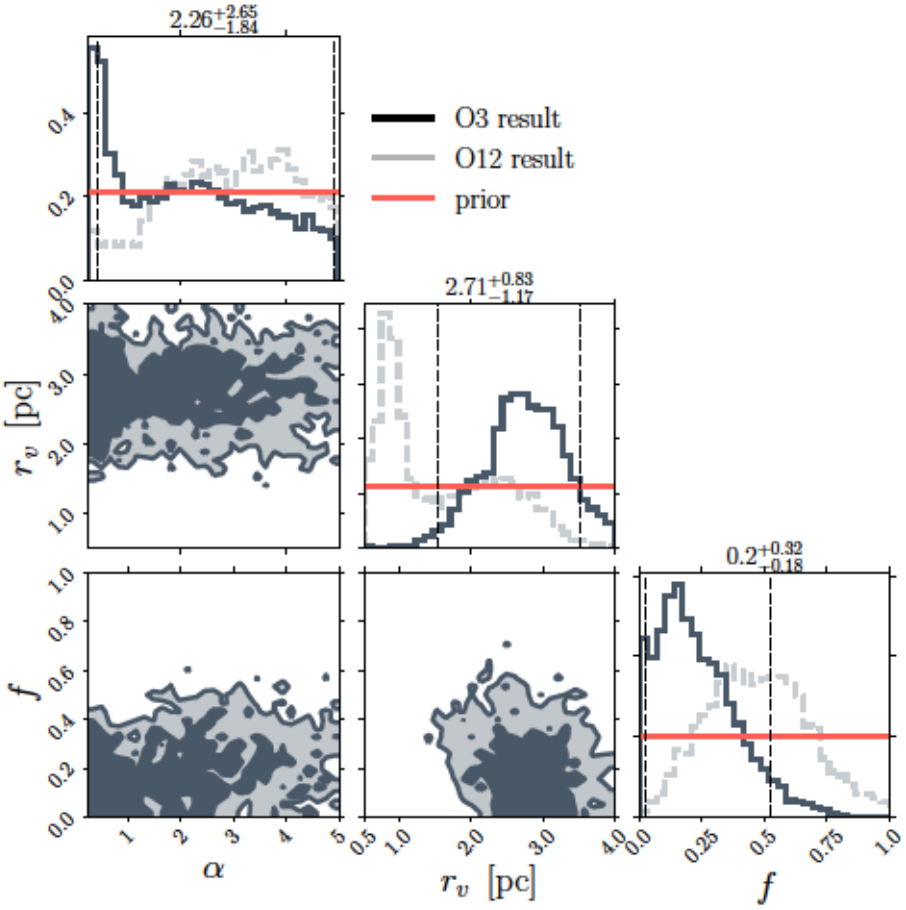

Figure 5.3: The posterior distribution of our model inferred by using all BBHs up to GWTC-2. The contours represent 50% and 90% credible bounds. The grey lines in the 1D marginalized results are posterior distribution inferred by using only BBHs in GWTC-1.

$f = 0.522$ suggesting that the contribution from the isolated channel could still surpass the cluster formation channel.

Our posterior on the common envelope efficiency α shows a mild preference towards lower values. Our relative insensitivity to α is due to two effects. First, varying α changes the mass distributions predicted by `COSMIC` by only a factor of a few, so one need more events for the difference in distribution with difference α to become statistically significant. Second, since the mixing fraction favours the cluster formation channel over the isolated formation channel, the effective number of events which was used to constrained the common envelope efficiency is even smaller.

In contrast, the initial cluster virial radius r_v is reasonably well-constrained, since our module suggests that more BBH mergers originate in GCs than in isolation. There are 5 events with a component mass larger than 60 $M_\odot$, which make up more than 10% of the entire dataset. As clusters with larger initial virial radii tend to yield more massive mergers at higher redshift (including hierarchical mergers with masses in the pair-instability gap), the excess of high-mass events hints that the majority of clusters may have been born with moderately large virial radius (we predict a median value of 2.71 pc). We also find the constraint on r_v correlates with f mildly. By taking a thin bin of posterior samples with $f = 0$, we found the median and standard deviation of r_v are $(2.79, 0.44)$; With $f = 0.5$, the median and standard deviation of r_v are $(2.65, 0.64)$. While the shift of median is rather insignificant, the posterior distribution is less constrained when mixed with `COSMIC` ($f > 0$) because we have less effective events to constrain `CMC`.

Figure 5.4 shows our inferred primary mass distribution, marginalized over our posterior on f, α, and r_v. For comparison, the light blue band indicates the mass spectrum inferred by the LVC using their phenomenological "Multi-Peak" model, where the primary mass distribution is modeled as the superposition of a power law with two additional Gaussians that can capture the onset of pair instability and the presence of high-mass hierarchical mergers, if present [15]. Despite their very different parametrizations, both models yield qualitatively similar structure at moderate and high masses: a steep drop near $\sim 45\,M_\odot$ (corresponding to the onset of the pair instability mass gap in our model) followed by a plateau and possible secondary peak near $80\,M_\odot$ due to second-generation mergers in GCs.

5.5 Discussion

Previous analyses [335, 357] have shown a cluster's initial r_v plays a prominent role in the cluster's long-term dynamical evolution. In particular, GCs born with smaller initial r_v (and thus shorter relaxation times), are more likely to have undergone core collapse by the present day. In this case, the relative ratio of core-collapsed to non-core-collapsed GCs observed at present may provide a complementary constraint upon the initial r_v distribution [335]. Taking the Milky Way GCs as a representative sample, roughly 80 % of clusters have well-resolved cores (i.e., are non-core-collapsed) at present [358], potentially hinting that relatively large initial r_v are typical, consistent with the predictions from our GWTC-2

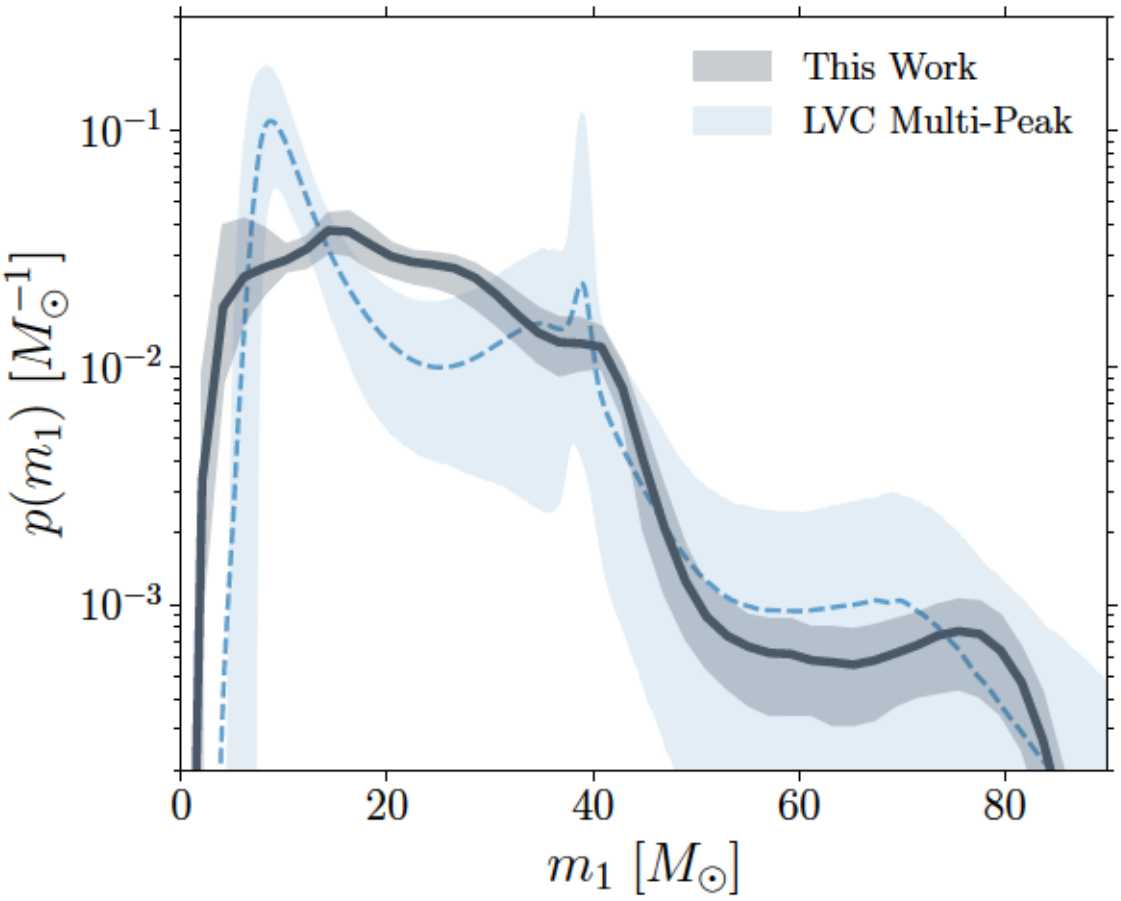

Figure 5.4: The primary mass distribution (shaded grey) inferred by our mixture model. Specifically, the shaded band shows the central 90% credible bound on $p(m_1)$ as a function of primary mass, while the solid line marks the population predictive distribution: the inferred probability distribution on m_1 after marginalization over the field-cluster mixing fraction f, common envelope efficiency α, and initial cluster virial radius r_v. For comparison, the shaded blue band marks the analogous result obtained by the LVC under their "Multi-Peak" mass model; the dashed blue line is the corresponding population predictive distribution.

Table 5.2: Event rates for each hyper-parameter and formation scenario. Rates are given for $z < 0.1$ and in comoving volume per time.

Isolated binaries								
α	0.25	0.5	0.75	1	2	3	4	5
Γ_α [Gpc^{-3}yr^{-1}]	63.8	62.5	66.5	72.2	76.6	75.1	73.9	72.1
Globular clusters								
r_v [pc]	0.5		1		2		4	
Γ_{r_v} [Gpc^{-3}yr^{-1}]	31.6		26.8		20.9		8.7	

inference.

There are a number of assumptions made in this work that can be improved upon in the future. To safeguard against systematic model uncertainties, we do not include merger rates in our inference. For completeness, we report the comoving merger rate at $z < 0.1$ under each formation channel and hyper-parameter choice in Table 5.2. The local merger rates from the isolated formation channel are lie near the maximum value of the 90% confidence intervals of the reported merger rates inferred from GWTC-2 of $23.9^{+14.9}_{-8.6}\,\mathrm{Gpc}^{-3}\,\mathrm{yr}^{-1}$. This illustrates a potential systematic bias in the other parameters which define the isolated binary formation models. In particular, `COSMIC` assumes that natal kicks for BHs are drawn from a Maxwellian distribution with $\sigma = 265\,\mathrm{km/s}$ and then weighted by the amount of mass that falls back onto the proto-compact-object during formation [348]. If stronger kicks are assumed, BBHs with lower masses will preferentially be unbound, altering both the merger rate and mass distributions in the isolated formation scenario [191, 359, 360]. `COSMIC` also assumes that stable Roche-overflow mass transfer is conservative, which may over predict the orbital evolution of a mass transferring binary [361].This is further compounded by our uncertain choice, following [362], of the mass ratios for which mass transfer is assumed to be dynamically unstable leading to a common envelope. If mass transfer proceeds stably for a wider range of mass ratios, fewer systems will experience dramatic orbital tightening during common envelope, potentially lowering predicted merger rates. We leave a full study of the combined effects of BH natal kicks, common envelope, mass transfer stability, and accretion efficiency to a future study.

Although the rate estimates from clusters shown in Table 5.2 match well the reported comoving rate inferred from GWTC-2, the cluster estimates also feature several uncertainties. A major uncertainty is the assumed cluster formation history. Observations of young stellar

clusters in the local universe [363] indicate that initial cluster virial radii are roughly independent of cluster birth time and metallicity, however this is highly uncertain. If r_v does vary with cluster birth time, it may substantially affect the conclusions of this study. Furthermore, the cluster birth time distribution itself is highly uncertain. Current theories of cluster formation fall into two main categories: clusters formed through active star formation [344, 364] and clusters formed due to the collapse of dark matter halos during or before the epoch of reionization [365]. Here, we have assumed the former scenario but if a large population of present-day GCs were instead born during reionization, our results may again change significantly. Future work should consider more carefully the various possible assumptions regarding cluster formation scenarios and the dependence of cluster properties such as r_v on these various scenarios.

There are many valuable routes by which this present analysis may be expanded in the future. As features in the BBH spin distribution begin to be robustly resolved [15, 234, 366, 367, 368, 369], future analyses can incorporate spin measurements alongside mass and redshift. Future measurements of orbital eccentricity may additionally help to discriminate between formation scenarios [340, 370, 371]. Finally, due to the still moderate number of events, in this work we restricted purely to BBHs and considered only CE and GC formation, neglecting other proposed formation channels such as primordial BHs, nuclear star clusters, open clusters, stellar triples, and AGN disks; future analysis can incorporate a greater diversity of formation scenarios, as in Ref. [369], and seek to self-consistently include neutron star and neutron star-black hole binaries alongside BBHs. We note that our results, which favor BBH formation in GCs, are in slight tension with those of Ref. [369], which identifies a preference for CE evolution. This tension may be due to a number of differences in the underlying models and data analysis methods used, including the methods for estimating selection effects (we adopt a pipeline-based false alarm threshold, compared to the optimal signal-to-noise threshold employed in Ref. [246]), the number of formation channels considered, the broader coverage of r_v in our `CMC` models (our inferred value of $r_v \approx 2.7\,\mathrm{pc}$ is outside the r_v range considered in Ref. [246]), and our unique ability to continuously sample over otherwise discretized parameters like α and r_v.

To conclude, we have extracted the mixing fraction of BBHs formed in isolated binaries and GCs while simultaneously placing continuous constraints on the channel-specific hyper-parameters, notably the initial virial radius of GCs where the BBHs were formed. Our

work marks an important milestone of learning astrophysics from populations of observed GW events. Instead of constraining a physics-agnostic phenomenological model, we use a population of GW events to place constraints on physical parameters such as mixing fraction directly. Furthermore, our model suggests that the GC properties inferred from the detected GW population are consistent with electromagnetic observations of present-day GCs, notably cluster core radii distributions. This result may be readily compared with other independent measurements to test theories of GC formation and evolution. As the number of GW detections increases in the future and theoretical models improve, one can apply the same methodology to discover and test a plethora of astrophysical theories more precisely.

Chapter 6

Constraining the primordial black hole scenario with Bayesian inference and machine learning: the GWTC-2 gravitational wave catalog

Primordial black holes (PBHs) might be formed in the early Universe and could comprise at least a fraction of the dark matter. Using the recently released GWTC-2 dataset from the third observing run of the LIGO-Virgo Collaboration, we investigate whether current observations are compatible with the hypothesis that all black hole mergers detected so far are of primordial origin. We constrain PBH formation models within a hierarchical Bayesian inference framework based on deep learning techniques, finding best-fit values for distinctive features of these models, including the PBH initial mass function, the fraction of PBHs in dark matter, and the accretion efficiency. The presence of several spinning binaries in the GWTC-2 dataset favors a scenario in which PBHs accrete and spin up. Our results indicate that PBHs may comprise only a fraction smaller than 0.3% of the total dark matter, and that the predicted PBH abundance is still compatible with other constraints.

6.1 Introduction

Gravitational wave (GW) astronomy is reshaping our understanding of the Universe. When taken individually, the black hole (BH) binary merger events announced before October 2020 by the LIGO-Virgo Collaboration (LVC) [32, 33, 181, 372] have firmly demonstrated that BHs form binaries that can merger within a Hubble time; that at least some of them have nonzero spins, possibly inducing precession in the orbital motion (see e.g. [372]); and that they can exist in mass ranges that challenge the current stellar-formation paradigm [32, 33, 372]. Finally, their coalescence signal is fully consistent with the predictions of general relativity, providing novel and stringent bounds on modified gravity theories [233, 298, 373].

The recently released GWTC-2 dataset from the first part of the third observing run (O3a) [31] marks the onset of a transition from individual-event analyses to population studies: the number of BH merger events detected so far has more than quadrupled compared to the O1-O2 runs, making population studies particularly relevant [15].

Meanwhile, GW observations have renewed interest in trying to understand the nature of the observed population of BHs, from an astrophysical, cosmological, and theoretical standpoint [374].

The two most popular astrophysical formation channels are isolated binary evolution in the field and dynamical formation in clusters (see e.g. [375, 376] for reviews). For isolated binaries, a common-envelope phase in between the formation of the two BHs is usually invoked to harden the binary and catalyze mergers. Alternatively, dynamical channels predict that binary BHs form and harden through three-body encounters in dense stellar clusters. Other popular binary BH formation scenarios include chemically homogenous evolution [377, 378], AGN disks [379, 380, 381], and secular interactions in triple systems [382, 383, 384]. Different formation pathways leave different imprints on the properties of the binary BH population, including the binary masses, spins, eccentricities, and redshift evolution. Measuring these distributions informs us on the environment in which binary BHs form and evolve [190, 232, 240, 242, 246].

In this paper we will focus on another interesting possibility: that some of (if not all) the detected BH binaries are of primordial origin, i.e. they are composed of primordial black holes (PBHs), whose formation took place in the early epochs of the Universe (see Refs. [175,

180, 385] for recent reviews). This scenario is also motivated by the fact that PBHs could comprise the entirety (or a fraction) of the dark matter (DM) in the Universe, and several studies on the confrontation between the PBH scenario and GW data have been performed so far in the literature [169, 176, 386, 387, 388, 389, 390, 391, 392, 393, 394, 395, 396, 397, 398].

Our aim is to constrain PBH population models using the entire dataset of BH binaries reported in the GWTC-2. We shall do so by applying hierarchical Bayesian inference based on deep learning techniques to find the best-fit parameters of the PBH model (including the PBH abundance), which can be then confronted to constraints coming from other observations.

The outline of this paper is as follows. In Sec. 6.2 we describe the PBH simulations used in this study. In Sec. 6.3 we review the data analysis pipeline, and in Sec. 6.4 we apply it to public LVC GWTC-2 data. In Sec. 6.5 we compare GW constraints on the fraction of PBHs in DM with those coming from other observations. In Sec. 11.4 we summarize our findings and highlight future research directions. Throughout this paper we use geometrical units ($G = c = 1$).

6.2 Key Predictions of the PBH scenario

In this section we review the main theoretical predictions for the PBH scenario. More technical details can be found in Ref. [393] and references therein. After reviewing PBH formation, we report the key steps necessary to compute the merger rate, depending on the PBH mass function and abundance. We also summarize our model for accretion onto PBHs in binaries, because accretion has been shown to affect in a critical way the mass ratio, spins, merger rate, and overall abundance of the PBH population [179, 208, 393].

There are several models giving rise to a cosmologically significant population of PBHs. In the most likely scenario, the formation of PBHs occurs from the collapse of large overdensities in the primordial Universe, when radiation dominates the energy density budget [399, 400, 401]. The formation of a PBH of mass m takes place deep in the radiation-dominated era at a typical redshift $z_{\rm i} \simeq 2 \cdot 10^{11} (m/M_\odot)^{-1/2}$. The resulting mass distribution depends on the characteristic size and statistical properties of the density perturbations, directly connected to the curvature perturbations produced during the inflationary epoch. A useful model-

independent parametrization of the mass function at the formation redshift $z_{\rm i}$ (here and below we will use a subscript "i" to indicate quantities evaluated at the formation epoch) is represented by the log-normal function

$$\psi(m, z_{\rm i}) = \frac{1}{\sqrt{2\pi}\sigma m} \exp\left(-\frac{\log^2(m/M_c)}{2\sigma^2}\right) \tag{6.1}$$

in terms of its width σ and reference mass scale M_c. Such a mass function describes a population arising from a symmetric peak in the power spectrum of curvature perturbations and captures a wide variety of models [402, 403].

Since large perturbations tend to have nearly-spherical shape [404] and the collapse takes place in a radiation-dominated Universe, the initial adimensional spin parameter $\chi \equiv |J|/m^2$ is expected to be below the percent level [405, 406], with the characteristic value given by

$$\chi_{\rm i} \sim 10^{-2}\sqrt{1-\gamma^2}, \tag{6.2}$$

in terms of the width parameter γ of the power spectrum [405].

During the cosmological history, PBHs in binaries may undergo a period of significant baryonic mass accretion, which impacts their individual masses [407, 408, 409] and spins [208, 393, 410]. As the typical size of a binary is smaller than its corresponding Bondi radius, the infall of gas is driven by the binary system as a whole. This means that both PBHs experience accretion from the gas with an enhanced density. Accretion onto the two individual PBHs is also modulated by their masses and orbital velocities. By defining the mass ratio as $q \equiv m_2/m_1 \leq 1$, one can write the individual accretion rates as

$$\dot{m}_1 = \dot{m}_{\rm bin}\frac{1}{\sqrt{2(1+q)}}, \qquad \dot{m}_2 = \dot{m}_{\rm bin}\frac{\sqrt{q}}{\sqrt{2(1+q)}}, \tag{6.3}$$

in terms of the Bondi-Hoyle mass accretion rate of the binary system

$$\dot{m}_{\rm bin} = 4\pi\lambda m_H n_{\rm gas} v_{\rm eff}^{-3} M_{\rm tot}^2, \tag{6.4}$$

where $M_{\rm tot} = m_1 + m_2$ is the total mass and dots denote derivatives with respect to time. The expression above is explicitly dependent on the binary's effective velocity $v_{\rm eff}$ relative to the baryons with cosmic mean density $n_{\rm gas}$ and hydrogen mass m_H. The accretion

formula (6.4) adopts the Newtonian approximation; as recently pointed out in Ref. [411], general-relativistic effects may lead to a significant increase in the mass accretion rate. However, since the accretion rate decreases by several orders of magnitude for PBH masses $\lesssim 10 M_\odot$ [408], even an order-of-magnitude increase in $\dot{m}$ does not change the predictions of our model significantly. The accretion parameter λ tracks the effects of the Hubble expansion, the coupling of the CMB radiation to the gas through Compton scattering, and the gas viscosity [407]. Also, since PBHs in the mass range of interest for LVC observations can comprise only a fraction of the DM due to the current constraints on their abundance, accretion onto PBHs should also include the presence of an additional DM halo forming around the PBHs [408, 412, 413] (either isolated or in binaries). The DM halo acts as a catalyst enhancing the gas accretion rate, and its effect is taken into account in λ (see Appendix B of Ref. [208] for details). We account for the sharp decrease in the accretion efficiency around the epoch of structure formation [390, 414, 415] by defining a cutoff redshift $z_{\rm cutoff}$ after which we neglect accretion. Because of the uncertainties in the model (such as X-ray pre-heating [416], details of the structure formation, and feedbacks of local, global [408, 417] and mechanical type [418]), the cutoff redshift is relatively unconstrained. At variance with previous work [208, 393, 410], in which $z_{\rm cutoff}$ was fixed to some reference value, here we consider it as a parameter of the PBH accretion model (more precisely, a "hyperparameter" of our model, see below) that we will fit to GW data, along with the other model parameters.

A consequence of PBH accretion in binaries is that the lighter binary component always accretes more efficiently, and therefore an initial mass ratio different from unity would grow as

$$\dot{q} = q\left(\frac{\dot{m}_2}{m_2} - \frac{\dot{m}_1}{m_1}\right) > 0. \tag{6.5}$$

Accretion also modifies the PBH mass distribution, making it broader at high masses and producing a high-mass tail that can be orders of magnitude above its corresponding value at formation. Furthermore, accretion also affects the total fraction of PBHs in DM $f_{\rm PBH}$ in a redshift-dependent fashion according to the relation [179]

$$f_{\rm PBH}(z) = \frac{\langle m(z)\rangle}{\langle m(z_{\rm i})\rangle (f_{\rm PBH}^{-1}(z_{\rm i}) - 1) + \langle m(z)\rangle}, \tag{6.6}$$

where

$$\langle m(z) \rangle = \int \mathrm{d}m \, m \, \psi(m, z) \tag{6.7}$$

is the average mass. This effect is of crucial importance when comparing the physical parameters to the existing experimental constraints [179], as we will do below.

Since the fraction of PBHs which underwent mergers is of the order of $\mathcal{O}(10^{-2} f_{\rm PBH}^{16/37})$ [419, 420], the overall PBH population is largely dominated by isolated PBHs, for which accretion is described in detail in Refs. [179, 208] and references therein. This implies that the fraction of second-generation PBH mergers is expected to be negligible in the LIGO/Virgo band [208, 419, 420], contrarily to the astrophysical scenario, in which second-generation mergers may play a significant role (see e.g. [207, 236, 421, 422]).

In addition to changing the masses, the infalling accreting gas onto a PBH can carry angular momentum, which crucially determines the geometry of the accretion flow and the evolution of the PBH spin [423]. For accretion onto a PBH binary, the nonspherical geometry can give rise to a geometrically thin accretion disk as long as the accretion rate (normalized to the Eddington rate) is larger than unity [408, 424, 425]. Only when this condition is satisfied the angular momentum transfer on each PBH is very efficient, and mass accretion is accompanied by an increase of the PBH spin according to the equation

$$\dot{\chi} = g(\chi) \frac{\dot{m}}{m}, \tag{6.8}$$

in terms of the function $g(\chi)$, which is derived using the geodesic model of disk accretion [426] (see e.g. [393, 427, 428]). We consider Thorne's spin limit $\chi_{\rm max} = 0.998$, which is dictated by radiation effects [429] (see also [430]).

In particular, besides the angular-momentum transfer, the geometry of the disk crucially depends also on the accretion rate. If the mass accretion rate is sub-Eddington and nonspherical, an advection-dominated accretion flow (ADAF) may form [431]. For accretion rates close to the Eddington limit, one expects the formation of a geometrically thin disk [408, 424], for which the angular momentum transfer can be described with a geodesic model [426]. For moderately super-Eddington rates, the accretion luminosity might be strong enough that the disk "puffs up" and becomes slim [432]. A larger accretion rate would imply geometrically thicker disks, with possible differences in the accretion luminosity

and angular momentum transfer [432]. In such a scenario, accretion of angular momentum would be more complex, even though numerical simulations suggest that the time-scale for spin evolution is not significantly modified [430]. For the PBH masses under consideration, one does not exceed the Eddington accretion rate significantly, and therefore the thin-disk model should provide a reasonable approximation.

One of the clear predictions of the primordial scenario is that the spin of the lighter PBH in the binary is larger than that of the heavier PBH, because the spin-up is mainly produced by accretion and the secondary component typically accretes more.

A key observable inferred by GW observations is the binary's effective spin parameter

$$\chi_{\rm eff} \equiv \frac{\chi_1 \cos\theta_1 + q\chi_2 \cos\theta_2}{1+q}\,, \tag{6.9}$$

defined in terms of the individual BH spin magnitudes χ_j $(j = 1, 2)$, and the angles θ_1 and θ_2 between the orbital angular momentum and the individual spin directions. When forming PBH binaries, the spin directions are expected to be uncorrelated, and therefore uniformly distributed on the two-sphere.

When accretion is relevant in spinning up the PBHs, the accretion geometry is complex and the spin directions are expected to remain uncorrelated, as the orientations of the disks formed around each PBH are independent. This is because the characteristic orbital distance is comparable to (or smaller than) the individual PBH Bondi radii. This scenario differs, for instance, from the common envelope phase giving rise to astrophysical BH binary mergers: in that case both of the individual BH spins are expected to be aligned with the orbital angular momentum of the binary (see e.g. [307, 433, 434, 435]).

In the absence of primordial non-Gaussianities, the PBH locations in space at the formation epoch follow a Poisson distribution [436, 437, 438, 439]. Depending on the initial abundance $f_{\rm PBH}(z_{\rm i})$ and mass function $\psi(m, z_{\rm i})$, one can compute how often binaries form in the early Universe by evaluating the probability that a binary system decouples from the Hubble flow. The initial distribution of the orbital parameters also depends on the spatial distribution of the surrounding population of PBHs, as well as density perturbations adding an initial torque to the binary system. On top of that, following Ref. [176], one can introduce a correction S to the merger rate, accounting for the possible disruption of binaries due to

Table 6.1: Event parameters ($\boldsymbol{\theta}$) of the binary and hyperparameters ($\boldsymbol{\lambda}$) of the PBH model used in this work.

Event parameters $\boldsymbol{\theta}$	
m_1	Source-frame primary mass
m_2	Source-frame secondary mass
$\chi_{\rm eff}$	Effective spin
z	Merger redshift
Hyperparameters $\boldsymbol{\lambda}$	
M_c	Peak reference mass of the log-normal distribution
σ	Variance of the log-normal mass distribution
$f_{\rm PBH}$	Fraction of PBHs in DM at formation
$z_{\rm cutoff}$	Accretion cutoff redshift

their interaction with the environment at high redshifts. Finally, introducing the effect of accretion, and following the discussion in Ref. [393] and references therein, one can compute the PBH merger rate as follows

$$\begin{aligned}
\mathrm{d}R = & \frac{1.6\times10^6}{\mathrm{Gpc^3\,yr}} f_{\rm PBH}^{\frac{53}{37}}(z_{\rm i})\eta^{-\frac{34}{37}}(z_{\rm i})\left(\frac{t}{t_0}\right)^{-\frac{34}{37}}\left(\frac{M^{\rm i}_{\rm tot}}{M_\odot}\right)^{-\frac{32}{37}} \\
& \times S\left(M^{\rm i}_{\rm tot}, f_{\rm PBH}(z_{\rm i})\right)\psi(m^{\rm i}_1, z_{\rm i})\psi(m^{\rm i}_2, z_{\rm i}) \\
& \times \exp\left[\frac{12}{37}\int_{t_{\rm i}}^{t_{\rm cutoff}} \mathrm{d}t\left(\frac{\dot{M}_{\rm tot}}{M_{\rm tot}} + 2\frac{\dot{\mu}}{\mu}\right)\right] \\
& \times \left(\frac{\eta(z_{\rm cutoff})}{\eta(z_{\rm i})}\right)^{3/37}\left(\frac{M_{\rm tot}(z_{\rm cutoff})}{M_{\rm tot}(z_{\rm i})}\right)^{9/37} \mathrm{d}m^{\rm i}_1\mathrm{d}m^{\rm i}_2,
\end{aligned} \tag{6.10}$$

where $\mu = m_1 m_2/M_{\rm tot}$, $\eta = \mu/M_{\rm tot}$, and t_0 is the current age of the Universe. The corrective factors in the last two lines account for the evolution of the masses from the initial redshift $z_{\rm i}$ to the cutoff redshift $z_{\rm cutoff}$ and the corresponding shrinking of the semimajor axis of the orbit due to accretion [393] (see also [440]). This effect dominates and drives the binary evolution up to the cutoff redshift, after which the binary evolution is uniquely driven by energy loss through GW emission [441, 442]. Notice that the merger rate at small redshift ($z < z_{\rm cutoff}$) has a universal scaling given by $t^{-34/37}$, which is independent of the other model parameters. Also, for the small values of $f_{\rm PBH}$ which will be selected out in our analysis (see Sec. 6.4), the clustering of PBHs plays no role [398, 443].

In summary, the parameters describing each PBH binary, along with the "hyperparameters" describing the PBH model, are listed in Table 8.1. In order to perform the analysis discussed

in the following section, we built a catalog of simulations, producing the PBH merger population for the full set of hyperparameters $\boldsymbol{\lambda}$. Each element in the catalog contains a population of 10^5 merger events with the characteristics described above. In the region of (M_c, σ) of interest for our analysis, a value of the cutoff redshift around $z_{\rm cutoff} \sim 30$ or larger would correspond to a scenario where accretion is negligible for most of the PBH merger population.

6.3 Data Analysis

In this section we give a brief introduction to the data analysis methods used in this work. We refer the reader to more comprehensive descriptions in the literature [77, 85, 265, 444]. In short, we use an implementation of hierarchical Bayesian inference based on deep learning techniques to constrain PBH formation models given LVC data.

Astrophysical models predict intrinsic properties of individual GW sources (such as the masses and spins of the binary components), while GW interferometers record a time series of the GW-induced strain in the detectors. Before we can compare the model to the data, we must convert these time series into astrophysically meaningful quantities through a parameter estimation process [85]. The LVC's Gravitational Wave Open Science Center provides the output of this parameter estimation process as a collection of posteriors characterizing the expectation value and uncertainty on the properties of individual merger events, i.e. $p(\boldsymbol{\theta}|\boldsymbol{d}_i)$, where $\boldsymbol{\theta}$ is a vector of source parameters, and $\boldsymbol{d}_i$ labels the time series of the i-th event in the catalog.

By Bayes' theorem, given some data $\boldsymbol{d}$, the posterior probability of the signal from an astrophysical source with parameters $\boldsymbol{\theta}$ is $p(\boldsymbol{\theta}|\boldsymbol{d}) \propto p(\boldsymbol{d}|\boldsymbol{\theta})p(\boldsymbol{\theta})$, where $p(\boldsymbol{d}|\boldsymbol{\theta})$ is the likelihood of observing the data given our model of the astrophysical signal and detector, and $p(\boldsymbol{\theta})$ is our assumed prior on the source parameters. The prior encodes our previous knowledge of the underlying physics (e.g., mass should not be negative), and plays an important role in interpreting the results [267, 268]. Within the PBH scenario, the prior distributions of the binary parameters according to the model of Sec. 6.2 is different from the priors used by the LVC, and this can affect the inference of the individual source parameters [445]. Crucially, our procedure does not rely on the priors because we reweigh them, and it is therefore valid

also in the PBH scenario.

A hierarchical Bayesian analysis parametrizes the choice of priors by some vector of hyper-parameters $\boldsymbol{\lambda}$, whose posterior distribution can be inferred from the data

$$p(\boldsymbol{\lambda}|\boldsymbol{d}) \propto p(\boldsymbol{\lambda}) \int p(\boldsymbol{d}|\boldsymbol{\theta}) p_{\rm pop}(\boldsymbol{\theta}|\boldsymbol{\lambda}) \mathrm{d}\boldsymbol{\theta}, \tag{6.11}$$

where $p(\boldsymbol{d}|\boldsymbol{\theta})$ is the single-event likelihood, $p(\boldsymbol{\lambda})$ is now a prior on the hyperparameters, and $p_{\rm pop}(\boldsymbol{\theta}|\boldsymbol{\lambda})$ is the *population likelihood*, equivalent to a prior parametrized by some hyperparameters. The parameters describing single events (e.g. masses, redshifts) are also referred to as *event parameters*, while the hyperparameters describing the entire sample (e.g. the fraction of DM in PBHs) can be also referred to as *population parameters*.

An astrophysical population model characterized by population parameters $\boldsymbol{\lambda}$ will predict some distribution of event parameters $\boldsymbol{\theta}$ such that the differential rate $\frac{\mathrm{dr}}{\mathrm{d}\boldsymbol{\theta}}(\boldsymbol{\lambda})$ is given by

$$\frac{\mathrm{dr}}{\mathrm{d}\boldsymbol{\theta}}(\boldsymbol{\lambda}) = R(\boldsymbol{\lambda})\, p_{\rm pop}(\boldsymbol{\theta}|\boldsymbol{\lambda})\,, \tag{6.12}$$

where $\int p_{\rm pop}(\boldsymbol{\theta}|\boldsymbol{\lambda})\mathrm{d}\boldsymbol{\theta} = 1$, and the total rate $R(\boldsymbol{\lambda})$ is typically measured in yr^{-1}. The predicted number of events is $N(\boldsymbol{\lambda}) = \int \frac{\mathrm{dr}}{\mathrm{d}\boldsymbol{\theta}}(\boldsymbol{\lambda})\mathrm{d}\boldsymbol{\theta} \times T_{\rm obs}$, where $T_{\rm obs}$ is the duration of the observing run(s). We can take into account selection effects caused by the sensitivity of the detectors through a function $0 \leq p_{\rm det}(\boldsymbol{\theta}) \leq 1$, corresponding to the probability that an event with parameters $\boldsymbol{\theta}$ would be detectable. The observable distribution is then given by

$$\frac{\mathrm{dr}_{\rm det}}{\mathrm{d}\boldsymbol{\theta}}(\boldsymbol{\lambda}) = R(\boldsymbol{\lambda})\, p_{\rm pop}(\boldsymbol{\theta}|\boldsymbol{\lambda})\, p_{\rm det}(\boldsymbol{\theta})\,, \tag{6.13}$$

and the expected number of observations is $N_{\rm det}(\boldsymbol{\lambda}) = \int \mathrm{d}\boldsymbol{\theta}(\mathrm{dr}_{\rm det}/\mathrm{d}\boldsymbol{\theta})(\boldsymbol{\lambda}) \times \mathrm{T}_{\rm obs}$.

All of these ingredients enter the population posterior, which has the standard expression for an inhomogeneous Poisson process (cf. [74, 83, 84, 85] for detailed derivations). In particular, the population posterior reads

$$\begin{aligned} p(\boldsymbol{\lambda}|\boldsymbol{d}) \propto\ & \pi(\boldsymbol{\lambda})\, e^{-N_{\rm det}(\boldsymbol{\lambda})} N(\boldsymbol{\lambda})^{N_{\rm obs}} \\ & \times \prod_{i=1}^{N_{\rm obs}} \int \frac{p(\boldsymbol{\theta}_i|\boldsymbol{d})}{\pi(\boldsymbol{\theta}_i)} p_{\rm pop}(\boldsymbol{\theta}_i|\boldsymbol{\lambda}) \mathrm{d}\boldsymbol{\theta}_i\,, \end{aligned} \tag{6.14}$$

where $N_{\rm obs}$ is the number of observations and $\pi(\boldsymbol{\lambda})$ is some assumed population prior. If one wishes to exclude rate information from the inference, marginalizing over $N(\boldsymbol{\lambda})$ with prior $\propto 1/N(\boldsymbol{\lambda})$ yields [86]

$$p(\boldsymbol{\lambda}|\boldsymbol{d}) \propto \pi(\boldsymbol{\lambda}) \prod_{i=1}^{N_{\rm obs}} \int \frac{p(\boldsymbol{\theta}_i|\boldsymbol{d})}{\pi(\boldsymbol{\theta}_i)} \frac{p_{\rm pop}(\boldsymbol{\theta}_i|\boldsymbol{\lambda})}{\alpha(\boldsymbol{\lambda})} \mathrm{d}\boldsymbol{\theta}_i \,, \tag{6.15}$$

where $\alpha(\boldsymbol{\lambda})$ is the fraction of events one would detect given a population (also known as the selection bias), and

$$\alpha(\boldsymbol{\lambda}) = \int p_{\rm pop}(\boldsymbol{\theta}'|\boldsymbol{\lambda}) p_{\rm det}(\boldsymbol{\theta}') \mathrm{d}\boldsymbol{\theta}' = \frac{N_{\rm det}(\boldsymbol{\lambda})}{N(\boldsymbol{\lambda})}. \tag{6.16}$$

In order to accurately capture the detector response to account for the selection bias, one should reweight the injection campaign released by LIGO [446] according to the method described in [352]. However, the domain of masses in our model is larger than the domain where the injection campaign was performed ($2M_\odot < m_1, m_2 < 100\ M_\odot$), which means that the probability density function describing our model is not normalized within the domain of the injection campaign. This induces severe inaccuracy in estimating the selection bias with the reweighting method, so we use a more crude but more well-behaved method to estimate the selection bias. For O1 and O2 data, it has been shown that approximating $p_{\rm det}(\boldsymbol{\theta})$ with the single-detector semianalytic approximation of Refs. [78, 79] and a signal-to-noise ratio threshold of 8 yields results in good agreement with large-scale injection campaigns [62, 82]. We used `aLIGOEarlyHighSensitivityP1200087` (`aLIGOMidHighSensitivityP1200087`), as implemented in `pycbc`, as our O1-O2 (O3a) sensitivity curves. To evaluate the selection bias integral of Eq. (6.16) we can again use importance sampling. Given a synthetic catalog, we compute $\alpha(\boldsymbol{\lambda})$ by taking the average $p_{\rm det}(\boldsymbol{\theta})$ of events in the catalog according to Eq. (6.16). The network can be used both to evaluate the likelihood function and to generate new simulations. At any given point in the hyperparameter space, we generate 10^5 samples using our network, then evaluate the selection bias with the code described in Ref. [447].

The event posterior probability distribution function $p(\boldsymbol{\theta}_i|\boldsymbol{d})$ is often given in the form of $\mathcal{S}_i$ discrete samples by a parameter estimation process [197, 269]. As clear from Eq. (6.15), we weighted out the priors on the event parameters $\pi(\boldsymbol{\theta}_i)$, so they do not contribute to $p(\boldsymbol{\lambda}|\boldsymbol{d})$. We can now make use of the posterior samples in the population inference, thus

avoiding unnecessary reevaluations of $p(\boldsymbol{d}|\boldsymbol{\theta})$ and significantly reducing the computation load for each population inference run. The integral in Eq. (6.14) can be evaluated by using importance sampling, i.e. by computing the expectation value of the prior-reweighted population likelihood, which can be turned into a discrete sum over the samples of the event posterior probability distribution function

$$p(\boldsymbol{\lambda}|\boldsymbol{d}) = \pi(\boldsymbol{\lambda}) e^{-N_{\rm det}(\boldsymbol{\lambda})} N(\boldsymbol{\lambda})^{N_{\rm obs}} \prod_{i=1}^{N_{\rm obs}} \frac{1}{\mathcal{S}_i} \sum_{j=1}^{\mathcal{S}_i} \frac{p_{\rm pop}({}^j\boldsymbol{\theta}_i|\boldsymbol{\lambda})}{\pi({}^j\boldsymbol{\theta}_i)}, \tag{6.17}$$

where j labels the j-th sample of the i-th event.

We train a deep learning emulator on the simulations described in Sec. 6.2 to evaluate the population likelihood $p_{\rm pop}(\boldsymbol{\theta}|\boldsymbol{\lambda})$. Here we give some details on the network's architecture. A more detailed discussion of the neural network and of the training procedure can be found in Refs. [191, 192]. We use a masked autoregressive flow network [264] with 10 hidden layers, each layer having 1024 units as our main architecture. We train two variants using the same architecture and data, one with 4 observables $\{m_1, q, \chi_{\rm eff}, z\}$ and 3 hyperparameters $\{M_c, \sigma, z_{\rm cutoff}\}$, and another one where we exclude $\chi_{\rm eff}$ from the observables. Note that we follow the LVC convention to enforce $m_1 > m_2$. We do not train on $f_{\rm PBH}$, because it affects only the overall rate, but not the shape of the population likelihood. Our training set contains 2100 simulations with different combinations of hyperparameters, and 10^5 sample points in the observable space per simulation, adding up to 2.1×10^8 sample points on the parameter-hyperparameter space in total. As customary in training neural networks, 80% of the data are used for training, 10% are used for validation during the training to avoid overfitting, and the remaining 10% is used to test the results independently. We train the network for 100 epochs on a Nvidia K80 GPU to ensure convergence. The code for the neural network is written in PYTHON with PYTORCH [253].

The final piece we need is the predicted number of events $N(\boldsymbol{\lambda})$. In order to compute the latter, we first need to have a rate function, which requires running a full simulation, then summing over the rate for each individual event. Therefore, computing the number of events is as expensive as generating the simulation itself. We employ a simple network to interpolate the rate as a function of the 4 hyperparameters, as described in Ref. [447]. We have checked that the median error in our interpolation method is $\sim 0.04\%$, with 98% of

the errors being smaller than 3%, therefore the interpolation error is negligible compared to statistical uncertainties. Once we know the intrinsic merger rate $R(\boldsymbol{\lambda})$, we can trivially obtain the observed merger rate as $R_{\rm det}(\boldsymbol{\lambda}) = \alpha(\boldsymbol{\lambda})R(\boldsymbol{\lambda})$ (see Eq. (6.16)). Once we have the rate function, we can multiply the rate by the effective observational time to obtain the predicted number of events. For O1-O2 (O3a), there are ~ 166.6 (183.3) days of coincident data.

Among all the binary events included in the GWTC-2 catalog, we use the same subset selected for the population analysis in Ref. [15]. In particular, we exclude events with large false-alarm rate (GW190426, GW190719, GW190909) and events where the secondary binary component has mass smaller than $3M_\odot$ (GW170817, GW190425, GW190814). Therefore, our dataset includes 44 events.

Among the events with $m_2 < 3M_\odot$, an electromagnetic counterpart was detected and identified with a kilonova only for GW170817 [29], showing that at least one of the binary components (and most likely both) is a neutron star. However, in the absence of a counterpart, it is much more uncertain to assess whether the light components of the other two events (GW190425 and GW190814) are indeed neutron stars. In fact it cannot be excluded that these events have a different, and possibly primordial, origin [33]. Here we excluded these events (identified by the LVC as neutron-star or mixed binaries) to conform with the LVC population analysis [15]. Including them would be an interesting extension of our work. However, we expect that the inclusion of only two not particularly loud events (GW190425 and GW190814) out of $44+2$ potential binary BHs would not change our results significantly.

We adopt the OVERALL_POSTERIOR provided in [448] for events in GWTC-1, and the PUBLICATIONSAMPLES provided in [449] for events in the GWTC-2 catalog. We apply both the model with effective spin and without effective spin to analyze the data, with a uniform population prior in the range where we trained our emulator. We sample Eq. (6.17) using the MCMC package `emcee` [96].

6.4 Inference from the GWTC-2 catalog

In this section we describe the results of our analysis of GWTC-2 events. The best-fit hyperparameters obtained are summarized in Table 6.2.

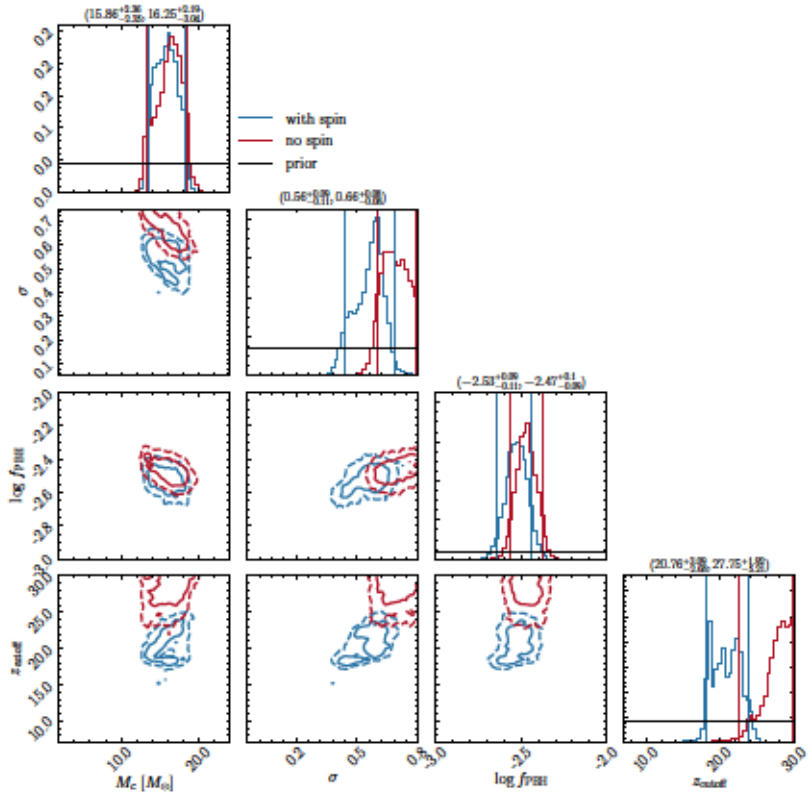

Figure 6.1: Population posterior using the 44 GWTC-2 BH binary events. Blue lines are obtained using four observables (m_1, m_2, $\chi_{\rm eff}$, z), whereas red lines do not consider the effective spin in the inference. Solid (dashed) contours represent 68% (95%) confidence intervals. The solid black lines indicate the priors assumed for the population hyperparameters. The first (second) number in parentheses is the hyperparameter range inferred by including (omitting) $\chi_{\rm eff}$ from the inference.

Table 6.2: Hyperparameters of the PBH model inferred using $(m_1, m_2, \chi_{\rm eff}, z)$ and GWTC-2 data.

$M_c[M_\odot]$	$15.86^{+2.36}_{-2.35}$
σ	$0.56^{+0.09}_{-0.11}$
$\log f_{\rm PBH}$	$-2.53^{+0.09}_{-0.11}$
$z_{\rm cutoff}$	$20.76^{+3.09}_{-2.68}$

Our analysis has several improvements with respect to the existing literature. First, many attempts to perform population inference neglected the role of accretion (see e.g. [176, 396, 420, 450]), which was shown to be relevant [393]. We can only compare with studies of the GWTC-1 dataset which neglected accretion if we restrict to large values of $z_{\rm cutoff}$. In this limit, our results are in general agreement with previous work. Recently, some of us [393] studied the impact of PBH accretion on the merger rate and on the distribution of binary parameters, inferring the PBH population properties from a maximum-likelihood analysis of the GWTC-1 dataset. For a fixed accretion $z_{\rm cutoff}$, we have checked that those results are compatible with the present analysis. Here, for the first time, we treat $z_{\rm cutoff}$ as a free hyperparameter and we infer its posterior distribution. A second major improvement with respect to Ref. [393] is that we now include the effective spin information in the Bayesian inference.

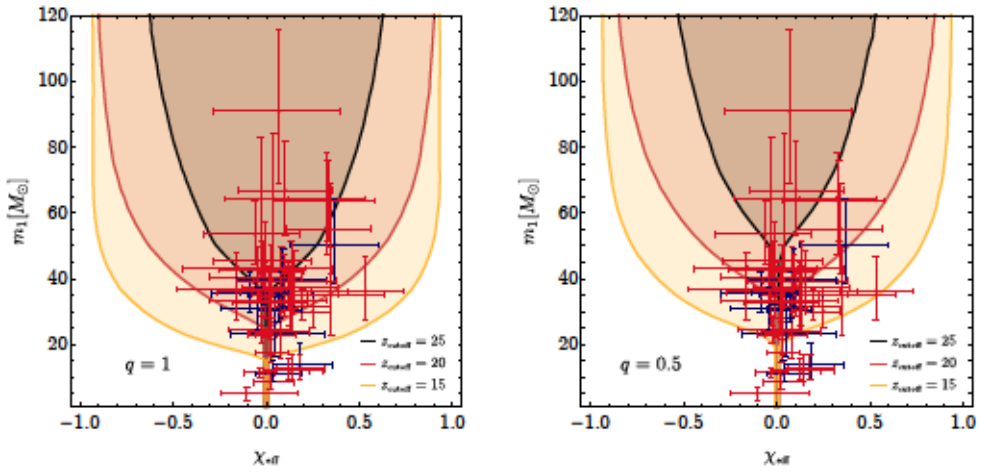

Figure 6.2: Prediction for the $\chi_{\rm eff}$ distribution as a function of the primary BH mass m_1 and cutoff redshift, at 2σ confidence level, for the best PBH scenario inferred from the GWTC-2 dataset. In blue we show the events from the GWTC-1; in red, the new events reported after the O3a observing run.

In Fig. 6.1 we show the posterior distribution of PBH hyperparameters obtained by applying hierarchical Bayesian inference to the GWTC-2 dataset. In order to highlight the information content coming from effective spin measurements, we compare inference results obtained with and without the use of spin information. When we neglect $\chi_{\rm eff}$, the mass distribution of the events in the catalog favors high values of $z_{\rm cutoff}$, making accretion less relevant. When we include $\chi_{\rm eff}$, the best-fit value of the characteristic scale of the initial mass function

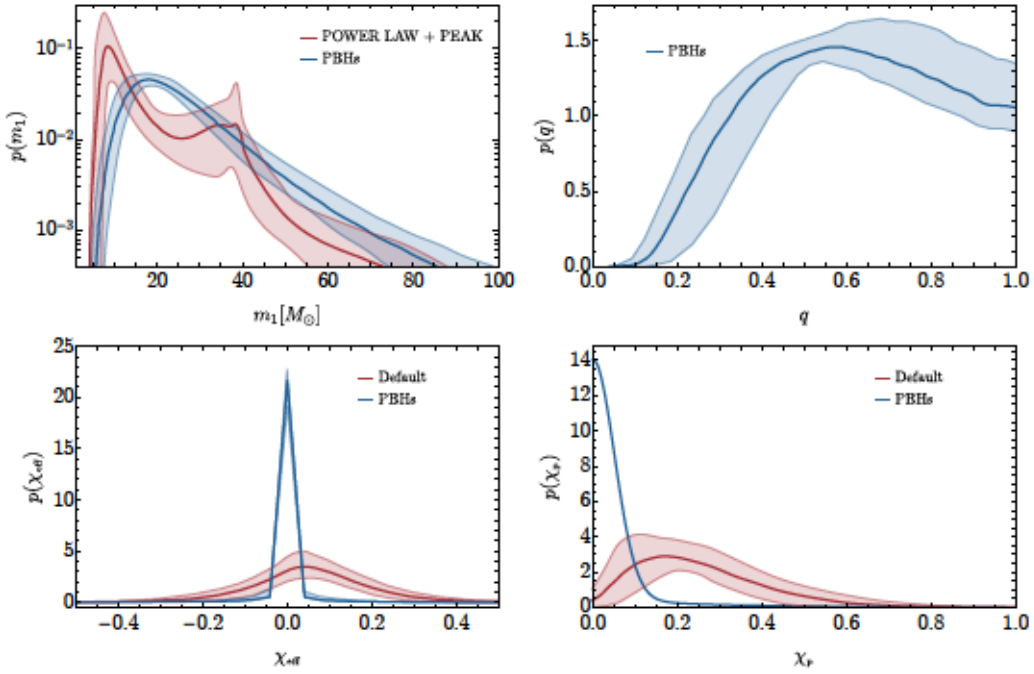

Figure 6.3: Distribution of the primary mass m_1 (top left), mass ratio q (top right), effective spin $\chi_{\rm eff}$ (bottom left) and precession spin $\chi_{\rm p}$ (bottom right) from our best-fit model when we include $\chi_{\rm eff}$ (but not $\chi_{\rm p}$) in the inference. For comparison, we also show the 90% CL distributions found by the LVC in Ref. [15] for astrophysical sources.

M_c decreases only slightly, but the posterior of $z_{\rm cutoff}$ gets narrower and peaks at smaller values. This is because several events in O3a have effective spin not compatible with zero, and accretion is necessary to spin up PBHs. This also affects the posterior of σ (the initial width of the PBH mass function), which gets narrower and peaks at a smaller value, because accretion broadens the mass function. As expected, the PBH abundance is found to be relatively stable with respect to changes of the other hyperparameters: we find $f_{\rm PBH} \simeq 3{\cdot}10^{-3}$, indicating that this population of PBHs can comprise at most a subpercent fraction of the totality of the DM.

In Fig. 6.2 we show the 2σ confidence intervals of the effective spin parameter distribution predicted by the PBH model in terms of the primary component mass, for different values of the mass ratio. The values of the cutoff redshift have been chosen around the 2σ range obtained from best-fitting the primordial scenario considering the GWTC-2 dataset. Following Refs. [208, 393], for each mass value m_1, we have averaged over the individual spin directions with respect to the total angular momentum assuming isotropic and independent distributions. Because of the stronger impact of accretion on binaries with a larger total mass, one finds an enhancement of the PBH spins with respect to the small values inherited at formation only above a certain threshold. The distributions shown in Fig. 6.2 highlight the transition from initially vanishing values of the spins to large values depending on the binary masses and accretion strength. Since the transition from negligible to large values of the spins is pushed towards smaller masses as the cutoff is reduced (i.e. stronger accretion), the presence of several spinning binaries in the GWTC-2 catalog leads to a preference towards smaller values of $z_{\rm cutoff}$. Blue points with error bars are data from the GWTC-1, while red points are new detections from the O3a run, as reported by the LVC using agnostic priors.

In Fig. 6.3 we show the distribution of the most relevant binary parameters (primary mass m_1, mass ratio q, effective spin $\chi_{\rm eff}$, and precession spin $\chi_{\rm p}$) inferred from our best-fit model. On the top left, we plot the marginalized posterior probability for the primary mass m_1 for the PBH scenario, adding also for comparison the corresponding preferred result found in Ref. [15] assuming a "Power-law + Peak" mass function. On the top right, we plot the marginalized distribution for the mass ratio in the PBH case. Notice that, due to the preferred relatively high value of the cutoff redshift and the significant width of the mass function, the distribution is peaked at $q \sim 0.5$ (had we found a smaller value of $z_{\rm cutoff}$ the distribution would have peaked at higher values of the mass ratio as predicted by the PBH

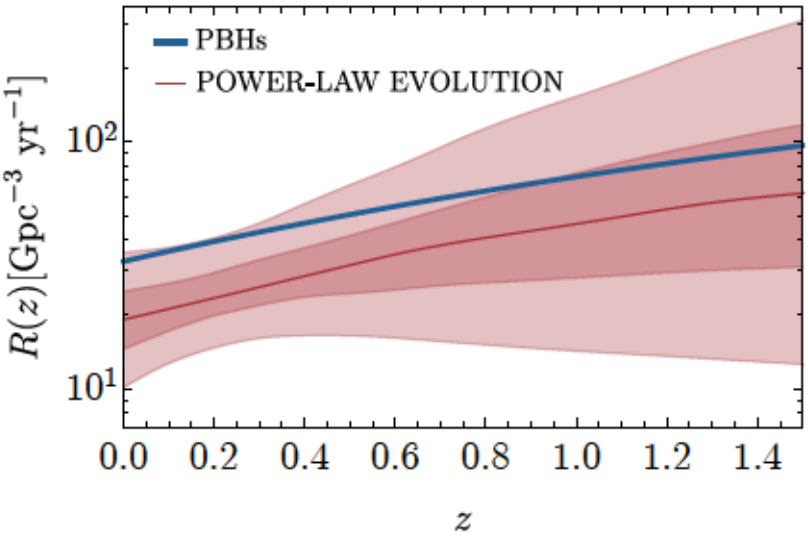

Figure 6.4: PBH merger rate density evolution given by Eq. (6.10) for the best-fit population (blue line). For comparison, we also show (in red) the 50% (90%) confidence level for the merger rate found by the LVC [15] adopting a power-law evolution model for astrophysical sources.

scenario with accretion [208, 393]). On the bottom we plot the marginalized distributions for the effective spin parameter $\chi_{\rm eff}$ and the precession spin $\chi_{\rm p}$, which parametrizes the spin components perpendicular to the binary angular momentum responsible for the precession of the orbital plane, both for the PBH scenario and the so-called "Default" model, see Appendix D.1 of Ref. [15]. In both cases, the probability distributions inferred from the PBH model show a narrow peak around zero since the best-fit PBH mass function is dominated by relatively small masses, which are correlated with small spins. This is not in contrast with the fact that we find a preference for an accreting PBH model due to the presence of several (moderately) spinning binaries in the catalog. Indeed, we stress that Fig. 6.3 shows the population distribution, which does not account for selection effects (current detectors favor the observation of large masses). This explains the difference with the "Default" model, for which masses and spins are not correlated, giving rise to a peak at nonvanishing spins and broader distributions.

Finally, in Fig. 6.4 we compare the prediction for the evolution as a function of redshift of the merger rate density $R(z)$, as given by Eq. (6.10) for the best-fit PBH model, with the power-law evolution model for astrophysical sources found in Ref. [15]. Interestingly,

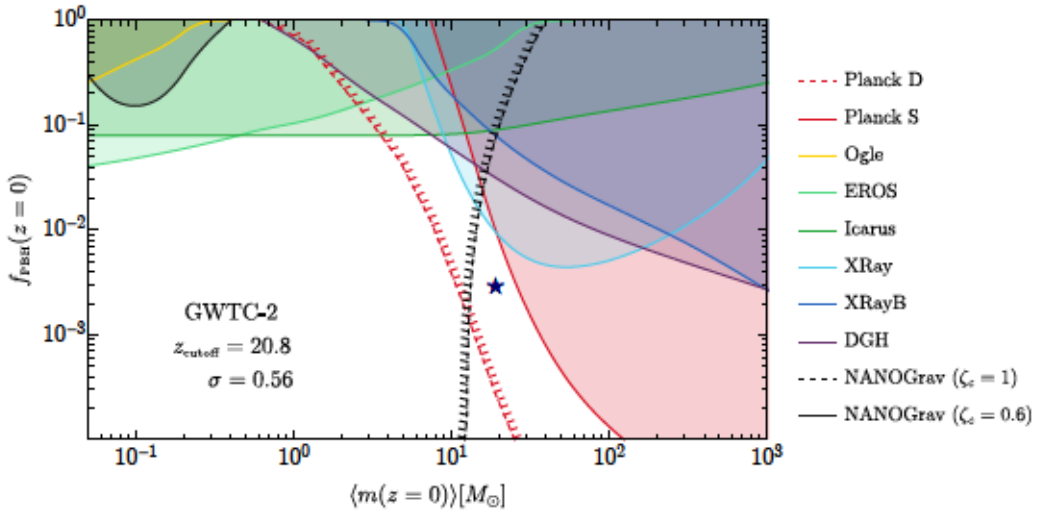

Figure 6.5: Summary of the constraints on the present PBH abundance $f_{\rm PBH}(z=0)$ as a function of the mean present PBH mass $\langle m(z=0)\rangle$. The blue star indicates the median values for the population parameters $\{M_c, \sigma, f_{\rm PBH}, z_{\rm cutoff}\}$ inferred with the GWTC-2 dataset. We have indicated by the red and black dashed lines, respectively, the bounds from Planck D and NANOGrav, which carry uncertainties (see the main text for details). The perpendicular dashes point towards the would-be excluded regions.

the latter is slightly less steep than the $R(z) \propto (1+z)^{2.7}$ behavior predicted from the star formation rate [451], although current observational errors are still too large to draw any conclusion. At any rate, the measured merger rate evolution is compatible with the PBH scenario, which predicts less mergers compared to the stellar-origin scenario in the high redshift side of the LVC horizon. Furthermore, the PBH scenario predicts a merger rate which increases monotonically also at redshifts beyond the LVC horizon, while in the astrophysical case the rate is expected to decrease soon after the $z \sim 2$ star formation rate peak redshift (unless there is a significant contribution from Population III binaries, which could produce a second peak at large redshift). This difference is of particular interest for third-generation GW detectors, which may be able to detect mergers up to redshift $z \simeq \mathcal{O}(10^2)$ [42, 452].

6.5 Constraints on the PBH abundance

In this section we compare the PBH abundance found to explain the observed BH merger events within the PBH scenario to other existing constraints. We refer to the recent reviews [175, 180] and references therein for more details.

In the mass range of interest for our discussion, the most relevant constraints come from CMB anisotropies [417, 453]. PBHs start accreting gas in the early Universe in a process accompanied by emission of ionizing radiation, to which CMB temperature and polarization fluctuations are very sensitive. The constraints derived in [453] also take into account the catalysing effect of the early DM halo forming around individual PBHs, as discussed in Sec. 6.2. Due to uncertainties in the accretion physics, the authors analyze two alternative scenarios believed to bracket uncertainties: the accreting gas is either in a disk or in a spherical geometry (Planck D/S respectively). The relevant electromagnetic emission takes place in the redshift range $300 \lesssim z \lesssim 600$. This means that the spherical model (Planck S) is expected to be more accurate, as a thin accretion disk could form only at much smaller redshift [408], as discussed in Sec. 6.2. Also, since the relevant emission takes place at high redshift, its physics is independent of uncertainties in the accretion model due to the onset of structure formation. Finally, as inferred from the results of the N-body simulation performed in Ref. [443], clustering at that early epochs is not relevant (see also [391]).

Other constraints come from comparing the *late time* emission of electromagnetic signals from interstellar gas accretion onto PBHs with observations of galactic radio and X-ray isolated sources (XRay) [454, 455] and X-ray binaries (XRayB) [456], Dwarf Galaxy Heating (DGH) due to interactions of PBHs with the interstellar medium using data from Leo T dwarf galaxy observations [457] and lensing searches of massive compact halo objects (MACHOs) towards the Large Magellanic Clouds (EROS) [458], fast transient events near critical curves of massive galaxy clusters (Icarus) [459], and observations of stars in the Galactic bulge by the Optical Gravitational Lensing Experiment (Ogle) [460].

Finally, the NANOGrav experiment searching for a stochastic GW background in the frequency range close to $f \simeq 1\,\mathrm{yr}^{-1}$ would be able to detect the GWs induced at second order by the curvature perturbations responsible for PBH formation. We show the constraint obtained by the null observation in the 11-yr dataset [461]. We stress that this is only

applicable for PBHs formed from the collapse of density perturbations and in the absence of non-Gaussianities (see [462, 463, 464, 465, 466]). The NANOGrav collaboration has recently released a new dataset based on 12.5 yrs of observations, claiming that the previous constraint should relax due to an improved treatment of the intrinsic pulsar red noise [467]. The collaboration also claims strong evidence for a stochastic common-spectrum process [467] in the new dataset, which could be explained by PBH formation [468, 469, 470, 471, 472] (although the signal could also be ascribed to supermassive BH binaries [473], cosmic strings [474, 475, 476, 477], phase transitions in a dark sector [478, 479, 480], or other scenarios [481, 482, 483, 484, 485]). As the new constraint would have a similar impact in the mass range of interest, here we choose to show the 11-yr constraint as a reference [461].

Notice that the bounds, typically derived for a monochromatic PBH population, can be adapted to extended mass functions using the techniques described in [403, 486]. One should bear in mind the difference between constraints applying to high-redshift abundances and masses (such as Planck D/S and NANOGrav, which probe the early Universe physics) and the ones constraining late-time Universe quantities after the onset of structure formation. The evolution of masses and $f_{\rm PBH}$ with accretion requires constraints to be treated as described in detail in Ref. [179]. The main effect of accretion is to alleviate early Universe CMB constraints by shifting them to higher *late-time* mass ranges and making them weaker due to the growth of $f_{\rm PBH}$ [cf. Eq. (6.6)].

6.5.1 The GWTC-2 dataset confronts the PBH constraints

In Fig. 6.5 we collect all constraints on the PBH abundance and compare them to the population inferred from the GWTC-2 dataset.

At face value, if interpreted as coming from the PBH scenario, the GWTC-2 events seem to be in tension with Planck D. However, one should consider this conclusion with a grain of salt. As already mentioned, the assumption of a thin disk in the Planck D constraint is less reliable at high redshift [408] with respect to spherical accretion (Planck S, which is compatible with GWTC-2).

We also take the opportunity to notice that the constraint from the NANOGrav 11-yr data from Ref. [461] has large systematic uncertainties, above all in their choice of the threshold

$\zeta_c = 1$ for PBH formation (where ζ is the curvature perturbation responsible for the creation of PBHs upon collapse). In order to account for these uncertainties, we have shown how the constraint is relaxed by choosing a threshold $\zeta_c = 0.6$ motivated by state-of-art numerical simulations [487] (see also the discussion in Ref. [385]). Given the uncertainties discussed above, in Fig. 6.5 we have decided to show the Planck D and the more stringent NANOGrav constraints ($\zeta_c = 1$) by dashed lines without filling the corresponding excluded region.

In conclusion, assuming that all of the events in the GWTC-2 catalog are originated from PBHs is not in contrast with current observational constraints.

6.6 Discussion

This paper is a first step toward systematically testing various models for the formation of BH binaries. We use a machine learning enhanced population analysis pipeline to constrain the PBH scenario with the latest GWTC-2 data. We find a preference for a scenario in which PBHs experience a phase of accretion before the reionization epoch and spin up. We also find that PBHs may form about 0.3% of the DM in the Universe. This abundance is still compatible with other constraints.

This work can also be considered as a proof of principle, which can be extended in various directions by relaxing some of the assumptions of our analysis. We have assumed that every binary BH detection has a primordial origin, neglecting other formation channels. This is obviously a very strong assumption. In the future, we will mix the PBH simulation with different astrophysical populations, such as isolated and dynamically-formed binaries, to produce a more comprehensive inference model. Furthermore, it would be interesting to extend the analysis to different PBH mass functions and accretion models.

For simplicity, we account for selection bias using a semianalytical noise model, which was checked against previous detection rate estimates. However our single-detector approximation is expected to fail as the sensitivity improves and more detectors join the network. Furthermore, we are using the signal-to-noise ratio instead of the false-alarm rate as our detection statistics, at variance with the LVC search pipelines. Recent work uses machine learning techniques to better capture the detector network response [447, 488]. Future work should incorporate these techniques once they are validated against the results produced by

a search pipeline, to better account for the selection bias.

Chapter 7

Probing the existence of ultralight bosons with a single gravitational-wave measurement

Light bosons, proposed as a possible solution to various problems in fundamental physics and cosmology[489, 490, 491], include a broad class of candidates for beyond the Standard Model physics, such as dilatons and moduli[492], wave dark matter[493] and axion-like particles[494]. If light bosons exist in nature, they will spontaneously form "clouds" by extracting rotational energy from rotating massive black holes through superradiance, a classical wave amplification process that has been studied for decades[495, 496]. The superradiant growth of the cloud sets the geometry of the final black hole, and the black hole geometry determines the shape of the cloud[427, 497, 498]. Hence, both the black hole geometry and the cloud encode information about the light boson. For this reason, measurements of the gravitational field of the black hole/cloud system (as encoded in gravitational waves) are over-determined. We show that a single gravitational wave measurement can be used to verify the existence of light bosons by model selection, rule out alternative explanations for the signal, and measure the boson mass. Such measurements can be done generically for bosons in the mass range $[10^{-16.5}, 10^{-14}]$ eV using LISA observations of extreme mass-ratio inspirals.

7.1 Introduction

Gravitational waves allow us to measure to exquisite accuracy the host black hole mass and spin (M, a), which gives us a model prediction for the boson cloud profile. We match this prediction with a direct measurement of the properties of the boson cloud profile (as encoded in two "shape parameters" A and B, defined below) to confirm the model with no tuneable parameters. Such confirmation is possible when superradiant instability has occurred, and the black hole/cloud system is in equilibrium during the measurement.

Superradiance occurs when the boson Compton wavelength $\lambda = \hbar/(m_s c)$ is comparable with the black hole's Schwarzschild radius $R = 2GM/c^2$, or $R/\lambda = 0.15(M/10^6 M_\odot)(m_s c^2/10^{-17}\mathrm{eV}) \sim 1$. Then the instability quickly extracts rotational energy from the black hole, leading the black hole/cloud system to equilibrium on a so-called "Regge trajectory"[498], where the rotational frequency of the boson (which from now on, for simplicity, we assume to be a scalar field) is comparable to the black hole rotational frequency[427, 498]:

$$\mu_s^{(1)} \simeq \frac{a}{2Mr_+}, \tag{7.1}$$

where $\mu_s \equiv m_s/\hbar$ is the boson mass, $r_+ = \sqrt{M^2 - a^2} + M$ is the outer horizon of the rotating black hole, and from now on we will use geometrical units ($G = c = 1$). The superscript (1) labels one of three possible experimental ways to measure the mass [Eqs. (7.1)-(7.3)]. To a good approximation, the scalar field profile in the equilibrium configuration is well described by[427, 499] $\varphi(t, r, \theta, \phi) = ABre^{-Br/2}\cos(\phi - \omega_R t)\sin\theta$. Here A is the scalar field amplitude, $B = M\mu_s^2$ is a "scale" parameter (note that the radial profile of the cloud has a maximum at $r_{\max} = 2/B$), and $\omega_R \simeq \mu_s$. Both A and B are determined through independent physical processes: A is set by the evolution of the black hole/cloud system, while B is set by the black hole geometry when the black hole/cloud system is in equilibrium.

For typical black hole/cloud systems of interest $M\mu_s \sim 1$, so that the field oscillation time scale $\sim 1/\omega_R$ is of the order of seconds (hence much shorter than the Laser Interferometric Space Antenna (LISA) observation time $T_{\rm obs}$) when $M \sim 10^6 M_\odot$. Therefore we can time-average the gravitational potential generated by the cloud. In the equatorial plane, the result has the form $\Phi_b(r) = \Phi_b(A, B, M, r)$ (see Eq. (7.11) in the method). By imposing that $\Phi_b(r) \sim -M_s/r$ at large r, where M_s is the total mass in the boson cloud, we can relate

the scalar field amplitude to its mass: $A = (\mu_s^2 M^{3/2} M_s^{1/2})/[8\pi(4-\mu_s^2 M^2)]^{1/2}$. Therefore, if we can measure the amplitude A and scale B of the scalar cloud we get two more estimates of the boson mass:

$$\mu_s^{(2)} = (M/B)^{-1/2} \tag{7.2}$$

and

$$\mu_s^{(3)} \simeq 2\left[\frac{\pi A^2}{M M_s}\left(\sqrt{1+\frac{2M_s}{A^2 M\pi}}-1\right)\right]^{1/2}. \tag{7.3}$$

To infer $\mu_s^{(3)}$, we need an estimate for the mass of the boson cloud M_s. Although M_s can be obtained from the evolution of the black hole/cloud system[427] given $\mu_s^{(1)}$ measured from Eq. (7.1), the host's initial spin and accretion rate are unknown, and therefore M_s can have any value in a range $M_s \in [0, M_s^{\rm max}]$. We fix $M_s^{\rm max}$ by assuming that the initial black hole spin (pre-superradiant amplification) is maximal. Even under this conservative estimate, we find that the ultralight boson hypothesis can be either confirmed or ruled out.

The superradiant instability occurs on a time scale $\tau_{\rm inst} \sim 10^5 {\rm yr}\, j_{\rm in}^{-1}(10^6 M_\odot/M)^8(10^{-17}{\rm eV}/m_s c^2)^9$, where $j_{\rm in}$ denotes the dimensionless spin of the black hole before the occurrence of the superradiant instability[497, 500]. Once the nonaxisymmetric boson cloud has grown, it dissipates through gravitational waves on a much longer time scale

$\tau_{\rm GW} \sim 5\times 10^{11}{\rm yr}\, j_{\rm in}^{-1}\left(10^6 M_\odot/M\right)^{14}\left(10^{-17}{\rm eV}/m_s c^2\right)^{15}$. Therefore we can assume that the superradiant instability occurs quickly ($\tau_{\rm inst} \ll \tau_{\rm GW}$) and that the black hole/cloud system is in equilibrium over a typical LISA observation time $T_{\rm obs} \sim 1{\rm yr} \ll \tau_{\rm inst} \ll \tau_{\rm GW}$. The black hole/cloud system will remain in equilibrium even if there is accretion, because the (Salpeter) accretion timescale $\tau_{\rm acc} \gg T_{\rm obs}$[427].

From an observational standpoint, there is no reason why three independent measurements of the boson mass using Eqs. (7.1), (7.2) and (7.3) should yield the same result, unless the superradiant instability hypothesis is correct. The gravitational waveform emitted by the EMRI of a small compact object orbiting the black hole/cloud system encodes both the host geometry and the gravitational potential of the cloud, making it possible to either confirm this hypothesis if the measurements are self-consistent or rule it out if they are not. In other

words, a measurement of either $\mu_s^{(i)}$ $(i = 1, 2, 3)$ gives the boson mass only *if* the boson cloud exists. However, a self-consistent measurement of *more than one* $\mu_s^{(i)}$ confirms the existence of the cloud.

EMRI observations by LISA can measure both the mass and spin of the host black hole to better than 1% accuracy[58]. Matter effects may be resolved when the density of the surrounding material is sufficiently high: in fact, such matter effects are resolvable even when the density is much smaller than expected from boson clouds[501]. Therefore, as we show below, the tests we just outlined can be performed with LISA EMRI observations. For illustration: if the mass $M = 10^5\, M_\odot$ and spin $a = 0.6M$ can be measured to an accuracy $\sim$1%, and A and B (with degeneracies) may be measured to an accuracy $\sim$10%, taking the 95% confidence interval of $M_s \in [0, 0.1M]$. Then the three estimates of the ultralight boson particle $\mu_s^{(1)}$, $\mu_s^{(2)}$ and $\mu_s^{(3)}$ would have errors $\sim$12%, 8% and 69%, respectively.

7.2 Methods

Posterior estimation. We consider a LISA EMRI signal from a black hole/cloud system and use Nested Sampling (as implemented in `MultiNest`[502, 503, 504]) to evaluate the posterior distribution of our measurement, with the likelihood defined for colored gaussian noise following the LISA power spectral density (PSD)[505]

$$\log \mathcal{L}(\vec{\theta}, A, B) = (s, h(\vec{\theta}, A, B)) - \frac{1}{2}(h(\vec{\theta}, A, B), h(\vec{\theta}, A, B)). \tag{7.4}$$

Here s is the injected signal, which we assume to be noiseless (this is approximately true at high SNR, as in our chosen scenario) and $h(\vec{\theta}, A, B)$ is the gravitational-wave template at 3.5 PN order[506, 507, 508] for a detector oriented optimally for the plus polarized wave, which we use in our parameter estimation to sample over both binary parameters $\vec{\theta}$ and matter parameters A, B.

The gravitational potential due to the cloud is included at lowest PN order[501]:

$$h(f) = h(f) e^{i(\psi(f) + \Delta\psi_{\rm matter}(f) + 2\pi f t_c + 2\phi_c)}, \tag{7.5}$$

where $h(f)$, $\psi(f)$ are the amplitude and phase of the gravitational wave, $\Delta\psi_{\rm matter}(f)$ is the

phase shift due to matter effects, and $(t_c,\, \phi_c)$ are the time and phase of coalescence.

The inner product (a, b) is defined as

$$(a,b) = 4\,\mathrm{Re}\left[\int_0^\infty \frac{a(f)b^*(f)}{S_n(f)}df\right], \tag{7.6}$$

where $S_n(f)$ is the LISA PSD[505]. We take the absolute value of the inner product to maximize over the phase of coalescence[509, 510]. In our parameter estimation, we simulate a single gravitational-wave event with given parameters and sample over binary masses $(m_1,\, m_2)$, aligned spins $(s_1,\, s_2)$, time of coalescence t_c, and boson cloud parameters $(A,\, B)$: see Eq. (7.11).

Since the nested sampling approach is computationally expensive, we use the Fisher information matrix approach[511] to explore the full parameter space (Figure 7.2). The elements of the Fisher matrix are calculated by taking the inner product between derivatives of waveform

$$\Gamma_{ab} \equiv \left(\frac{\partial h}{\partial\theta^a}, \frac{\partial h}{\partial\theta^b}\right). \tag{7.7}$$

The measurement uncertainties and correlations are given by

$$\begin{aligned} \Delta\theta^a &= \sqrt{\Sigma^{aa}}, \\ c_{ab} &= \frac{\Sigma^{ab}}{\sqrt{\Sigma^{aa}\Sigma^{bb}}}, \end{aligned} \tag{7.8}$$

respectively, where $\Sigma^{ab} = \Gamma^{-1}_{ab}$. In this approach, we implemented the gravitational-wave template at 2PN order[511]. We have verified that the Fisher matrix estimates are consistent with the nested sampling results.

Bayes factors. We define three hypotheses: (1) there is a matter cloud produced by ultralight bosons ($\mathcal{H}_{\rm Cloud}$); (2) there is some matter distribution similar to a bosonic cloud, but not necessarily produced by ultralight bosons: i.e., Eqs. (7.1)-(7.3) are not necessarily

satisfied ($\mathcal{H}_{\rm Other}$); and (3) there is no cloud ($\mathcal{H}_{\rm No\ cloud}$). The corresponding evidences are:

$$\begin{aligned}
\mathcal{Z}_{\rm Cloud} &= \int \mathcal{L}(\vec{\theta}, f(M,a,M_s), g(M,a))\pi(\vec{\theta})\pi(M_s)d\vec{\theta}dM_s, \\
\mathcal{Z}_{\rm Other} &= \int \mathcal{L}(\vec{\theta}, A, B)\pi(\vec{\theta})\pi(A)\pi(B)d\vec{\theta}dAdB, \\
\mathcal{Z}_{\rm No\ cloud} &= \int \mathcal{L}(\vec{\theta}, 0, 0)\pi(\vec{\theta})d\vec{\theta},
\end{aligned} \tag{7.9}$$

with

$$\begin{aligned}
f(M,a,M_s) &= \frac{a^2}{4\sqrt{2\pi}\,(1+\alpha)}\sqrt{\frac{M_s}{32M^5\,(1+\alpha)-17a^2M^3}}, \\
g(M,a) &= \frac{a^2}{4M^3\,(1+\alpha)^2},
\end{aligned} \tag{7.10}$$

where $\alpha \equiv \sqrt{1-(a/M)^2}$, $\vec{\theta}$ are the binary parameters, $\mathcal{L}(\vec{\theta}, A, B)$ is the likelihood, and $f(M,a,M_s)$ and $g(M,a)$ can be found by solving Eqs. (7.1)-(7.3) for A and B. We computed the Bayes factor of two hypotheses $\mathcal{H}_x$ and $\mathcal{H}_y$, i.e. the ratio $\mathcal{B}^y_x = \mathcal{Z}_y/\mathcal{Z}_x$, using nested sampling. Since alternative hypotheses typically cause only small corrections to the gravitational waveform, we set conservatively a uniform prior on (A, B) so that the effect on the waveform phase is at most of order percent, but still measurable ($\gtrsim 1$ rad). We additionally cut off the prior at a maximum of ($3A$, $3B$), to be conservative. Setting a completely uniform prior or allowing for negligible phase deviations would yield more optimistic results. M_s is set to be uniform over $M_s \in [0, 0.1]M$. When using the Fisher information matrix, we compute the Bayes factors following standard methods[512]. We have verified that the results are compatible with the nested sampling analysis.

Waveform. We estimate the waveform by perturbing the energy balance equation[501]. The gravitational potential produced by the boson cloud is[499]

$$\begin{aligned}
\Phi_b(r) \simeq \big[\pi A^2 e^{-Br}\big(&-MB^6r^5 - 2B^5r^4(M-2r) \\
&-12B^4r^3(M-2r) + 8B^3r^2(10r-3M) \\
&-16B^2r(M-10r) + 16e^{Br}\left(B^3Mr^2 - 4B^2r^2\right. \\
&\left.+BM-12\right) - 16B(M-12r) + 192)\big] \,/\, \left(2B^4Mr^3\right).
\end{aligned} \tag{7.11}$$

We expand the phase shift to first order in $\Phi_b/\Phi_{\rm BH}$, where $\Phi_{\rm BH}$ is the gravitational potential

in the absence of the cloud. This introduces a correction to Kepler's law and the energy balance and changes the accumulated orbital phase shift. The phase shift due to matter can be computed from the orbital energy balance equation[501]

$$\frac{dE_{\rm orbit}}{dt} + \frac{dE_{\rm gw}}{dt} = 0, \tag{7.12}$$

where

$$\begin{aligned} \frac{dE_{\rm orbit}}{dt} &= \frac{d}{dt}\left(\frac{1}{2}\mu v^2 + \mu\Phi(r)\right), \\ \frac{dE_{\rm gw}}{dt} &= \frac{32\mu^2 r^4 \omega^6}{5}, \end{aligned} \tag{7.13}$$

and $\Phi(r) = -M/r + \Phi_b(r)$. Here μ is the small compact object mass, v is the velocity of the companion, and ω is the orbital angular frequency. This gives the rate of change of the orbital radius

$$r'(t) = -\frac{32\mu^2 r^4 \omega^6}{5\left[\mu v v'(r) + \mu\Phi'(r)\right]}, \tag{7.14}$$

which can be translated to the total gravitational-wave phase shift using the stationary phase approximation[19]:

$$\Delta\psi_{\rm matter} = 2\pi f t(f) - 2\phi(f), \tag{7.15}$$

where the time and orbital phase are given by

$$\begin{aligned} t(f) &= \int \frac{1}{r'(t)} dr, \\ \phi(f) &= \int \frac{\omega}{r'(t)} dr. \end{aligned} \tag{7.16}$$

where we only consider matter contribution. The mapping between the orbital radius and the gravitational-wave frequency may be solved by inverting the following relation for r

$$\omega(f) = \pi f = \sqrt{\frac{\Phi'(r)}{\mu r}}, \tag{7.17}$$

and expanding to first order in $\epsilon = \Phi_b/\Phi_{\rm BH}$[501]. We have included first-order corrections from matter effects, and verified that second-order corrections cause negligible phase corrections in the gravitational waveform at percent level in the case that we consider here.

Dark matter mini-spike. To illustrate a case where our black hole/cloud test discriminates other effects from boson clouds, we consider a black hole surrounded by a dark matter mini-spike (similar constructions were used in previous work[501]). We assume the mini-spike density to follow a power-law

$$\rho(r) = \rho_{\rm sp}\left(\frac{r}{r_{\rm sp}}\right)^{-\alpha}, \tag{7.18}$$

where $\rho_{\rm sp}$ and $r_{\rm sp}$ are the density and radius normalization constants, and α gives the steepness of the profile. We follow[501] to construct the orbital phase shift of the gravitational wave due to the mini-spike. To assess whether the dark matter mini-spike can mimic a boson cloud we first construct the orbital phase shift due to a dark matter spike, then we fit the results using a boson cloud, but treating the A and B parameters as free. We set $\rho_{\rm sp} = 3\times 10^5 M_\odot/{\rm AU}^3$, $\alpha = 1$ and $r_{\rm sp} = 6M$, which causes an orbital shift of similar order as the boson cloud in our example scenario.

We chose the dark matter mini-spike parameters to mimic boson cloud effects. If we had chosen the dark matter mini-spike profile expected to form through adiabatic growth from a seed black hole in a typical cuspy dark matter environment with density $\sim {\rm GeV/cm}^3$ at 100 kpc [Ref. 513], or if we had chosen different values of α, the discriminatory power of our test would have improved even further.

7.3 Results

As a proof of principle, let us first consider a case study of a system where it is indeed possible to confirm the existence of ultralight bosons with LISA. We construct an EMRI gravitational-wave template in the black hole/cloud potential of Eq. (7.11), where A and B are free parameters. Following previous work[501], to compute the evolution we include the lowest post-Newtonian (PN) order in the phasing as well as the leading order contribution from matter effects. We also add spin-dependent PN corrections to the *inspiral* waveform (as implemented in the LIGO Algorithm Library[514]), which allows us to estimate the black hole spin[506, 508]. Since the waveform includes matter effects, an EMRI observation allows us to infer *both* the boson cloud and host black hole properties: in particular, by matched filtering we can recover the masses and (aligned) spin of the central black hole, as well as the boson cloud amplitude and steepness parameters (A and B).

To be specific, we consider gravitational waves from a stellar-mass black hole ($m = 60\ M_\odot$, $a' = 0$) inspiralling into a supermassive black hole ($M = 10^5\ M_\odot$, $a = 0.6M$) surrounded by a cloud generated by bosons of mass $\mu_s = 2.26 \times 10^{-16}$ eV, with total cloud mass $M_s = 0.05M$, one year observation time and a LISA signal-to-noise ratio (SNR) $(h, h)^{1/2} = 97$, which corresponds to redshift $z \sim 1$[58, 515]. We use a nested sampling Markov-Chain Monte Carlo algorithm to recover three independent posteriors $\mu_s^{(i)}$ ($i = 1, 2, 3$) from measurements of M, a, A and B. Figure 7.1 (top panel) shows that in this case we confirm the ultralight boson hypothesis because all three measurements overlap. In the bottom panel of Figure 7.1 we consider instead the gravitational wave signal produced by a small compact object falling into a black hole surrounded by a dark matter mini-spike with $\rho_{\rm sp} = 3 \times 10^5 M_\odot/{\rm AU}^3$, $\alpha = 1$ and $r_{\rm sp} = 6M$ (see "Methods" for the motivation for the parameters)[501, 516]. In this case we can rule out ultralight bosons as a source of the matter distribution, because the recovered ultralight boson masses do not overlap.

It is natural to ask whether the case study shown above is generic: can similar measurements be done across a range of binary parameters and boson masses? To answer this question we simulated one year of LISA EMRI observations for different boson masses by varying the host spin $j \in [0.4, 0.98]$, mass M, and SNR. To sample this large parameter space we used a (much faster) Fisher information matrix calculation to recover parameters. As shown in Figure 7.2, we found that it is possible to carry out consistency checks for two or more of the $\mu_s^{(i)}$'s for a broad range of binary parameters and for boson masses $\mu_s \in [10^{-17}, 10^{-14}]$ eV. Extending the observation time improves the lower bound, but masses $\mu_s \lesssim 10^{-20}$ eV result in unmeasurable effects (the waveform phase correction due to the cloud contributes less than one gravitational-wave cycle). At the opposite end of the mass range, black hole/cloud systems with $\mu_s \gtrsim 10^{-14}$ eV would produce EMRI signals outside of the LISA sensitivity band.

7.4 Discussion

Our work is meant to be a proof-of-principle demonstration that binary pulsar-like tests of ultralight bosons are possible through EMRI observations with LISA, but future efforts to model the system more precisely will be required for the practical implementation of this program in the LISA data-analysis. Gravitational waves from EMRIs can be computed to

high accuracy for astrophysical massive black holes in isolation, which are characterized only by their mass and spin, but surrounding matter can back-react on the binary. Back-reaction effects are small for the high mass ratios considered here, but they can be relevant for comparable-mass binaries.

Furthermore, it will be interesting to take into account the possibility of "mode mixing": perturbations due to the small orbiting companion can mix superradiating modes with "dumping" (infalling) levels of the cloud, causing the cloud to collapse before the binary can trace its properties[517]. If this occurs, our test will yield a null result with non-overlapping distributions for the $\mu^{(i)}$'s, as we would not measure the effects of the cloud. The disturbance on the cloud due to a companion is an active area of research: recent work suggests that the boson cloud would, in fact, survive mode mixing in the high mass ratio scenario studied in this paper when the small object is in a corotating orbit[518], and then a measurement would be possible. Counter-rotating EMRIs are less likely to be detectable by LISA[519]. Numerical estimates of the cloud mass after depletion can be approximated by the phenomenological fits $\sim M_s(1-\exp\left(-10q^{1.2}(M\mu_s)^{0.18}\right))$ and $\sim M_s(1-\exp\left(-2.3q^{0.9}-10(M\mu_s)^{3/2}\right))$ for co-rotating and counter-rotating orbits, respectively, as long as $q \lesssim 0.1$ and $M\mu_s \lesssim 0.2$ [Ref. 518]. Cloud depletion can therefore be neglected for most EMRIs, except for a narrow region of parameter space involving astrophysically rare counter-rotating orbits.

We have accounted for possible degeneracies between the binary parameters and effects due to the boson cloud using nested sampling to simultaneously infer the binary's intrinsic parameters (masses, spins), the cloud properties and the merger time (maximizing over the phase of the wave). The effect of the cloud is a slow cumulative shift uniquely tied to the cloud's density profile, so (as expected) we found that the degeneracy between the orbital parameters of the binary and the cloud parameters is small. Figure 7.1 shows that the consistency test can be performed for SNRs that can be achieved with LISA[58]. We have also verified that the consistency test is possible when including eccentricity corrections at first order in the gravitational-wave phasing[520].

Following previous work[427, 499] we focus on the most unstable mode, as it accounts for most of the matter distribution. Higher modes are unlikely to be observed because they would only become unstable on much longer timescales ($\tau_{\rm inst}^{\rm HM} \sim 10^7$ years for the illustrative case considered here)[500]. This is appropriate for the present order-of-magnitude estimate

of the effect of the matter distribution. However, the next-to-leading order mode can be filled through superradiance on a time scale one or two orders of magnitude higher than the first mode's dissipation time-scale. If the fundamental mode is depleted via gravitational radiation, our proposed test can still be performed by replacing Eqs. (7.1)-(7.3) with the equivalent expression for the next-to-leading order mode.

For simplicity, we assumed that the small compact object is in an equatorial orbit and we computed the gravitational potential for real scalar fields. However our results also apply to complex scalar fields where the potential is stationary[521]. In the same spirit we used PN waveforms with aligned spins, as opposed to more realistic, fully precessing EMRI waveforms with eccentricity[58, 522, 523]. These corrections will matter in LISA data analysis, but they only contribute a fraction of the total phase shift, and so they can be omitted for order-of-magnitude estimates. We have also checked the convergence of the PN expansion by comparing the accumulated phase shift of the highest term relative to the next-to-highest term, finding the difference to be negligible at the percent level. Another interesting effect is that, because the potential of a boson cloud is not spherically symmetric, orbital resonances could result in angular momentum transfer between the companion and the cloud, increasing the orbital eccentricity[499]. These resonances are an interesting topic for future study, but we verified that they do not occur for the orbital parameters considered here.

In conclusion, the possibility to obtain three independent measurements of ultralight boson masses which can be cross-compared for consistency is mostly unaffected by the corrections listed above. We have demonstrated that LISA EMRI observations, in a realistic SNR range, can be used to confirm (or rule out) the formation of ultralight boson condensates around astrophysical black holes in the mass range $\mu_s \in [10^{-16.5}, 10^{-14}]\,\mathrm{eV}$, directly probing the existence of ultralight bosons. More accurate waveform models and more accurate treatments of superradiance (including higher-order modes and possible transitions among superradiant states) will be needed for an implementation of this idea in LISA data analysis.

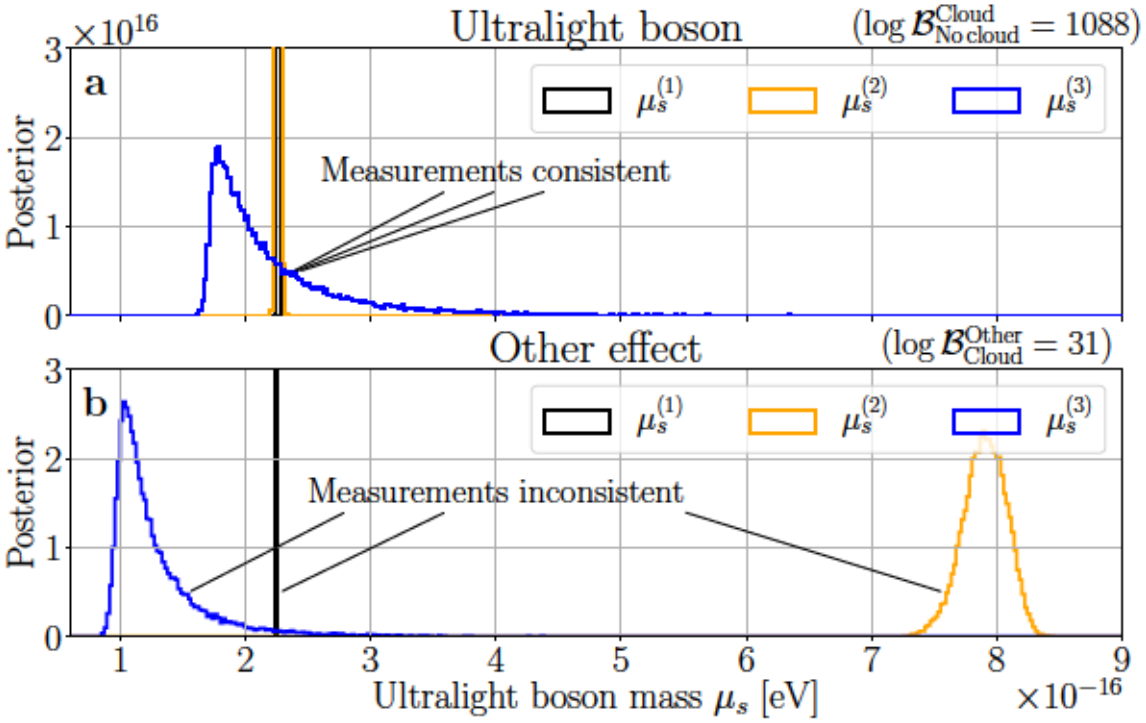

Figure 7.1: **Three independent posterior distribution measurements of ultralight boson particle masses $\mu_s^{(1)}$ (black), $\mu_s^{(2)}$ (orange) and $\mu_s^{(3)}$ (blue) [see Eqs. (7.1)-(7.3)] from a single gravitational-wave observation with LISA.** Panel **a**: the signal is produced by an EMRI into a black hole/cloud system with $\mu_s = 2.26 \times 10^{-16}$ eV. All three measurements overlap with each other, favouring the presence of the cloud over the "no cloud" hypothesis with Bayes factors $\log B^{\text{Cloud}}_{\text{No cloud}} > 1000$ (top-right). Panel **b**: the black hole has the same properties, but the "cloud" is produced by a dark matter mini-spike. Measurements do not overlap, ruling out the boson cloud hypothesis with Bayes factors $\log B^{\text{Other}}_{\text{Cloud}} > 30$.

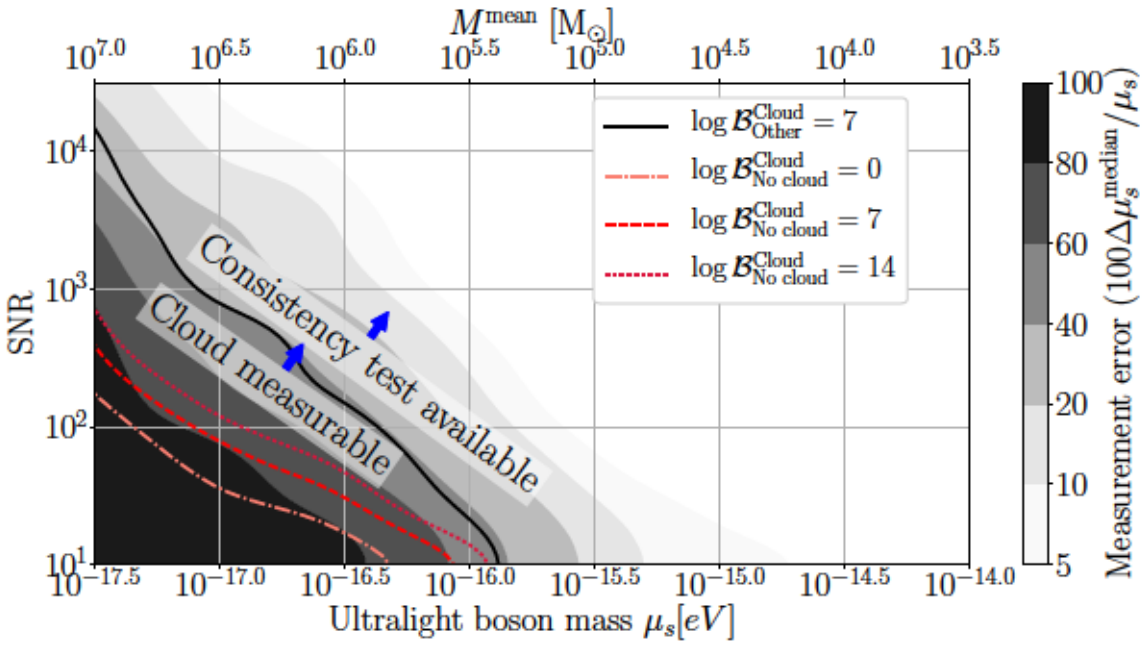

Figure 7.2: **Median error of the measurements $\mu_s^{(1,2,3)}$ in color as a function of the SNR and ultralight boson mass μ_s and mean host black hole mass $M^{\rm mean}$.** The consistency test is available across a wide $\mu_s \in [10^{-16.5}, 10^{-14}]$ eV (i.e. above the black contour, $\log \mathcal{B}^{\rm Cloud}_{\rm Other} = 7$). The presence of the cloud can be inferred over $\mu_s \in [10^{-17}, 10^{-14}]$ eV (above the red dashed contour, $\log \mathcal{B}^{\rm Cloud}_{\rm No\ cloud} = 7$). We have simulated a population of binaries distributed logarithmically across host mass $M \in [10^3, 10^7]\mathrm{M}_\odot$ and mass ratio $q \in [10^{-3}, 10^{-2}]$, and linearly in host spin $j \in [0.4, 0.98]$. We average all measurements over spin, and use a Gaussian filter on the data for visualization purposes. The black solid contour corresponds to $\log \mathcal{B}^{\rm Cloud}_{\rm Other} = 7$; the red dash-dotted, dashed, and pink dotted contours correspond to $\log \mathcal{B}^{\rm Cloud}_{\rm No\ Cloud} = 0$, 7 and 14, respectively.

Chapter 8

On the possibility of detecting ultra-short period exoplanets with LISA

[6] recently reexamined the possibility of detecting gravitational waves from exoplanets, claiming that three ultra-short period systems would be observable by LISA. We revisit their analysis and conclude that the currently known exoplanetary systems are unlikely to be detectable, even assuming a LISA observation time $T_{\rm obs} = 4$ yrs. Conclusive statements on the detectability of one of these systems, GP Com b, will require better knowledge of the system's properties, as well as more careful modeling of both LISA's response and the galactic confusion noise. Still, the possibility of exoplanet detection with LISA is interesting enough to warrant further study, as gravitational waves could yield dynamical properties that are difficult to constrain with electromagnetic observations.

8.1 Introduction

The idea of using space-based gravitational-wave (GW) observations with LISA to detect exoplanets was proposed almost 20 years ago. At the time only about 20 such systems were known. Even taking into account that eccentric systems could produce significant GW power

Table 8.1: Parameters of the most promising exoplanetary systems for GW detection (note that, as discussed in the text, the classification of these systems as exoplanets is questionable). All parameters are taken from the online exoplanet catalog `http://exoplanet.eu/catalog/`, with the exception of quantities labeled with † [3], ‡ [4], § [5], and *[6]. Here D_L, $M_{\rm star}[M_\odot]$ and $M_{\rm planet}[M_{\rm J}]$ denote the luminosity distance, mass of the star in solar masses, and mass of the planet in Jupiter masses, while $(\bar{\theta}_S, \bar{\phi}_S)$, ι and P denote the sky location (in ecliptic coordinates), inclination and orbital period of the binary.

Name	D_L [pc]	$M_{\rm star}[M_\odot]$	$M_{\rm planet}[M_{\rm J}]$	$\bar{\theta}_S$ [deg]	$\bar{\phi}_S$ [deg]	ι[deg]	P [days]
GP Com b	$72.83 \pm 0.32^{\dagger}$	$0.435^{\ddagger}$	26.2 ± 16.6	$23.00^{\dagger}$	$187.72^{\dagger}$	55.5 ± 22.5	0.032
V396 Hya b	$93.51 \pm 1.29^{\dagger}$	$0.345^{\ddagger}$	18.3 ± 12.2	$-14.50^{\dagger}$	$205.73^{\dagger}$	52 ± 27	0.045^{*}
J1433 b	$224.52 \pm 10.22^{\dagger}$	$0.8 \pm 0.07^{\S}$	57.1 ± 0.7	$23.89^{\dagger}$	$212.37^{\dagger}$	84.36	0.054

at higher harmonics, and that some of these exoplanets could resonantly excite the oscillation modes of the star they are orbiting, none of them was found to be detectable [524, 525, 526].

However, the number of known exoplanets is now in the thousands and exoplanet surveys point to a very large population of planetary systems in our Galaxy, with more than one planet per star on average [527] and free-floating planets outnumbering the stars [528]. Many of these planetary systems are dramatically different than our own, with hot Jupiters, highly eccentric and inclined orbits, as well as entire systems of tightly-packed inner planets. Such a rich and varied population of exoplanetary systems strains our current understanding of planetary system formation and evolution. A few years ago [529] showed that the stochastic GW background produced by these systems would peak at $\sim 10^{-5}$ Hz, with characteristic amplitude about two orders of magnitude below LISA's sensitivity, though as the exoplanet discovery space expands, our estimates of this background will evolve.

[6] recently revisited the possibility of detecting exoplanets with LISA. They computed the characteristic strain for some ultra-short period exoplanets from an online catalog[1], and claimed that three systems (GP Com b, V396 Hya b, and J1433 b) have characteristic GW strains large enough to be observable using the original LISA design [7, henceforth "Classic LISA"] in one year of integration, ignoring the galactic confusion noise: cf. Fig. 2 of [6].

In Table 8.1 we collected all relevant known properties (to the best of our knowledge) for these three systems. Note that the companions of GP Com b and V396 Hya b have masses in the exoplanet range, but they are donors of AM CVn-type interacting binaries [4], while J1433 b consists of an irradiated brown-dwarf companion to an accreting white

[1] `http://exoplanet.eu/catalog/`

dwarf [5]. Therefore the classification of these three binaries as exoplanetary systems is, at best, debatable.

Given the GW strain amplitude $h(t)$, the characteristic strain h_c for a monochromatic circular binaries with orbital frequency $f_{\rm orb} = 2\pi/P$ emitting GWs at frequency $f = 2f_{\rm orb}$ over an observation time $T_{\rm obs}$ can be defined as $h_c = \left[2f \int_0^{T_{\rm obs}} dt\ h(t)^2\right]^{1/2}$ [530]. In Fig. 8.1 we follow the conventions established in [8] – cf. e.g. their Fig. 6 – to plot the characteristic strain along with the *effective non-sky averaged* noise power spectral density of various LISA designs for two readout channels, related to the sky-averaged noise power spectral density by $S_n(f) = \frac{3}{10} S_n^{\rm SA}(f)$ [8].[2] Brown triangles correspond to the sky-averaged characteristic strain [8, solid black], while cyan error bars correspond to the range of h_c consistent with uncertainties in the source parameters (cf. Table 8.1). The case for detectability of these three systems with either the current or Classic LISA design based on a characteristic strain calculation is, at best, inconclusive.

As discussed in [8], plots of the characteristic strain h_c are useful as rough assessments of detectability, but any conclusions must ultimately be based on a signal-to-noise ratio (SNR) calculation. For monochromatic sources, the SNR is defined as $\rho = (h|h)^{1/2}$, where

$$(h|h) = \frac{2}{S_n(f)} \int_0^{T_{\rm obs}} dt\ h(t)^2. \tag{8.1}$$

To claim detectability, the source of interest must have SNR ρ larger than a certain threshold, which for monochromatic systems is usually taken to be $\rho_{\rm thr} = 5$ [533]. This is somewhat optimistic: the Mock LISA Data Challenges suggest that $\rho_{\rm thr}$ is likely to be larger than 5 [534]. [535] even report undetected sources with $\rho \sim 10$, though this will likely improve with more research in GW data analysis.

Unfortunately, [6] did not quantify the SNR of these systems. Furthermore, they used the outdated "Classic LISA" noise curve [7] and they did not take into account the fact that galactic binaries produce a significant confusion noise, which is important at the frequencies of interest for exoplanetary systems. Here we revisit their analysis for the three planetary systems that are most promising for GW detection. We use updated parameters for these

[2] We remark that this convention differs from the conventions used in [531] and [532], where the SNRs coming from the strain amplitudes h_α ($\alpha = 1, 2$) in the two channels are added in quadrature and $S_n(f) = \frac{3}{20} S_n^{\rm SA}(f)$.

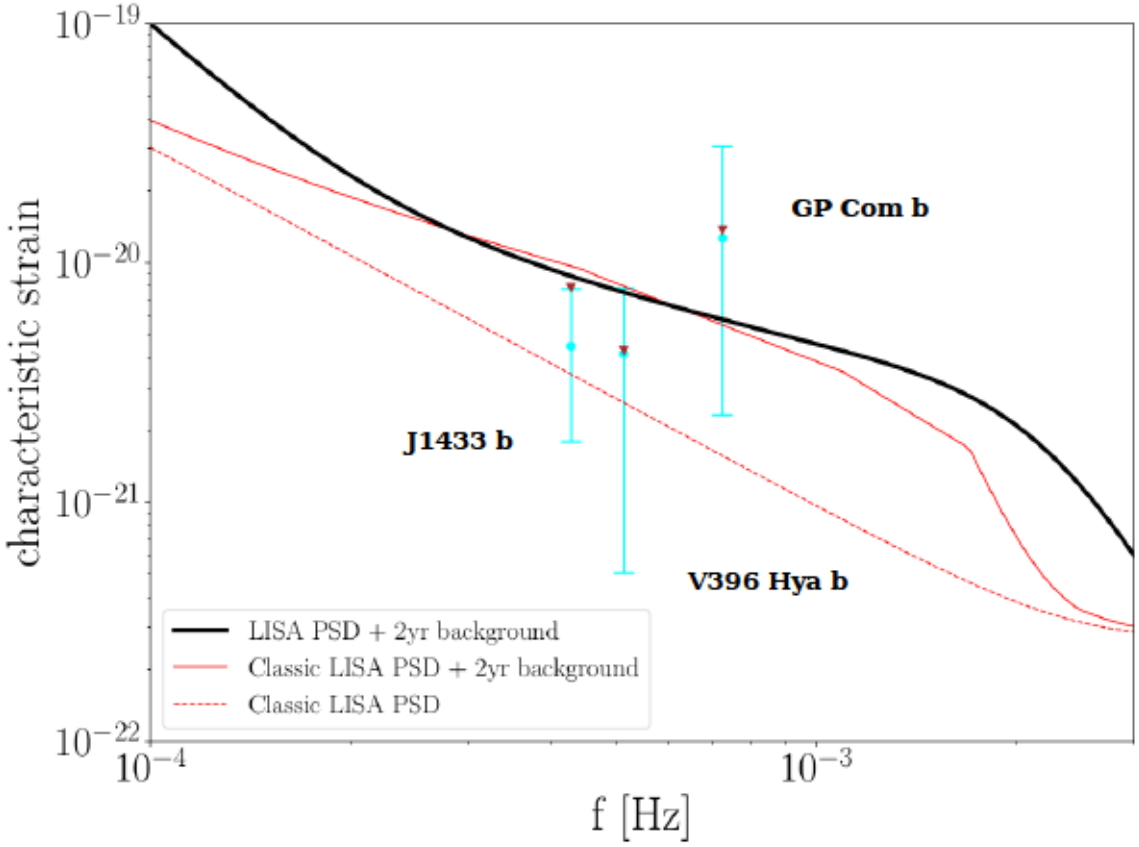

Figure 8.1: Characteristic strain h_c of the loudest exoplanetary candidates plotted along with $\sqrt{fS_n(f)}$, where $S_n(f)$ is the *effective non-sky averaged* noise power spectral density for Classic LISA without galactic confusion noise [7, dashed red], as adopted in [6]; Classic LISA with galactic confusion noise (solid red); and the current LISA design with galactic confusion noise [8, solid black]. The galactic confusion background and h_c are computed assuming $T_{\rm obs} = 2$ yrs. Cyan dots with error bars correspond to the non-sky averaged SNR, allowing for uncertainties on the source parameters; brown inverted triangles correspond to the sky- and orientation-averaged SNR.

Table 8.2: SNR for the loudest sources considered in [6], using the noise power spectral density for Classic LISA [7, columns 2, 3 and 4] and the current LISA design [8, columns 5 and 6]. The second row indicates whether we included galactic confusion noise or not. The third row lists the assumed observation time $T_{\rm obs}$ (in yrs). Numbers in square brackets are the maximum and minimum SNRs consistent with parameter uncertainties for the given source. In round parentheses we report the sky location and orientation averaged SNR.

	Classic LISA			LISA	
Confusion	No	No	Yes	Yes	Yes
$T_{\rm obs}$ (yrs)	1	2	2	2	4
GP Com b	$5.56^{[13.91]}_{[0.97]}$ (6.20)	$8.05^{[19.37]}_{[1.38]}$ (8.76)	$2.29^{[5.51]}_{[0.39]}$ (2.49)	$2.03^{[4.87]}_{[0.35]}$ (2.21)	$3.31^{[8.05]}_{[0.54]}$ (3.62)
V396 Hya b	$1.21^{[2.04]}_{[0.14]}$ (1.17)	$1.73^{[3.01]}_{[0.19]}$ (1.65)	$0.56^{[0.98]}_{[0.06]}$ (0.54)	$0.52^{[0.92]}_{[0.06]}$ (0.50)	$0.82^{[1.37]}_{[0.09]}$ (0.76)
J1433 b	$1.12^{[1.61]}_{[0.41]}$ (1.63)	$1.52^{[2.28]}_{[0.55]}$ (2.30)	$0.54^{[0.80]}_{[0.20]}$ (0.81)	$0.50^{[0.74]}_{[0.18]}$ (0.75)	$0.73^{[1.11]}_{[0.27]}$ (1.11)

systems (including uncertainties, when available) and we adopt the most recent estimates for the LISA sensitivity curve, including galactic confusion noise. The parameters of the three systems under consideration are listed in Table 8.1.

8.2 Method

We model the motion of the LISA detector and compute the SNR using a nonspinning, quasicircular time-domain waveform following [531], so that $h(t)$ is given by

$$h(t) = \frac{\sqrt{3}}{2}\frac{2\mathcal{M}^{5/3}}{D_L}(\pi f)^{2/3}\tilde{A}(t) \times \cos\left(\int_0^t 2\pi f(t')dt' + \varphi_p(t) + \varphi_D(t)\right), \tag{8.2}$$

where $f(t')$ is given in equation (1.3) of [536]. Here $\tilde{A}(t)$, $\varphi_p(t)$ and $\varphi_D(t)$ are the amplitude modulation, polarization phase and Doppler phase due to LISA's motion (see Appendix 8.4 for details). For a binary with component masses (m_1, m_2) and total mass $M = m_1 + m_2$ the waveform depends on nine parameters: luminosity distance D_L, chirp mass $\mathcal{M} = \eta^{3/5}M$, symmetric mass ratio $\eta = m_1 m_2/M^2$, time of coalescence t_c, phase of coalescence ϕ_c, sky location $(\bar{\theta}_S, \bar{\phi}_S)$ and orbital angular momentum direction $(\bar{\theta}_L, \bar{\phi}_L)$. The overbar means that the sky location and binary orientation angles are defined in ecliptic coordinates. In order to give an estimate of the possible range of SNR, for each source we create Monte Carlo samples based on the parameter uncertainties listed in Table 8.1. Our waveforms depend

on the sky location in the solar system barycenter frame, while the sky location $(\theta_S^{\rm eq}, \phi_S^{\rm eq})$ and inclination ι are given in equatorial coordinates (electromagnetic observations do not give information on the polarization angle ψ). In order to translate the waveform from the solar system barycenter frame to an Earth-centered frame, we must solve for the geometric angles in ecliptic coordinates as functions of geometric angles in equatorial coordinates. Translating the sky location from ecliptic coordinates to equatorial coordinates is trivial, but the mapping from the orbital angular momentum direction to the inclination angle is more complicated. Therefore we draw samples in the LISA (solar system barycenter frame) coordinates, compute the SNR, and display the maximum and minimum SNRs which are consistent with the parameter uncertainties of each source. Our results, which we have checked to be in agreement with the sky-location and orientation averaged results of [8], are shown in Table 8.2.

If we fix the detectability threshold at $\rho_{\rm thr} = 5$, none of the currently known systems has $\rho > \rho_{\rm thr}$, even assuming coherent integration over the nominal LISA mission lifetime, i.e. $T_{\rm obs} = 4$ yrs [50]. GP Com b – whose companion is a donor in an AM CVn-type interacting binary [4], so it can hardly be classified as an exoplanet – would be marginally detectable with the "Classic LISA" design, and it is marginally detectable by the current LISA design in four years only if we consider the most optimistic SNR values allowed by parameter uncertainties. A more reliable assessment of the detectability of this system will require better knowledge of the system's properties, as well as more careful modeling of LISA's response and of the galactic confusion noise [see e.g. 537]. For V396 Hya b and J1433 b, the SNR is always lower than the detection threshold. Detection thresholds can be lowered if we incorporate information from electromagnetic measurements into the GW search, but a quantitative assessment of this issue is beyond the scope of this paper [see e.g. 538].

8.3 Discussion

The search for ultra-short period exoplanets is certainly an exciting scientific target for LISA. We hope that our considerations will motivate further work to optimize data analysis methods, to reduce the noise power spectral density at low frequencies, and to improve our understanding of the galactic confusion noise. It will be interesting to model the exoplanet parameter space that would be detectable by LISA (including galactic exoplanets and

brown dwarf populations) to better understand the potential of GW observations and their complementarity with respect to traditional detection methods.

8.4 Antenna Pattern

In this section we write down, for completeness, the antenna pattern expressions used in our non angle-averaged SNR calculation. Following [531], we denote the LISA-based coordinate system by unbarred quantities, while barred quantities refer to the fixed ecliptic coordinate system. The amplitude modulation in equation 8.2 is given by

$$\tilde{A}(t) = \sqrt{\left[1 + (\hat{\mathbf{L}} \cdot \mathbf{n})^2\right]^2 {F_+}^2 + 4(\hat{\mathbf{L}} \cdot \mathbf{n})^2 {F_\times}^2}, \tag{8.3}$$

where $\hat{\mathbf{L}}$ and $-\mathbf{n}$ are the unit vector along the binary's orbital angular momentum and the GW direction of propagation, respectively. The pattern functions F_+ and $F_\times$ are defined as

$$\begin{aligned} F_+(\theta_S, \phi_S, \psi_S) &= \frac{1}{2}(1 + \cos^2\theta_S)\cos 2\phi_S \cos 2\psi_S \\ &\quad - \cos\theta_S \sin 2\phi_S \sin 2\psi_S, \\ F_\times(\theta_S, \phi_S, \psi_S) &= \frac{1}{2}(1 + \cos^2\theta_S)\cos 2\phi_S \sin 2\psi_S \\ &\quad + \cos\theta_S \sin 2\phi_S \cos 2\psi_S. \end{aligned} \tag{8.4}$$

The angles (θ_S, ϕ_S) specify the source location, while ψ_S denotes the the polarization angle:

$$\tan\psi_S(t) = \frac{\hat{\mathbf{L}} \cdot \mathbf{z} - (\hat{\mathbf{L}} \cdot \mathbf{n})(\mathbf{z} \cdot \mathbf{n})}{\mathbf{n} \cdot (\hat{\mathbf{L}} \times \mathbf{z})}, \tag{8.5}$$

where $\mathbf{z}$ is the unit normal to the LISA detector plane.

The scalar products can be written as

$$\mathbf{z} \cdot \mathbf{n} = \cos\theta_S, \tag{8.6}$$

$$\hat{\mathbf{L}} \cdot \mathbf{z} = \frac{1}{2}\cos\bar{\theta}_L - \frac{\sqrt{3}}{2}\sin\bar{\theta}_L \cos\left(\bar{\phi}(t) - \bar{\phi}_L\right), \tag{8.7}$$

$$\hat{\mathbf{L}} \cdot \mathbf{n} = \cos\bar{\theta}_L \cos\bar{\theta}_S + \sin\bar{\theta}_L \sin\bar{\theta}_S \cos\left(\bar{\phi}_L - \bar{\phi}_S\right), \tag{8.8}$$

and

$$\begin{aligned}\mathbf{n}\cdot(\hat{\mathbf{L}}\times\mathbf{z}) &= \frac{1}{2}\sin\bar{\theta}_L\sin\bar{\theta}_S\sin\big(\bar{\phi}_L-\bar{\phi}_S\big)\\ &-\frac{\sqrt{3}}{2}\cos\bar{\phi}(t)\left(\cos\bar{\theta}_L\sin\bar{\theta}_S\sin\bar{\phi}_S-\cos\bar{\theta}_S\sin\bar{\theta}_L\sin\bar{\phi}_L\right)\\ &-\frac{\sqrt{3}}{2}\sin\bar{\phi}(t)\left(\cos\bar{\theta}_S\sin\bar{\theta}_L\cos\bar{\phi}_L-\cos\bar{\theta}_L\sin\bar{\theta}_S\cos\bar{\phi}_S\right).\end{aligned} \tag{8.9}$$

The polarization and Doppler phases in equation 8.2 are given by

$$\varphi_p(t) = \tan^{-1}\left[\frac{2(\hat{\mathbf{L}}\cdot\mathbf{n})F_\times(t)}{(1+(\hat{\mathbf{L}}\cdot\mathbf{n})^2)F_+(t)}\right] \tag{8.10}$$

$$\varphi_D(t) = \frac{2\pi f}{c}R\sin\bar{\theta}_S\cos\big(\bar{\phi}(t)-\bar{\phi}_S\big), \tag{8.11}$$

where R = 1AU and $\bar{\phi}(t)=\bar{\phi}_0+2\pi t/T$. Here $T=1$ yr is the orbital period of LISA, and $\bar{\phi}_0$ is a constant specifying the detector's location at time $t=0$.

Assuming no precession of the orbital angular momentum, the time-dependent LISA related angles (θ_S,ϕ_S,ψ_S) can be expressed in terms of the time-independent angles defined in the ecliptic coordinates $(\bar{\theta}_S,\bar{\phi}_S,\bar{\theta}_L,\bar{\phi}_L)$ through the following relations:

$$\cos\theta_S(t) = \frac{1}{2}\cos\bar{\theta}_S-\frac{\sqrt{3}}{2}\sin\bar{\theta}_S\cos\big(\bar{\phi}(t)-\bar{\phi}_S\big), \tag{8.12a}$$

$$\begin{aligned}\phi_S(t) &= \alpha_0+\frac{2\pi t}{T}\\ &+\tan^{-1}\left[\frac{\sqrt{3}\cos\bar{\theta}_S+\sin\bar{\theta}_S\cos\big(\bar{\phi}(t)-\bar{\phi}_S\big)}{2\sin\bar{\theta}_S\sin\big(\bar{\phi}(t)-\bar{\phi}_S\big)}\right],\end{aligned} \tag{8.12b}$$

where α_0 is a constant specifying the orientation of the detector arms at $t=0$.

We set $\alpha_0=0$ and $\bar{\phi}_0=0$ in our calculations, but we checked that varying α_0 and $\bar{\phi}_0$ has an insignificant effect on the SNR as long as the observation period $T_{\rm obs}\gtrsim 1$ yr.

Chapter 9

Multiband gravitational-wave event rates and stellar physics

Joint gravitational-wave detections of stellar-mass black-hole binaries by ground- and space-based observatories will provide unprecedented opportunities for fundamental physics and astronomy. We present a semianalytic method to estimate multiband event rates by combining selection effects of ground-based interferometers (like LIGO/Virgo) and space missions (like LISA). We forecast the expected number of multiband detections first by using information from current LIGO/Virgo data, and then through population synthesis simulations of binary stars. We estimate that few to tens of LISA detections can be used to predict mergers detectable on the ground. Conversely, hundreds of events could potentially be extracted from the LISA data stream using prior information from ground detections. In general, the merger signal of binaries observable by LISA is strong enough to be unambiguously identified by both current and future ground-based detectors. Therefore third-generation detectors will not increase the number of multiband detections compared to LIGO/Virgo. We use population synthesis simulations of isolated binary stars to explore some of the stellar physics that could be constrained with multiband events, and we show that specific formation pathways might be overrepresented in multiband events compared to ground-only detections.

9.1 Science with multiband events

The profound implications of LIGO's revolutionary discoveries for the LISA mission became clear soon after the first gravitational wave (GW) detection [539]. Black hole (BH) binaries of masses comparable to GW150914 merge at frequencies of $\sim 100\,\mathrm{Hz}$, where ground-based interferometers are most sensitive, but their mHz emission from the early inspiral is strong enough to be observed by LISA. LISA observations of the inspiral could provide good estimates of binary parameters such as the merger time and sky location, thus serving as forewarnings for GW merger observations from the ground and (possibly) electromagnetic counterparts.

Multiband GW astronomy is now an important part of the LISA science case [50]. Many authors have argued that LISA could make significant contributions to our understanding of stellar-mass BH astrophysics [540, 541, 542, 543, 544, 544, 545, 546, 547, 548, 549, 550]. One reason is that LISA could potentially measure binary properties that may not be accessible from the ground. For instance, eccentricity is a common signature of dynamical formation channels. Eccentricity in the LIGO band is typically expected to be too low to be detectable (see e.g. [551]), because eccentric binaries quickly circularize under gravitational radiation reaction. However the eccentricity of dynamically formed binaries may be large enough to be measurable by LISA, giving us important clues about their formation history.

Joint LIGO-LISA detections also open up the possibility to perform new and more powerful tests of general relativity. For instance, some theories of gravity predict additional GW emission channels [552]. The combined analysis of LISA inspirals and ground-based mergers will put extremely stringent constraints on, e.g., dipolar radiation [553]. GW cosmology will also improve with mHz detections of stellar-mass BHs, because LISA's sky-localization properties make them unique standard sirens in the local Universe [554, 555].

The prospect of multiband GW astronomy led to a flourishing of new data analysis and experimental ideas. Advanced warning information on the merger time might allow ground-based operations to be specifically adjusted. For example, by ensuring all the detectors on the ground are taking data at the right time – or perhaps even by tuning their optical properties [556] – we could achieve a qualitatively better characterization of specific "golden" sources. Data streams from ground- and space-based detector networks can also be combined

to enrich the scientific payoff of *both* experiments. Binary properties measured with LISA could be used as a prior to improve ground-based parameter estimation pipelines [557]. Vice versa, ground-based detections can be exploited to revisit past LISA data looking for coincident triggers [558]. The effectiveness of waveform templates to characterize stellar-mass BHs with LISA is also being actively investigated [559].

Whether or not LISA will be able to deliver such revolutionary science crucially depends on the expected rates of multiband BH events [539, 560, 561]. The scope of this paper is twofold:

1. We present a new procedure to convert merger rates measured by (or predicted for) ground-based detectors into multiband event rates. Our method relies on estimating the "effective time window" in which sources remain visible by LISA.

2. We make use of this method to explore the physics of massive binary stars that can potentially be uncovered with multiband GW detections. We first present "model-agnostic" estimates based only on current observational bounds from LIGO/Virgo. We then compute rates using population synthesis models of isolated BH binaries.

This paper is organized as follows. In Sec. 9.2 we describe our method to compute event rates. Section 9.3 translates the current event rate measured by LIGO/Virgo into predictions for LISA. In Sec. 9.4 we apply our findings to state-of-the-art population synthesis simulations of merging stellar-mass BHs. In Sec. 9.5 we compare against previous estimates and discuss topics that should be addressed in future research. To improve readability, we present some of our results in Appendix 9.6 (these include, in particular, long tables listing multiband rates for different assumptions and population synthesis models). In Appendix 9.7 we discuss the horizon redshift of ground- and space-based detectors. Throughout the paper we use geometrical units ($G = c = 1$) and we use values of the cosmological parameters drawn from Ref. [332].

9.2 Combining event rates

An astrophysical BH binary is described by a set of intrinsic parameters λ. Depending on the model/measurements available, these might include quantities like source-frame

masses $m_1 > m_2$, spin vectors $\boldsymbol{\chi}_1$ and $\boldsymbol{\chi}_2$ and binary eccentricity e. Sources are located at a cosmological redshift z, where the intrinsic merger rate is $\mathcal{R}(z)$ (this typically measured in units of $\mathrm{Gpc}^{-3}\ \mathrm{yr}^{-1}$).

Let us now examine selection effects for ground- and space-based detectors separately.

9.2.1 Detection rate from the ground

Ground-based detection rates r (in units of yr^{-1}) are related to the intrinsic merger rate via

$$r_{\rm ground} = \iint dz d\lambda\, \mathcal{R}(z)\, p(\lambda) \frac{dV_c(z)}{dz} \frac{1}{1+z}\, p_{\rm det}(\lambda, z)\,, \tag{9.1}$$

where $dV_c(z)/dz$ is the shell of comoving volume at redshift z, the factor $1/(1+z)$ accounts for the Universe's expansion between emission and detection, $p(\lambda)$ is the probability density function of the intrinsic parameters, and $0 \leq p_{\rm det}(\lambda, z) \leq 1$ is a detection probability.

The accurate estimate of the detector's sensitivity volume is a crucial element in current LIGO/Virgo analyses, and is typically based on injections campaigns into search pipelines [62, 82, 562]. Here we implement a common (but accurate) approximation. We model $p_{\rm det}$ using the cumulative distribution of the projection parameter [74, 78, 79, 93, 563, 564, 565]

$$\omega = \sqrt{\frac{(1+\cos^2\iota)^2}{4} F_+^2(\theta,\phi,\psi) + \cos^2\iota F_\times^2(\theta,\phi,\psi)} \leq 1\,, \tag{9.2}$$

where

$$F_+ = \frac{1}{2}\left(1+\cos^2\theta\right)\cos 2\phi\cos 2\psi - \cos\theta \sin 2\phi \sin 2\psi\,, \tag{9.3}$$

$$F_\times = \frac{1}{2}\left(1+\cos^2\theta\right)\cos 2\phi\sin 2\psi + \cos\theta \sin 2\phi \cos 2\psi\,, \tag{9.4}$$

are the single-detector antenna pattern functions. The parameter ω is an analytic function of binary inclination ι, sky location θ and ϕ, and polarization angle ψ which encapsulates all the angular dependence of the signal-to-noise ratio (SNR). The SNR of a generic binary is given by $\rho = \omega \times \rho_{\rm opt}$, where $\rho_{\rm opt}$ is the SNR of an optimally oriented source with the same parameters λ and z. The probability density function $p(\omega)$ is obtained using Eqs. (9.2)-(9.4) and assuming that $\cos\iota$, $\cos\theta$, ϕ and ψ are uniformly distributed. Selection effects are then

implemented with a SNR threshold $\rho_{\rm thr}$ by evaluating

$$p_{\rm det}(\lambda, z) = \int_{\rho_{\rm thr}/\rho_{\rm opt}(\lambda,z)}^{1} p(\omega) d\omega \,. \tag{9.5}$$

This simplified approach, which is widely used in the literature, has been found to be a good approximation to more accurate estimates of detector selection effects based on simulated signals and false-alarm rates (see [62, 82] for comparisons).

In the following, we compute $\rho_{\rm opt}$ using the waveform model of Ref. [81] and the noise curves of either LIGO at design sensitivity [94] or the proposed third-generation detector Cosmic Explorer [566] (hereafter "3g" or "3rd gen."). For ground-based detectors, we set $\rho_{\rm thr} = 8$ [82]. Equation (9.5) is evaluated by Monte Carlo integration [80].

9.2.2 Detection rate from space

Estimates of selection effects for space-based detectors must necessarily take into account the mission duration. According to current design choices, the nominal (extended) LISA mission duration is $T_{\rm obs} = 4\,(10)$ yr [50].

GWs emitted by a binary that will merge in a time $t_{\rm merger}$ are detected with frequency [567]

$$f(t_{\rm merger}) = \frac{5^{3/8}}{8\pi} [M_c(1+z)]^{-5/8} t_{\rm merger}^{-3/8} \,, \tag{9.6}$$

where $M_c = (m_1 m_2)^{3/5}/(m_1+m_2)^{1/5}$ is the source-frame chirp mass. After a time $T_{\rm obs}$, the same source will be visible with frequency $f(t_{\rm merger} - T_{\rm obs})$, unless it has merged before. The source's SNR during the entire mission duration is given by

$$\rho^2(t_{\rm merger}) = 4 \int_{f(t_{\rm merger})}^{f[\max(t_{\rm merger}-T_{\rm obs}),0]} \frac{|\tilde{h}(f)|^2}{S_n(f)} df \,. \tag{9.7}$$

We use the sky-averaged noise curve $S_n(f)$ of Ref. [568]. We approximate the strain $\tilde{h}$ and the merger frequency $f(0)$ as in Ref. [569]. Stellar-mass BH binaries emit in the mHz regime at very wide separations, where spin effects can be safely neglected [559].

Figure 9.1 shows the function $\rho(t_{\rm merger})$ for some representative BH binaries. The SNR is

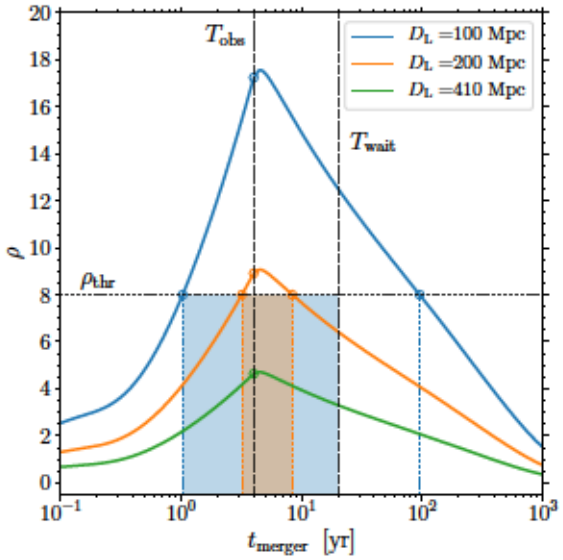

Figure 9.1: Sky-averaged SNR ρ for LISA as a function of the binary merger time $t_{\rm merger}$. Solid colored lines indicate three sources with masses of $29M_\odot$ and $36M_\odot$, like those of GW150914 [9], placed at luminosity distances $D_{\rm L} = 100, 200$, and 410 Mpc (the latter being compatible with the actual GW150914 event). The optimal SNR is obtained at merger times close to the mission lifetime $T_{\rm obs} = 4$ yr (dashed line). The closest sources are found above the threshold $\rho_{\rm thr} = 8$ during the time window marked by the dotted lines. This can be further restricted if only sources merging within a time $T_{\rm wait}$ (dashed line) are sought for. Shaded colored regions indicate effective time window that determines the multiband rate.

expected to decrease for large values of $t_{\rm merger}$ because the binary does not chirp much, i.e. $f(t_{\rm merger}) \simeq f(t_{\rm merger} - T_{\rm obs})$. The SNR is also expected to be low if the binary is too close to merger, because $f(t_{\rm merger})$ falls outside the LISA sensitivity band. The largest SNR is obtained for $t_{\rm merger} \sim T_{\rm obs}$, corresponding to the case where the binary spends the longest time chirping in the LISA band. As shown in Fig. 9.1, the maximum of ρ is actually located at mergers times slightly larger than $T_{\rm obs}$, such that none of the available mission lifetime is "wasted" at frequencies $\gtrsim 1$ Hz where LISA is blind.

We now wish to impose a SNR threshold. A conservative threshold $\rho_{\rm thr} = 8$ is typically considered sufficient to extract signals from the LISA data stream [570]. For the specific case of multiband observations, [558] recently pointed out that ground-based detections could be used *a posteriori* to dig deeper into the LISA noise, thus lowering the effective SNR threshold to $\rho_{\rm thr} \simeq 4$.

Let us denote with $t_{\rm thr1}$ and $t_{\rm thr,2}$ the roots (if any) of the equation

$$\rho(t_{\rm merger}) = \rho_{\rm thr}\,. \tag{9.8}$$

The quantity $|t_{\rm thr1} - t_{\rm thr2}|$ provides an estimate of the time window in which a merging BH binary is visible from space (cf. Fig. 9.1). The number of observations for a space-based detectors can thus be estimated by

$$\begin{aligned} N_{\rm space} = \iint dz d\lambda\, \mathcal{R}(z)\, p(\lambda) \frac{dV_c(z)}{dz} \frac{1}{1+z} \\ \times \left| t_{\rm thr1}(\lambda, z) - t_{\rm thr2}(\lambda, z) \right|, \end{aligned} \tag{9.9}$$

while the detection rate is

$$r_{\rm space} = \frac{N_{\rm space}}{T_{\rm obs}}\,. \tag{9.10}$$

Let us note that $N_{\rm space}$ does not depends on $T_{\rm obs}$ explicitly, but only implicitly through the SNR.

9.2.3 Multiband detection rate

Finally, we are interested in the combined ground + space detection rate. In this context, it might be desirable to impose that detections by the two instruments should happen within a time frame $T_{\rm wait}$. Longer merger times are discarded and the effective merger time window is consequently reduced (cf. Fig. 9.1). The multiband detection rate is obtained by combining the ground-based detectability $p_{\rm det}$ with the space time window, restricted to merger times smaller than $T_{\rm wait}$. One obtains

$$N_{\rm multib} = \mathcal{F} \iint dz d\lambda \, \mathcal{R}(z) \, p(\lambda) \frac{dV_c(z)}{dz} \frac{1}{1+z} \, p_{\rm det}(\lambda, z) \\ \times \Big| \min\left[t_{\rm thr1}(\lambda, z), T_{\rm wait}\right] - \min\left[t_{\rm thr2}(\lambda, z), T_{\rm wait}\right] \Big| , \tag{9.11}$$

where $0 \leq \mathcal{F} \leq 1$ is the duty cycle of the ground-based network during the space-mission lifetime. The multiband detection rate is then given by

$$r_{\rm multib} = \frac{N_{\rm multib}}{\mathcal{F} \, T_{\rm obs}} . \tag{9.12}$$

For simplicity, in the rest of the paper we set $\mathcal{F} = 1$ –a value which hopefully is indicative of future scenarios with ground-based networks of 4 or more instruments. The duty cycle only enters Eq. (9.11) linearly and cancels out in Eq. (9.12). Our results for $N_{\rm multib}$ can be trivially rescaled to other values of $\mathcal{F}$. Unless specified otherwise, we set $T_{\rm wait} = 5 \times T_{\rm obs}$.

9.3 Predictions based on current data

We now present some simple estimates based on the merger rate measured by LIGO/Virgo using 10 BH binary detections [9]. The intrinsic merger rate $\mathcal{R}$ is strongly correlated with the parameter distribution $p(\lambda)$. In this section we only consider nonspinning BHs, i.e. $\lambda = \{m_1, m_2\}$.

In Ref. [9], two mass distributions $p(m_1, m_2)$ were used.

(i) In the first model, primary masses are distributed according to a Salpeter power law and secondary masses are distributed uniformly: $p(m_1) \propto m_1^{-2.3}$, $p(m_2|m_1) = \text{const.}$ The merger rate was measured to be $\mathcal{R} = 57^{+40}_{-25}$ Gpc^{-3}yr^{-1} [62] (where errors refer to

90% credibility and results from two independent pipelines have been combined).

(ii) In the second model, both masses are distributed uniformly in log: $p(m_1, m_2) \propto 1/m_1 m_2$. This choice lowers the measured rate to $\mathcal{R} = 19^{+13}_{-8.2}$ Gpc^{-3}yr^{-1} [62].

We refer to these variations as "powerlaw" and "log", respectively. For each of these two choices, we take the median[1] as well as the lower and upper edges of the 90% confidence interval. This results in three estimates for $\mathcal{R}$ that we refer to as "median", "lower" and "upper". We assume $m_1, m_2 \in [5M_\odot, 50M_\odot]$ as in Ref. [9].

We integrate Eq. (9.1) with standard Monte-Carlo methods to obtain detection rates r and number of observations N for ground-based detectors, space missions and multiband scenarios. Our results are summarized Fig. 9.2. Additional details are reported in Appendix 9.6.

We estimate that LISA will observe $3-12$ stellar-mass BH binaries with SNR greater than 8 during its nominal mission of duration $T_{\rm obs} = 4$ yr. An extension to $T_{\rm obs} = 10$ yr will deliver $10-50$ sources in total. As for multiband detections, a 4 yr (10 yr) LISA mission will provide forewarnings to ground-based observatories for a number of events between 0 and 4 (4 and 22). Note that, in this case, we only consider binaries that merge within a time $T_{\rm wait} = 5 \times T_{\rm obs}$ [cf. Eq. (9.11)]

Weaker signals could be extracted from the LISA data stream by leveraging the information provided by ground-based interferometers [558]. With a lower threshold $\rho_{\rm LISA} > 4$, the number of multiband events increases by about a factor of ~ 5. We predict $N \sim 5-30$ $(35-170)$ for $T_{\rm obs} = 4$ yr (10 yr). While the number of detections for which LISA will be able to predict the merger time (i.e. $\rho_{\rm LISA} > 8$) is compatible with zero in the most pessimistic cases, our analysis confidently predict multiple binaries with $\rho_{\rm LISA} > 4$ that can be extracted *after* ground-based detections have been made.

Interestingly, the noise level of the ground-based instrument does not play a role in this estimate. A "LISA+LIGO" or a "LISA+3g" network will deliver the same multiband binaries. This feature can be understood in terms of the horizon redshifts of the instruments involved (cf. Appendix 9.7). LIGO (3g) can observe a $30+30M_\odot$ binary up to $z \sim 1.2$

[1] Fig. 12 in Ref. [9] suggests that the posterior distribution of $\mathcal{R}$ is approximately log-normal. An estimate of the expectation values $\int \mathcal{R} d\mathcal{R}$ based on the reported 90% confidence interval returns values within 5% of the medians.

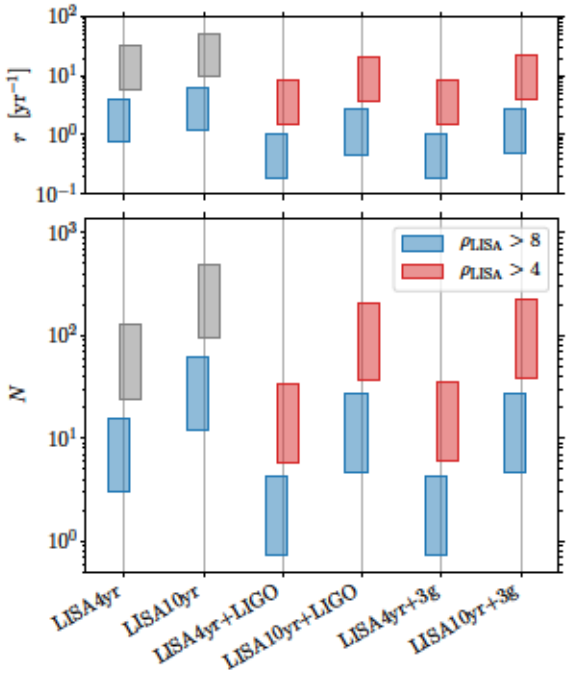

Figure 9.2: Expected detection rates (top) and number of observations (bottom) of stellar-mass BH binaries observable from either space-based detectors alone or space- and ground-based observatories. We consider two possible outcomes of the LISA mission with duration of 4 and 10 yr, together with current (LIGO) and future (Cosmic Explorer, "3g") ground-based instruments. We present results obtained by extremizing over two mass spectra ("powerlaw" and "log") and three estimate of the intrinsic merger rate ("lower", "median", "upper"); see text for details. We assume two possible LISA SNR thresholds, meant to indicate scenarios where multiband detections are realized first from space and then from the ground ($\rho_{\rm LISA} > 8$, blue), or vice versa ($\rho_{\rm LISA} > 4$, red). The latter case is not possible for LISA alone unless data analysis techniques dramatically improve (gray).

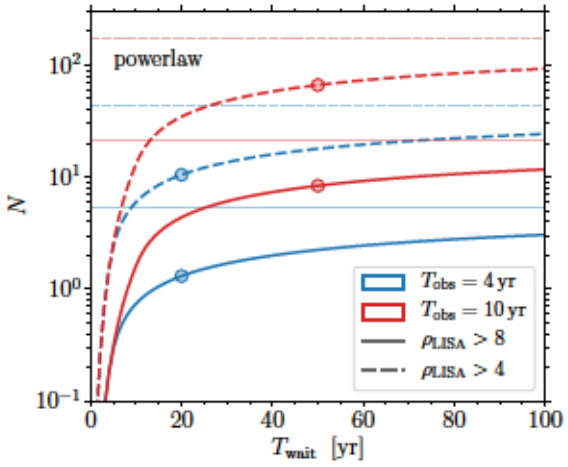

Figure 9.3: Number of multiband events as a function of the time lag between space-and ground-based detection. We assume a LISA mission duration of $T_{\rm obs} = 4$ yr (blue) and 10 yr (red) and a LISA SNR threshold of 8 (solid) and 4 (dashed). Circles mark our default choice $T_{\rm wait} = 5 \times T_{\rm obs}$. Shaded horizontal lines indicate the number of events predicted by the LISA mission alone, irrespectively of whether they are observable from the ground. This figure is produced assuming the "powerlaw" mass spectrum and the "median" assumption for the intrinsic merger rate. Results are very similar if LIGO or a third-generation ground-based detector is considered; for concreteness, here we use LIGO.

(35), while LISA is restricted to $z \lesssim 0.4$. All the sources that are invisible to LIGO but will be observed by a third-generation detector are invisible to LISA as well. Obviously, more sensitive detectors will allow for more accurate characterizations of the sources. But regarding multiband detections rates, second- and third-generation detectors behave essentially the same.

The time lag between ground- and space-based observations is investigated in Fig. 9.3, where we show the number of expected events as a function of $T_{\rm wait}$. For very large waiting times, the number of multiband observations $N_{\rm multib}$ approaches the value predicted for the LISA mission alone $N_{\rm space}$. However, it does not exactly tend to it because of selection effects in the ground-based detector: Eq. (9.9) and Eq. (9.11) differ by a factor $p_{\rm det}(\lambda, z)$ as $T_{\rm wait} \to \infty$. As outlined above, the sensitivity of the ground-based detector hardly matters and the difference between $N_{\rm space}$ and $N_{\rm multib}(T_{\rm wait} \to \infty)$ is consequently very small. Figure 9.3 shows that one only needs to wait for a time comparable to the mission lifetime to observe a good fraction of the multiband binaries. The number of observations rises steeply for $T_{\rm wait} \lesssim T_{\rm obs}$, and then flattens for larger values (our default choice $T_{\rm wait} = 5 \times T_{\rm obs}$ falls in

the latter regime). The role of $T_{\rm wait}$ is to filter out binaries with large merging times (cf. Fig. 9.1). Those same binaries do not chirp much and are, therefore, likely to have SNRs below threshold. In particular, we find $N_{\rm multib}(T_{\rm wait}=T_{\rm obs})/N_{\rm space}\simeq 10\%$.

Figure 9.4 shows the detectable distributions of total masses M and redshifts z predicted in these scenarios. For concreteness, we use a LISA SNR threshold of 8, but results hold qualitatively for $\rho_{\rm LISA} > 4$ as well. A few interesting trends are present. First, LISA observations strongly select binaries with total mass $M \gtrsim 60M_\odot$. The GW emission frequency f is related to the total mass and the binary separation r by $f=\sqrt{M/\pi^2 r^3}$: low-mass sources emit in the LISA band when their orbital separation is too large for their GW radiation to be detectable. Second, all stellar-mass BH binaries detectable by LISA are relatively local, with redshifts $z\lesssim 0.1$ (cf. Appendix 9.7). Among all the stellar-mass BH binaries detectable from the ground, only those with $M\gtrsim 60M_\odot$ and $z\lesssim 0.1$ are accessible from space.

The case of multiband detections is not only determined by the LISA sensitivity, but also by the time between the two sets of observations one is willing to wait. In this paper, we denote as "multiband" only those binaries for which space and ground observations are separated at most by a time $T_{\rm wait}$ (which is set to 50 yr in Fig. 9.4). The multiband detection rate is lower than the rate for LISA alone because binaries with merger time longer than $T_{\rm wait}$ are discarded.

This feature is particularly evident in the dr/dz distribution (right panels of Fig. 9.4). For $z\lesssim 0.02$, the LISA detection rate exceeds that of ground-based detectors. This might seem counterintuitive at first, but it is actually expected because binaries spend a longer time at the low frequencies accessible from space [$t\propto f^{-8/3}$ from Eq.(9.6)]. For sources at very low redshifts, the effective merger time window $|t_{\rm thr1}-t_{\rm thr2}|$ of Eq. (9.9) can be as long as $\sim 10^4$ yr. The threshold $T_{\rm wait}$ largely removes this effect. If binaries with very long merger time are considered not interesting, the predicted multiband detection rate approaches those of ground-based detectors at low redshifts. As stressed above, the sensitivity of the ground based interferometer plays a minor role: in other terms, $p_{\rm det}\lesssim 1$ whenever Eq. (9.8) admits roots.

9.4 Population synthesis predictions

We now apply our rate analysis to state-of-the-art population synthesis simulations of spinning BH binaries formed from binary stars. In particular, we only consider isolated systems that evolved through a common-envelope phase (for a review on BH binary formation channels see, e.g., Ref. [571]). We use publicly available distributions presented in Refs. [75, 90]. We perform stellar evolutions with the STARTRACK [67, 572] population-synthesis code, and add spins in postprocessing using the prescriptions of Refs. [75, 573] and the PRECESSION [89] code.

Among the spin variations presented in Ref. [75], for simplicity we restrict ourselves to the "time-uniform" model, i.e. we adopt a physically motivated prescription for tidal alignment timescale and we assume that BH spins are uniformly distributed in magnitude between zero and the Kerr bound. We vary a single population parameter, namely the magnitude of the kicks imparted at BH formation [574]. Natal kicks are distributed according to a Maxwellian distribution with 1D dispersion $\sigma \in [0, 265]$ km/s, independently of the star's mass. This is a simple, one-parameter family of models that allows us to bracket the expected detection rates [75, 575].

Our dataset contains distributions of BH masses and spins, i.e. $\lambda = \{m_1, m_2, \boldsymbol{\chi}_1, \boldsymbol{\chi}_2\}$. We integrate Eq. (9.1) with Monte Carlo techniques accounting for the expected distributions of zero-age-main-sequence stars, as well as the expected redshift- and metallicity-dependent star-formation rate [93, 576].

9.4.1 Multiband rates and number of detections

Figures 9.5, 9.6 and 9.7 show results for a single representative stellar evolution model with $\sigma = 50$ km/s. This choice yields detection rates consistent with LIGO observations, and it is in agreement with current mass and spin misalignment constraints [103, 104, 572] (see also Refs. [93, 101, 577] for kick measurements with x-ray binaries data). We present rates and numbers of detected binaries as a function of $\rho_{\rm LISA}$ evaluated at $t_{\rm merger} = T_{\rm obs}$, cf. Eq. (9.7). This value can be considered as a simple estimator of the strength of the LISA signal, but it is understood that detection rates are computed by varying over $t_{\rm merger}$, as detailed in Sec. 9.2.

In Fig. 9.5 we illustrates the expected LISA SNR distribution of GW sources detectable from the ground (i.e., histogram entries are weighted by the ground-based detection rate $r_{\rm ground}$). Crucially, we find that the rate is a very steep function of $\rho_{\rm LISA}$. Lowering the SNR threshold from ~ 8 to ~ 4 raises the ground-based rate by a factor $\sim (8/4)^3 = 8$. Any data-analysis or experimental technique which increases, even marginally, the LISA redshift horizon is expected to have significant consequences for multiband detections. According to Eq. (9.10), extending the mission duration from 4 to 10 yrs will increase the accessible rate by a factor of ~ 3, thus delivering $\sim 3 \times 10/4 = 7.5$ times more detected sources.

Compared to LIGO, the increased sensitivity of third-generation detectors is only relevant for binaries with $\rho_{\rm LISA} \lesssim 2$, which are too faint to be identified in the LISA data. For concreteness, in the following we show multiband rates computed using the LIGO noise curve, but results would be unchanged if we considered Cosmic Explorer instead.

Figure 9.6 shows the LISA SNR distribution restricted to those fewer (multiband) sources that are accessible from both ground and space. As expected, the multiband rate steeply decreases as the SNR threshold is approached. It is worth noting, however, that the distributions of Fig. 9.6 do not present a sharp and unphysical cutoff, but they decrease smoothly as $\rho \to \rho_{\rm thr}$. This is a direct consequence of the procedure presented in Sec. 9.2: LISA observes for a time $T_{\rm obs}$ but, in general, sources will not inspiral all the way to merger during that time. Their effective SNR is, therefore, somewhat smaller than $\rho_{\rm LISA}(T_{\rm obs})$.

A summary of these results is presented in Fig. 9.7, where we show the cumulative distribution of the number of multiband events. For this specific model with $\sigma = 50$ km/s, a LISA mission of $T_{\rm obs} = 4$ (10) yr will deliver ~ 2 (~ 20) multiband sources with SNR greater than 8. About ~ 20 (~ 130) more sources will be seen with $4 < \rho_{\rm LISA}(T_{\rm obs}) < 8$.

We explore the uncertainties of our predictions on $r_{\rm multib}$ and $N_{\rm multib}$ in Fig. 9.8, where we vary the strength of the kicks imparted at BH formation from $\sigma = 0$ km/s to 265 km/s [92] (see Appendix 9.6 for additional details). As σ increases, more and more binaries are unbound by supernova explosions, and the detection rate consequently decreases. We report variations of a factor ~ 30. It is worth noting that only moderately extreme cases ($\sigma \gtrsim 150$ km/s, $T_{\rm obs} = 4$ yr) present $N_{\rm multib} < 1$. Therefore, we predict that the LISA space mission will detect a few – but possibly dozens – sources which are also observable from the ground. These events (with $\rho_{\rm LISA} > 8$) are going provide forewarnings for ground-based operations,

but about $\mathcal{O}(100)$ more events with $\rho_{\rm LISA} > 4$ could potentially be extracted from the LISA data stream in coincidence with sources that have already been observed from Earth.

9.4.2 Stellar progenitors

Multiband GW detections offer new opportunities to explore the physics of massive stars (see e.g. Refs. [541, 542, 544]). By leveraging our STARTRACK+PRECESSION simulations [75], we now investigate which specific formation subchannels are more likely to produce multiband sources.

Figure 9.9 shows the detectable distributions of total mass, mass ratio, redshift and effective spin [9, 578, 579] for our simulation with $\sigma = 50$ km/s. Binaries are weighted by detectability with either ground-based detectors alone, or multiband networks. The main trends are driven by the same considerations already presented in Sec. 9.3: among the ground-based sources, only those with large enough mass and small enough redshift are detectable by LISA and can be multiband sources.

The results of Fig. 9.9 let us immediately infer the value of the multiband horizon redshift averaged over a suitable stellar population. For $T_{\rm obs} = 4$ (10) yr, we find that only binaries at $z \lesssim 0.07$ (0.12) can be observed with $\rho_{\rm LISA} > 8$ and provide forewarnings for ground-based operations. The largest redshift increases by about a factor 2 if the SNR threshold is relaxed to $\rho_{\rm LISA} > 4$. These findings are in agreement with the horizon redshifts of the LISA detector alone (Appendix 9.7), thus confirming that the space-based detector sensitivity is going to be limiting component of future multiband networks.

The high-mass filter is also a rather strong effect. For $M \lesssim 30M_\odot$, the multiband detection rate is 3-5 orders of magnitude smaller than the LIGO one. While only $\sim 28\%$ of the LIGO detection rate comes from binaries with $M > 60M_\odot$, that fraction increases to $\sim 50\%$ for multiband observations. Multiband detections do not appear to prefer specific values of mass ratios and/or spins (Fig. 9.9). This is expected, because both of these parameters enter the waveform at relatively high post-Newtonian order, and the effects of high post-Newtonian orders are negligible at low frequencies.

The key stellar mechanism to form GW sources from massive binary stars in galactic fields is the so-called *common-envelope* phase [580, 581]. As one of the two stars enters its

late evolutionary stages, its outer layers can engulf the binary's orbit. Two stellar cores evolve inside a single envelope, which dissipates its binding energy by shrinking the binary separation.

As in Ref. [75], we divide the results of our simulations into eight mutually exclusive subchannels depending on the formation time of the more (BH1) and less (BH2) massive objects, as well as the occurrence of the common-envelope phase (CE). The more massive BH usually originates from the more massive star and form first (i.e. "BH1" comes before "BH2"). For a minority of the systems, mass transfer might reverse the binary mass ratio, causing the secondary BH to form first (i.e. "BH2" before "BH1"). Common envelope typically occurs either in between the two supernovae (i.e. "BH CE BH"), or before the first one (i.e. "CE BH BH"). The relative importance of these two subchannels crucially depends on the magnitude of the supernova kicks [75]. For $\sigma \lesssim 100$ km/s, the dominant channel is "BH1 CE BH2", with the common-envelope phase involving the inspiral of an already formed BH and the core of the other progenitor. For $\sigma \gtrsim 100$ km/s, the first supernova kick is likely to unbind the stellar binary, unless it has hardened before. In this case, the majority of the detection rate comes from the "CE BH1 BH2" subchannel. Other subchannels with zero or two common-envelope phases are, in general, highly subdominant.

Figure 9.10 shows how the fraction of detectable sources in each of these pathways is impacted by multiband detections. Scenarios with early common envelopes ("CE BH BH") are generally overrepresented in multiband observations compared to either LIGO or third-generation detectors alone. These sources are, on average, more massive than their "BH CE BH" counterparts, and therefore more likely to be detected by LISA. The "CE BH BH" scenarios include the most massive stellar progenitors and BHs formed at low metallicity, while the "BH CE BH" binaries form copiously at all metallicities from pairs of $O(40M_\odot)$ stars. The sensitivity of third-generation detectors peaks at lower masses compared to LIGO, and it will allow them to observe more "BH CE BH" binaries.

Sources where BH1 forms before BH2 are not only more numerous, but also heavier than those where the lighter object forms first. Strong mass transfer is required to reverse the binary mass ratio and form the lighter BH from the heavier star. Since mass transfer is expected to be nonconservative, this implies that more mass is, on average, lost in the "BH2 BH1" scenarios [576]. As shown in Fig. 9.10, those subchannels are slightly more probable

in multiband detections compared to ground-based observations.

The few binaries that manage to merge without a common-envelope phase (i.e. "BH BH") also appear to be somewhat preferred by multiband scenarios. The statistics in the simulations of Ref. [75], however, is too small to draw confident conclusions from this observation.

To summarize, the main trends observed in Fig. 9.10 can all be understood in terms of the source total mass and its impact on LISA detectability. For reference, in our model with $\sigma = 50$ km/s the medians of the total mass M weighted by LIGO detections rates are $\sim 44M_\odot$ for "BH1 CE BH2", $\sim 38M_\odot$ for "BH2 CE BH1", $\sim 54M_\odot$ for "CE BH1 BH2", and $\sim 49M_\odot$ for "CE BH2 BH1".

9.5 Comparisons and prospects

We presented a new, semianalytic approach to compute detection rates for multiband GW sources by properly combining selection effects of ground- and space-based detectors. Our treatment relies on (i) labeling sources by their merger time, and (ii) defining an "effective time window" where their SNR is above threshold [see Eq. (9.9)]. We first exemplified the method by using the relatively model-independent LIGO/Virgo estimate of the intrinsic merger rate, and then we explored in detail the population of multiband GW sources predicted by simulations of isolated binary stars. We plan to extend our analysis to dynamical formation scenarios in future work.

There were some previous attempts at estimating multiband detection rates [539, 560, 561]. The calculation presented by Refs. [539, 560] is essentially equivalent to our own calculation in Sec. 9.3. Instead of explicitly considering a time window, those calculations randomize over the binary emission frequency (or, equivalently, $t_{\rm merger}$) and apply the SNR cut to each Monte Carlo sample. In particular, Ref. [560] presents results using the same LISA noise curve used in this work, and quotes values of $N_{\rm obs}$ which are up to two orders of magnitude higher than ours. These differences can be reconciled by noting that Refs. [539, 560] used the intrinsic merger rate $\mathcal{R}$ from Ref. [82], which is now superseded by Ref. [9].

[561] presented a mostly analytical calculation of the expected number of stellar-mass BH

binaries detections by LISA. They used the now-outdated LISA noise curves from Ref. [582], but their N2A2 configuration with $T_{\rm obs} = 5$ yr should be reasonably close to our calculations with $T_{\rm obs} = 4$ yr (see also [560]). They fix the chirp mass of all sources to $M_c = 28M_\odot$ and the intrinsic rate to $\mathcal{R} = 100$ Gpc^{-3}yr^{-1} to obtain ~ 30 (300) observable sources that do (do not) merge within $T_{\rm obs}$. Their estimate is in rough agreement with our findings once M_c and $\mathcal{R}$ are properly rescaled.

Much of our analysis emphasized that LISA will be the limiting instrument of a multiband network. If a binary is detectable by LISA, it will also be observed by a ground-based observatory with high SNR (although it might take a very long time to merge). The sensitivity of the ground-based detector does not matter when estimating multiband detection rate. Differences between the current LIGO/Virgo network and future third-generation detectors impact the rate only for highly subthreshold events with $\rho_{\rm LISA} \lesssim 2$. Our predictions are presented assuming a ground-based network duty cycle $\mathcal{F}$ equal to 100%, thus envisioning future scenarios with multiple instruments operating concurrently. The merger time of multiband events can be predicted within $1-10$s [539], allowing to plan ground operations accordingly.

Of all stellar-mass BH binaries detected from the ground, LISA will select a specific subpopulation. In particular, sources must be more massive than $\sim 60M_\odot$ and closer than ~ 500 Mpc, but the precise thresholds depend on the specifications of the LISA mission.

In Fig. 9.9 we compare our stellar calculations to posterior distributions from all LIGO/Virgo observations to date [9]. Out of the 10 BH binary events observed so far, 5 have $z \lesssim 0.1$, 3 have $0.1 \lesssim z \lesssim 0.2$, and 2 have $z \gtrsim 0.3$. Even with this limited sample, one can immediately see that expanding the LISA horizon redshift from ~ 0.1 to ~ 0.2 might dramatically increase our prospects of performing multiband observations. Our more detailed analysis confirms this expectation. Because of the steep dependence of the detection rate on the LISA SNR, an extension of the LISA mission duration and/or data-analysis techniques that can lower the SNR threshold will increase the number of events by orders of magnitude.

The sharp high-mass cutoff in the multiband detectability might have other surprising consequences. In the populations considered here, the total mass of the binary is limited to $M \lesssim 100M_\odot$ by construction. The distributions of Sec. 9.3 explicitly exclude BHs larger than $50M_\odot$ [9]. The simulations used in Sec. 9.3 are generated assuming that pair-instability

pulsation Supernovae and pair-instability Supernovae [91, 583, 584, 585, 586] efficiently prevent the formation of BHs heavier than $\sim 45 M_{\odot}$. This is a rather pessimistic assumption, as the cutoff might be as large as $\sim 52 M_{\odot}$ [587]. It is also important to note that stars are predicted to form BHs with mass $\gtrsim 130 M_{\odot}$, for which Supernova instabilities are too weak to disrupt the progenitor star [587]. Second-generation mergers [72, 588] might also populate this upper mass gap. If such massive BHs exist, they are expected to contribute prominently to the multiband event rates [589, 590].

If realized, multiband GW detections will crown the science return of the LISA mission with revolutionary astronomy, fundamental physics and cosmology. The analysis presented in this paper confirms that this is indeed an exciting possibility.

Data to reproduce results of this paper are publicly available at github.com/dgerosa/spops [90]. We thank Baoyi Chen, Ron Tso, Chris Moore, Antoine Klein, and Alberto Vecchio for discussions. We thank [568] for publicly sharing their codes to compute LISA SNRs and [565] for publicly sharing their code to compute redshifted volumes, which was used for benchmarking. Calculations of $p_{\rm det}$ are performed with the GWDET [80] code which makes use of PYCBC [591] and LAL [514]. The distributions used in Sec. 9.4 are publicly available at [90], and are obtained with the STARTRACK [67] and PRECESSION [89] codes. D.G. is supported by NASA through Einstein Postdoctoral Fellowship Grant No. PF6-170152 awarded by the Chandra X-ray Center, operated by the Smithsonian Astrophysical Observatory for NASA under Contract NAS8-03060. E.B. and K.W.K.W. are supported by NSF Grant No. PHY-1841464, NSF Grant No. AST-1841358, NSF-XSEDE Grant No. PHY-090003, and NASA ATP Grant No. 17-ATP17-0225. R.O'S. is supported by NSF Grants No. PHY-1707965 and No. PHY-1607520. This work has received funding from the European Union's H2020 research and innovation programme under the Marie Skłodowska-Curie Grant Agreement No. 690904. KB acknowledges partial support from the Polish National Science Center (NCN) grants OPUS (2015/19/B/ST9/01099) and Maestro (2015/18/A/ST9/00746). The authors would like to acknowledge networking support by the European COST Action CA16104. Computational work was performed on Caltech cluster Wheeler supported by the Sherman Fairchild Foundation and Caltech, on the University of Birmingham's BlueBEAR cluster, and at the Maryland Advanced Research Computing Center (MARCC).

9.6 Additional results

In this Appendix we provide some of our rate calculations in tabular format. In particular, Table 9.1 lists results from the Monte Carlo runs of Sec. 9.3 for all choices of mass distribution, intrinsic merger rate and detector specifications. Table 9.2 complements Sec. 9.4 with detailed rates and number of observations from all of our population-synthesis simulations. It is worth stressing that the catalogs used to generate Table 9.2 are produced by initializing zero-age-main-sequence stars at cosmological distances and by considering only BHs that merge before $z = 0$. Many more *nonmerging* BH binaries are potentially detectable by LISA [592], but they were not considered here.

9.7 Horizon redshifts

A prerequisite (and by-product) of the rate analysis presented in this paper is the calculation of the horizon redshift, defined as the largest redshift at which a binary with given parameters λ is observable. More precisely, we define the horizon redshift $z_{\rm h}$ as the solution of the equations $\rho_{\rm opt}(\lambda, z_{\rm h}) = \rho_{\rm thr}$ for ground-based detectors, and $\rho(t_{\rm merger}{=}T_{\rm obs}, \lambda, z_h) = \rho_{\rm thr}$ for LISA.

Results for LIGO [94] and Cosmic Explorer [566] are shown in the top panels of Fig. 9.11. Current detectors are most sensitive to binaries with $m_1 + m_2 \sim 100M_\odot$ and can reach $z_{\rm hor} \sim 2$. The sensitivity of third-generation detectors, on the other hand, is expected to peak at lower masses $m_1 + m_2 \sim 10M_\odot$. Future interferometers will observe binaries out to $z_{\rm h} \gtrsim 30$, thus detecting all stellar-mass BH mergers in the Universe [39, 566].

The middle and bottom panels of Fig. 9.11 show forecasts for LISA, assuming different choices for the mission duration and SNR threshold. For the stellar-mass BH binaries considered here, the LISA sensitivity peaks at the high end of the mass spectrum, where sources spend the longest time chirping in the detector's sensitivity window. With an extended mission duration of $T_{\rm obs} = 10$ yr and an optimistic SNR threshold of $\rho_{\rm thr} = 4$, the furthest detectable binaries are located at $z_{\rm h} \sim 0.25$. This is well below the reach of current and future ground-based detectors.

				r [yr^{-1}]			N		
				Lower	Median	Upper	Lower	Median	Upper
LISA	$T_{\rm obs} = 10$ yr	$\rho_{\rm LISA} > 8$	powerlaw	1.18	2.11	3.59	11.84	21.09	35.88
			log	1.70	2.99	5.03	16.99	29.89	50.33
	$T_{\rm obs} = 10$ yr	$\rho_{\rm LISA} > 4$	powerlaw	(9.68)	(17.24)	(29.34)	(96.79)	(172.41)	(293.40)
			log	(13.45)	(23.67)	(39.86)	(134.52)	(236.66)	(398.58)
	$T_{\rm obs} = 4$ yr	$\rho_{\rm LISA} > 8$	powerlaw	0.76	1.36	2.31	3.04	5.42	9.23
			log	1.08	1.90	3.19	4.31	7.58	12.77
	$T_{\rm obs} = 4$ yr	$\rho_{\rm LISA} > 4$	powerlaw	(6.01)	(10.71)	(18.23)	(24.06)	(42.85)	(72.92)
			log	(8.73)	(15.35)	(25.86)	(34.90)	(61.41)	(103.42)
LISA+LIGO	$T_{\rm obs} = 10$ yr	$\rho_{\rm LISA} > 8$	powerlaw	0.47	0.83	1.42	4.69	8.35	14.21
			log	0.74	1.31	2.20	7.44	13.09	22.05
	$T_{\rm obs} = 10$ yr	$\rho_{\rm LISA} > 4$	powerlaw	3.71	6.61	11.26	37.13	66.14	112.56
			log	5.79	10.18	17.15	57.89	101.84	171.51
	$T_{\rm obs} = 4$ yr	$\rho_{\rm LISA} > 8$	powerlaw	0.18	0.33	0.56	0.73	1.30	2.22
			log	0.29	0.51	0.87	1.17	2.06	3.46
	$T_{\rm obs} = 4$ yr	$\rho_{\rm LISA} > 4$	powerlaw	1.47	2.62	4.45	5.87	10.46	17.80
			log	2.35	4.14	6.98	9.42	16.57	27.90
LISA+3g	$T_{\rm obs} = 10$ yr	$\rho_{\rm LISA} > 8$	powerlaw	0.48	0.85	1.44	4.75	8.47	14.41
			log	0.76	1.33	2.24	7.55	13.29	22.38
	$T_{\rm obs} = 10$ yr	$\rho_{\rm LISA} > 4$	powerlaw	3.91	6.96	11.84	39.07	69.60	118.45
			log	6.11	10.75	18.11	61.13	107.55	181.13
	$T_{\rm obs} = 4$ yr	$\rho_{\rm LISA} > 8$	powerlaw	0.18	0.33	0.56	0.74	1.32	2.24
			log	0.29	0.52	0.87	1.18	2.07	3.49
	$T_{\rm obs} = 4$ yr	$\rho_{\rm LISA} > 4$	powerlaw	1.51	2.69	4.59	6.05	10.78	18.34
			log	2.43	4.27	7.20	9.71	17.09	28.78
LIGO	($z < 0.3$)		powerlaw	48.93	87.15	148.31			
			log	31.51	55.43	93.35			
3rd gen.	($z < 0.3$)		powerlaw	205.23	365.56	622.09			
			log	69.34	121.99	205.46			

Table 9.1: Detection rates r and number of observations N inferred from current LIGO/Virgo measurements of the intrinsic merger rate (cf. Sec. 9.3). Results are reported for the LISA mission alone [Eqs. (9.9)], as well as combined detections with the ground-based interferometers LIGO and Cosmic Explorer ("3g") [Eq. (9.11)]. For each estimate, we report three values ("lower", "median", "upper") to bracket uncertainties. Rates are estimated using the two populations of Ref. [9] ("powerlaw" and "log") assuming both the nominal ($T_{\rm obs}$=4yr) and the extended ($T_{\rm obs}$=10yr) duration for the LISA mission. Events with $\rho_{\rm LISA} > 8$ can be distinguished from space and will serve as predictions for the ground-based instruments. Events with $\rho_{\rm LISA} > 4$ are not likely to be observed by LISA alone (hence the parentheses in the "LISA" entries of the table) but will be observable using ground-based detections as priors. For comparison, we also report the predicted event rate for LIGO at design sensitivity and Cosmic Explorer in the local Universe ($z < 0.3$).

r [yr^{-1}]			Natal kick σ 0 km/s	25 km/s	50 km/s	70 km/s	130 km/s	200 km/s	265 km/s
LISA	$T_{\rm obs} = 10$ yr	$\rho_{\rm LISA} > 8$	14.40	9.11	4.75	3.00	1.71	0.80	0.41
	$T_{\rm obs} = 10$ yr	$\rho_{\rm LISA} > 4$	(124.25)	(78.34)	(40.12)	(25.36)	(13.39)	(6.16)	(3.62)
	$T_{\rm obs} = 4$ yr	$\rho_{\rm LISA} > 8$	8.91	5.59	2.98	1.88	1.06	0.50	0.25
	$T_{\rm obs} = 4$ yr	$\rho_{\rm LISA} > 4$	(74.52)	(47.24)	(24.45)	(15.39)	(8.64)	(4.01)	(2.16)
LISA+LIGO	$T_{\rm obs} = 10$ yr	$\rho_{\rm LISA} > 8$	5.31	3.39	1.76	1.09	0.71	0.33	0.17
	$T_{\rm obs} = 10$ yr	$\rho_{\rm LISA} > 4$	48.68	30.20	15.49	9.65	5.21	2.38	1.59
	$T_{\rm obs} = 4$ yr	$\rho_{\rm LISA} > 8$	1.90	1.21	0.64	0.40	0.27	0.13	0.06
	$T_{\rm obs} = 4$ yr	$\rho_{\rm LISA} > 4$	17.08	10.72	5.55	3.38	2.10	0.97	0.60
LISA+3g	$T_{\rm obs} = 10$ yr	$\rho_{\rm LISA} > 8$	5.36	3.43	1.78	1.10	0.71	0.34	0.18
	$T_{\rm obs} = 10$ yr	$\rho_{\rm LISA} > 4$	50.63	31.40	16.15	10.06	5.43	2.49	1.67
	$T_{\rm obs} = 4$ yr	$\rho_{\rm LISA} > 8$	1.91	1.22	0.64	0.40	0.28	0.13	0.06
	$T_{\rm obs} = 4$ yr	$\rho_{\rm LISA} > 4$	17.46	10.96	5.69	3.46	2.15	1.00	0.61
LIGO			3.2×10^{3}	1.9×10^{3}	8.9×10^{2}	5.6×10^{2}	2.4×10^{2}	1.1×10^{2}	6.4×10^{1}
3rd gen.			9.4×10^{5}	7.7×10^{5}	4.4×10^{5}	2.9×10^{5}	1.3×10^{5}	6.4×10^{4}	3.8×10^{4}

N			Natal kick σ 0 km/s	25 km/s	50 km/s	70 km/s	130 km/s	200 km/s	265 km/s
LISA	$T_{\rm obs} = 10$ yr	$\rho_{\rm LISA} > 8$	143.96	91.12	47.54	30.03	17.06	7.97	4.08
	$T_{\rm obs} = 10$ yr	$\rho_{\rm LISA} > 4$	(1242.46)	(783.39)	(401.24)	(253.59)	(133.94)	(61.58)	(36.23)
	$T_{\rm obs} = 4$ yr	$\rho_{\rm LISA} > 8$	35.65	22.35	11.93	7.52	4.25	2.01	0.99
	$T_{\rm obs} = 4$ yr	$\rho_{\rm LISA} > 4$	(298.09)	(188.94)	(97.79)	(61.57)	(34.55)	(16.06)	(8.64)
LISA+LIGO	$T_{\rm obs} = 10$ yr	$\rho_{\rm LISA} > 8$	53.10	33.95	17.61	10.90	7.05	3.32	1.75
	$T_{\rm obs} = 10$ yr	$\rho_{\rm LISA} > 4$	486.80	302.03	154.89	96.51	52.07	23.81	15.94
	$T_{\rm obs} = 4$ yr	$\rho_{\rm LISA} > 8$	7.58	4.85	2.55	1.59	1.10	0.52	0.26
	$T_{\rm obs} = 4$ yr	$\rho_{\rm LISA} > 4$	68.32	42.89	22.21	13.51	8.39	3.89	2.38
LISA+3g	$T_{\rm obs} = 10$ yr	$\rho_{\rm LISA} > 8$	53.64	34.30	17.80	11.02	7.14	3.36	1.77
	$T_{\rm obs} = 10$ yr	$\rho_{\rm LISA} > 4$	506.34	314.05	161.47	100.61	54.31	24.85	16.74
	$T_{\rm obs} = 4$ yr	$\rho_{\rm LISA} > 8$	7.62	4.88	2.57	1.59	1.11	0.52	0.26
	$T_{\rm obs} = 4$ yr	$\rho_{\rm LISA} > 4$	69.84	43.85	22.74	13.82	8.60	3.98	2.44

Table 9.2: Detection rates (r, top) and number of events (N, bottom) for ground-based detectors (LIGO, Cosmic Explorer "3g"), space missions (LISA) and multiband scenarios as predicted by population synthesis simulations of binary stars (cf. Sec. 9.4). We present results from 7 simulations, where we only vary the magnitude of kicks imparted to BHs at birth ($\sigma = 0$, 25, 50, 70, 130, 200, 265 km/s). We consider two different LISA mission durations $T_{\rm obs} = 4, 10$ yr and SNR thresholds $\rho_{\rm LISA} > 8, 4$. Events with $\rho_{\rm LISA} > 4$ can only be extracted using ground-based data as priors, and are therefore indicated in parenthesis for LISA alone.

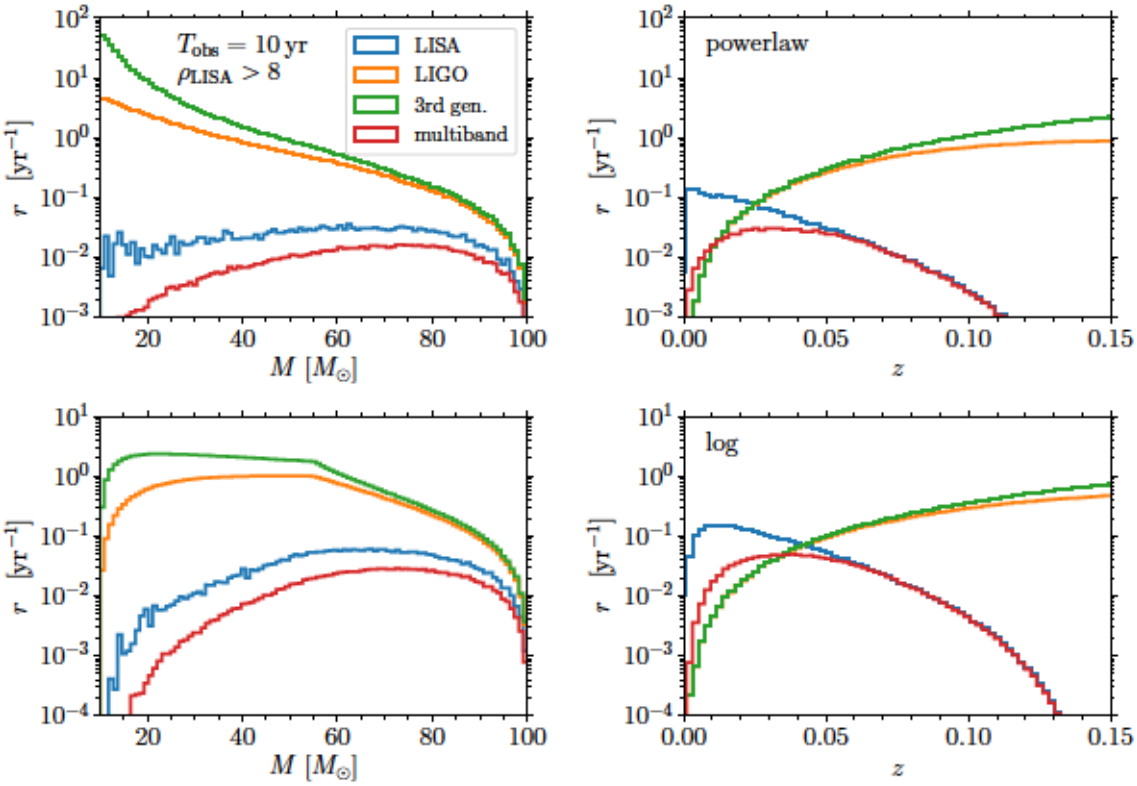

Figure 9.4: Marginalized event-rate distribution of total mass $M = m_1 + m_2$ (left panels) and redshift z (right panel) of stellar-mass BH binaries detectable by LISA, LIGO, Cosmic Explorer ("3rd gen."), and multiband scenarios. On the y-axis we show dr/dM and dr/dz from Eq. (9.1) times the bin sizes ΔM and Δz, such that the sum of the histogram entries is equal to the total rate r. Multiband distributions are identical if a "LISA+LIGO" or a "LISA+3g" network is considered. Results are restricted to the local Universe ($z < 0.3$) and obtained using the "median" value of $\mathcal{R}$ from Ref. [9]. We assume the "powerlaw" (top) and "log" (bottom) mass spectra, a LISA mission duration 10 yr, and a SNR threshold of 8 (see text for details).

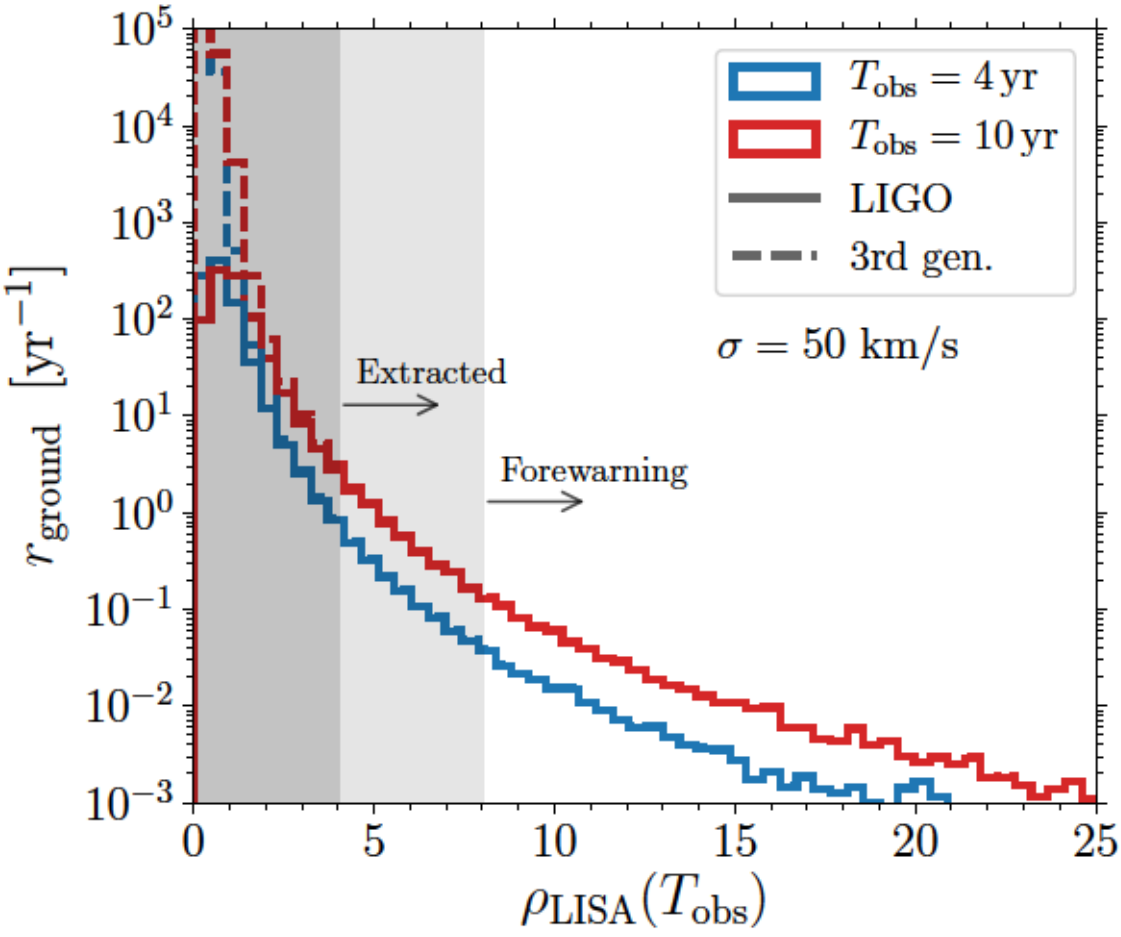

Figure 9.5: Distribution BH binaries detectable from the ground as a function of the SNR in LISA. The x-axis shows $\rho_{\rm LISA}$ evaluated at $T_{\rm obs}$ (as a proxy for the strength of the signal), while the y-axis shows the ground-based detection rate per bin. Results are presented for a single population synthesis simulation with supernova kick parameter $\sigma = 50$ km/s. We assume a LISA mission duration of $T_{\rm obs} = 4$ yr (blue) and 10 yr (red), and compute ground-based selection effects using either LIGO (solid) or Cosmic Explorer (dashed).

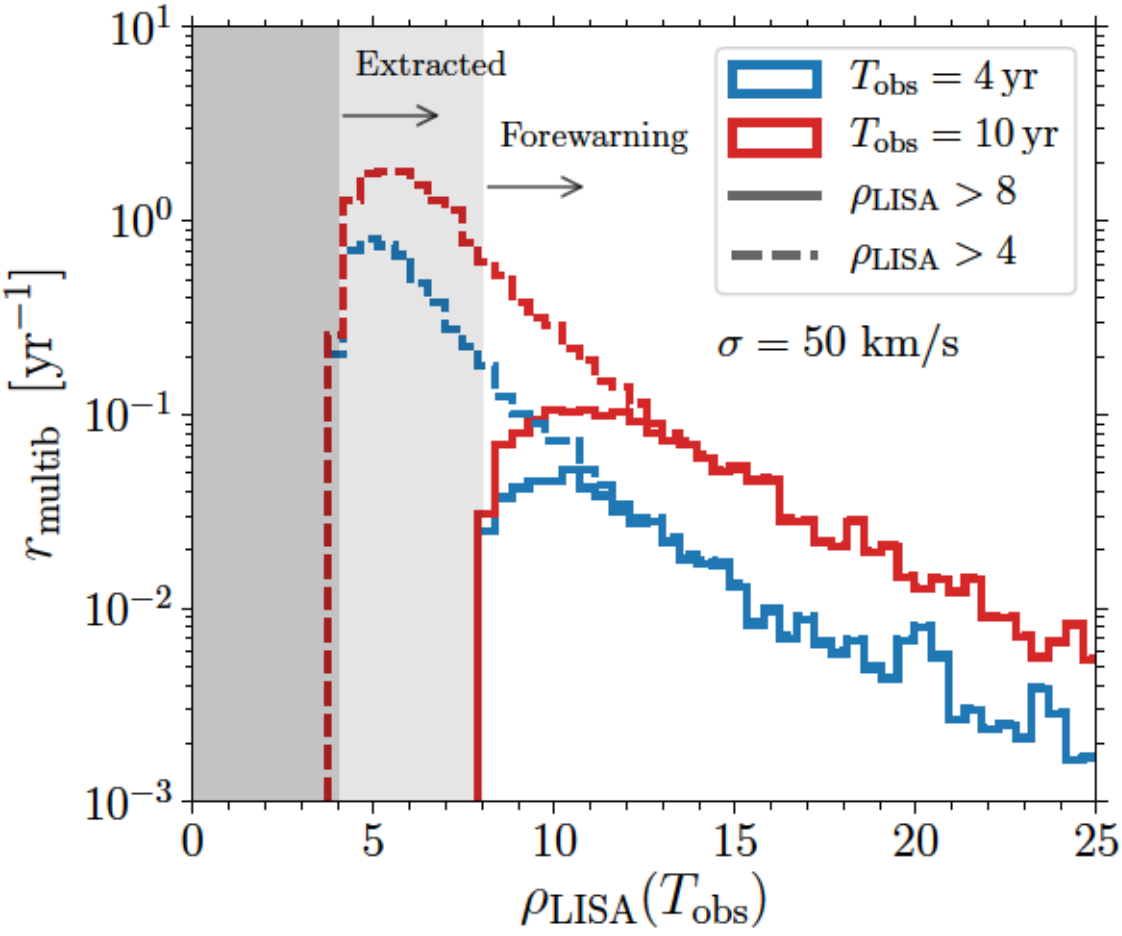

Figure 9.6: Distribution of LISA SNRs for multiband BH binaries. The x-axis shows $\rho_{\rm LISA}$ evaluated at $T_{\rm obs}$ (as a proxy for the strength of the signal), while the y-axis shows the multiband detection rate per bin. Results are presented for a single population synthesis simulation with supernova kick parameter $\sigma = 50$ km/s. We assume a LISA mission duration of $T_{\rm obs} = 4$ yr (blue) and 10 yr (red) and a LISA SNR threshold of 8 ("forewarning", solid) and 4 ("extracted", dashed). Results appear identical if LIGO or a third-generation ground-based detector is considered. We set $T_{\rm wait} = 5 \times T_{\rm obs}$, i.e. either 20 or 50 yr.

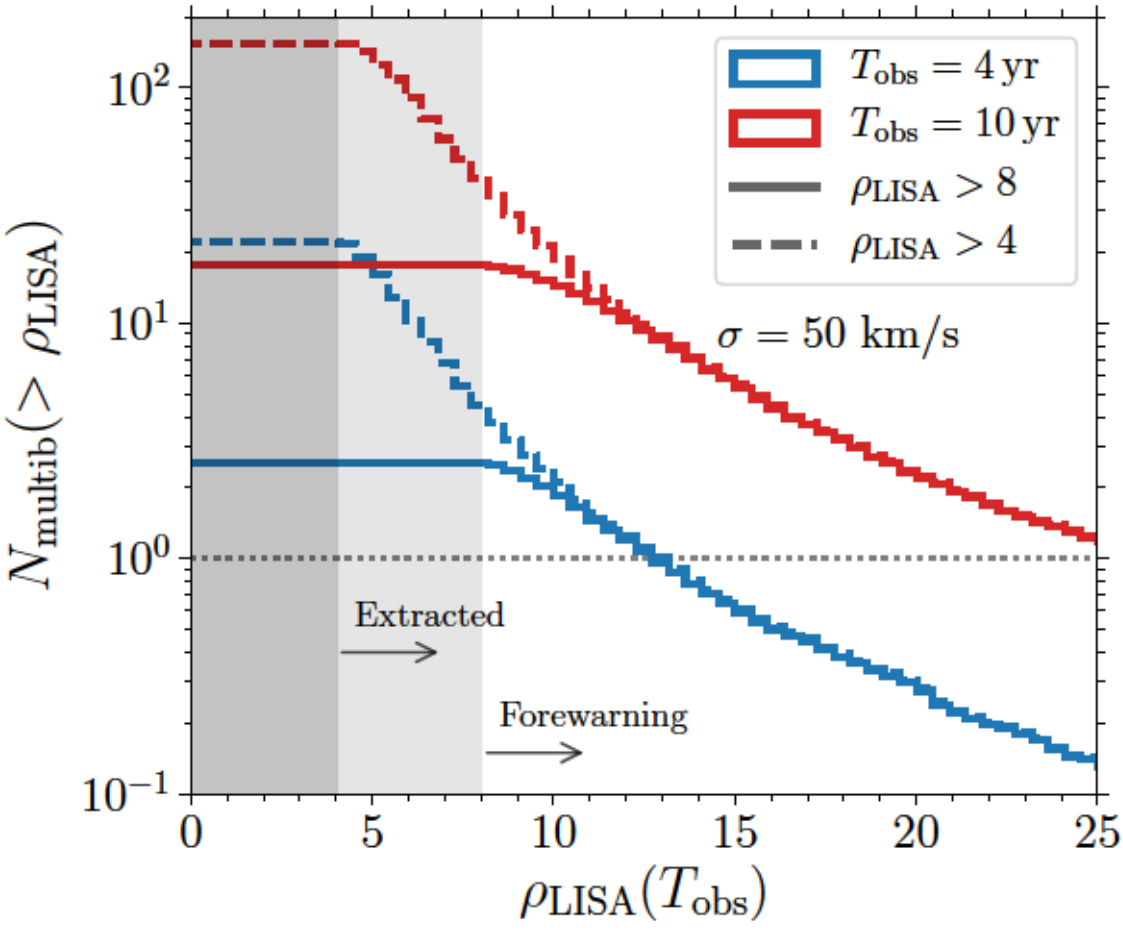

Figure 9.7: Cumulative number of expected multiband detections as a function of the LISA SNR. Results are presented for a single population synthesis simulation with supernova kick parameter $\sigma = 50$ km/s. We assume a LISA mission duration of $T_{\rm obs} = 4$ yr (blue) and 10 yr (red) and a LISA SNR threshold of 8 ("forewarning", solid) and 4 ("extracted", dashed). Results appear identical if LIGO or a third-generation ground-based detector is considered. We set $T_{\rm wait} = 5 \times T_{\rm obs}$, i.e. either 20 or 50 yr.

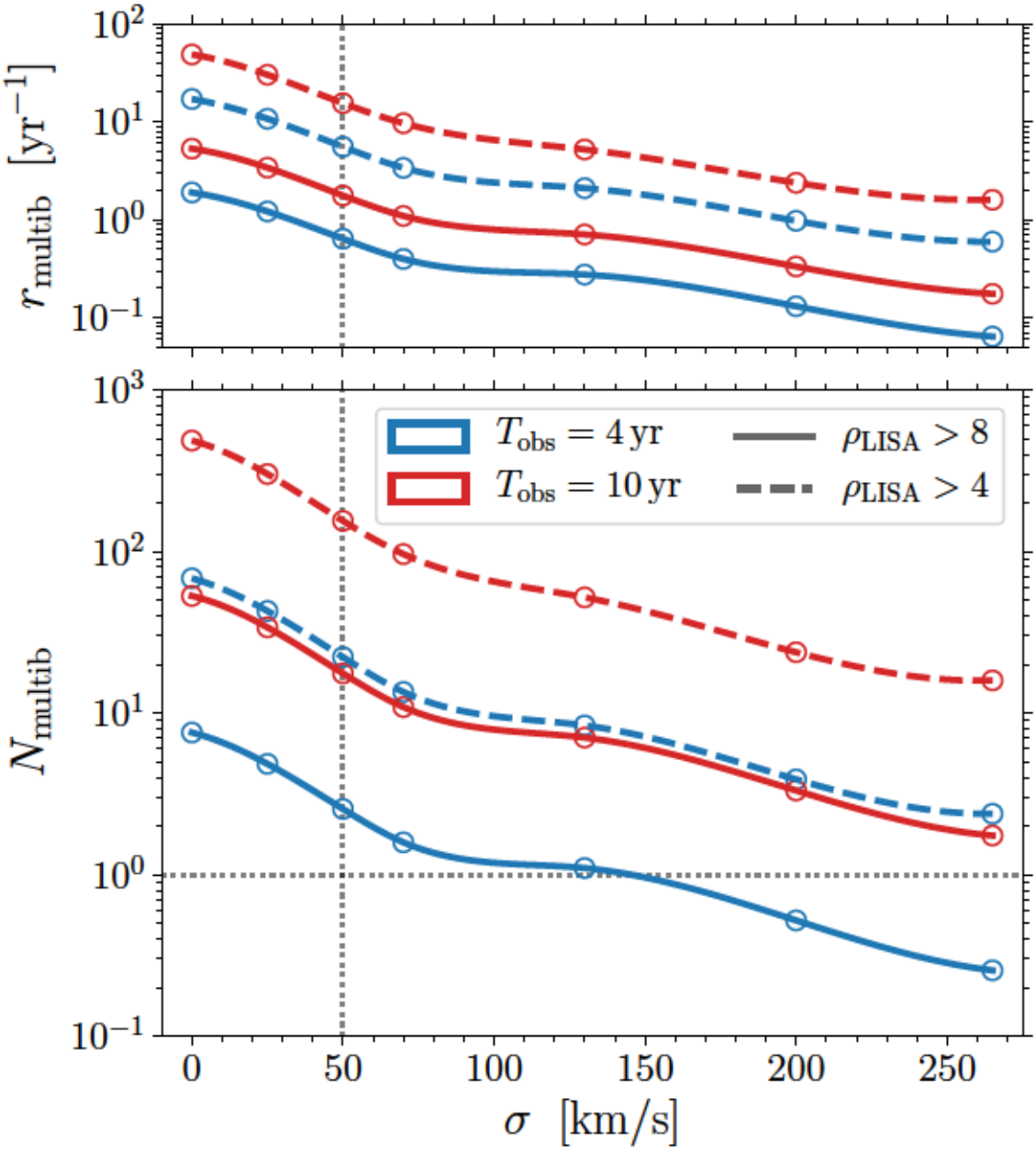

Figure 9.8: Multiband detection rates (top) and number of events (bottom) predicted by population synthesis simulations of binary stars. We present results from 7 different simulations with varying supernova kicks, where the 1D dispersion σ ranges from 0 km/s (no kicks) to 265 km/s (BHs receives full kicks as inferred from galactic pulsars). Blue (red) curves show results assuming a LISA mission duration of 4 yr (10 yr); solid (dashed) lines assumes a LISA SNR threshold of 8 (4). The vertical dotted line at $\sigma = 50$ km/s marks the model used in Figs. 9.5-9.7. Results appear identical if LIGO or a third-generation ground-based detector is considered. We set $T_{\rm wait} = 5 \times T_{\rm obs}$, i.e. either 20 or 50 yr. Data to reproduce this figure are reported in Table 9.2.

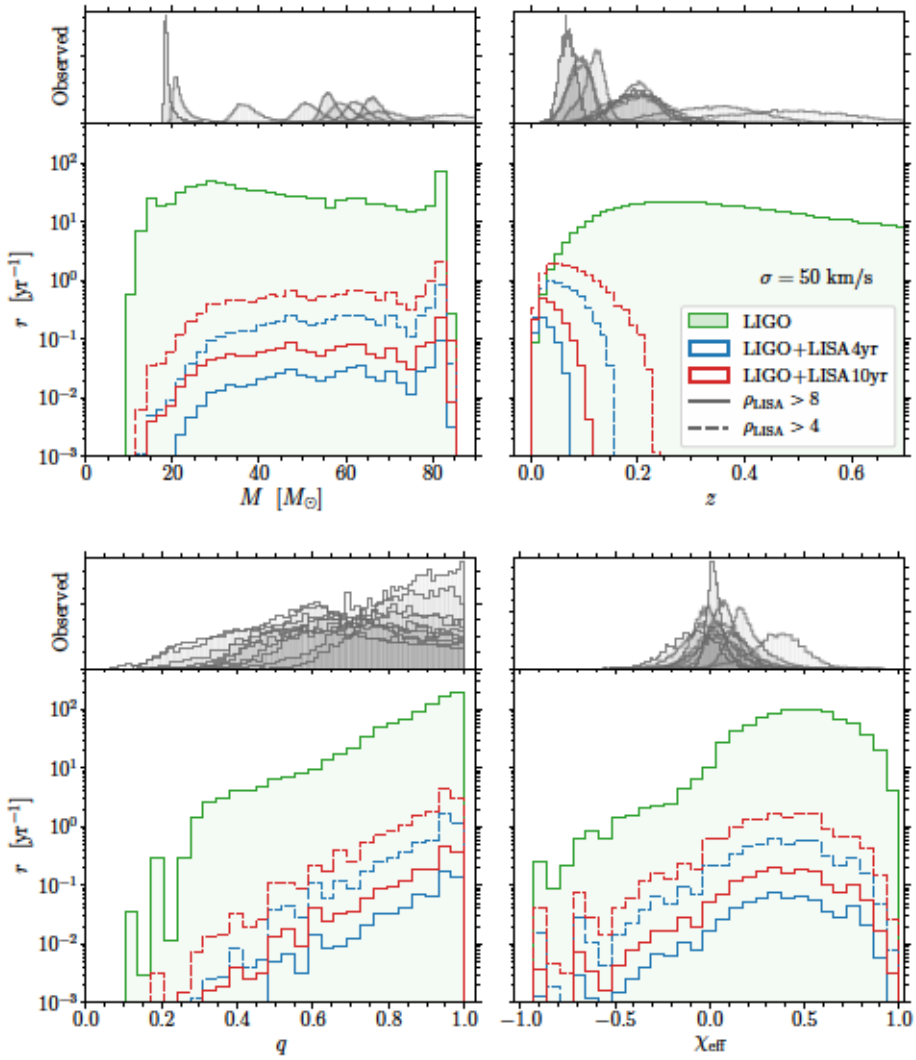

Figure 9.9: Marginalized distributions of total mass $M = m_1 + m_2$ (top left), mass ratio $q = m_2/m_1$ (bottom left), redshift z (top right) and effective spin $\chi_{\rm eff}$ (bottom left) detectable by multiband GW networks. Larger panels show results from a population synthesis distribution with supernova kick parameter $\sigma = 50$ km/s. The LIGO detection rate is shown in green, while multiband rates are shown in blue and red assuming a LISA mission duration of 4 and 10 years, respectively. For the multiband distributions, solid (dashed) lines are obtained with a LISA SNR threshold of 8 (4); results appear identical if LIGO or a third-generation ground-based detector is considered. The top smaller panels shows posterior distributions of the first 10 binary BH mergers detected by LIGO/Virgo [9].

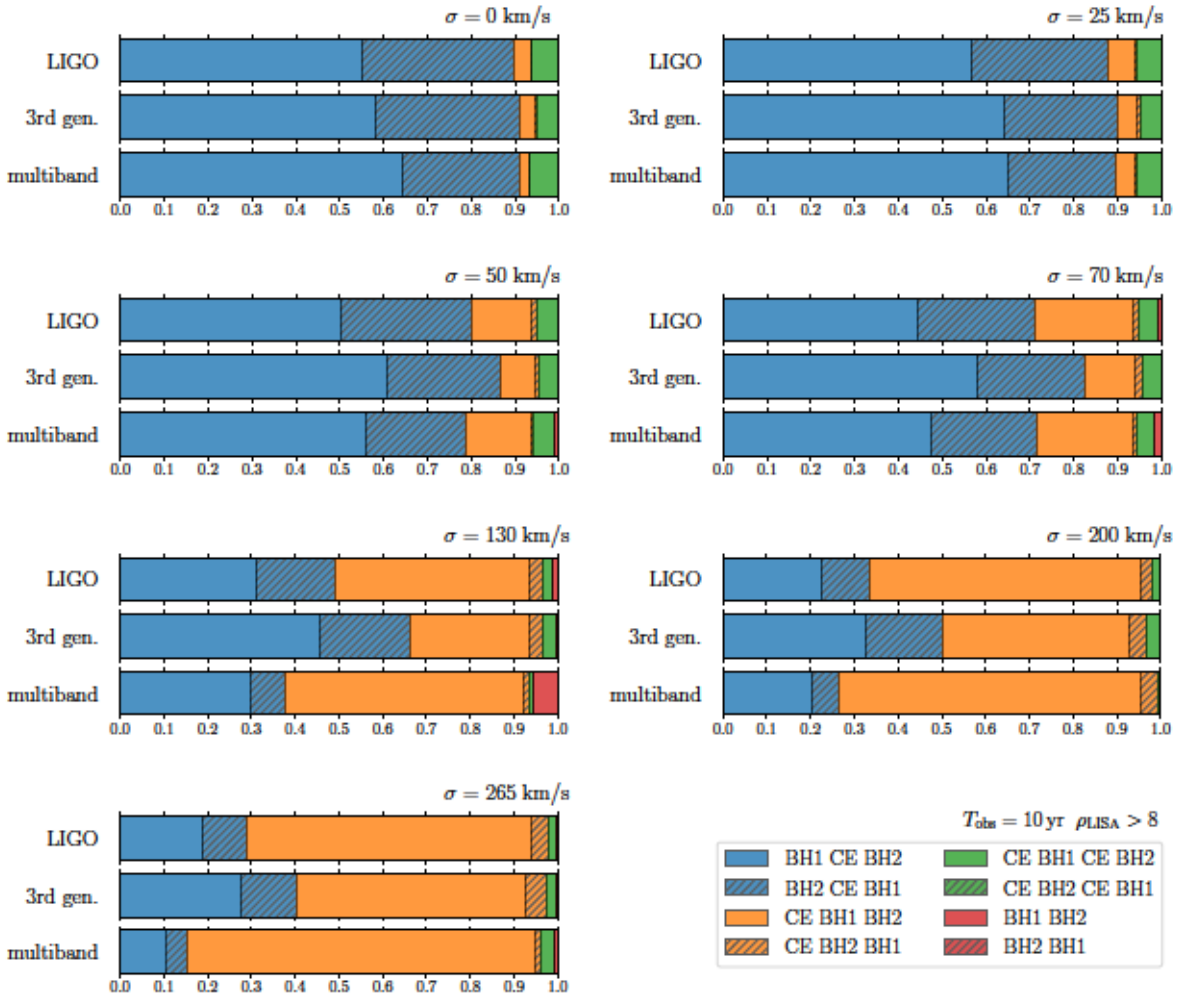

Figure 9.10: Fractional contribution to the detection rate from BH binaries formed via different subchannels. Each panel contains results from a different population synthesis simulation, where the strength of the supernova kicks is varied from $\sigma = 0$ (top left) to 265 km/s (bottom). Binaries are classified according to the order of the formation of the heavier object (BH1), the formation of the lighter object (BH2) and the occurrence of a common-envelope phase (CE). Top, middle and bottom bars of each panel refer to LIGO, Cosmic Explorer and multiband detections, respectively. Multiband results are computed assuming $T_{obs} = 10$ yr, $\rho_{LISA} > 8$ and the LIGO ground-based detector (but result are unchanged if a LISA+3g network is considered).

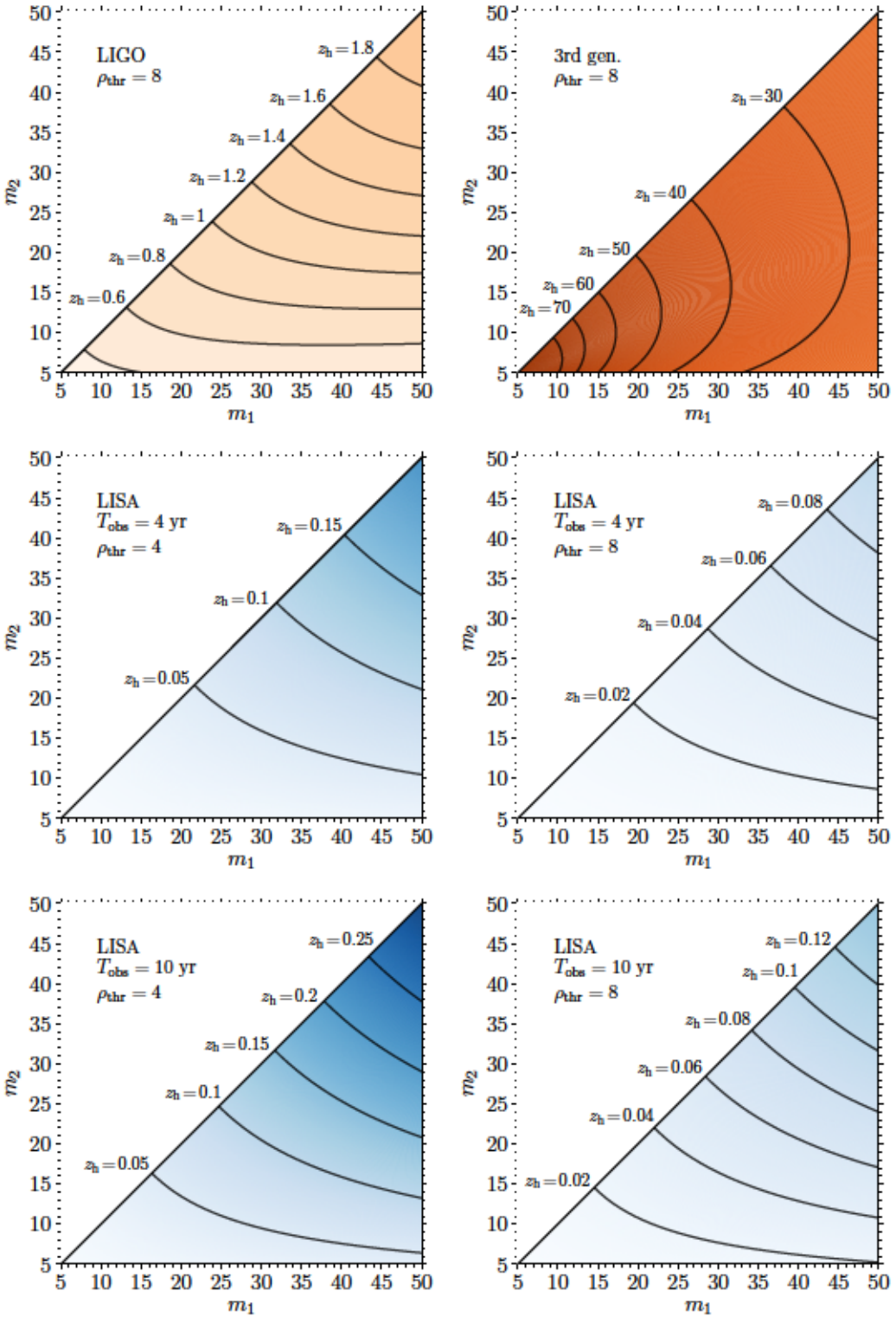

Figure 9.11: Stellar-mass BH binary horizon redshifts $z_{\rm h}$ for ground- and space-based GW detectors as a function of the BH masses $m_1 > m_2$. Top panels are produced assuming LIGO at design sensitivity and the proposed third-generation detection Cosmic Explorer, together with the standard threshold $\rho_{\rm thr} = 8$. Bottom and middle panels show results for the LISA space mission, assuming different mission duration of $T_{\rm obs} = 4$, 10 yr and SNR thresholds $\rho_{\rm thr} = 4$, 8. For simplicity, here we assume nonspinning sources.

Chapter 10

Expanding the LISA Horizon from the Ground

The Laser Interferometer Space Antenna (LISA) gravitational-wave (GW) observatory will be limited in its ability to detect mergers of binary black holes (BBHs) in the stellar-mass range. A future ground-based detector network, meanwhile, will achieve by the LISA launch date a sensitivity that ensures complete detection of all mergers within a volume $>\mathcal{O}(10)\,\mathrm{Gpc}^3$. We propose a method to use the information from the ground to revisit the LISA data in search for sub-threshold events. By discarding spurious triggers that do not overlap with the ground-based catalogue, we show that the signal-to-noise threshold ρ_{LISA} employed in LISA can be significantly lowered, greatly boosting the detection rate. The efficiency of this method depends predominantly on the rate of false-alarm increase when the threshold is lowered and on the uncertainty in the parameter estimation for the LISA events. As an example, we demonstrate that while all current LIGO BBH-merger detections would have evaded detection by LISA when employing a standard $\rho_{\mathrm{LISA}} = 8$ threshold, this method will allow us to easily (possibly) detect an event similar to GW150914 (GW170814) in LISA. Overall, we estimate that the total rate of stellar-mass BBH mergers detected by LISA can be boosted by a factor ~ 4 ($\gtrsim 8$) under conservative (optimistic) assumptions. This will enable new tests using multi-band GW observations, significantly aided by the greatly increased lever arm in frequency.

10.1 Introduction

Multi-band measurements of GWs [593] from coalescing binary black holes (BBHs) can open the door to a wide array of invaluable studies. Spanning a wider range of frequencies will increase sensitivity to eccentric orbits, which can be used to distinguish between different binary formation channels, improve merger-rate estimation, allow for more precise tests of gravity and assist in instrument calibration. Better science will be enabled if many events are detected in both a ground-based network (Ground) and a space observatory such as LISA.

Unfortunately, LISA will not be nearly as sensitive as the Ground detectors to stellar-mass BBH mergers. This issue affects in particular "multiband" inspiral events, for which the GW frequency drifts from the LISA to the Ground band during the LISA observation window. This condition determines a minimum frequency at which the event can appear in LISA (typically $\gtrsim 10^{-2}\,\mathrm{Hz}$ for stellar-mass BBHs). Taking advanced LIGO (aLIGO) at design sensitivity as an example and adopting a similar signal-to-noise threshold of $\rho = 8$ in both experiments, the fraction of aLIGO events that will be detectable in LISA is less than 1%.

If we can manage to lower the LISA signal-to-noise threshold, the horizon distance (which is the maximum distance at which a source is detectable) will grow, and the increase in accessible volume will result in a rapid rise in the multi-band detection rate. Setting a lower threshold, however, means that we increase the risk of classifying noise triggers as real events (false alarms). The false-alarm rate (FAR) is a steep function of ρ [594].

In this *Letter* we propose a method to discard spurious LISA triggers that show up as the signal-to-noise threshold is lowered, using information from the Ground. We show that a large number of random noise triggers can be filtered out by imposing consistency with Ground measurements for multiple parameters in tandem.

10.2 Method

The procedure is as follows: we first set an initial threshold, e.g. $\rho_{\rm LISA} = 8$, and determine which (real) events in the Ground catalogue are detectable in LISA with this threshold. The parameters of all LISA candidate events identified with this threshold are then compared with

those in the Ground list (taking into account the LISA parameter-estimation uncertainty), and those that do not overlap with any real event are discarded. We lower the threshold and iterate this procedure until the probability that a random trigger is consistent with some Ground event becomes significant.

Figure 10.1 illustrates the concept of filtering spurious triggers using only t_c, the time of coalescence, as the discarding parameter. Compared with the entire LISA observation time, $\mathcal{O}(1)$ years, the typical uncertainty on t_c as determined by LISA is ~ 7 orders of magnitude smaller, $\mathcal{O}(10)$ seconds. With $\mathcal{O}(1000)$ events expected to be detected from the Ground within the volume accessible by LISA with $\rho_{\rm LISA} \gtrsim 5$, we should therefore be able to filter out roughly $\gtrsim 10^4$ random triggers based on t_c alone. This will allow a detection of events with $\rho_{\rm LISA} \sim 7$, such as GW150914 [21], over the LISA mission lifetime. We will see that incorporating additional parameters may enable a multi-band detection of events with $\rho_{\rm LISA} \sim 4$, such as GW170814 [595].

In what follows we choose to focus on three waveform ingredients: the source masses, sky location and merger time. We will test the efficiency of our proposed method based on a Fisher matrix analysis to estimate the parameter estimation uncertainty in the LISA band [511], and report the potential improvement in the LISA event rate given different assumptions about the FAR and the BBH mass function.

We assume the posteriors to be Gaussian, so a trigger is characterized by its k-dimensional vector of best-fit parameter values $\vec{\mu}$ and covariance matrix Σ. The problem of consistency checking between the LISA and Ground measurements corresponds to finding the overlap between two volumes in a multi-dimensional space given some metric. We claim that two measurements taken by LISA and the Ground agree with each other if they meet the following criterion:

$$D(\vec{\mu}_{\rm LISA}, \vec{\mu}_{\rm Ground}, \Sigma_{\rm LISA}, \Sigma_{\rm Ground}) \leq \chi^2_k(p), \tag{10.1}$$

where D is a function that gives the distance between two points in the high-dimensional space under some metric, and $\chi^2_k(p)$ is the quantile function for probability p of the Chi-Squared distribution with k degrees of freedom.

A typical source in LISA will be characterized by $k = 9$ parameters (when taking into

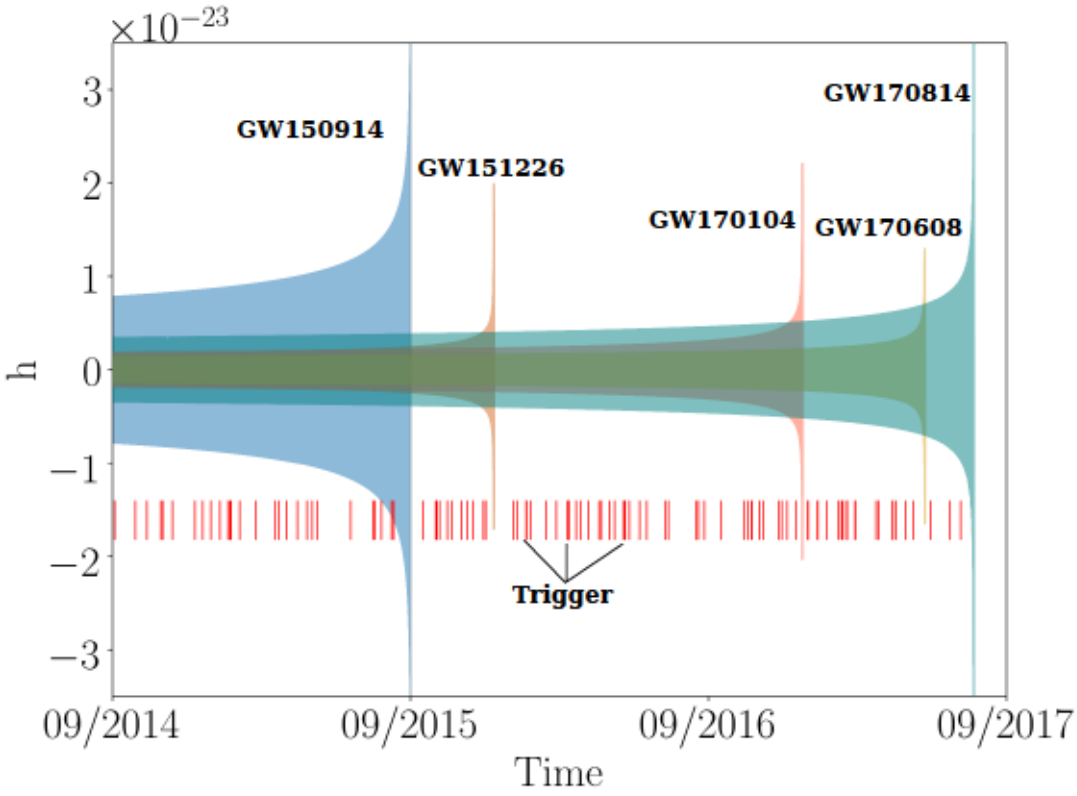

Figure 10.1: Illustration of our method to discard LISA triggers. The waveforms are those of the gravitational events which were observed by aLIGO in its O1 and O2 runs (2015-2017). GW150914 would have had the highest signal-to-noise in LISA, $\rho_{\rm LISA}=7$, while GW170814 would have had $\rho_{\rm LISA}=4.5$ (assuming 4 years of integration time), both of which are below the conventional $\rho=8$ threshold. The red stripes indicate the merger time of LISA triggers (their width set by the uncertainty). If a trigger does not agree with any of the events detected from the Ground, it can be discarded as random noise (or as an astrophysical event whose merger will appear in LIGO in the future and is thus irrelevant for our purposes). We show that if LISA had started observing in 2011, it would have been possible to lower its signal-to-noise threshold and recover GW150914, and potentially also GW170814. The other events would have been out of reach.

account the antenna pattern), so the exact two-point distance problem would be solved in an 18-dimensional space, and hence it can be computationally intensive. Instead of solving the problem exactly, we calculate the volume bounded by $\chi^2_k(p)$ in the parameter space centered at the best-fit value for each parameter that is given by the more precise measurement between the Ground and LISA. Since most of the sources will be detected from the Ground with signal-to-noise well above threshold, the Ground measurements can be treated as the "true" values (neglecting any systematic bias). The consistent volume in parameter space of a particular source with parameters $\vec{\theta}$ will be well-approximated by the ellipsoid

$$V(\vec{\theta}, p) = \left(\frac{\chi^2_k(p)}{\chi^2_k(0.67)}\right)^k \sqrt{(2\pi)^k |\Sigma_{\rm LISA}(\vec{\theta})|}, \tag{10.2}$$

where $|\Sigma_{\rm LISA}(\vec{\theta})|$ denotes the determinant of the covariance matrix given by LISA using the most recent noise power spectral density $S_n(f)$ [505], and $\chi^2_k(0.67)$ corresponds to a bound at "1σ" level. The fraction of triggers which are consistent between the two detectors is then given by

$$f_c(\rho, T) = \frac{\int d\vec{\theta}\; n_s(\vec{\theta}, \rho, T) \int_{V(\vec{\theta},p)} d\vec{\theta'}\, n_b(\vec{\theta'})}{\int n_b(\vec{\theta'}) d\vec{\theta'}}, \tag{10.3}$$

where $n_s(\vec{\theta}, \rho, T)$ is the number of astrophysical (real) events which LISA is sensitive to (all of which are detectable from the Ground) for a given vector $\vec{\theta}$ of source parameters, a signal-to-noise threshold $\rho_{\rm LISA}$, and integration time T; $n_b(\vec{\theta'})$ is the number density of LISA triggers as a function of $\vec{\theta'}$ in the search parameter space.

The most important ingredient in our analysis is the relationship between the threshold $\rho_{\rm LISA}$ and the number of expected background triggers, which we call the "FAR curve." At this time, there is no reliable estimate for the LISA FAR curve. We therefore use as a proxy the results of the LIGO Mock Data Challenge [594], which suggest that the number of background triggers increases by about two orders of magnitude when the signal-to-noise threshold is decreased by one (we use their Experiment 3, which is the most relevant for our study). This agrees with the recent findings of Ref. [596].

We can then define the *effective* LISA threshold as

$$\rho^{\rm eff}_{\rm LISA}(T) = \rho^{0}_{\rm LISA} + \log_{\Gamma}(f_c(\rho^{\rm eff}_{\rm LISA}, T)), \tag{10.4}$$

where $\rho^{0}_{\rm LISA}$ is the conventional signal-to-noise threshold, Γ is the FAR and T is the integration time in LISA. Eq. (10.4) is the crux of the method proposed in this work.

The FAR curve given in Ref. [594] has a slope $\Gamma \sim 100$ and is not shown below $\rho = 5.5$. As a conservative estimate, we impose an exponential cutoff $e^{-3(\rho-5.5)}$ starting at $\rho=5.5$, essentially preventing any improvement beyond $\rho = 5$. We also consider a more optimistic case in which we extrapolate the FAR curve with a similar cutoff at $\rho = 4$. Given the volume permitted by a single source, Eq. (10.2), the number density n_s of real sources in the parameter space and the FAR function, we are now ready to obtain $\rho_{\rm eff}$ by solving Eq. (10.4) self-consistently.

In order to compute the second integral in Eq. (10.3), we need to estimate $\Sigma_{\rm LISA}$. We adopt a modification of the Fisher matrix code from Ref. [511] to calculate the uncertainties on source parameters. As explained above, we calculate $\rho^{\rm eff}_{\rm LISA}(T)$ using the three groups of parameters which contribute the most to the fraction of discarded events f_c:
(i) Time of coalescence t_c: we care only for events that will merge in the Ground frequency band and assume that noise triggers will be distributed uniformly in the LISA observation window, which is determined by T.
(ii) Component masses (M_1, M_2): we assume that noise triggers will pick up a random template in the template bank, and calculate the fraction f_c assuming noise triggers are distributed uniformly in the (M_1, M_2) plane. The uncertainty on either component mass is normally $\sim 10\%$ of the measured value, but due to the strong correlation between the two component masses [182], the allowed volume in the parameter space is typically much smaller than 10%. This volume is related to the uncertainty in chirp mass measurement, which is expected to be quite small in LISA (as BBHs spend many cycles in its frequency band). Typically the probability of a noise trigger being consistent with one real event is $\sim 10^{-6}$.
(iii) Sky location (θ_S, ϕ_S): We assume that noise triggers will be uniformly distributed across the sky. LISA will be able to localize sources to within $\mathcal{O}(10)\,{\rm deg}^2$ [597]. Comparing to the whole sky, the probability of a noise trigger being consistent with one event is $\lesssim 10^{-3}$.

Our figure-of-merit is the number of additional sources we can recover in LISA by replacing the conventional threshold $\rho^0_{\rm LISA}$ with $\rho^{\rm eff}_{\rm LISA}$. This of course depends on the astrophysical BBH merger rate. Multiband events probed by LISA are in the local Universe, so we can assume the merger rate R to be constant in redshift. We denote by Λ the mean rate of events of astrophysical origin above a certain signal-to-noise threshold, given by $\Lambda = R\,\langle VT\rangle$, where $\langle VT\rangle$ is the time and population-averaged space-time volume accessible to the detector at the chosen threshold $\rho^{\rm th}$, defined as [598]

$$\langle VT\rangle = T\int dz d\vec{\theta}\,\frac{dV_c}{dz}\frac{1}{1+z}s(\vec{\theta})f(z,\vec{\theta},\rho^{\rm th}), \tag{10.5}$$

where V_c is the comoving volume, $s(\vec{\theta})$ is the injected distribution of source parameters, and $0 \leq f(z,\vec{\theta},\rho^{\rm th}) \leq 1$ is the fraction of injections detectable by the experiment.

In order to calculate $\langle VT\rangle$, we need to solve for the horizon distance and redshifted volume as a function of source parameters [599], and then marginalize over an input population $s(\vec{\theta})$. We consider sources characterized by 9 parameters: the two component masses (M_1, M_2), time of coalescence t_c, phase of coalescence ϕ_c, luminosity distance D_L, sky locations of the source $(\bar{\theta}_S, \bar{\phi}_S)$, and the orbital angular momentum direction $(\bar{\theta}_L, \bar{\phi}_L)$. In practice, we sample over the two component masses and four sky locations, with t_c and ϕ_c arbitrarily set to zero.

For the injected mass distribution, we follow Ref. [288] and define the probability density function (PDF) of M_1

$$P(M_1) \equiv A_{M_1} {M_1}^{-\alpha}\mathcal{H}(M_1 - M_{\rm gap})e^{-(M_1/M_{\rm cut})^2}, \tag{10.6}$$

where A_{M_1} is a normalization constant, $\mathcal{H}$ is the Heaviside function, $M_{\rm gap}$ is the minimum mass of a stellar black hole (assumed to be $5M_\odot$), and by default we set the upper cutoff $M_{\rm cut} = 40M_\odot$ [238, 600, 601]. To account for uncertainty regarding these choices, we also calculate our results using two other mass functions: in one we replace the Gaussian cutoff with a sharp step function $P(M) \propto \mathcal{H}(M_\odot - M_{\rm cut})$, and in another with an exponential cutoff $P(M) \propto e^{-M_1/M_{\rm cut}}$. For all cases we limit the maximum component mass to $100M_\odot$. Finally, given a value for M_1, we define the PDF of M_2 as a uniform distribution ranging

from $M_{\rm gap}$ to M_1 [182, 288]:

$$P(M_2 \mid M_1) \equiv A_{M_2}\mathcal{H}(M_2 - M_{\rm gap})\mathcal{H}(M_1 - M_2). \tag{10.7}$$

For the sky locations, we assume sources are uniformly distributed on the celestial sphere. In principle one should generate a 6-dimensional sample in the mass–sky-location parameters space, but this is quite computationally intensive. In practice, we average over a reasonable amount of sources distributed across the sky and compress the calculation of $\langle VT\rangle$ to two (mass) dimensions.

The next term we need is $f(z, \vec{\theta}, \rho^{\rm th})$, which is related to the horizon redshift of the source. The LISA signal-to-noise of a source with frequency-domain waveform $\tilde{h}(f)$ at some luminosity distance is given by [602]

$$\rho^2 = 4\int_{f_{\rm min}}^{f_{\rm max}} \frac{\tilde{h}^*(f)\tilde{h}(f)}{S_n(f)}df, \tag{10.8}$$

where $f_{\rm min}$ and $f_{\rm max}$ are the initial and final frequencies. We get the horizon redshift, and hence $f(z, \vec{\theta}, \rho^{\rm th})$, by setting $\rho = \rho^{\rm th}$.

When calculating the uncertainty and signal-to-noise for a given source, we need to integrate the waveform over a certain frequency range. Since we are interested in sources which can in principle be detected in both LISA and the Ground, we set $f_{\rm max} = 1\,{\rm Hz}$ (the conventional upper cutoff on the LISA noise curve). To determine $f_{\rm min}$, we require that a source drifts from the LISA band to the Ground band in less than a total time T. The chirp time of a source with chirp mass $\mathcal{M}$ (in the observer frame) is given by [603]

$$t = \int_{f_{\rm min}}^{f_{\rm max}} df \frac{5c^5}{96\pi^{8/3}}(G\mathcal{M})^{-5/3}f^{-11/3}. \tag{10.9}$$

To determine $f_{\rm min}(\vec{\theta})$ we solve Eq. (10.9) setting $t \equiv T$.

10.3 Result

In Figure 10.2 we plot our main result: $\Lambda_{\rho_{\rm eff}}/\Lambda_{\rho=8}$, the increase in detection rate compared to using the standard $\rho = 8$ threshold, under different assumptions. We see that using the Ground information can boost the number of detections in LISA by a factor $\sim$4, under the conservative choice for the FAR.

Since our figure-of-merit compares total rates, and we assume a constant merger rate density per comoving volume, the uncertainties in the merger rate cancel out. The dominant uncertainty in our result stems from the FAR. With a more optimistic choice of FAR the boost factor can increase up to ~ 8: the LISA sampling rate [51] sets a lower limit on the threshold.

The next source of uncertainty is due to the choice of mass function. The increase in detection rate is biased toward the lower end of the mass function, and so it is more significant for mass functions that favor lower mass events. This uncertainty amounts to $\sim$5%. A uniform-in-log mass function should yield similar results [596].

10.4 Discussion

Various assumptions we have made here can be improved upon. For example, in checking for consistency between LISA and the Ground we considered only the volume allowed by the LISA covariance matrix, instead of solving the exact two-point problem. This is a reasonable assumption, based on the expected sensitivity of Ground observatories by the time LISA flies.

We also took the distribution of noise triggers to be uniform in the parameters of interest. This assumption is valid for time of coalescence and sky location, but it may not be accurate for the two component masses. Search template banks for ground-based detectors typically have more templates at the low-mass end [604, 605, 606]. More realistic template banks for LISA, when available, can be used to replace the uniform distribution employed here. If the LISA and Ground templates are qualitatively similar, this replacement should increase the discarding power at the higher-mass end compared to the uniform case, and therefore improve the boost in rate.

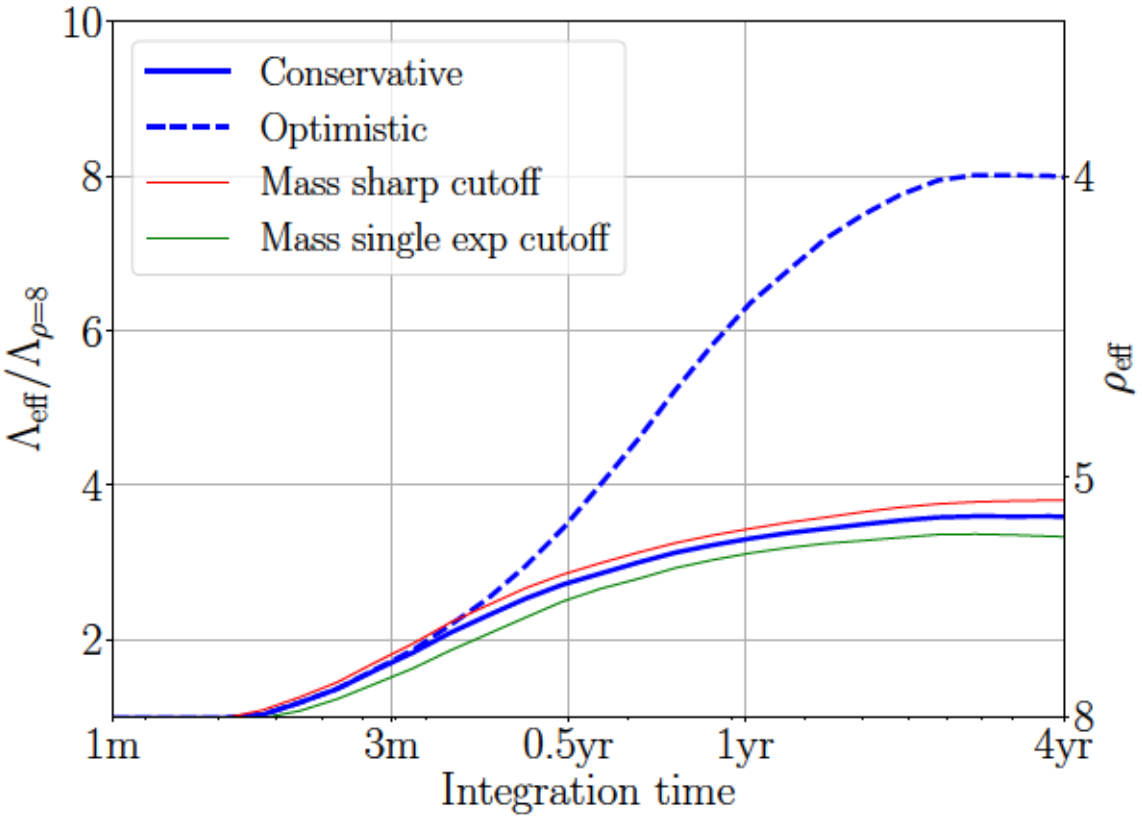

Figure 10.2: The boost in the LISA detection rate enabled by our method, compared to setting the standard signal-to-noise threshold of $\rho = 8$, and assuming that all sources are observed for the integration time T given in Eq. (10.9). The blue solid line shows the rate increase using a FAR function with a cutoff at $\rho = 5$ and a mass function with a Gaussian cutoff. The dashed-blue line corresponds to a more optimistic FAR function, where the cutoff is at $\rho = 4$. For comparison, we show in red and green the result when using a mass function with a sharp cutoff at $50M_\odot$ and a single-exponential cutoff at $40M_\odot$, respectively.

Another approximation we made was to extrapolate our Fisher matrix calculation into the low signal-to-noise regime, where it generally serves only as a lower bound of the uncertainties [273]. A more realistic estimate of the uncertainties can be achieved with other parameter estimation approaches, such as the Markov Chain Monte Carlo method [607]. We hope that our work will motivate participants in the ongoing LISA Data Challenges [608] to verify and improve our FAR estimates.

To conclude, while the idea to use LISA detections to alert ground-based experiments about pending mergers has been explored before [593], we have investigated for the first time the

potential of exploiting the opposite route.

We have introduced in this *Letter* a method to recover sub-threshold stellar-mass BBH merger events from the LISA data stream using information from the subsequent ground-based measurements of these events. Our analysis forecasts a remarkable increase – by a factor of 4 to 8, depending on the assumptions – in the number of LISA detections. While our estimate was restricted to multi-band sources whose merger is detected from the Ground during the LISA lifetime, the same algorithm can be continuously applied for events that merge after LISA has finished its mission, yielding more detections.

The increase in number of multi-band GW detections can bring forth a plethora of rewards. For example, improvements in parameter estimation and modeling constraints will enable novel tests of extreme gravity theories [609, 610, 611, 612, 613]. Most notably, discrimination between different BBH-formation channels using eccentricity [520, 614, 615, 616, 617, 618], spins [234, 236, 310, 366, 434], and other waveform features [619, 620, 621] will greatly benefit from the larger lever arm in frequency garnered from these measurements.

Chapter 11

Binary radial velocity measurements with space-based gravitational-wave detectors

Unlike traditional electromagnetic measurements, gravitational-wave observations are not affected by crowding and extinction. For this reason, compact object binaries orbiting around a massive black hole can be used as probes of the inner environment of the black hole in regions inaccessible to traditional astronomical measurements. The orbit of the binary's barycenter around the massive black hole will cause a Doppler shift in the gravitational waveform which is in principle measurable by future space-based gravitational-wave interferometers, such as the Laser Interferometer Space Antenna (LISA). We investigate the conditions under which these Doppler shifts are observable by LISA. Our results imply that Doppler shift observations can be used to study the central region of globular clusters in the Milky Way, as well the central environment of extragalactic massive black holes.

11.1 Introduction

The direct detection of gravitational waves (GWs) by the LIGO/Virgo collaboration is the beginning of a new era in black hole (BH) astronomy [181, 232] and tests of strong field

gravity [27]. All GW observations so far constrained the properties of BHs (or neutron stars) in binary systems. This is in stark contrast with "traditional" astronomical BH observations, which rely on the interaction of isolated BHs with the surrounding environment, such as nearby stars [622, 623, 624] and accreting matter [424, 625, 626, 627]. By their very nature, these electromagnetic observations are subject to modelling and systematic uncertainties, weakening the supporting observational evidence for BHs and our ability to measure their parameters. For example, the very existence of intermediate-mass BHs (IMBHs) is still under debate [628, 629].

Recent work considered various astrophysical processes, other than cosmological redshift [630], which may introduce measurable Doppler shifts in gravitational waveforms [619, 631, 632, 633, 634], and the astrophysical properties that could be inferred from such measurements. Doppler shift measurements in gravitational waveforms extend the class of astrophysical systems that can be studied with GW detectors beyond the strong-field merger and collapse of compact objects.

Unlike electromagnetic measurements, GW measurements do not have multiple emission lines that can be used to independently identify the Doppler shift: an event moving at constant line-of-sight velocity is degenerate with a heavier system without proper motion [see e.g. 602]. For the proper motion to be detectable, we need to observe *variations* in the line-of sight velocity.

One of the most common astrophysical systems that can produce potentially detectable Doppler shifts are hierarchical triples. In the hierarchical triple scenario, the orbital period of the binary around the third body should not be too large compared to the the observation period: if it is, the observed velocity of the binary will be approximately constant during the observation, hence indistinguishable from a system of different mass without proper motion. This also means that longer observation periods help us resolve larger velocity variation timescales. In contrast with Earth-based interferometers, which typically observe binary inspirals and mergers lasting for seconds or minutes, the Laser Interferometer Space Antenna (LISA) [50] will measure inspiral events lasting as long as a few years, and it is therefore more sensitive to Doppler shifts in the gravitational waveform.

With a few exceptions [634], most recent studies considered LISA sources where the third body has mass comparable to the GW-emitting binary [633, 635, 636] or much smaller

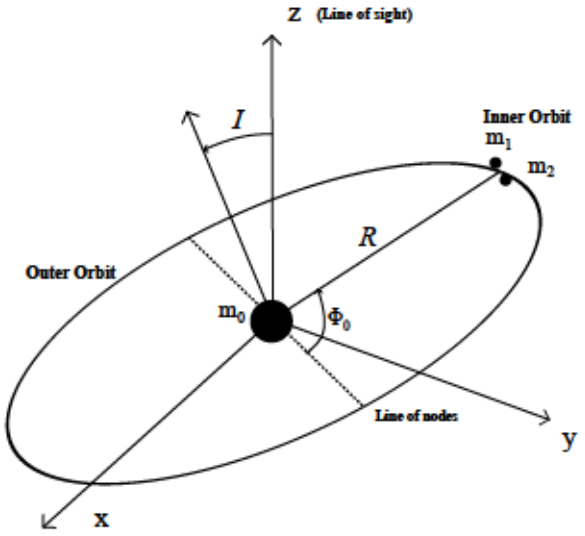

Figure 11.1: Illustration of the geometry of the system.

than the GW-emitting binary [637, 638, 639]. In this work we focus on the complementary scenario where the third body is a BH of mass *much larger* than the GW-emitting binary, and we ask: how close to the BH should the GW-emitting binary be in order to yield meaningful constraints on the properties of the third body? We show that observationally interesting scenarios include (i) white dwarf binaries (WDWDs) orbiting around IMBHs, (ii) stellar-origin BH binaries (SOBHs) similar to those detected by LIGO/Virgo orbiting around a nearby supermassive BH (SMBH) such as the one at our own galactic center, and (iii) IMBH binaries orbiting around extragalactic SMBHs.

The structure of the paper is as follows. In section 11.2 we describe our model for the gravitational waveform, and we review the Fisher matrix technique used in our parameter estimation calculations. In section 11.3 we present our main results. In section 11.4 we discuss the limitations of our work, their scientific implications, and directions for future work.

11.2 Doppler-shifted waveform model and parameter estimation

The geometry of the triple system we consider is sketched in Fig. 11.1. The z axis is oriented along the line of sight. The GW-emitting binary components, with masses m_1 and m_2, are on a circular "inner" orbit; m_0 is the mass of the third body (a massive BH); I is the angle between the line of sight and the orbital angular momentum of the GW-emitting binary, whose barycenter is assumed to be on a circular "outer" orbit about the third body; R is the radius of this circular orbit. Let $M_{\rm tot} = m_0 + m_1 + m_2$ be the total mass of the triple. We assume that the separation between the components of the inner binary is much smaller than R, i.e. that the period of the inner orbit is much shorter than the period

$$P_0 = 2\pi\sqrt{\frac{R^3}{M_{\rm tot}}} \tag{11.1}$$

of the outer orbit. Under this assumption, we can model the dynamics of the inner and outer orbits separately. The line-of-sight velocity $v(t)$ for a distant observer located on the z axis is

$$v(t) = v_{||}\cos\left(\frac{2\pi t}{P_0} + \Phi_0\right), \tag{11.2}$$

where

$$v_{||} = \frac{m_0}{M_{\rm tot}}\frac{2\pi R\sin I}{P_0} \tag{11.3}$$

is the magnitude of the line-of-sight velocity. The initial observed phase of the outer orbit Φ_0 is equal to zero when the GW-emitting binary is traveling along the line of sight. Here and below we use geometrical units ($G = c = 1$).

Let us now consider the effect of the Doppler modulation on the gravitational waveform. We model the nonspinning, quasicircular binary waveform by expanding the phasing up to second post-Newtonian (2PN) order, including modulations due to LISA's orbital motion and effects due to the source location in the sky [511]. In the time domain, the waveform is

given by

$$h(t) = \frac{2\mathcal{M}^{5/3}}{D_L}\left[\pi f(t)\right]^{2/3} \times \frac{\sqrt{3}}{2}\bar{A}(t)\cos\Psi_0(t)\,, \tag{11.4}$$

where

$$\Psi_0(t) = 2\pi\int_0^t f(t')dt' + \varphi_p(t) + \varphi_D(t)\,, \tag{11.5}$$

$f(t)$ is the GW frequency at time t in the observer frame, and D_L is the luminosity distance of the source. Here $M = m_1 + m_2$ is the observed total mass, $\eta = m_1 m_2/M^2$ the symmetric mass ratio, and $\mathcal{M} = \eta^{3/5}M$ the chirp mass of the inner binary. The factor $\frac{\sqrt{3}}{2}$ accounts for the fact that the two independent LISA interferometer "arms" are at angles of 60°. The terms $\bar{A}(t)$, $\varphi_p(t)$, $\varphi_D(t)$ are amplitude, polarization and Doppler-phase modulations that arise from the orbital motion of LISA, respectively. They can be expressed as functions of the binary's orbital frequency f, sky location $(\bar{\theta}_S, \bar{\phi}_S)$ and orbital angular momentum direction $(\bar{\theta}_L, \bar{\phi}_L)$, where overbars denote quantities in the Solar System barycenter frame. Detailed expressions can be found in [640].

The possibility to detect cosmological effects in gravitational waveforms was discussed in great detail by [630], while the detectability of astrophysical Doppler shifts induced by planetary systems around WDWD binaries was studied by [637]. The line-of-sight velocity changes the observer-frame frequency of the source through a Doppler shift $f_O = f_S(1+v)$. This results into an additional phasing term in the waveform: $\Psi_0(t) \to \Psi_0(t) + \phi_{\rm pm}(t)$ [619, 634, 635, 636, 637], where the proper-motion modulation $\phi_{\rm pm}(t)$ is related to the velocity profile $v(t)$ of Eq. (11.2) by

$$\phi_{\rm pm}(t) = 2\pi\int_0^t v(t')f(t')dt'\,. \tag{11.6}$$

If we omit the effect of proper motion in the analysis of LISA data this phase shift will appear as a residual, which contains information on the properties of the outer orbit.

Our waveform model depends on 12 parameters, which we will denote collectively as $\boldsymbol{\theta} = \{\theta_i\}$. Nine of these parameters – i.e. $\{D_L, \mathcal{M}, \eta, t_c, \phi_c, \bar{\theta}_S, \bar{\theta}_L, \bar{\phi}_S, \bar{\phi}_L\}$, where t_c and ϕ_c are the coalescence time and phase [270], respectively – characterize the inner binary; the

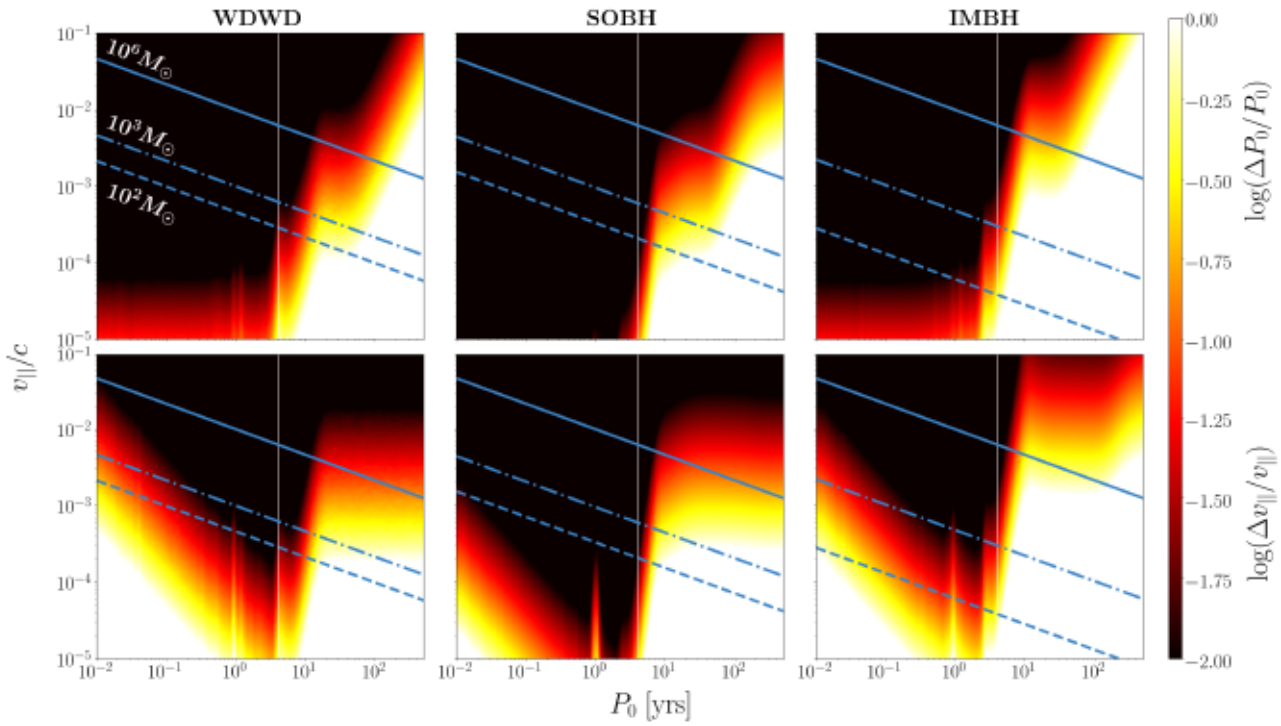

Figure 11.2: Contour plots of the logarithmic relative error in the orbital period P_0 (top row) and magnitude of the line-of-sight velocity $v_{||}$ (bottom row) in the (P_0, $v_{||}$) plane. The three columns correspond to our three chosen physical systems at fixed SNR $\rho = 10$: WDWD at 10^{-3}Hz (left), SOBH (middle) and IMBH (right). In the regions above the solid, dash-dotted and dashed lines the third body must have mass larger than 10^6 $M_\odot$, 10^3 $M_\odot$ and 10^2 $M_\odot$, respectively, to produce the observed Doppler shift. The vertical white line corresponds to the nominal LISA mission lifetime $T_{\rm obs} = 4$ yr.

remaining three parameters $\{v_{||}, P_0, \Phi_0\}$ characterize the outer orbit. Sampling the entire 12-dimensional parameter space is computationally expensive. To estimate whether the outer orbit parameters responsible for the Doppler modulation are measurable we use a Fisher matrix analysis [511]. For a source with signal-to-noise ratio (SNR) ρ, defined in terms of the LISA one-sided spectral density $S_n(f)$ as

$$\rho^2 = 2 \sum_{\alpha=I,II} \int_0^{T_{\rm obs}} dt \frac{|h_\alpha(t)|^2}{S_n(f(t))}, \tag{11.7}$$

in the large-SNR approximation the uncertainties in the source parameters are inversely proportional to ρ: $\Delta\theta^i \propto 1/\rho$. These uncertainties are given by the diagonal terms of the covariance matrix Σ: $\Delta\theta^i = \sqrt{\Sigma_{ii}}$ where $\Sigma = \Gamma^{-1}$ is the inverse of the Fisher information matrix, with elements

$$\Gamma_{ij} \equiv 2 \sum_{\alpha=I,II} \int_0^{T_{\rm obs}} dt \frac{\partial h_\alpha(t)}{\partial\theta^i} \frac{\partial h_\alpha(t)}{\partial\theta^j} \frac{1}{S_n(f(t))}. \tag{11.8}$$

Here $T_{\rm obs}$ is the observation time, and α labels the two independent LISA data channels.

11.3 Results

Sampling over the 12-dimensional parameter space is computationally expensive, so we consider three specific examples to determine typical conditions under which Doppler modulations may be detectable by LISA:

1. a 0.6–0.6 $M_\odot$ WDWD binary with a source-frame GW frequency 10^{-3} Hz;
2. a GW150914-like 36–29 $M_\odot$ SOBH binary inspiral starting 5 yr before merger;
3. a 10^3–10^3 $M_\odot$ IMBH binary inspiral starting 5 yr before merger.

All masses listed above are in the source frame. We consider an observation time $T_{\rm obs} = 4$ yr, corresponding to the nominal LISA mission lifetime [51]. We place the sources at a luminosity distance such that the two-detector LISA SNR is either $\rho = 10$ or $\rho = 100$. For convenience, these luminosity distances are listed in Table 11.1. For simplicity we set $t_c = \phi_c = 0$ and we choose the orientation parameters to be $\{\bar{\theta}_S, \bar{\theta}_L, \bar{\phi}_S, \bar{\phi}_L\} = \{\arccos(0.3), \arccos(-0.2), 5, 4\}$

Table 11.1: Luminosity distance for the three source classes considered in this paper.

ρ	WDWD	SOBH	IMBH
10	1.40 kpc	178 Mpc	5720 Mpc
100	0.140 kpc	16.9 Mpc	679 Mpc

for all three sources. We have verified that our choice of orientation parameters does not significantly affect our conclusions (it mainly affects the measurement accuracy by a rescaling of the SNR).

We sample over the outer binary parameters $v_{||}$ and P_0 within the range $v_{||}/c \in [10^{-5}, 10^{-1}]$ and $P_0 \in [10^{-2}, 500]$ yr. If $P_0 < T_{\rm obs}$ the choice of the outer initial orbital phase Φ_0 does not significantly affect the measurement, since we can measure a whole modulation cycle from the outer orbit, and therefore we set $\Phi_0 = 0$. If instead $P_0 > T_{\rm obs}$ the choice of Φ_0 can affect the uncertainties and correlations between parameters. We postpone a more detailed investigation of this regime to future work. For computational efficiency we compute parameter estimation uncertainties following the frequency-domain method of [641] for inspiralling binaries (SOBH and IMBH), while we use the time-domain procedure described in Sec. 11.2 for WDWD binaries, where the inspiral is negligible.

Figure 11.2 shows uncertainties in $v_{||}$ and P_0 as a function of the simulated $v_{||}$ and P_0. On the left of each of the panels, $P_0 < T_{\rm obs}$, and the correlation between the parameters of interest is small. In this case $f(t)$ is approximately constant, so we can pull it out of the integral in Eq. (11.6) to find

$$\phi_{\rm pm} = \frac{v_{||} P_0}{2\pi} \sin\left(\frac{2\pi t}{P_0} + \Phi_0\right). \tag{11.9}$$

Then, ignoring correlations between parameters, the fractional uncertainty on $v_{||}$ and P_0 scales as

$$\frac{\Delta v_{||}}{v_{||}} \propto \sqrt{(\Gamma^{-1})_{v_{||}v_{||}}} \frac{1}{v_{||}} \propto \frac{1}{\rho v_{||} P_0}, \tag{11.10a}$$

$$\frac{\Delta P_0}{P_0} \propto \sqrt{(\Gamma^{-1})_{P_0 P_0}} \frac{1}{P_0} \propto \frac{1}{\rho v_{||}}. \tag{11.10b}$$

This is consistent with the behavior observed in Figure 11.2. The spike in the uncertainty on $v_{||}$ occurs when $P_0 \sim 1$ yr: in this case the Doppler modulation due to the motion of the

source is hard to measure because it is degenerate with the Doppler phase from the motion of the LISA detector [cf. 638].

Just as in electromagnetic measurements based on the radial velocity method, the observed velocity profile is completely degenerate with inclination. Eq. (11.3) can be rewritten as

$$\frac{m_0 R \sin I}{M_{\rm tot}} = \frac{P_0 v_{||}}{2\pi} \,. \tag{11.11}$$

Therefore R and $\sin I$ (or m_0 and $\sin I$) cannot be measured independently from Doppler shift measurements of $v_{||}$ and P_0. For any given measurement of ($v_{||}$, P_0) we can still place a lower bound on m_0 (and a corresponding upper bound on R) by setting $\sin I = 1$. The blue lines in Figure 11.2 map the measured values of $v_{||}$ and P_0 to the minimum mass of the third body $m_0^{\rm min}$ necessary to produce the observed Doppler shift using Eq. (11.3). For example, if we measure a signal consistent with $v_{||} = 10^{-2}c$ and $P_0 = 2$ years, the third body must have mass $m_0 > m_0^{\rm min} \sim 10^3\ M_\odot$.

While in Figure 11.2 we characterized our ability to observe the binary's proper motion in terms of the observables $v_{||}$ and P_0, from an astrophysical standpoint it is more useful to use the mass of the third body m_0 and the outer orbital radius R. We can translate the results on the observability of the Doppler shift in the ($v_{||}$, P_0) plane (Figure 11.2) to criteria for the observability of the Doppler shift in the (m_0, $R \sin I$) plane, as shown in Figure 11.3. The shaded regions in this plot are not sampled in our parameter estimation survey for one of the following reasons: the period P_0 is too long ($P_0 > 500$ yr, upper-left shaded triangle), too short ($P_0 < 0.01$ yr, bottom-right), or the magnitude of the line-of-sight velocity $v_{||} > 0.1$, so that the nonrelativistic approximation becomes unreliable.

The solid and dashed lines show how close the inner binary can be to a third body of mass m_0 for the proper motion Doppler signature to be observable: below those lines, fractional uncertainties in *both* $v_{||}$ and P_0 are smaller than 10% for binary signals with SNR $\rho = 10$ (solid lines) or $\rho = 100$ (dashed lines). The "bumps" in each of the solid and dashed lines correspond to the slight plateau in the uncertainty on P_0 in the high-P_0 regime (cf. the upper row of Figure 11.2). For astrophysical purposes, it is more useful to translate these SNR values into the horizon distances listed in Table 11.1 and to keep in mind that the source SNR is inversely proportional to the luminosity distance (at least for binaries in the

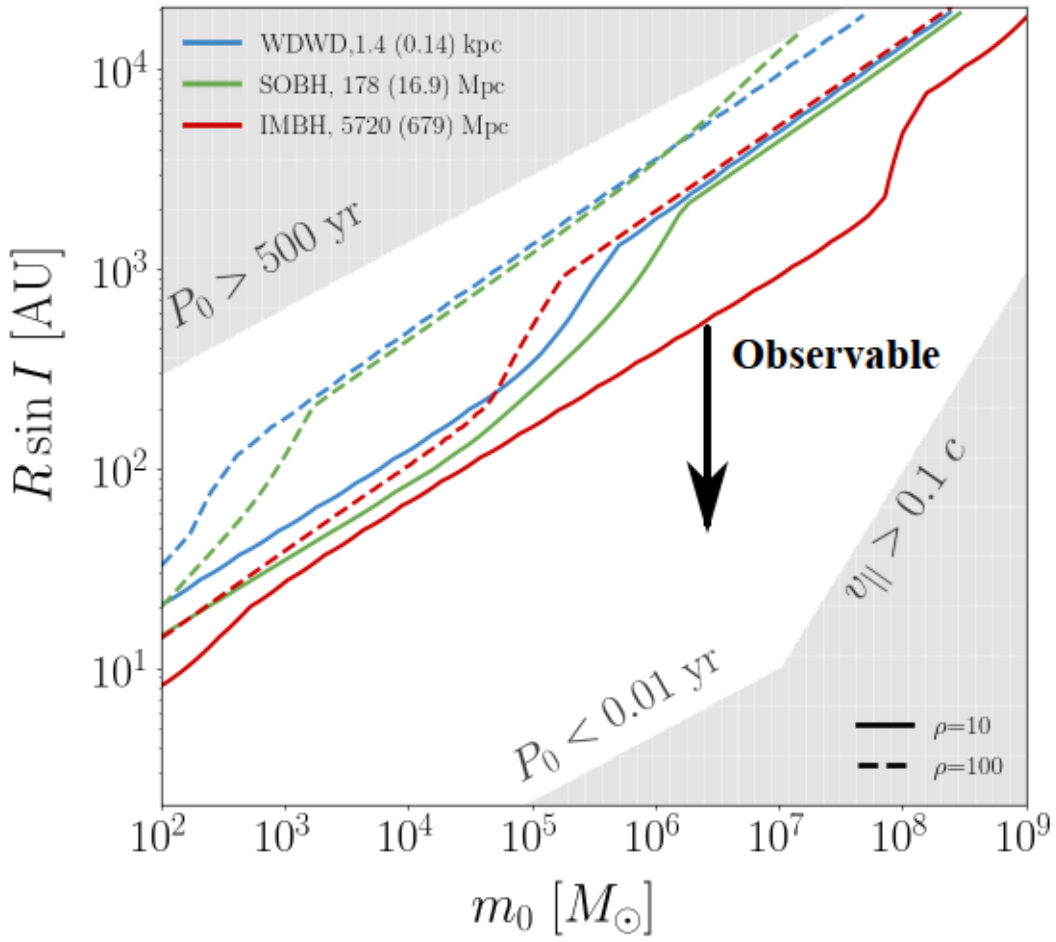

Figure 11.3: Region in the $(m_0, R\sin I)$ plane where the Doppler shift is observable: below each of the representative lines in this plot *both* P_0 and $v_{||}$ are measured to better than 10% uncertainty. The blue, green and red lines correspond to WDWD, SOBH and IMBH inner binaries, respectively. The solid lines refer to binaries that are barely detectable ($\rho = 10$); the corresponding luminosity distances are given in Table 11.1 and in the legend. The dashed lines refer to loud detections with $\rho = 100$. The shaded regions were not sampled in our parameter estimation calculations (see the text).

local universe, such as WDWDs, where cosmological effects are negligible). Recall also that for sources at distances where cosmological effects are non-negligible (SOBHs and IMBHs) the observed chirp mass of the source is redshifted to $(1+z)\mathcal{M}$ [602, 630].

While we considered a wide range of possible values for m_0 and $R\sin I$, it is clear from Table 11.1 that the three source classes are of interest in different astrophysical scenarios. WDWD systems can be detected by LISA within a few kpc, and their Doppler modulation could be used to identify IMBHs in nearby stellar clusters. SOBHs can be detected within ~ 200 Mpc, and their Doppler modulation could be used to probe the center of nearby galaxies at $z \lesssim 0.05$. IMBHs can be detected out to ~ 6 Gpc, so Doppler modulations could be used to study galaxy formation out to redshifts $z \sim 1$. Note that the horizon distance of the source has a strong dependence on the inner binary mass and sky location (which were fixed in our study for computational reasons), therefore the numbers quoted above should be considered as illustrative for each astrophysical scenario, rather than as rigorous detection limits.

11.4 Discussion

This study is a proof-of-principle investigation of the conditions under which Doppler shifts in gravitational waveforms could be measurable by LISA.

Our analysis differs in several ways from recent work by [619] and [635]. [619] carry out a Fisher matrix analysis using a six-parameter model, including chirp mass, symmetric mass ratio, distance, time and phase of coalescence and an acceleration parameter Y. They do not account for LISA's orbital motion and the source orientation, while we do. This is crucial: the measurability of Doppler effects depends on the relative magnitude of the orbital period of the source with respect to LISA's orbital period. There are features (most notably the spike in uncertainties when the period of the outer orbit is close to 1 yr) that can only be accounted for when LISA's motion is considered. Besides, ignoring degeneracies (e.g. between the inclination of the source and the chirp mass) can lead to overly optimistic parameter estimation. Another important difference is that the acceleration parameter Y used in [619] is a linear approximation of the phase shift we considered here, so their phase shift is linear in time: see e.g. their Eq. (7). This corresponds to a special case of our

analysis: the long-period regime. In this regime the correlation between the velocity of the source and the period of the outer orbit is important, but it was ignored in [619] . Besides, a measurement of their parameter Y cannot be translated into a measurement of the third body's mass and of the orbital radius of the binary R around the third body: at least one more variable is needed to get a lower bound on the mass of the third body.

[635] and [619] consider mostly SOBHs as gravitational-wave sources, while we also considered WDWD binaries and IMBH binaries. As we show in our work, the detectability of Doppler effects depends dramatically on the choice of source. Besides, both [619] and [635] focus on the acceleration effect. The values of the ϵ parameter introduced in Eq. (51) of [635] correspond to orbital periods $\gtrsim 10^4$ yr, well beyond the range considered in our study.

In this exploratory study we have made simplifying assumptions that we discuss below, and that should be relaxed in more realistic scenarios.

The assumption of a circular outer orbit can be considered conservative, because eccentricity in the outer orbit makes Doppler shifts easier to observe [636]. In general, there will be a trade-off between the detectability gain due to large variations in $v_{||}$ near pericenter and the fact that (because of Kepler's second law) it is statistically more likely to find astrophysical systems near apocenter. The distribution of the outer and inner orbital eccentricities plays an important role when computing rates of LISA events with observable Doppler shifts [520, 615, 616, 618, 634, 642, 643, 644, 645], and we plan to address this issue in future work.

We modelled the outer orbit using Newtonian dynamics. This should be sufficient for most astrophysical systems of interest: the dominant corrections to the equations of motion enter at order $(v/c)^2$, and therefore they should be mostly negligible even for $v_{||} \sim 0.1c$. Furthermore, the dominant post-Newtonian correction increases the orbital period [see e.g. 646], hence it improves the observability bounds shown in Figure 11.3 for given orbital parameters. In this sense, once again, our predictions are conservative.

In principle we can convolve the Doppler observability criteria shown in Figure 11.3 with astrophysical models to predict the number of events for which LISA will be able to observe Doppler shifts. Vice versa, we could use LISA observations of Doppler shifts (or the lack thereof) to constrain astrophysical models. A detailed discussion of the astrophysical implications of our results is beyond the scope of this paper. In the hope to stimulate

further research, we briefly discuss some astrophysical scenarios that could lead to observable Doppler shifts for the three source classes considered in this paper: WDWD, SOBH and IMBH binaries.

(i) WDWDs: WDWD systems can be detected by LISA within a few kpc, and their Doppler modulation could be used to identify IMBHs in nearby stellar clusters. There is a broad range of estimates of the number of binaries detectable by LISA in Milky Way globular clusters, with some of the latest estimates ranging from a few to tens of events [620]. The uncertainties are dominated by assumptions on cluster models, such as the binary fraction [647, 648, 649, 650] and the efficiency of different dynamical processes [651, 652, 653]. The number of WDWD events with an observable proper motion signature in LISA could be used to set constraints on these cluster models.

(ii) SOBHs: SOBHs can be detected by LISA within $\sim$ 200 Mpc, and their Doppler modulation could be used to probe the center of nearby galaxies at $z \lesssim 0.05$. The LIGO/Virgo collaboration has already detected 10 BH-BH binary mergers [232], and yet there is no consensus on the astrophysical origin of these mergers [181]. One possibility is that these compact binaries are formed in the vicinity of AGNs [see e.g. 654]. Indeed, the presence of X-ray binaries [655] and hypervelocity stars [656, 657] close to our galactic center indicates that a large number of binaries exist in galactic nuclei. Gaseous drags or three-body interactions in AGN disks can lead to very hard binaries that should coalesce within a Hubble time [380]. [383] showed that the merger rates of such binaries could be comparable to other dynamical channels. The merger process is very efficient if these binaries lie within ~ 0.1 pc, resulting in a significant fraction of mergers happening very close to the SMBH. Furthermore, compact objects embedded in AGN disks create density perturbations, resulting in torques that lead to inward migration of the compact object. Sometimes this torque changes sign, leading to the formation of migration traps at $40M - 600M$ from the central objects [658] which could act as hotbeds for the formation of BH-BH binaries. In summary, there are various scenarios that could lead to SOBH binaries merging very close to an SMBH. These systems may have detectable Doppler shifts that could serve as smoking guns for binary formation in AGNs. It is even possible that SMBH mass measurements from Doppler-shifted GWs could complement and/or improve electromagnetic estimates of the AGN mass.

Another interesting scenario was proposed by [659] and [660]. These authors proposed that

some extreme mass-ratio inspirals (EMRIs) could actually be *binary* BH systems inspiralling into a supermassive BHs. These "binary EMRIs" (or b-EMRIs) source GWs both through the motion of the inner BH-BH binary and through the inspiral of the b-EMRI. If such sources exist, the Doppler shift in the GWs from the BH-BH binary could allow us to estimate the SMBH mass. The Doppler-shift estimate of the central SMBH mass could be used as an independent check of the parameters estimated using the gravitational radiation from the b-EMRI inspiral.

(iii) IMBHs: IMBH binaries can be detected by LISA out to a few Gpc, so Doppler modulations could be used to study galaxy formation out to redshifts $z \sim 1$. Despite claims of a connection between IMBHs and ultra-luminous X-ray sources [661] and other observational evidence [662, 663, 664, 665], there is still no conclusive observational confirmation of the existence of IMBHs [see e.g. 629, for a review]. IMBH detections could bridge the gap between SOBHs and SMBHs, and help us understand how SMBH were born and grew. In some scenarios, clusters containing IMBHs sink towards the galactic nucleus through dynamical friction, and upon evaporation deposit their IMBHs near the galactic center [666]. The IMBHs then form binaries and eventually merge, forming an SMBH. Some of these IMBH binaries could end up in orbit around a more massive central object [667, 668], and orbital Doppler shifts could lead to biases in their estimated masses [669, 670]. GW detections of these systems by Earth- or space-based interferometers could provide conclusive evidence of SMBH formation through runaway IMBH collisions.

In conclusion, several astrophysical GW sources are expected to form triple systems where the main GW emission from an "inner" orbit is affected by Doppler modulations due to the "outer" orbital motion of the binary around a third body. LISA (unlike ground based detectors) may observe the radiation from the inner binary for months or years. GW searches and parameter estimation methods rely on waveform modelling, so failure to account for Doppler modulations could introduce systematics in parameter estimation and reduce the efficiency of GW searches [635]. In this paper we argued that, more interestingly, these effects may be observable, enabling GW detectors to probe weak-field astrophysical processes through the Doppler modulations of their strong-field inspiral dynamics. We investigated the conditions under which LISA may place meaningful constraints on the third body's properties, and we identified and discussed some classes of astrophysical systems of particular interest as observational targets.

We plan to extend the present research in two main directions: (i) by developing more realistic (and complex) possibilities for the orbital motion and GW emission of the triples, and (ii) by using astrophysical models to identify the most promising astrophysical systems that could lead to LISA detections of Doppler modulations.

Bibliography

[1] A. Akmal, V. R. Pandharipande, and D. G. Ravenhall. The Equation of state of nucleon matter and neutron star structure. *Phys. Rev.*, C58:1804–1828, 1998.

[2] Mark Alford, Matt Braby, M. W. Paris, and Sanjay Reddy. Hybrid stars that masquerade as neutron stars. *Astrophys. J.*, 629:969–978, 2005.

[3] Gaia Collaboration. VizieR Online Data Catalog: Gaia DR2 (Gaia Collaboration, 2018). *VizieR Online Data Catalog*, page I/345, April 2018.

[4] T. Kupfer, D. Steeghs, P. J. Groot, T. R. Marsh, G. Nelemans, and G. H. A. Roelofs. UVES and X-Shooter spectroscopy of the emission line AM CVn systems GP Com and V396 Hya. MNRAS, 457(2):1828–1841, April 2016.

[5] Juan V. Hernández Santisteban, Christian Knigge, Stuart P. Littlefair, Rene P. Breton, Vikram S. Dhillon, Boris T. Gänsicke, Thomas R. Marsh, Magaretha L. Pretorius, John Southworth, and Peter H. Hauschildt. An irradiated brown-dwarf companion to an accreting white dwarf. Nature, 533(7603):366–368, May 2016.

[6] J. V. Cunha, F. E. Silva, and J. A. S. Lima. Gravitational waves from ultra-short period exoplanets. MNRAS, 480(1):L28–L32, October 2018.

[7] Shane L. Larson, William A. Hiscock, and Ronald W. Hellings. Sensitivity curves for

spaceborne gravitational wave interferometers. PRD, 62(6):062001, September 2000.

[8] Travis Robson, Neil J. Cornish, and Chang Liu. The construction and use of LISA sensitivity curves. *Classical and Quantum Gravity*, 36(10):105011, May 2019.

[9] B. P. Abbott et al. GWTC-1: A Gravitational-Wave Transient Catalog of Compact Binary Mergers Observed by LIGO and Virgo during the First and Second Observing Runs. *Physical Review X*, 9(3):031040, November 2018.

[10] F. Douchin and P. Haensel. A unified equation of state of dense matter and neutron star structure. *Astron. Astrophys.*, 380:151, 2001.

[11] H. Müther, M. Prakash, and T. L. Ainsworth. The nuclear symmetry energy in relativistic Brueckner-Hartree-Fock calculations. *Physics Letters B*, 199(4):469–474, December 1987.

[12] Benjamin D. Lackey, Mohit Nayyar, and Benjamin J. Owen. Observational constraints on hyperons in neutron stars. *Phys. Rev.*, D73:024021, 2006.

[13] B. P. Abbott et al. GW170817: Measurements of neutron star radii and equation of state. *Phys. Rev. Lett.*, 121(16):161101, 2018.

[14] Francesco Pannarale, Emanuele Berti, Koutarou Kyutoku, Benjamin D. Lackey, and Masaru Shibata. Gravitational-wave cutoff frequencies of tidally disruptive neutron star-black hole binary mergers. *Phys. Rev. D*, 92(8):081504, 2015.

[15] R. Abbott et al. Population Properties of Compact Objects from the Second LIGO-Virgo Gravitational-Wave Transient Catalog. 10 2020.

[16] Charles W. Misner, K. S. Thorne, and J. A. Wheeler. *Gravitation*. W. H. Freeman, San Francisco, 1973.

[17] E. Poisson and C.M. Will. *Gravity: Newtonian, Post-Newtonian, Relativistic.* Cambridge University Press, 2014.

[18] J.B. Hartle. *Gravity: An Introduction to Einstein's General Relativity.* Addison-Wesley, 2003.

[19] Michele Maggiore. *Gravitational Waves. Vol. 1: Theory and Experiments.* Oxford Master Series in Physics. Oxford University Press, 2007.

[20] Michele Maggiore. *Gravitational Waves. Vol. 2: Astrophysics and Cosmology.* Oxford University Press, 3 2018.

[21] B. P. Abbott et al. Observation of Gravitational Waves from a Binary Black Hole Merger. *Phys. Rev. Lett.*, 116(6):061102, 2016.

[22] J. Needham. *Science and Civilisation in China: Volume 3, Mathematics and the Sciences of the Heavens and the Earth.* Science and Civilisation in China. Cambridge University Press, 1959.

[23] Stillman Drake. *Galileo: Pioneer Scientist.* University of Toronto Press, 1990.

[24] Ray W. Klebesadel, Ian B. Strong, and Roy A. Olson. Observations of Gamma-Ray Bursts of Cosmic Origin. ApJ, 182:L85, June 1973.

[25] G. F. Smoot, C. L. Bennett, A. Kogut, E. L. Wright, J. Aymon, N. W. Boggess, E. S. Cheng, G. de Amici, S. Gulkis, M. G. Hauser, G. Hinshaw, P. D. Jackson, M. Janssen, E. Kaita, T. Kelsall, P. Keegstra, C. Lineweaver, K. Loewenstein, P. Lubin, J. Mather, S. S. Meyer, S. H. Moseley, T. Murdock, L. Rokke, R. F. Silverberg, L. Tenorio, R. Weiss, and D. T. Wilkinson. Structure in the COBE Differential Microwave Radiometer First-Year Maps. ApJ, 396:L1, September 1992.

[26] C. L. Bennett, A. Banday, K. M. Gorski, G. Hinshaw, P. Jackson, P. Keegstra, A. Kogut, George F. Smoot, D. T. Wilkinson, and E. L. Wright. Four year COBE DMR cosmic microwave background observations: Maps and basic results. *Astrophys. J. Lett.*, 464:L1–L4, 1996.

[27] B. P. Abbott, R. Abbott, T. D. Abbott, M. R. Abernathy, F. Acernese, K. Ackley, C. Adams, T. Adams, P. Addesso, R. X. Adhikari, and et al. Tests of General Relativity with GW150914. *Physical Review Letters*, 116(22):221101, June 2016.

[28] B. P. Abbott et al. GW170817: Observation of Gravitational Waves from a Binary Neutron Star Inspiral. *Phys. Rev. Lett.*, 119(16):161101, 2017.

[29] B.P. Abbott et al. Multi-messenger Observations of a Binary Neutron Star Merger. *Astrophys. J. Lett.*, 848(2):L12, 2017.

[30] B.P. Abbott et al. Gravitational Waves and Gamma-rays from a Binary Neutron Star Merger: GW170817 and GRB 170817A. *Astrophys. J.*, 848(2):L13, 2017.

[31] R. Abbott et al. GWTC-2: Compact Binary Coalescences Observed by LIGO and Virgo During the First Half of the Third Observing Run. 10 2020.

[32] R. Abbott et al. GW190521: A Binary Black Hole Merger with a Total Mass of 150 $M_{\odot}$. *Phys. Rev. Lett.*, 125(10):101102, 2020.

[33] R. Abbott et al. GW190814: Gravitational Waves from the Coalescence of a 23 Solar Mass Black Hole with a 2.6 Solar Mass Compact Object. *Astrophys. J. Lett.*, 896(2):L44, 2020.

[34] T. Akutsu et al. KAGRA: 2.5 Generation Interferometric Gravitational Wave Detector. *Nature Astron.*, 3(1):35–40, 2019.

[35] C. S. Unnikrishnan. IndIGO and LIGO-India: Scope and plans for gravitational wave research and precision metrology in India. *Int. J. Mod. Phys. D*, 22:1341010, 2013.

[36] David Shoemaker. Gravitational wave astronomy with LIGO and similar detectors in the next decade. 4 2019.

[37] B. P. Abbott et al. Prospects for Observing and Localizing Gravitational-Wave Transients with Advanced LIGO, Advanced Virgo and KAGRA. *Living Rev. Rel.*, 21(1):3, 2018.

[38] Hiroki Takeda, Atsushi Nishizawa, Yuta Michimura, Koji Nagano, Kentaro Komori, Masaki Ando, and Kazuhiro Hayama. Polarization test of gravitational waves from compact binary coalescences. *Phys. Rev. D*, 98(2):022008, 2018.

[39] M. Punturo, M. Abernathy, F. Acernese, B. Allen, N. Andersson, K. Arun, F. Barone, B. Barr, M. Barsuglia, M. Beker, N. Beveridge, S. Birindelli, S. Bose, L. Bosi, S. Braccini, C. Bradaschia, T. Bulik, E. Calloni, G. Cella, E. Chassande Mottin, S. Chelkowski, A. Chincarini, J. Clark, E. Coccia, C. Colacino, J. Colas, A. Cumming, L. Cunningham, E. Cuoco, S. Danilishin, K. Danzmann, G. De Luca, R. De Salvo, T. Dent, R. De Rosa, L. Di Fiore, A. Di Virgilio, M. Doets, V. Fafone, P. Falferi, R. Flaminio, J. Franc, F. Frasconi, A. Freise, P. Fulda, J. Gair, G. Gemme, A. Gennai, A. Giazotto, K. Glampedakis, M. Granata, H. Grote, G. Guidi, G. Hammond, M. Hannam, J. Harms, D. Heinert, M. Hendry, I. Heng, E. Hennes, S. Hild, J. Hough, S. Husa, S. Huttner, G. Jones, F. Khalili, K. Kokeyama, K. Kokkotas, B. Krishnan, M. Lorenzini, H. Lück, E. Majorana, I. Mandel, V. Mandic, I. Martin, C. Michel, Y. Minenkov, N. Morgado, S. Mosca, B. Mours, H. Muller-Ebhardt, P. Murray, R. Nawrodt, J. Nel-

son, R. Oshaughnessy, C. D. Ott, C. Palomba, A. Paoli, G. Parguez, A. Pasqualetti, R. Passaquieti, D. Passuello, L. Pinard, R. Poggiani, P. Popolizio, M. Prato, P. Puppo, D. Rabeling, P. Rapagnani, J. Read, T. Regimbau, H. Rehbein, S. Reid, L. Rezzolla, F. Ricci, F. Richard, A. Rocchi, S. Rowan, A. Rüdiger, B. Sassolas, B. Sathyaprakash, R. Schnabel, C. Schwarz, P. Seidel, A. Sintes, K. Somiya, F. Speirits, K. Strain, S. Strigin, P. Sutton, S. Tarabrin, A. Thüring, J. van den Brand, C. van Leewen, M. van Veggel, C. van den Broeck, A. Vecchio, J. Veitch, F. Vetrano, A. Vicere, S. Vyatchanin, B. Willke, G. Woan, P. Wolfango, and K. Yamamoto. The Einstein Telescope: a third-generation gravitational wave observatory. *Classical and Quantum Gravity*, 27(19):194002, October 2010.

[40] M. Punturo et al. The Einstein Telescope: A third-generation gravitational wave observatory. *Class. Quant. Grav.*, 27:194002, 2010.

[41] B. Sathyaprakash et al. Scientific Objectives of Einstein Telescope. *Class. Quant. Grav.*, 29:124013, 2012. [Erratum: Class.Quant.Grav. 30, 079501 (2013)].

[42] Michele Maggiore et al. Science Case for the Einstein Telescope. *JCAP*, 03:050, 2020.

[43] David Reitze et al. Cosmic Explorer: The U.S. Contribution to Gravitational-Wave Astronomy beyond LIGO. *Bull. Am. Astron. Soc.*, 51:035, 7 2019.

[44] Vishal Baibhav, Emanuele Berti, Davide Gerosa, Michela Mapelli, Nicola Giacobbo, Yann Bouffanais, and Ugo N. Di Carlo. Gravitational-wave detection rates for compact binaries formed in isolation: LIGO/Virgo O3 and beyond. *Phys. Rev.*, D100(6):064060, 2019.

[45] B. P. Abbott et al. A gravitational-wave measurement of the Hubble constant following

the second observing run of Advanced LIGO and Virgo. 2019.

[46] Hsin-Yu Chen, Philip S. Cowperthwaite, Brian D. Metzger, and Edo Berger. A Program for Multimessenger Standard Siren Cosmology in the Era of LIGO A+, Rubin Observatory, and Beyond. *Astrophys. J. Lett.*, 908(1):L4, 2021.

[47] David Radice, Viktoriya Morozova, Adam Burrows, David Vartanyan, and Hiroki Nagakura. Characterizing the Gravitational Wave Signal from Core-Collapse Supernovae. *Astrophys. J. Lett.*, 876(1):L9, 2019.

[48] Ken K. Y. Ng, Kaze W. K. Wong, Tom Broadhurst, and Tjonnie G. F. Li. Precise LIGO Lensing Rate Predictions for Binary Black Holes. *Phys. Rev. D*, 97(2):023012, 2018.

[49] Salvatore Vitale and Matthew Evans. Parameter estimation for binary black holes with networks of third generation gravitational-wave detectors. *Phys. Rev. D*, 95(6):064052, 2017.

[50] Pau Amaro-Seoane, Heather Audley, Stanislav Babak, John Baker, Enrico Barausse, Peter Bender, Emanuele Berti, Pierre Binetruy, Michael Born, Daniele Bortoluzzi, Jordan Camp, Chiara Caprini, Vitor Cardoso, Monica Colpi, John Conklin, Neil Cornish, Curt Cutler, Karsten Danzmann, Rita Dolesi, Luigi Ferraioli, Valerio Ferroni, Ewan Fitzsimons, Jonathan Gair, Lluis Gesa Bote, Domenico Giardini, Ferran Gibert, Catia Grimani, Hubert Halloin, Gerhard Heinzel, Thomas Hertog, Martin Hewitson, Kelly Holley-Bockelmann, Daniel Hollington, Mauro Hueller, Henri Inchauspe, Philippe Jetzer, Nikos Karnesis, Christian Killow, Antoine Klein, Bill Klipstein, Natalia Korsakova, Shane L Larson, Jeffrey Livas, Ivan Lloro, Nary Man, Davor Mance, Joseph Martino,

Ignacio Mateos, Kirk McKenzie, Sean T McWilliams, Cole Miller, Guido Mueller, Germano Nardini, Gijs Nelemans, Miquel Nofrarias, Antoine Petiteau, Paolo Pivato, Eric Plagnol, Ed Porter, Jens Reiche, David Robertson, Norna Robertson, Elena Rossi, Giuliana Russano, Bernard Schutz, Alberto Sesana, David Shoemaker, Jacob Slutsky, Carlos F. Sopuerta, Tim Sumner, Nicola Tamanini, Ira Thorpe, Michael Troebs, Michele Vallisneri, Alberto Vecchio, Daniele Vetrugno, Stefano Vitale, Marta Volonteri, Gudrun Wanner, Harry Ward, Peter Wass, William Weber, John Ziemer, and Peter Zweifel. Laser Interferometer Space Antenna. *arXiv e-prints*, page arXiv:1702.00786, February 2017.

[51] Pau Amaro-Seoane et al. Laser Interferometer Space Antenna. *ArXiv e-prints*, 2 2017.

[52] Emanuele Berti, Vitor Cardoso, and Clifford M. Will. On gravitational-wave spectroscopy of massive black holes with the space interferometer LISA. *Phys. Rev. D*, 73:064030, 2006.

[53] Emanuele Berti, Alberto Sesana, Enrico Barausse, Vitor Cardoso, and Krzysztof Belczynski. Spectroscopy of Kerr black holes with Earth- and space-based interferometers. *Phys. Rev. Lett.*, 117(10):101102, 2016.

[54] Nicola Tamanini, Chiara Caprini, Enrico Barausse, Alberto Sesana, Antoine Klein, and Antoine Petiteau. Science with the space-based interferometer eLISA. III: Probing the expansion of the Universe using gravitational wave standard sirens. *JCAP*, 04:002, 2016.

[55] Neil Cornish and Travis Robson. Galactic binary science with the new LISA design. *J. Phys. Conf. Ser.*, 840(1):012024, 2017.

[56] Pau Amaro Seoane et al. The Gravitational Universe. 5 2013.

[57] Christopher P. L. Berry, Scott A. Hughes, Carlos F. Sopuerta, Alvin J. K. Chua, Anna Heffernan, Kelly Holley-Bockelmann, Deyan P. Mihaylov, M. Coleman Miller, and Alberto Sesana. The unique potential of extreme mass-ratio inspirals for gravitational-wave astronomy. 3 2019.

[58] Stanislav Babak, Jonathan Gair, Alberto Sesana, Enrico Barausse, Carlos F. Sopuerta, Christopher P. L. Berry, Emanuele Berti, Pau Amaro-Seoane, Antoine Petiteau, and Antoine Klein. Science with the space-based interferometer LISA. V: Extreme mass-ratio inspirals. *Phys. Rev. D*, 95(10):103012, 2017.

[59] Enrico Barausse, Vitor Cardoso, and Paolo Pani. Environmental Effects for Gravitational-wave Astrophysics. *J. Phys. Conf. Ser.*, 610(1):012044, 2015.

[60] Alvin J. K. Chua, Sonke Hee, Will J. Handley, Edward Higson, Christopher J. Moore, Jonathan R. Gair, Michael P. Hobson, and Anthony N. Lasenby. Towards a framework for testing general relativity with extreme-mass-ratio-inspiral observations. *Mon. Not. Roy. Astron. Soc.*, 478(1):28–40, 2018.

[61] T. Venumadhav, B. Zackay, J. Roulet, L. Dai, and M. Zaldarriaga. New Binary Black Hole Mergers in the Second Observing Run of Advanced LIGO and Advanced Virgo. April 2019.

[62] B. P. Abbott et al. Binary Black Hole Population Properties Inferred from the First and Second Observing Runs of Advanced LIGO and Advanced Virgo. ApJ, 882(2):L24, November 2018.

[63] I. Mandel, W. M. Farr, A. Colonna, S. Stevenson, P. Tiňo, and J. Veitch. Model-

independent inference on compact-binary observations. MNRAS, 465:3254–3260, March 2017.

[64] J. R. Hurley, C. A. Tout, and O. R. Pols. Evolution of binary stars and the effect of tides on binary populations. MNRAS, 329:897–928, February 2002.

[65] S. Stevenson, A. Vigna-Gómez, I. Mandel, J. W. Barrett, C. J. Neijssel, D. Perkins, and S. E. de Mink. Formation of the first three gravitational-wave observations through isolated binary evolution. *Nature Communications*, 8:14906, April 2017.

[66] N. Giacobbo and M. Mapelli. The progenitors of compact-object binaries: impact of metallicity, common envelope and natal kicks. MNRAS, 480:2011–2030, October 2018.

[67] Krzysztof Belczynski, Vassiliki Kalogera, Frederic A. Rasio, Ronald E. Taam, Andreas Zezas, Tomasz Bulik, Thomas J. Maccarone, and Natalia Ivanova. Compact Object Modeling with the StarTrack Population Synthesis Code. ApJS, 174(1):223–260, January 2008.

[68] B. Pattabiraman, S. Umbreit, W.-k. Liao, A. Choudhary, V. Kalogera, G. Memik, and F. A. Rasio. A Parallel Monte Carlo Code for Simulating Collisional N-body Systems. ApJS, 204:15, February 2013.

[69] M. Giersz, D. C. Heggie, J. R. Hurley, and A. Hypki. MOCCA code for star cluster simulations - II. Comparison with N-body simulations. MNRAS, 431:2184–2199, May 2013.

[70] M. Zevin, C. Pankow, C. L. Rodriguez, L. Sampson, E. Chase, V. Kalogera, and F. A. Rasio. Constraining Formation Models of Binary Black Holes with Gravitational-wave Observations. ApJ, 846:82, September 2017.

[71] S. Stevenson, C. P. L. Berry, and I. Mandel. Hierarchical analysis of gravitational-wave measurements of binary black hole spin-orbit misalignments. MNRAS, 471:2801–2811, November 2017.

[72] Davide Gerosa and Emanuele Berti. Are merging black holes born from stellar collapse or previous mergers? PRD, 95(12):124046, June 2017.

[73] Y. Bouffanais, M. Mapelli, D. Gerosa, U. N. Di Carlo, N. Giacobbo, E. Berti, and V. Baibhav. Constraining the fraction of binary black holes formed in isolation and young star clusters with gravitational-wave data. *arXiv e-prints*, May 2019.

[74] S. R. Taylor and D. Gerosa. Mining gravitational-wave catalogs to understand binary stellar evolution: A new hierarchical Bayesian framework. PRD, 98(8):083017, October 2018.

[75] D. Gerosa, E. Berti, R. O'Shaughnessy, K. Belczynski, M. Kesden, D. Wysocki, and W. Gladysz. Spin orientations of merging black holes formed from the evolution of stellar binaries. PRD, 98(8):084036, October 2018.

[76] S. Vitale, D. Gerosa, C.-J. Haster, K. Chatziioannou, and A. Zimmerman. Impact of Bayesian Priors on the Characterization of Binary Black Hole Coalescences. PRL, 119(25):251103, December 2017.

[77] Sebastian M. Gaebel, John Veitch, Thomas Dent, and Will M. Farr. Digging the population of compact binary mergers out of the noise. MNRAS, 484(3):4008–4023, April 2019.

[78] L. S. Finn and D. F. Chernoff. Observing binary inspiral in gravitational radiation: One interferometer. PRD, 47(6):2198–2219, March 1993.

[79] L. S. Finn. Binary inspiral, gravitational radiation, and cosmology. PRD, 53(6):2878–2894, March 1996.

[80] D. Gerosa. GWDET, *github.com/dgerosa/gwdet, doi.org/10.5281/zenodo.889966*, 2018.

[81] M. Hannam, P. Schmidt, A. Bohé, L. Haegel, S. Husa, F. Ohme, G. Pratten, and M. Pürrer. Simple Model of Complete Precessing Black-Hole-Binary Gravitational Waveforms. PRL, 113(15):151101, October 2014.

[82] B. P. Abbott et al. The Rate of Binary Black Hole Mergers Inferred from Advanced LIGO Observations Surrounding GW150914. ApJ, 833(1):L1, December 2016.

[83] T. J. Loredo. Accounting for Source Uncertainties in Analyses of Astronomical Survey Data. *American Institute of Physics Conference Series*, 735:195–206, November 2004.

[84] I. Mandel, W. M. Farr, and J. R. Gair. Extracting distribution parameters from multiple uncertain observations with selection biases. MNRAS, 486:1086–1093, June 2019.

[85] E. Thrane and C. Talbot. An introduction to Bayesian inference in gravitational-wave astronomy: Parameter estimation, model selection, and hierarchical models. PASA, 36:e010, March 2019.

[86] M. Fishbach, D. E. Holz, and W. M. Farr. Does the Black Hole Merger Rate Evolve with Redshift? ApJ, 863:L41, August 2018.

[87] K. A. Postnov and L. R. Yungelson. The Evolution of Compact Binary Star Systems. LRR, 17:3, May 2014.

[88] D. Gerosa, S. Ma, K. W. K. Wong, E. Berti, R. O'Shaughnessy, Y. Chen, and K. Belczynski. Multiband gravitational-wave event rates and stellar physics. PRD,

99(10):103004, May 2019.

[89] D. Gerosa and M. Kesden. precession: Dynamics of spinning black-hole binaries with python. PRD, 93(12):124066, June 2016.

[90] D. Gerosa. spops. SPOPS, *github.com/dgerosa/spops, doi.org/10.5281/zenodo.2551791*, 2019.

[91] K. Belczynski, A. Heger, W. Gladysz, A. J. Ruiter, S. Woosley, G. Wiktorowicz, H.-Y. Chen, T. Bulik, R. O'Shaughnessy, D. E. Holz, C. L. Fryer, and E. Berti. The effect of pair-instability mass loss on black-hole mergers. A&A, 594:A97, October 2016.

[92] G. Hobbs, D. R. Lorimer, A. G. Lyne, and M. Kramer. A statistical study of 233 pulsar proper motions. MNRAS, 360(3):974–992, July 2005.

[93] K. Belczynski, S. Repetto, D. E. Holz, R. O'Shaughnessy, T. Bulik, E. Berti, C. Fryer, and M. Dominik. Compact Binary Merger Rates: Comparison with LIGO/Virgo Upper Limits. ApJ, 819(2):108, March 2016.

[94] B. P. Abbott et al. Prospects for observing and localizing gravitational-wave transients with Advanced LIGO, Advanced Virgo and KAGRA. LRR, 21(1):3, April 2018.

[95] F. Pedregosa, G. Varoquaux, A. Gramfort, V. Michel, B. Thirion, O. Grisel, M. Blondel, P. Prettenhofer, R. Weiss, V. Dubourg, J. Vanderplas, A. Passos, D. Cournapeau, M. Brucher, M. Perrot, and E. Duchesnay. Scikit-learn: Machine learning in Python. *Journal of Machine Learning Research*, 12:2825–2830, 2011.

[96] Daniel Foreman-Mackey, David W. Hogg, Dustin Lang, and Jonathan Goodman. emcee: The MCMC Hammer. PASP, 125(925):306, March 2013.

[97] B. P. Abbott et al. Binary Black Hole Mergers in the First Advanced LIGO Observing

Run. PRX, 6(4):041015, October 2016. (Erratum: PRX 8, 3, 039903).

[98] M. Vallisneri, J. Kanner, R. Williams, A. Weinstein, and B. Stephens. The LIGO Open Science Center. *Journal of Physics Conference Series*, 610:012021, May 2015.

[99] S. Kullback and R. A. Leibler. On information and sufficiency. *Ann. Math. Statist.*, 22(1):79–86, 03 1951.

[100] S. Repetto, A. P. Igoshev, and G. Nelemans. The Galactic distribution of X-ray binaries and its implications for compact object formation and natal kicks. MNRAS, 467:298–310, May 2017.

[101] I. Mandel. Estimates of black hole natal kick velocities from observations of low-mass X-ray binaries. MNRAS, 456(1):578–581, February 2016.

[102] P. Atri, J. C. A. Miller-Jones, A. Bahramian, R. M. Plotkin, P. G. Jonker, G. Nelemans, T. J. Maccarone, G. R. Sivakoff, A. T. Deller, S. Chaty, M. A. P. Torres, S. Horiuchi, J. McCallum, T. Natusch, C. J. Phillips, J. Stevens, and S. Weston. Potential kick velocity distribution of black hole X-ray binaries and implications for natal kicks. MNRAS, 489:3116–3134, November 2019.

[103] R. O'Shaughnessy, D. Gerosa, and D. Wysocki. Inferences about Supernova Physics from Gravitational-Wave Measurements: GW151226 Spin Misalignment as an Indicator of Strong Black-Hole Natal Kicks. PRL, 119(1):011101, July 2017.

[104] D. Wysocki, D. Gerosa, R. O'Shaughnessy, K. Belczynski, W. Gladysz, E. Berti, M. Kesden, and D. E. Holz. Explaining LIGO's observations via isolated binary evolution with natal kicks. PRD, 97(4):043014, February 2018.

[105] C. L. Fryer, K. Belczynski, G. Wiktorowicz, M. Dominik, V. Kalogera, and D. E. Holz.

Compact Remnant Mass Function: Dependence on the Explosion Mechanism and Metallicity. ApJ, 749:91, April 2012.

[106] B. P. Abbott et al. GW151226: Observation of Gravitational Waves from a 22-Solar-Mass Binary Black Hole Coalescence. *Phys. Rev. Lett.*, 116(24):241103, 2016.

[107] Benjamin P. Abbott et al. GW170104: Observation of a 50-Solar-Mass Binary Black Hole Coalescence at Redshift 0.2. *Phys. Rev. Lett.*, 118(22):221101, 2017. [Erratum: Phys. Rev. Lett.121,no.12,129901(2018)].

[108] B. P. Abbott et al. GW170814: A Three-Detector Observation of Gravitational Waves from a Binary Black Hole Coalescence. *Phys. Rev. Lett.*, 119(14):141101, 2017.

[109] J. Aasi et al. Advanced LIGO. *Class. Quant. Grav.*, 32:074001, 2015.

[110] F. Acernese et al. Advanced Virgo: a second-generation interferometric gravitational wave detector. *Class. Quant. Grav.*, 32(2):024001, 2015.

[111] B. P. Abbott et al. Properties of the binary neutron star merger GW170817. *Phys. Rev.*, X9(1):011001, 2019.

[112] J.M. Lattimer and D.N. Schramm. Black-hole-neutron-star collisions. *Astrophys. J.*, 192:L145, 1974.

[113] Soumi De, Daniel Finstad, James M. Lattimer, Duncan A. Brown, Edo Berger, and Christopher M. Biwer. Tidal Deformabilities and Radii of Neutron Stars from the Observation of GW170817. *Phys. Rev. Lett.*, 121(9):091102, 2018. [Erratum: Phys.Rev.Lett. 121, 259902 (2018)].

[114] Benjamin P Abbott et al. Model comparison from LIGO–Virgo data on GW170817's binary components and consequences for the merger remnant. *Class. Quant. Grav.*,

37(4):045006, 2020.

[115] Philippe Landry, Reed Essick, and Katerina Chatziioannou. Nonparametric constraints on neutron star matter with existing and upcoming gravitational wave and pulsar observations. 2020.

[116] Wolfgang Kastaun and Frank Ohme. Finite tidal effects in GW170817: Observational evidence or model assumptions? *Phys. Rev. D*, 100(10):103023, 2019.

[117] B. P. Abbott et al. GW190425: Observation of a Compact Binary Coalescence with Total Mass $\sim 3.4 M_{\odot}$. 2020.

[118] Ming-Zhe Han, Shao-Peng Tang, Yi-Ming Hu, Yin-Jie Li, Jin-Liang Jiang, Zhi-Ping Jin, Yi-Zhong Fan, and Da-Ming Wei. Is GW190425 consistent with being a neutron star−black hole merger? *Astrophys. J. Lett.*, 891(1):L5, 2020.

[119] Brian D. Metzger. Kilonovae. *Living Rev. Rel.*, 20(1):3, 2017.

[120] Tanja Hinderer et al. Distinguishing the nature of comparable-mass neutron star binary systems with multimessenger observations: GW170817 case study. *Phys. Rev. D*, 100(6):06321, 2019.

[121] Michael W. Coughlin and Tim Dietrich. Can a black hole–neutron star merger explain GW170817, AT2017gfo, and GRB170817A? *Phys. Rev. D*, 100(4):043011, 2019.

[122] Daniel M. Siegel. GW170817–the first observed neutron star merger and its kilonova: implications for the astrophysical site of the r-process. *Eur. Phys. J. A*, 55(11):203, 2019.

[123] Koutarou Kyutoku, Sho Fujibayashi, Kota Hayashi, Kyohei Kawaguchi, Kenta Kiuchi, Masaru Shibata, and Masaomi Tanaka. On the Possibility of GW190425 Being a Black

Hole–Neutron Star Binary Merger. *Astrophys. J. Lett.*, 890(1):L4, 2020.

[124] Claudio Barbieri, Om Sharan Salafia, Monica Colpi, Giancarlo Ghirlanda, Albino Perego, and Alberto Colombo. Filling the Mass Gap: How Kilonova Observations can Unveil the Nature of the Compact Object Merging with the Neutron Star. *Astrophys. J. Lett.*, 887(2):L35, 2019.

[125] Francois Foucart, Tanja Hinderer, and Samaya Nissanke. Remnant baryon mass in neutron star-black hole mergers: Predictions for binary neutron star mimickers and rapidly spinning black holes. *Phys. Rev.*, D98(8):081501, 2018.

[126] Francesco Zappa, Sebastiano Bernuzzi, Francesco Pannarale, Michela Mapelli, and Nicola Giacobbo. Black-Hole Remnants from Black-Hole–Neutron-Star Mergers. *Phys. Rev. Lett.*, 123(4):041102, 2019.

[127] F. Foucart, M.D. Duez, L.E. Kidder, S. Nissanke, H.P. Pfeiffer, and M.A. Scheel. Numerical simulations of neutron star-black hole binaries in the near-equal-mass regime. *Phys. Rev. D*, 99(10):103025, 2019.

[128] Kyohei Kawaguchi, Masaru Shibata, and Masaomi Tanaka. Constraint on the ejecta mass for a black hole-neutron star merger event candidate S190814bv. 2 2020.

[129] Tanja Hinderer. Tidal Love numbers of neutron stars. *Astrophys. J.*, 677:1216–1220, 2008.

[130] Taylor Binnington and Eric Poisson. Relativistic theory of tidal Love numbers. *Phys. Rev.*, D80:084018, 2009.

[131] Thibault Damour and Alessandro Nagar. Relativistic tidal properties of neutron stars. *Phys. Rev. D*, 80:084035, 2009.

[132] Philippe Landry and Eric Poisson. Tidal deformation of a slowly rotating material body. External metric. *Phys. Rev. D*, 91:104018, 2015.

[133] Paolo Pani, Leonardo Gualtieri, Andrea Maselli, and Valeria Ferrari. Tidal deformations of a spinning compact object. *Phys. Rev. D*, 92(2):024010, 2015.

[134] Samuel E. Gralla. On the Ambiguity in Relativistic Tidal Deformability. *Class. Quant. Grav.*, 35(8):085002, 2018.

[135] Mark Hannam, Duncan A. Brown, Stephen Fairhurst, Chris L. Fryer, and Ian W. Harry. When can gravitational-wave observations distinguish between black holes and neutron stars? *Astrophys. J.*, 766:L14, 2013.

[136] Antonios Tsokaros, Milton Ruiz, Stuart L. Shapiro, Lunan Sun, and Kōji Uryū. Great Impostors: Extremely Compact, Merging Binary Neutron Stars in the Mass Gap Posing as Binary Black Holes. *Phys. Rev. Lett.*, 124(7):071101, 2020.

[137] Katerina Chatziioannou, Carl-Johan Haster, and Aaron Zimmerman. Measuring the neutron star tidal deformability with equation-of-state-independent relations and gravitational waves. *Phys. Rev.*, D97(10):104036, 2018.

[138] Huan Yang, William E. East, and Luis Lehner. Can we distinguish low mass black holes in neutron star binaries? *Astrophys. J.*, 856(2):110, 2018. [Erratum: Astrophys. J.870,no.2,139(2019)].

[139] Hsin-Yu Chen and Katerina Chatziioannou. Distinguishing binary neutron star from neutron star-black hole mergers with gravitational waves. 2019.

[140] Sophia Han and Andrew W. Steiner. Tidal deformability with sharp phase transitions in (binary) neutron stars. *Phys. Rev. D*, 99(8):083014, 2019.

[141] Hsin-Yu Chen, Paul M. Chesler, and Abraham Loeb. Searching for exotic cores with binary neutron star inspirals. *Astrophys. J.*, 893(1):L4, 2020.

[142] An Chen, Nathan K. Johnson-McDaniel, Tim Dietrich, and Reetika Dudi. Distinguishing high-mass binary neutron stars from binary black holes with second- and third-generation gravitational wave observatories. 1 2020.

[143] Sayak Datta, Khun Sang Phukon, and Sukanta Bose. Recognizing black holes in gravitational-wave observations: Telling apart impostors in mass-gap binaries. 4 2020.

[144] Hector O. Silva, Hajime Sotani, and Emanuele Berti. Low-mass neutron stars: universal relations, the nuclear symmetry energy and gravitational radiation. *Mon. Not. Roy. Astron. Soc.*, 459(4):4378–4388, 2016.

[145] Yudai Suwa, Takashi Yoshida, Masaru Shibata, Hideyuki Umeda, and Koh Takahashi. On the minimum mass of neutron stars. *Mon. Not. Roy. Astron. Soc.*, 481(3):3305–3312, 2018.

[146] H. Thankful Cromartie et al. Relativistic Shapiro delay measurements of an extremely massive millisecond pulsar. *Nat. Astron.*, 4(1):72–76, 2019.

[147] John Antoniadis, Thomas M. Tauris, Feryal Ozel, Ewan Barr, David J. Champion, and Paulo C. C. Freire. The millisecond pulsar mass distribution: Evidence for bimodality and constraints on the maximum neutron star mass. 2016.

[148] Justin Alsing, Hector O. Silva, and Emanuele Berti. Evidence for a maximum mass cut-off in the neutron star mass distribution and constraints on the equation of state. *Monthly Notices of the RAS*, 478(1):1377–1391, July 2018.

[149] Vassiliki Kalogera and Gordon Baym. The maximum mass of a neutron star. *Astrophys.*

J., 470:L61–L64, 1996.

[150] I. Bombaci. The maximum mass of a neutron star. *Astronomy and Astrophysics*, 305:871, January 1996.

[151] G. Srinivasan. The maximum mass of neutron stars. *Bulletin of the Astronomical Society of India*, 30:523–547, September 2002.

[152] N. Chamel, P. Haensel, J. L. Zdunik, and A. F. Fantina. On the Maximum Mass of Neutron Stars. *Int. J. Mod. Phys.*, E22:1330018, 2013.

[153] Masaru Shibata, Enping Zhou, Kenta Kiuchi, and Sho Fujibayashi. Constraint on the maximum mass of neutron stars using GW170817 event. PRD, 100(2):023015, July 2019.

[154] Luciano Rezzolla, Elias R. Most, and Lukas R. Weih. Using gravitational-wave observations and quasi-universal relations to constrain the maximum mass of neutron stars. *Astrophys. J.*, 852(2):L25, 2018. [Astrophys. J. Lett.852,L25(2018)].

[155] Shunke Ai, He Gao, and Bing Zhang. What constraints on the neutron star maximum mass can one pose from GW170817 observations? 2019.

[156] Paulo Cesar Carvalho Freire, Scott M. Ransom, Steve Begin, Ingrid H. Stairs, Jason W.T. Hessels, Lucille H. Frey, and Fernando Camilo. Eight New Millisecond Pulsars in NGC 6440 and NGC 6441. *Astrophys. J.*, 675:670, 2008.

[157] Clifford E. Rhoades, Jr. and Remo Ruffini. Maximum mass of a neutron star. *Phys. Rev. Lett.*, 32:324–327, 1974.

[158] T.M. Tauris et al. Formation of Double Neutron Star Systems. *Astrophys. J.*, 846(2):170, 2017.

[159] Jeff J. Andrews and Ilya Mandel. Double Neutron Star Populations and Formation Channels. *Astrophys. J.*, 880(1):L8, 2019.

[160] Alejandro Vigna-Gómez, Morgan MacLeod, Coenraad J. Neijssel, Floor S. Broekgaarden, Stephen Justham, George Howitt, Selma E. de Mink, and Ilya Mandel. Common-Envelope Episodes that lead to Double Neutron Star formation. 2020.

[161] Nicholas Farrow, Xing-Jiang Zhu, and Eric Thrane. The mass distribution of Galactic double neutron stars. *Astrophys. J.*, 876(1):18, 2019.

[162] Benjamin P Abbott et al. Exploring the Sensitivity of Next Generation Gravitational Wave Detectors. *Class. Quant. Grav.*, 34(4):044001, 2017.

[163] Isobel M. Romero-Shaw, Nicholas Farrow, Simon Stevenson, Eric Thrane, and Xing-Jiang Zhu. On the origin of GW190425. 2020.

[164] Stephen Hawking. Gravitationally collapsed objects of very low mass. *Mon. Not. Roy. Astron. Soc.*, 152:75, 1971.

[165] Bernard J. Carr and S. W. Hawking. Black holes in the early Universe. *Mon. Not. Roy. Astron. Soc.*, 168:399–415, 1974.

[166] Anne M. Green. Primordial Black Holes: sirens of the early Universe. *Fundam. Theor. Phys.*, 178:129–149, 2015.

[167] Rong-Gen Cai and Shao-Jiang Wang. Mass bound for primordial black hole from trans-Planckian censorship conjecture. *Phys. Rev.*, D101(4):043508, 2020.

[168] Albert Escrivà, Cristiano Germani, and Ravi K. Sheth. A universal threshold for primordial black hole formation. 2019.

[169] Andrew D. Gow, Christian T. Byrnes, Alex Hall, and John A. Peacock. Primordial

black hole merger rates: distributions for multiple LIGO observables. *JCAP*, 01(01):031, 2020.

[170] V. De Luca, G. Franciolini, and A. Riotto. On the Primordial Black Hole Mass Function for Broad Spectra. *Phys. Lett.*, B807:135550, 2020.

[171] Sam Young and Marcello Musso. Application of peaks theory to the abundance of primordial black holes. 2020.

[172] Jiong Lin, Qing Gao, Yungui Gong, Yizhou Lu, Chao Zhang, and Fengge Zhang. Primordial black holes and secondary gravitational waves from k/G inflation. 2020.

[173] Lang Liu, Zong-Kuan Guo, Rong-Gen Cai, and Sang Pyo Kim. Merger rate distribution of primordial black hole binaries with electric charges. 2020.

[174] Marco Roncadelli, Aldo Treves, and Roberto Turolla. Primordial black holes are again on the limelight. 1 2009.

[175] Misao Sasaki, Teruaki Suyama, Takahiro Tanaka, and Shuichiro Yokoyama. Primordial black holes—perspectives in gravitational wave astronomy. *Class. Quant. Grav.*, 35(6):063001, 2018.

[176] Martti Raidal, Christian Spethmann, Ville Vaskonen, and Hardi Veermäe. Formation and Evolution of Primordial Black Hole Binaries in the Early Universe. *JCAP*, 02:018, 2019.

[177] A. Albert et al. Constraining the Local Burst Rate Density of Primordial Black Holes with HAWC. 2019.

[178] Mark P. Hertzberg, Enrico D. Schiappacasse, and Tsutomu T. Yanagida. Axion Stars Nucleation in Dark Mini-Halos around Primordial Black Holes. 2020.

[179] V. De Luca, G. Franciolini, P. Pani, and A. Riotto. Constraints on Primordial Black Holes: the Importance of Accretion. *Phys. Rev. D*, 102(4):043505, 2020.

[180] Bernard Carr, Kazunori Kohri, Yuuiti Sendouda, and Jun'ichi Yokoyama. Constraints on Primordial Black Holes. 2 2020.

[181] B. P. Abbott et al. GWTC-1: A Gravitational-Wave Transient Catalog of Compact Binary Mergers Observed by LIGO and Virgo during the First and Second Observing Runs. *Phys. Rev.*, X9(3):031040, 2019.

[182] B. P. Abbott et al. Binary Black Hole Mergers in the first Advanced LIGO Observing Run. *Phys. Rev.*, X6(4):041015, 2016. [erratum: Phys. Rev.X8,no.3,039903(2018)].

[183] G. Raaijmakers et al. A NICER view of PSR J0030+0451: Implications for the dense matter equation of state. *Astrophys. J. Lett.*, 887:L22, 2019.

[184] Thomas E. Riley et al. A NICER View of PSR J0030+0451: Millisecond Pulsar Parameter Estimation. *Astrophys. J. Lett.*, 887:L21, 2019.

[185] M. C. Miller et al. PSR J0030+0451 Mass and Radius from NICER Data and Implications for the Properties of Neutron Star Matter. *Astrophys. J. Lett.*, 887:L24, 2019.

[186] Slavko Bogdanov et al. Constraining the Neutron Star Mass-Radius Relation and Dense Matter Equation of State with NICER. I. The Millisecond Pulsar X-ray Data Set. *Astrophys. J. Lett.*, 887(1):L25, 2019.

[187] Slavko Bogdanov et al. Constraining the Neutron Star Mass-Radius Relation and Dense Matter Equation of State with NICER. II. Emission from Hot Spots on a Rapidly Rotating Neutron Star. *Astrophys. J.*, 887(1):L26, 2019.

[188] Tanja Hinderer, Luciano Rezzolla, and Luca Baiotti. *Gravitational Waves from Merging Binary Neutron-Star Systems*, volume 457, pages 575–635. 2018.

[189] Eric Poisson. Tidal deformation of a slowly rotating black hole. *Phys. Rev.*, D91(4):044004, 2015.

[190] Stephen R. Taylor and Davide Gerosa. Mining Gravitational-wave Catalogs To Understand Binary Stellar Evolution: A New Hierarchical Bayesian Framework. *Phys. Rev.*, D98(8):083017, 2018.

[191] Kaze W. K. Wong and Davide Gerosa. Machine-learning interpolation of population-synthesis simulations to interpret gravitational-wave observations: a case study. *Phys. Rev.*, D100(8):083015, 2019.

[192] Kaze W.K. Wong, Gabriella Contardo, and Shirley Ho. Gravitational wave population inference with deep flow-based generative network. *Phys. Rev. D*, 101(12):123005, 2020.

[193] Matthew Pitkin, Stuart Reid, Sheila Rowan, and James Hough. Gravitational Wave Detection by Interferometry (Ground and Space). *Living Reviews in Relativity*, 14(1):5, July 2011.

[194] B. S. Sathyaprakash et al. Multimessenger Universe with Gravitational Waves from Binaries. 2019.

[195] Gregory Ashton, Moritz Hübner, Paul D. Lasky, Colm Talbot, Kendall Ackley, Sylvia Biscoveanu, Qi Chu, Atul Divarkala, Paul J. Easter, Boris Goncharov, Francisco Hernandez Vivanco, Jan Harms, Marcus E. Lower, Grant D. Meadors, Denyz Melchor, Ethan Payne, Matthew D. Pitkin, Jade Powell, Nikhil Sarin, Rory J. E. Smith, and

Eric Thrane. Bilby: Bayesian inference library, January 2019.

[196] Greg Ashton, Moritz Hübner, Paul Lasky, and Colm Talbot. Bilby: A User-Friendly Bayesian Inference Library, March 2019.

[197] Gregory Ashton et al. BILBY: A user-friendly Bayesian inference library for gravitational-wave astronomy. *Astrophys. J. Suppl.*, 241(2):27, 2019.

[198] Tim Dietrich et al. Matter imprints in waveform models for neutron star binaries: Tidal and self-spin effects. *Phys. Rev. D*, 99(2):024029, 2019.

[199] Tim Dietrich, Anuradha Samajdar, Sebastian Khan, Nathan K. Johnson-McDaniel, Reetika Dudi, and Wolfgang Tichy. Improving the NRTidal model for binary neutron star systems. *Phys. Rev.*, D100(4):044003, 2019.

[200] Francesco Pannarale, Emanuele Berti, Koutarou Kyutoku, and Masaru Shibata. Non-spinning black hole-neutron star mergers: a model for the amplitude of gravitational waveforms. *Phys. Rev. D*, 88(8):084011, 2013.

[201] Francesco Pannarale, Emanuele Berti, Koutarou Kyutoku, Benjamin D. Lackey, and Masaru Shibata. Aligned spin neutron star-black hole mergers: a gravitational waveform amplitude model. *Phys. Rev. D*, 92(8):084050, 2015.

[202] Christian Jürgen Krüger and Francois Foucart. Estimates for Disk and Ejecta Masses Produced in Compact Binary Mergers. *Phys. Rev. D*, 101(10):103002, 2020.

[203] Jonathan E. Thompson, Edward Fauchon-Jones, Sebastian Khan, Elisa Nitoglia, Francesco Pannarale, Tim Dietrich, and Mark Hannam. Modeling the gravitational wave signature of neutron star black hole coalescences: PhenomNSBH. 2 2020.

[204] V. Ferrari, L. Gualtieri, and F. Pannarale. Neutron star tidal disruption in mixed

binaries: the imprint of the equation of state. *Phys. Rev. D*, 81:064026, 2010.

[205] Andrea Maselli, Leonardo Gualtieri, and Valeria Ferrari. Constraining the equation of state of nuclear matter with gravitational wave observations: Tidal deformability and tidal disruption. *Phys. Rev. D*, 88(10):104040, 2013.

[206] M. Coleman Miller and Jon M. Miller. The Masses and Spins of Neutron Stars and Stellar-Mass Black Holes. *Phys. Rept.*, 548:1–34, 2014.

[207] Vishal Baibhav, Davide Gerosa, Emanuele Berti, Kaze W. K. Wong, Thomas Helfer, and Matthew Mould. The mass gap, the spin gap, and the origin of merging binary black holes. *Phys. Rev.*, D102(4):043002, 2020.

[208] V. De Luca, G. Franciolini, P. Pani, and A. Riotto. The Evolution of Primordial Black Holes and their Final Observable Spins. *JCAP*, 04:052, 2020.

[209] Thierry Mora and Clifford M. Will. A PostNewtonian diagnostic of quasiequilibrium binary configurations of compact objects. *Phys. Rev.*, D69:104021, 2004. [Erratum: Phys. Rev.D71,129901(2005)].

[210] Steven B. Giddings and Michelangelo L. Mangano. Astrophysical implications of hypothetical stable TeV-scale black holes. *Phys. Rev. D*, 78:035009, 2008.

[211] William E. East and Luis Lehner. Fate of a neutron star with an endoparasitic black hole and implications for dark matter. *Phys. Rev. D*, 100(12):124026, 2019.

[212] W. R. Gilks, S. Richardson, and D. J. Spiegelhalter. *Markov Chain Monte Carlo in Practice*. Chapman & Hall, London, UK, 1996.

[213] K. Belczynski, G. Wiktorowicz, C. Fryer, D. Holz, and V. Kalogera. Missing Black Holes Unveil The Supernova Explosion Mechanism. *Astrophys. J.*, 757:91, 2012.

[214] T. Nakamura. General Relativistic Collapse of Accreting Neutron Stars with Rotation. *Progress of Theoretical Physics*, 70(4):1144–1147, October 1983.

[215] Mario Vietri and Luigi Stella. Supranova events from spun-up neutron stars: an explosion in search of an observation. *Astrophys. J.*, 527:L43–L46, 1999.

[216] Andrew I. MacFadyen, Enrico Ramirez-Ruiz, and Weiqun Zhang. X-ray flares following short gamma-ray bursts from shock heating of binary stellar companions. 2005.

[217] Charles D. Dermer and Armen Atoyan. Collapse of neutron stars to black holes in binary systems: a model for short gamma ray bursts. *Astrophys. J.*, 643:L13–L16, 2006.

[218] Maya Fishbach, Daniel E. Holz, and Ben Farr. Are LIGO's Black Holes Made From Smaller Black Holes? *Astrophys. J.*, 840(2):L24, 2017.

[219] Davide Gerosa and Emanuele Berti. Are merging black holes born from stellar collapse or previous mergers? *Phys. Rev.*, D95(12):124046, 2017.

[220] Fabio Antonini and Frederic A. Rasio. Merging black hole binaries in galactic nuclei: implications for advanced-LIGO detections. *Astrophys. J.*, 831(2):187, 2016.

[221] Anuradha Gupta, Davide Gerosa, K. G. Arun, Emanuele Berti, Will Farr, and B. S. Sathyaprakash. Black holes in the low mass gap: Implications for gravitational wave observations. 2019.

[222] Claire S. Ye, Wen-fai Fong, Kyle Kremer, Carl L. Rodriguez, Sourav Chatterjee, Giacomo Fragione, and Frederic A. Rasio. On the Rate of Neutron Star Binary Mergers from Globular Clusters. *Astrophys. J.*, 888(1):L10, 2020.

[223] Giacomo Fragione, Abraham Loeb, and Frederic A. Rasio. Merging Black Holes in the

Low-mass and High-mass Gaps from 2+2 Quadruple Systems. 2020.

[224] William E. East, Frans Pretorius, and Branson C. Stephens. Eccentric black hole-neutron star mergers: effects of black hole spin and equation of state. *Phys. Rev. D*, 85:124009, 2012.

[225] Fabio Capela, Maxim Pshirkov, and Peter Tinyakov. Constraints on primordial black holes as dark matter candidates from capture by neutron stars. *Phys. Rev.*, D87(12):123524, 2013.

[226] George M. Fuller, Alexander Kusenko, and Volodymyr Takhistov. Primordial Black Holes and r-Process Nucleosynthesis. *Phys. Rev. Lett.*, 119(6):061101, 2017.

[227] I. Goldman and S. Nussinov. Weakly Interacting Massive Particles and Neutron Stars. *Phys. Rev.*, D40:3221–3230, 1989.

[228] Joseph Bramante and Tim Linden. Detecting Dark Matter with Imploding Pulsars in the Galactic Center. *Phys. Rev. Lett.*, 113(19):191301, 2014.

[229] Joseph Bramante, Tim Linden, and Yu-Dai Tsai. Searching for dark matter with neutron star mergers and quiet kilonovae. *Phys. Rev.*, D97(5):055016, 2018.

[230] Michele Vallisneri. Prospects for gravitational wave observations of neutron star tidal disruption in neutron star / black hole binaries. *Phys. Rev. Lett.*, 84:3519, 2000.

[231] `https://dcc.ligo.org/ligo-T1800133/public`.

[232] B. P. Abbott et al. Binary Black Hole Population Properties Inferred from the First and Second Observing Runs of Advanced LIGO and Advanced Virgo. *Astrophys. J.*, 882(2):L24, 2019.

[233] B. P. Abbott et al. Tests of General Relativity with the Binary Black Hole Signals

from the LIGO-Virgo Catalog GWTC-1. *Phys. Rev.*, D100(10):104036, 2019.

[234] Salvatore Vitale, Ryan Lynch, Riccardo Sturani, and Philip Graff. Use of gravitational waves to probe the formation channels of compact binaries. *Class. Quant. Grav.*, 34(3):03LT01, 2017.

[235] Will M. Farr, Simon Stevenson, M. Coleman Miller, Ilya Mandel, Ben Farr, and Alberto Vecchio. Distinguishing Spin-Aligned and Isotropic Black Hole Populations With Gravitational Waves. *Nature*, 548:426, 2017.

[236] Davide Gerosa and Emanuele Berti. Are merging black holes born from stellar collapse or previous mergers? *Phys. Rev.*, D95(12):124046, 2017.

[237] Marcus E. Lower, Eric Thrane, Paul D. Lasky, and Rory Smith. Measuring eccentricity in binary black hole inspirals with gravitational waves. *Phys. Rev.*, D98(8):083028, 2018.

[238] Maya Fishbach and Daniel E. Holz. Where Are LIGO's Big Black Holes? *Astrophys. J.*, 851(2):L25, 2017.

[239] Daniel Wysocki, Davide Gerosa, Richard O'Shaughnessy, Krzysztof Belczynski, Wojciech Gladysz, Emanuele Berti, Michael Kesden, and Daniel E. Holz. Explaining LIGO's observations via isolated binary evolution with natal kicks. *Phys. Rev.*, D97(4):043014, 2018.

[240] Javier Roulet and Matias Zaldarriaga. Constraints on binary black hole populations from LIGO–Virgo detections. *Mon. Not. Roy. Astron. Soc.*, 484(3):4216–4229, 2019.

[241] Colm Talbot and Eric Thrane. Measuring the binary black hole mass spectrum with an astrophysically motivated parameterization. *Astrophys. J.*, 856(2):173, 2018.

[242] Daniel Wysocki, Jacob Lange, and Richard O'Shaughnessy. Reconstructing phenomenological distributions of compact binaries via gravitational wave observations. *Phys. Rev.*, D100(4):043012, 2019.

[243] Krzysztof Belczynski, Michal Dominik, Tomasz Bulik, Richard O'Shaughnessy, Chris Fryer, and Daniel E. Holz. The effect of metallicity on the detection prospects for gravitational waves. *The Astrophysical Journal*, 715(2):L138–L141, May 2010.

[244] Carl L. Rodriguez, Michael Zevin, Pau Amaro-Seoane, Sourav Chatterjee, Kyle Kremer, Frederic A. Rasio, and Claire S. Ye. Black holes: The next generation—repeated mergers in dense star clusters and their gravitational-wave properties. *Phys. Rev.*, D100(4):043027, 2019.

[245] Simon Stevenson, Alejandro Vigna-Gómez, Ilya Mandel, Jim W. Barrett, Coenraad J. Neijssel, David Perkins, and Selma E. de Mink. Formation of the first three gravitational-wave observations through isolated binary evolution. 2017. [Nature Commun.8,14906(2017)].

[246] Michael Zevin, Chris Pankow, Carl L. Rodriguez, Laura Sampson, Eve Chase, Vassiliki Kalogera, and Frederic A. Rasio. Constraining Formation Models of Binary Black Holes with Gravitational-Wave Observations. *Astrophys. J.*, 846(1):82, 2017.

[247] Xingjiang Zhu, Eric Thrane, Stefan Oslowski, Yuri Levin, and Paul D. Lasky. Inferring the population properties of binary neutron stars with gravitational-wave measurements of spin. *Phys. Rev.*, D98:043002, 2018.

[248] Alex Krizhevsky, Ilya Sutskever, and Geoffrey Hinton. Imagenet classification with deep convolutional neural networks. *Neural Information Processing Systems*, 25, 01

2012.

[249] Ian J. Goodfellow, Jean Pouget-Abadie, Mehdi Mirza, Bing Xu, David Warde-Farley, Sherjil Ozair, Aaron Courville, and Yoshua Bengio. Generative Adversarial Networks. *arXiv e-prints*, page arXiv:1406.2661, June 2014.

[250] J. Nickolls. Scalable parallel programming with cuda introduction. In *2008 IEEE Hot Chips 20 Symposium (HCS)*, pages 1–9, August 2008.

[251] Norman P. Jouppi, Cliff Young, Nishant Patil, David Patterson, Gaurav Agrawal, Raminder Bajwa, Sarah Bates, Suresh Bhatia, Nan Boden, Al Borchers, Rick Boyle, Pierre-luc Cantin, Clifford Chao, Chris Clark, Jeremy Coriell, Mike Daley, Matt Dau, Jeffrey Dean, Ben Gelb, Tara Vazir Ghaemmaghami, Rajendra Gottipati, William Gulland , Robert Hagmann, C. Richard Ho, Doug Hogberg, John Hu, Robert Hundt, Dan Hurt, Julian Ibarz, Aaron Jaffey, Alek Jaworski, Alexander Kaplan, Harshit Khaitan, Andy Koch, Naveen Kumar, Steve Lacy, James Laudon, James Law, Diemthu Le, Chris Leary, Zhuyuan Liu, Kyle Lucke, Alan Lundin, Gordon MacKean, Adriana Maggiore, Maire Mahony, Kieran Miller, Rahul Nagarajan, Ravi Narayanaswami, Ray Ni, Kathy Nix, Thomas Norrie, Mark Omernick, Narayana Penukonda, Andy Phelps, Jonathan Ross, Matt Ross, Amir Salek, Emad Samadiani, Chris Severn, Gregory Sizikov, Matthew Snelham, Jed Souter, Dan Steinberg, Andy Swing, Mercedes Tan, Gregory Thorson, Bo Tian, Horia Toma, Erick Tuttle, Vijay Vasudevan, Richard Walter, Walter Wang, Eric Wilcox, and Doe Hyun Yoon. In-Datacenter Performance Analysis of a Tensor Processing Unit. *arXiv e-prints*, page arXiv:1704.04760, April 2017.

[252] Martín Abadi, Ashish Agarwal, Paul Barham, Eugene Brevdo, Zhifeng Chen, Craig Citro, Greg S. Corrado, Andy Davis, Jeffrey Dean, Matthieu Devin, Sanjay Ghemawat, Ian Goodfellow, Andrew Harp, Geoffrey Irving, Michael Isard, Yangqing Jia, Rafal Jozefowicz, Lukasz Kaiser, Manjunath Kudlur, Josh Levenberg, Dandelion Mané, Rajat Monga, Sherry Moore, Derek Murray, Chris Olah, Mike Schuster, Jonathon Shlens, Benoit Steiner, Ilya Sutskever, Kunal Talwar, Paul Tucker, Vincent Vanhoucke, Vijay Vasudevan, Fernanda Viégas, Oriol Vinyals, Pete Warden, Martin Wattenberg, Martin Wicke, Yuan Yu, and Xiaoqiang Zheng. TensorFlow: Large-scale machine learning on heterogeneous systems, 2015. Software available from tensorflow.org.

[253] Adam Paszke, Sam Gross, Soumith Chintala, Gregory Chanan, Edward Yang, Zachary DeVito, Zeming Lin, Alban Desmaison, Luca Antiga, and Adam Lerer. Automatic differentiation in pytorch. 2017.

[254] Daniel George and E. A. Huerta. Deep Learning for Real-time Gravitational Wave Detection and Parameter Estimation: Results with Advanced LIGO Data. *Phys. Lett.*, B778:64–70, 2018.

[255] Robert E. Colgan, K. Rainer Corley, Yenson Lau, Imre Bartos, John N. Wright, Zsuzsa Marka, and Szabolcs Marka. Efficient Gravitational-wave Glitch Identification from Environmental Data Through Machine Learning. 2019.

[256] Gabriele Vajente, Yiwen Huang, Maximiliano Isi, Jenne C. Driggers, Jeffrey S. Kissel, Marek J. Szczepanczyk, and Salvatore Vitale. Machine-learning non-stationary noise out of gravitational wave detectors. 2019.

[257] Hunter Gabbard, Michael Williams, Fergus Hayes, and Chris Messenger. Matching

matched filtering with deep networks for gravitational-wave astronomy. *Phys. Rev. Lett.*, 120(14):141103, 2018.

[258] Christoph Dreissigacker, Rahul Sharma, Chris Messenger, Ruining Zhao, and Reinhard Prix. Deep-Learning Continuous Gravitational Waves. *Phys. Rev.*, D100(4):044009, 2019.

[259] Hunter Gabbard, Chris Messenger, Ik Siong Heng, Francesco Tonolini, and Roderick Murray-Smith. Bayesian parameter estimation using conditional variational autoencoders for gravitational-wave astronomy. 2019.

[260] Stephen R. Green, Christine Simpson, and Jonathan Gair. Gravitational-wave parameter estimation with autoregressive neural network flows. 2020.

[261] Alvin J. K. Chua and Michele Vallisneri. Learning Bayesian posteriors with neural networks for gravitational-wave inference. *Phys. Rev. Lett.*, 124(4):041102, 2020.

[262] Miles D. Cranmer, Richard Galvez, Lauren Anderson, David N. Spergel, and Shirley Ho. Modeling the gaia color-magnitude diagram with bayesian neural flows to constrain distance estimates.

[263] Siyu He, Yin Li, Yu Feng, Shirley Ho, Siamak Ravanbakhsh, Wei Chen, and Barnabás Póczos. Learning to Predict the Cosmological Structure Formation. *Proc. Nat. Acad. Sci.*, 116(28):13825–13832, 2019.

[264] George Papamakarios, Theo Pavlakou, and Iain Murray. Masked Autoregressive Flow for Density Estimation. *arXiv e-prints*, page arXiv:1705.07057, May 2017.

[265] Ilya Mandel, Will M. Farr, and Jonathan R. Gair. Extracting distribution parameters from multiple uncertain observations with selection biases. *Mon. Not. Roy. Astron.*

Soc., 486(1):1086–1093, 2019.

[266] David W. Hogg, Adam D. Myers, and Jo Bovy. Inferring the eccentricity distribution. *The Astrophysical Journal*, 725(2):2166–2175, December 2010.

[267] Chris Pankow, Laura Sampson, Leah Perri, Eve Chase, Scott Coughlin, Michael Zevin, and Vassiliki Kalogera. Astrophysical Prior Information and Gravitational-wave Parameter Estimation. *Astrophys. J.*, 834(2):154, 2017.

[268] Salvatore Vitale, Davide Gerosa, Carl-Johan Haster, Katerina Chatziioannou, and Aaron Zimmerman. Impact of Bayesian Priors on the Characterization of Binary Black Hole Coalescences. *Phys. Rev. Lett.*, 119(25):251103, 2017.

[269] J. Veitch et al. Parameter estimation for compact binaries with ground-based gravitational-wave observations using the LALInference software library. *Phys. Rev.*, D91(4):042003, 2015.

[270] Eric Poisson and Clifford M. Will. Gravitational waves from inspiraling compact binaries: Parameter estimation using second postNewtonian wave forms. *Phys. Rev.*, D52:848–855, 1995.

[271] T. Sidery et al. Reconstructing the sky location of gravitational-wave detected compact binary systems: methodology for testing and comparison. *Phys. Rev.*, D89(8):084060, 2014.

[272] Jonathan R. Gair and Christopher J. Moore. Quantifying and mitigating bias in inference on gravitational wave source populations. *Phys. Rev.*, D91(12):124062, 2015.

[273] Michele Vallisneri. Use and abuse of the Fisher information matrix in the assessment of gravitational-wave parameter-estimation prospects. *Phys. Rev.*, D77:042001, 2008.

[274] C. Messenger and J. Veitch. Avoiding selection bias in gravitational wave astronomy. *New J. Phys.*, 15:053027, 2013.

[275] Ken K. Y. Ng, Salvatore Vitale, Aaron Zimmerman, Katerina Chatziioannou, Davide Gerosa, and Carl-Johan Haster. Gravitational-wave astrophysics with effective-spin measurements: asymmetries and selection biases. *Phys. Rev.*, D98(8):083007, 2018.

[276] Esteban Tabak and Cristina V. Turner. A family of nonparametric density estimation algorithms. *Communications on Pure and Applied Mathematics*, 66(2):145–164, 2 2013.

[277] Laurent Dinh, David Krueger, and Yoshua Bengio. NICE: Non-linear Independent Components Estimation. *arXiv e-prints*, page arXiv:1410.8516, October 2014.

[278] Laurent Dinh, Jascha Sohl-Dickstein, and Samy Bengio. Density estimation using Real NVP. *arXiv e-prints*, page arXiv:1605.08803, May 2016.

[279] Diederik P. Kingma and Prafulla Dhariwal. Glow: Generative Flow with Invertible 1x1 Convolutions. *arXiv e-prints*, page arXiv:1807.03039, July 2018.

[280] Micha Livne and David Fleet. TzK: Flow-Based Conditional Generative Model. *arXiv e-prints*, page arXiv:1902.01893, February 2019.

[281] Diederik P Kingma and Max Welling. Auto-Encoding Variational Bayes. *arXiv e-prints*, page arXiv:1312.6114, December 2013.

[282] Esteban G. Tabak and Eric Vanden-Eijnden. Density estimation by dual ascent of the log-likelihood. *Commun. Math. Sci.*, 8(1):217–233, 03 2010.

[283] Danilo Jimenez Rezende and Shakir Mohamed. Variational Inference with Normalizing Flows. *arXiv e-prints*, page arXiv:1505.05770, May 2015.

[284] Yoshua Bengio and Samy Bengio. Modeling high-dimensional discrete data with multi-layer neural networks. In *Proceedings of the 12th International Conference on Neural Information Processing Systems*, NIPS'99, page 400–406, Cambridge, MA, USA, 1999. MIT Press.

[285] Benigno Uria, Marc-Alexandre Côté, Karol Gregor, Iain Murray, and Hugo Larochelle. Neural Autoregressive Distribution Estimation. *arXiv e-prints*, page arXiv:1605.02226, May 2016.

[286] Diederik P. Kingma, Tim Salimans, Rafal Jozefowicz, Xi Chen, Ilya Sutskever, and Max Welling. Improving Variational Inference with Inverse Autoregressive Flow. *arXiv e-prints*, page arXiv:1606.04934, June 2016.

[287] `https://github.com/ikostrikov/pytorch-flows`.

[288] Ely D. Kovetz, Ilias Cholis, Patrick C. Breysse, and Marc Kamionkowski. Black hole mass function from gravitational wave measurements. *Phys. Rev.*, D95(10):103010, 2017.

[289] M. D. McKay, R. J. Beckman, and W. J. Conover. Comparison of three methods for selecting values of input variables in the analysis of output from a computer code. *Technometrics*, 21(2):239–245, 1979.

[290] Michal Dominik, Emanuele Berti, Richard O'Shaughnessy, Ilya Mandel, Krzysztof Belczynski, Christopher Fryer, Daniel E. Holz, Tomasz Bulik, and Francesco Pannarale. Double Compact Objects III: Gravitational Wave Detection Rates. *Astrophys. J.*, 806(2):263, 2015.

[291] Jim W. Barrett, Ilya Mandel, Coenraad J. Neijssel, Simon Stevenson, and Alejandro

Vigna-Gomez. Exploring the Parameter Space of Compact Binary Population Synthesis. *IAU Symp.*, 325:46–50, 2016.

[292] Nicola Giacobbo, Michela Mapelli, and Mario Spera. Merging black hole binaries: the effects of progenitor's metallicity, mass-loss rate and Eddington factor. *Mon. Not. Roy. Astron. Soc.*, 474(3):2959–2974, 2018.

[293] Katelyn Breivik et al. COSMIC Variance in Binary Population Synthesis. 2019.

[294] Juan Zamudio-Fernandez, Atakan Okan, Francisco Villaescusa-Navarro, Seda Bilaloglu, Asena Derin Cengiz, Siyu He, Laurence Perreault Levasseur, and Shirley Ho. HIGAN: Cosmic Neutral Hydrogen with Generative Adversarial Networks. 2019.

[295] R. S. de Souza, N. Yoshida, and K. Ioka. Populations III.1 and III.2 gamma-ray bursts: constraints on the event rate for future radio and X-ray surveys. A&A, 533:A32, September 2011.

[296] D. Thornton et al. A Population of Fast Radio Bursts at Cosmological Distances. *Science*, 341(6141):53–56, 2013.

[297] Gijs D. Mulders, Ilaria Pascucci, Dániel Apai, and Fred J. Ciesla. The Exoplanet Population Observation Simulator. I. The Inner Edges of Planetary Systems. AJ, 156(1):24, July 2018.

[298] R. Abbott et al. Tests of General Relativity with Binary Black Holes from the second LIGO-Virgo Gravitational-Wave Transient Catalog. 10 2020.

[299] A. Palmese et al. A statistical standard siren measurement of the Hubble constant from the LIGO/Virgo gravitational wave compact object merger GW190814 and Dark Energy Survey galaxies. *Astrophys. J.*, 900(2):L33, 2020.

[300] Robert Farmer, Mathieu Renzo, Selma de Mink, Maya Fishbach, and Stephen Justham. Constraints from gravitational wave detections of binary black hole mergers on the $^{12}C\,(\alpha,\gamma)^{16}O$ rate. *Astrophys. J.*, 902(2):L36, 2020.

[301] Yann Bouffanais, Michela Mapelli, Filippo Santoliquido, Nicola Giacobbo, Giuliano Iorio, and Guglielmo Costa. Constraining accretion efficiency in massive binary stars with LIGO-Virgo black holes. 10 2020.

[302] Thomas Callister, Maya Fishbach, Daniel Holz, and Will Farr. Shouts and Murmurs: Combining Individual Gravitational-Wave Sources with the Stochastic Background to Measure the History of Binary Black Hole Mergers. *Astrophys. J. Lett.*, 896(2):L32, 2020.

[303] Simeon Bird, Ilias Cholis, Julian B. Muñoz, Yacine Ali-Haïmoud, Marc Kamionkowski, Ely D. Kovetz, Alvise Raccanelli, and Adam G. Riess. Did LIGO Detect Dark Matter? *Physical Review Letters*, 116(20), May 2016.

[304] Fabio Antonini, Carl L Rodriguez, Cristobal Petrovich, and Caitlin L Fischer. Precessional dynamics of black hole triples: binary mergers with near-zero effective spin. *Monthly Notices of the Royal Astronomical Society: Letters*, 480(1):L58–L62, October 2018.

[305] Barry McKernan, K. E. Saavik Ford, J. Bellovary, N. W. C. Leigh, Z. Haiman, B. Kocsis, W. Lyra, M.-M. Mac Low, B. Metzger, M. O'Dowd, S. Endlich, and D. J. Rosen. Constraining Stellar-mass Black Hole Mergers in AGN Disks Detectable with LIGO. *The Astrophysical Journal*, 866(1):66, October 2018.

[306] Michal Dominik, Krzysztof Belczynski, Christopher Fryer, Daniel Holz, Emanuele

Berti, Tomasz Bulik, Ilya Mandel, and Richard O'Shaughnessy. Double Compact Objects I: The Significance of the Common Envelope on Merger Rates. *Astrophys. J.*, 759:52, 2012.

[307] K. Belczynski et al. Evolutionary roads leading to low effective spins, high black hole masses, and O1/O2 rates for LIGO/Virgo binary black holes. *Astron. Astrophys.*, 636:A104, 2020.

[308] Carl L. Rodriguez, Pau Amaro-Seoane, Sourav Chatterjee, and Frederic A. Rasio. Post-Newtonian Dynamics in Dense Star Clusters: Highly-Eccentric, Highly-Spinning, and Repeated Binary Black Hole Mergers. *Phys. Rev. Lett.*, 120(15):151101, 2018.

[309] Ugo N. Di Carlo, Nicola Giacobbo, Michela Mapelli, Mario Pasquato, Mario Spera, Long Wang, and Francesco Haardt. Merging black holes in young star clusters. *Mon. Not. Roy. Astron. Soc.*, 487(2):2947–2960, 2019.

[310] Carl L. Rodriguez, Michael Zevin, Chris Pankow, Vasilliki Kalogera, and Frederic A. Rasio. Illuminating Black Hole Binary Formation Channels with Spins in Advanced LIGO. *Astrophys. J. Lett.*, 832(1):L2, 2016.

[311] Y. Qin, T. Fragos, G. Meynet, J. Andrews, M. Sørensen, and H.F. Song. The spin of the second-born black hole in coalescing binary black holes. *Astron. Astrophys.*, 616:A28, 2018.

[312] Simone S. Bavera, Tassos Fragos, Ying Qin, Emmanouil Zapartas, Coenraad J. Neijssel, Ilya Mandel, Aldo Batta, Sebastian M. Gaebel, Chase Kimball, and Simon Stevenson. The origin of spin in binary black holes. Predicting the distributions of the main observables of Advanced LIGO. A&A, 635:A97, March 2020.

[313] Zoheyr Doctor, Daniel Wysocki, Richard O'Shaughnessy, Daniel E. Holz, and Ben Farr. Black Hole Coagulation: Modeling Hierarchical Mergers in Black Hole Populations. 11 2019.

[314] B. McKernan, K. E. S. Ford, R. O'Shaugnessy, and D. Wysocki. Monte Carlo simulations of black hole mergers in AGN discs: Low χ_{eff} mergers and predictions for LIGO. MNRAS, 494(1):1203–1216, April 2020.

[315] S. E. Woosley. Pulsational Pair-Instability Supernovae. *Astrophys. J.*, 836(2):244, 2017.

[316] R. Farmer, M. Renzo, S. E. de Mink, P. Marchant, and S. Justham. Mind the gap: The location of the lower edge of the pair instability supernovae black hole mass gap. 10 2019.

[317] Yann Bouffanais, Michela Mapelli, Davide Gerosa, Ugo N. Di Carlo, Nicola Giacobbo, Emanuele Berti, and Vishal Baibhav. Constraining the fraction of binary black holes formed in isolation and young star clusters with gravitational-wave data. *Astrophys. J.*, 886(1), 2019.

[318] Mohammadtaher Safarzadeh. The branching ratio of LIGO binary black holes. *Astrophys. J. Lett.*, 892(1):L8, 2020.

[319] Katelyn Breivik, Scott Coughlin, Michael Zevin, Carl L. Rodriguez, Kyle Kremer, Claire S. Ye, Jeff J. Andrews, Michael Kurkowski, Matthew C. Digman, Shane L. Larson, and Frederic A. Rasio. COSMIC Variance in Binary Population Synthesis. ApJ, 898(1):71, July 2020.

[320] J. R. Hurley, C. A. Tout, and O. R. Pols. Evolution of binary stars and the effect of

tides on binary populations. MNRAS, 329:897–928, February 2002.

[321] Michael Zevin, Mario Spera, Christopher P. L. Berry, and Vicky Kalogera. Exploring the Lower Mass Gap and Unequal Mass Regime in Compact Binary Evolution. ApJ, 899(1):L1, August 2020.

[322] Pavel Kroupa. On the variation of the initial mass function. MNRAS, 322(2):231–246, April 2001.

[323] H. Sana, S. E. de Mink, A. de Koter, N. Langer, C. J. Evans, M. Gieles, E. Gosset, R. G. Izzard, J. B. Le Bouquin, and F. R. N. Schneider. Binary Interaction Dominates the Evolution of Massive Stars. *Science*, 337(6093):444, July 2012.

[324] M. Renzo, E. Zapartas, S. E. de Mink, Y. Götberg, S. Justham, R. J. Farmer, R. G. Izzard, S. Toonen, and H. Sana. Massive runaway and walkaway stars. A study of the kinematical imprints of the physical processes governing the evolution and explosion of their binary progenitors. A&A, 624:A66, April 2019.

[325] N. Ivanova, S. Justham, X. Chen, O. De Marco, C. L. Fryer, E. Gaburov, H. Ge, E. Glebbeek, Z. Han, X. D. Li, G. Lu, T. Marsh, P. Podsiadlowski, A. Potter, N. Soker, R. Taam, T. M. Tauris, E. P. J. van den Heuvel, and R. F. Webbink. Common envelope evolution: where we stand and how we can move forward. A&A Rev., 21:59, February 2013.

[326] J. S. W. Claeys, O. R. Pols, R. G. Izzard, J. Vink, and F. W. M. Verbunt. Theoretical uncertainties of the Type Ia supernova rate. A&A, 563:A83, March 2014.

[327] M. Zorotovic, M. R. Schreiber, B. T. Gänsicke, and A. Nebot Gómez-Morán. Post-common-envelope binaries from SDSS. IX: Constraining the common-envelope efficiency.

A&A, 520:A86, September 2010.

[328] Orsola De Marco, Jean-Claude Passy, Maxwell Moe, Falk Herwig, Mordecai-Mark Mac Low, and Bill Paxton. On the α formalism for the common envelope interaction. MNRAS, 411(4):2277–2292, March 2011.

[329] Tassos Fragos, Jeff J. Andrews, Enrico Ramirez-Ruiz, Georges Meynet, Vicky Kalogera, Ronald E. Taam, and Andreas Zezas. The Complete Evolution of a Neutron-star Binary through a Common Envelope Phase Using 1D Hydrodynamic Simulations. ApJ, 883(2):L45, October 2019.

[330] N. Grevesse and A. J. Sauval. Standard Solar Composition. Space Sci. Rev., 85:161–174, May 1998.

[331] Piero Madau and Tassos Fragos. Radiation Backgrounds at Cosmic Dawn: X-Rays from Compact Binaries. ApJ, 840(1):39, May 2017.

[332] P. A. Ade et al. Planck 2015 results. XIII. Cosmological parameters. A&A, 594:A13, September 2016.

[333] Astropy Collaboration, T. P. Robitaille, E. J. Tollerud, et al. Astropy: A community Python package for astronomy. A&A, 558:A33, October 2013.

[334] Astropy Collaboration, A. M. Price-Whelan, B. M. SipHocz, et al. The Astropy Project: Building an Open-science Project and Status of the v2.0 Core Package. AJ, 156(3):123, September 2018.

[335] Kyle Kremer, Claire S. Ye, Nicholas Z. Rui, Newlin C. Weatherford, Sourav Chatterjee, Giacomo Fragione, Carl L. Rodriguez, Mario Spera, and Frederic A. Rasio. Modeling Dense Star Clusters in the Milky Way and Beyond with the CMC Cluster Catalog.

ApJS, 247(2):48, April 2020.

[336] Kriten J. Joshi, Frederic A. Rasio, S P Zwart, and Simon Portegies Zwart. Monte Carlo Simulations of Globular Cluster Evolution. I. Method and Test Calculations. *The Astrophysical Journal*, 540(2):969–982, 9 2000.

[337] Bharath Pattabiraman, Stefan Umbreit, Wei-keng Liao, Alok Choudhary, Vassiliki Kalogera, Gokhan Memik, and Frederic A. Rasio. A PARALLEL MONTE CARLO CODE FOR SIMULATING COLLISIONAL N -BODY SYSTEMS. *The Astrophysical Journal Supplement Series*, 204(2):15, 2 2013.

[338] Meagan Morscher, Bharath Pattabiraman, Carl Rodriguez, Frederic A. Rasio, and Stefan Umbreit. The Dynamical Evolution of Stellar Black Holes in Globular Clusters. ApJ, 800(1):9, February 2015.

[339] J. M. Fregeau and F. A. Rasio. Monte Carlo Simulations of Globular Cluster Evolution. IV. Direct Integration of Strong Interactions. *apj*, 658:1047–1061, April 2007.

[340] C. L. Rodriguez, P. Amaro-Seoane, S. Chatterjee, and F. A. Rasio. Post-Newtonian Dynamics in Dense Star Clusters: Highly Eccentric, Highly Spinning, and Repeated Binary Black Hole Mergers. *Physical Review Letters*, 120(15):151101, April 2018.

[341] J. R. Hurley, O. R. Pols, and C. A. Tout. Comprehensive analytic formulae for stellar evolution as a function of mass and metallicity. MNRAS, 315:543–569, July 2000.

[342] Pavel Kroupa. On the variation of the initial mass function. MNRAS, 322(2):231–246, April 2001.

[343] D. C. Heggie. Binary evolution in stellar dynamics. MNRAS, 173:729–787, December 1975.

[344] Kareem El-Badry, Eliot Quataert, Daniel R. Weisz, Nick Choksi, and Michael Boylan-Kolchin. The formation and hierarchical assembly of globular cluster populations. MNRAS, 482(4):4528–4552, February 2019.

[345] Carl L. Rodriguez and Abraham Loeb. Redshift Evolution of the Black Hole Merger Rate from Globular Clusters. ApJ, 866(1):L5, October 2018.

[346] Giacomo Fragione and Bence Kocsis. Black Hole Mergers from an Evolving Population of Globular Clusters. PRL, 121(16):161103, October 2018.

[347] Fabio Antonini and Mark Gieles. Merger rate of black hole binaries from globular clusters: theoretical error bars and comparison to gravitational wave data. *arXiv e-prints*, page arXiv:2009.01861, September 2020.

[348] Chris L. Fryer, Krzysztof Belczynski, Grzegorz Wiktorowicz, Michal Dominik, Vicky Kalogera, and Daniel E. Holz. Compact Remnant Mass Function: Dependence on the Explosion Mechanism and Metallicity. ApJ, 749(1):91, April 2012.

[349] K. Belczynski, A. Heger, W. Gladysz, A. J. Ruiter, S. Woosley, G. Wiktorowicz, H. Y. Chen, T. Bulik, R. O'Shaughnessy, D. E. Holz, C. L. Fryer, and E. Berti. The effect of pair-instability mass loss on black-hole mergers. A&A, 594:A97, October 2016.

[350] James Binney and Scott Tremaine. *Galactic dynamics*. 1987.

[351] Thomas J. Loredo. Accounting for Source Uncertainties in Analyses of Astronomical Survey Data. In Rainer Fischer, Roland Preuss, and Udo Von Toussaint, editors, *Bayesian Inference and Maximum Entropy Methods in Science and Engineering: 24th International Workshop on Bayesian Inference and Maximum Entropy Methods in Science and Engineering*, volume 735 of *American Institute of Physics Conference*

Series, pages 195–206, November 2004.

[352] Will M. Farr. Accuracy Requirements for Empirically Measured Selection Functions. *Research Notes of the American Astronomical Society*, 3(5):66, May 2019.

[353] J. Veitch, V. Raymond, B. Farr, W. Farr, P. Graff, S. Vitale, B. Aylott, K. Blackburn, N. Christensen, M. Coughlin, W. Del Pozzo, F. Feroz, J. Gair, C. J. Haster, V. Kalogera, T. Littenberg, I. Mandel, R. O'Shaughnessy, M. Pitkin, C. Rodriguez, C. Röver, T. Sidery, R. Smith, M. Van Der Sluys, A. Vecchio, W. Vousden, and L. Wade. Parameter estimation for compact binaries with ground-based gravitational-wave observations using the LALInference software library. PRD, 91(4):042003, February 2015.

[354] Michele Vallisneri, Jonah Kanner, Roy Williams, Alan Weinstein, and Branson Stephens. The LIGO Open Science Center. In *Journal of Physics Conference Series*, volume 610 of *Journal of Physics Conference Series*, page 012021, May 2015.

[355] LIGO Scientific Collaboration and Virgo Collaboration, 2019. `https://doi.org/10.7935/KSX7-QQ51`.

[356] LIGO Scientific Collaboration and Virgo Collaboration, 2019. `https://dcc.ligo.org/LIGO-P2000223/public`.

[357] Kyle Kremer, Sourav Chatterjee, Claire S. Ye, Carl L. Rodriguez, and Frederic A. Rasio. How Initial Size Governs Core Collapse in Globular Clusters. ApJ, 871(1):38, January 2019.

[358] William E. Harris. A Catalog of Parameters for Globular Clusters in the Milky Way. AJ, 112:1487, October 1996.

[359] Krzysztof Belczynski, Vassiliki Kalogera, and Tomasz Bulik. A Comprehensive Study of Binary Compact Objects as Gravitational Wave Sources: Evolutionary Channels, Rates, and Physical Properties. ApJ, 572(1):407–431, June 2002.

[360] K. Belczynski, J. Klencki, C. E. Fields, A. Olejak, E. Berti, G. Meynet, C. L. Fryer, D. E. Holz, R. O'Shaughnessy, D. A. Brown, T. Bulik, S. C. Leung, K. Nomoto, P. Madau, R. Hirschi, E. Kaiser, S. Jones, S. Mondal, M. Chruslinska, P. Drozda, D. Gerosa, Z. Doctor, M. Giersz, S. Ekstrom, C. Georgy, A. Askar, V. Baibhav, D. Wysocki, T. Natan, W. M. Farr, G. Wiktorowicz, M. Coleman Miller, B. Farr, and J. P. Lasota. Evolutionary roads leading to low effective spins, high black hole masses, and O1/O2 rates for LIGO/Virgo binary black holes. A&A, 636:A104, April 2020.

[361] L. A. C. van Son, S. E. De Mink, F. S. Broekgaarden, M. Renzo, S. Justham, E. Laplace, J. Morán-Fraile, D. D. Hendriks, and R. Farmer. Polluting the Pair-instability Mass Gap for Binary Black Holes through Super-Eddington Accretion in Isolated Binaries. ApJ, 897(1):100, July 2020.

[362] Krzysztof Belczynski, Vassiliki Kalogera, Frederic A. Rasio, Ronald E. Taam, Andreas Zezas, Tomasz Bulik, Thomas J. Maccarone, and Natalia Ivanova. Compact Object Modeling with the StarTrack Population Synthesis Code. ApJS, 174(1):223–260, January 2008.

[363] Simon F. Portegies Zwart, Stephen L. W. McMillan, and Mark Gieles. Young Massive Star Clusters. ARA&A, 48:431–493, September 2010.

[364] J. M. Diederik Kruijssen. Globular clusters as the relics of regular star formation in 'normal' high-redshift galaxies. MNRAS, 454(2):1658–1686, December 2015.

[365] S. M. Fall and M. J. Rees. A theory for the origin of globular clusters. ApJ, 298:18–26, November 1985.

[366] Simon Stevenson, Christopher P. L. Berry, and Ilya Mandel. Hierarchical analysis of gravitational-wave measurements of binary black hole spin–orbit misalignments. *Mon. Not. Roy. Astron. Soc.*, 471(3):2801–2811, 2017.

[367] Colm Talbot and Eric Thrane. Determining the population properties of spinning black holes. *Phys. Rev. D*, 96(2):023012, 2017.

[368] Simone S. Bavera, Tassos Fragos, Michael Zevin, Christopher P. L. Berry, Pablo Marchant, Jeff J. Andrews, Scott Coughlin, Aaron Dotter, Konstantinos Kovlakas, Devina Misra, Juan G. Serra-Perez, Ying Qin, Kyle A. Rocha, Jaime Román-Garza, Nam H. Tran, and Emmanouil Zapartas. The impact of mass-transfer physics on the observable properties of field binary black hole populations. *arXiv e-prints*, page arXiv:2010.16333, October 2020.

[369] Michael Zevin, Simone S. Bavera, Christopher P.L. Berry, Vicky Kalogera, Tassos Fragos, Pablo Marchant, Carl L. Rodriguez, Fabio Antonini, Daniel E. Holz, and Chris Pankow. One Channel to Rule Them All? Constraining the Origins of Binary Black Holes using Multiple Formation Pathways. 11 2020.

[370] Johan Samsing. Eccentric black hole mergers forming in globular clusters. *Physical Review D*, 97(10), May 2018.

[371] Isobel M Romero-Shaw, Paul D Lasky, and Eric Thrane. Searching for eccentricity: signatures of dynamical formation in the first gravitational-wave transient catalogue of ligo and virgo. *Monthly Notices of the Royal Astronomical Society*, 490(4):5210–5216,

October 2019.

[372] R. Abbott et al. GW190412: Observation of a Binary-Black-Hole Coalescence with Asymmetric Masses. *Phys. Rev.*, D102(4):043015, 4 2020.

[373] Emanuele Berti et al. Testing General Relativity with Present and Future Astrophysical Observations. *Class. Quant. Grav.*, 32:243001, 2015.

[374] Leor Barack et al. Black holes, gravitational waves and fundamental physics: a roadmap. *Class. Quant. Grav.*, 36(14):143001, 2019.

[375] Ilya Mandel and Alison Farmer. Merging stellar-mass binary black holes. 6 2018.

[376] Michela Mapelli. Astrophysics of stellar black holes. *Proc. Int. Sch. Phys. Fermi*, 200:87–121, 2020.

[377] Pablo Marchant, Norbert Langer, Philipp Podsiadlowski, Thomas M. Tauris, and Takashi J. Moriya. A new route towards merging massive black holes. *Astron. Astrophys.*, 588:A50, 2016.

[378] S. E. de Mink and I. Mandel. The chemically homogeneous evolutionary channel for binary black hole mergers: rates and properties of gravitational-wave events detectable by advanced LIGO. *Mon. Not. Roy. Astron. Soc.*, 460(4):3545–3553, 2016.

[379] N. W. C. Leigh et al. On the rate of black hole binary mergers in galactic nuclei due to dynamical hardening. *Mon. Not. Roy. Astron. Soc.*, 474(4):5672–5683, 2018.

[380] Nicholas C. Stone, Brian D. Metzger, and Zoltán Haiman. Assisted inspirals of stellar mass black holes embedded in AGN discs: solving the 'final au problem'. *Mon. Not. Roy. Astron. Soc.*, 464(1):946–954, 2017.

[381] Imre Bartos, Bence Kocsis, Zolt Haiman, and Szabolcs Márka. Rapid and Bright

Stellar-mass Binary Black Hole Mergers in Active Galactic Nuclei. *Astrophys. J.*, 835(2):165, 2017.

[382] Kedron Silsbee and Scott Tremaine. Lidov-Kozai Cycles with Gravitational Radiation: Merging Black Holes in Isolated Triple Systems. *Astrophys. J.*, 836(1):39, 2017.

[383] Bao-Minh Hoang, Smadar Naoz, Bence Kocsis, Frederic A. Rasio, and Fani Dosopoulou. Black Hole Mergers in Galactic Nuclei Induced by the Eccentric Kozai–Lidov Effect. *Astrophys. J.*, 856(2):140, 2018.

[384] Giacomo Fragione, Evgeni Grishin, Nathan W. C. Leigh, Hagai.B. Perets, and Rosalba Perna. Black hole and neutron star mergers in galactic nuclei. *Mon. Not. Roy. Astron. Soc.*, 488(1):47–63, 2019.

[385] Anne M. Green and Bradley J. Kavanagh. Primordial Black Holes as a dark matter candidate. 7 2020.

[386] Misao Sasaki, Teruaki Suyama, Takahiro Tanaka, and Shuichiro Yokoyama. Primordial Black Hole Scenario for the Gravitational-Wave Event GW150914. *Phys. Rev. Lett.*, 117(6):061101, 2016. [erratum: Phys. Rev. Lett.121,no.5,059901(2018)].

[387] Simeon Bird, Ilias Cholis, Julian B. Muñoz, Yacine Ali-Haïmoud, Marc Kamionkowski, Ely D. Kovetz, Alvise Raccanelli, and Adam G. Riess. Did LIGO detect dark matter? *Phys. Rev. Lett.*, 116(20):201301, 2016.

[388] Sebastien Clesse and Juan García-Bellido. The clustering of massive Primordial Black Holes as Dark Matter: measuring their mass distribution with Advanced LIGO. *Phys. Dark Univ.*, 15:142–147, 2017.

[389] Sai Wang, Yi-Fan Wang, Qing-Guo Huang, and Tjonnie G. F. Li. Constraints on the

Primordial Black Hole Abundance from the First Advanced LIGO Observation Run Using the Stochastic Gravitational-Wave Background. *Phys. Rev. Lett.*, 120(19):191102, 2018.

[390] Yacine Ali-Haïmoud, Ely D. Kovetz, and Marc Kamionkowski. Merger rate of primordial black-hole binaries. *Phys. Rev.*, D96(12):123523, 2017.

[391] Gert Hütsi, Martti Raidal, and Hardi Veermäe. Small-scale structure of primordial black hole dark matter and its implications for accretion. *Phys. Rev. D*, 100(8):083016, 2019.

[392] Ville Vaskonen and Hardi Veermäe. Lower bound on the primordial black hole merger rate. *Phys. Rev. D*, 101(4):043015, 2020.

[393] V. De Luca, G. Franciolini, P. Pani, and A. Riotto. Primordial Black Holes Confront LIGO/Virgo data: Current situation. *JCAP*, 06:044, 2020.

[394] Karsten Jedamzik. Primordial Black Hole Dark Matter and the LIGO/Virgo observations. *JCAP*, 09:022, 2020.

[395] Karsten Jedamzik. Evidence for primordial black hole dark matter from LIGO/Virgo merger rates. 7 2020.

[396] Alex Hall, Andrew D. Gow, and Christian T. Byrnes. Bayesian analysis of LIGO-Virgo mergers: Primordial vs. astrophysical black hole populations. 8 2020.

[397] V. De Luca, V. Desjacques, G. Franciolini, P. Pani, and A. Riotto. The GW190521 Mass Gap Event and the Primordial Black Hole Scenario. 9 2020.

[398] V. De Luca, V. Desjacques, G. Franciolini, and A. Riotto. The Clustering Evolution of Primordial Black Holes. 9 2020.

[399] S. Blinnikov, A. Dolgov, N. K. Porayko, and K. Postnov. Solving puzzles of GW150914 by primordial black holes. *JCAP*, 1611:036, 2016.

[400] P. Ivanov, P. Naselsky, and I. Novikov. Inflation and primordial black holes as dark matter. *Phys. Rev. D*, 50:7173–7178, 1994.

[401] P. Ivanov. Nonlinear metric perturbations and production of primordial black holes. *Phys. Rev. D*, 57:7145–7154, 1998.

[402] Alexandre Dolgov and Joseph Silk. Baryon isocurvature fluctuations at small scales and baryonic dark matter. *Phys. Rev. D*, 47:4244–4255, 1993.

[403] Bernard Carr, Martti Raidal, Tommi Tenkanen, Ville Vaskonen, and Hardi Veermäe. Primordial black hole constraints for extended mass functions. *Phys. Rev.*, D96(2):023514, 2017.

[404] James M. Bardeen, J.R. Bond, Nick Kaiser, and A.S. Szalay. The Statistics of Peaks of Gaussian Random Fields. *Astrophys. J.*, 304:15–61, 1986.

[405] V. De Luca, V. Desjacques, G. Franciolini, A. Malhotra, and A. Riotto. The initial spin probability distribution of primordial black holes. *JCAP*, 1905:018, 2019.

[406] Mehrdad Mirbabayi, Andrei Gruzinov, and Jorge Noreña. Spin of Primordial Black Holes. *JCAP*, 2003:017, 2020.

[407] Massimo Ricotti. Bondi accretion in the early universe. *Astrophys. J.*, 662:53–61, 2007.

[408] Massimo Ricotti, Jeremiah P. Ostriker, and Katherine J. Mack. Effect of Primordial Black Holes on the Cosmic Microwave Background and Cosmological Parameter Estimates. *Astrophys. J.*, 680:829, 2008.

[409] Jared R. Rice and Bing Zhang. Cosmological evolution of primordial black holes.

JHEAp, 13-14:22–31, 2017.

[410] Emanuele Berti and Marta Volonteri. Cosmological black hole spin evolution by mergers and accretion. *Astrophys. J.*, 684:822–828, 2008.

[411] Alejandro Cruz-Osorio and Luciano Rezzolla. Common-envelope Dynamics of a Stellar-mass Black Hole: General Relativistic Simulations. *Astrophys. J.*, 894(2):147, 2020.

[412] Julian Adamek, Christian T. Byrnes, Mateja Gosenca, and Shaun Hotchkiss. WIMPs and stellar-mass primordial black holes are incompatible. *Phys. Rev.*, D100(2):023506, 2019.

[413] Katherine J. Mack, Jeremiah P. Ostriker, and Massimo Ricotti. Growth of structure seeded by primordial black holes. *Astrophys. J.*, 665:1277–1287, 2007.

[414] G. Hasinger. Illuminating the dark ages: Cosmic backgrounds from accretion onto primordial black hole dark matter. 2020.

[415] Gert Hütsi, Martti Raidal, and Hardi Veermäe. Small-scale structure of primordial black hole dark matter and its implications for accretion. *Phys. Rev. D*, 100(8):083016, 2019.

[416] S. Peng Oh and Zoltan Haiman. Fossil HII regions: Self-limiting star formation at high redshift. *Mon. Not. Roy. Astron. Soc.*, 346:456, 2003.

[417] Yacine Ali-Haïmoud and Marc Kamionkowski. Cosmic microwave background limits on accreting primordial black holes. *Phys. Rev. D*, 95(4):043534, 2017.

[418] Valenti Bosch-Ramon and Nicola Bellomo. Mechanical feedback effects on primordial black hole accretion. *Astron. Astrophys.*, 638:A132, 2020.

[419] Lang Liu, Zong-Kuan Guo, and Rong-Gen Cai. Effects of the merger history on the merger rate density of primordial black hole binaries. *Eur. Phys. J.*, C79(8):717, 2019.

[420] You Wu. Merger history of primordial black-hole binaries. *Phys. Rev.*, D101(8):083008, 2020.

[421] Maya Fishbach, Daniel E. Holz, and Ben Farr. Are LIGO's Black Holes Made From Smaller Black Holes? *Astrophys. J. Lett.*, 840(2):L24, 2017.

[422] Chase Kimball, Colm Talbot, Christopher P. L. Berry, Matthew Carney, Michael Zevin, Eric Thrane, and Vicky Kalogera. Black hole genealogy: Identifying hierarchical mergers with gravitational waves. *Astrophys. J.*, 900(2):177, 2020.

[423] Emanuele Berti and Marta Volonteri. Cosmological black hole spin evolution by mergers and accretion. *Astrophys. J.*, 684:822–828, 2008.

[424] N. I. Shakura and R. A. Sunyaev. Black holes in binary systems. Observational appearance. *Astron. Astrophys.*, 24:337–355, 1973.

[425] I. D. Novikov and K. S. Thorne. Astrophysics of black holes. In *Black Holes (Les Astres Occlus)*, pages 343–450, January 1973.

[426] James M. Bardeen, William H. Press, and Saul A Teukolsky. Rotating black holes: Locally nonrotating frames, energy extraction, and scalar synchrotron radiation. *Astrophys. J.*, 178:347, 1972.

[427] Richard Brito, Vitor Cardoso, and Paolo Pani. Black holes as particle detectors: evolution of superradiant instabilities. *Class. Quant. Grav.*, 32(13):134001, 2015.

[428] Marta Volonteri, Piero Madau, Eliot Quataert, and Martin J. Rees. The Distribution and cosmic evolution of massive black hole spins. *Astrophys. J.*

[429] Kip S. Thorne. Disk accretion onto a black hole. 2. Evolution of the hole. *Astrophys. J.*, 191:507–520, 1974.

[430] Charles F. Gammie, Stuart L. Shapiro, and Jonathan C. McKinney. Black hole spin evolution. *Astrophys. J.*, 602:312–319, 2004.

[431] Ramesh Narayan and Insu Yi. Advection dominated accretion: Underfed black holes and neutron stars. *Astrophys. J.*, 452:710, 1995.

[432] M. A. Abramowicz, B. Czerny, J. P. Lasota, and E. Szuszkiewicz. Slim Accretion Disks. ApJ, 332:646, September 1988.

[433] Davide Gerosa, Michael Kesden, Emanuele Berti, Richard O'Shaughnessy, and Ulrich Sperhake. Resonant-plane locking and spin alignment in stellar-mass black-hole binaries: a diagnostic of compact-binary formation. *Phys. Rev.*, D87:104028, 2013.

[434] Davide Gerosa, Emanuele Berti, Richard O'Shaughnessy, Krzysztof Belczynski, Michael Kesden, Daniel Wysocki, and Wojciech Gladysz. Spin orientations of merging black holes formed from the evolution of stellar binaries. *Phys. Rev.*, D98(8):084036, 2018.

[435] Nathan Steinle and Michael Kesden. Pathways for producing binary black holes with large misaligned spins in the isolated formation channel. 2020.

[436] Yacine Ali-Haïmoud. Correlation Function of High-Threshold Regions and Application to the Initial Small-Scale Clustering of Primordial Black Holes. *Phys. Rev. Lett.*, 121(8):081304, 2018.

[437] Vincent Desjacques and Antonio Riotto. Spatial clustering of primordial black holes. *Phys. Rev. D*, 98(12):123533, 2018.

[438] Guillermo Ballesteros, Pasquale D. Serpico, and Marco Taoso. On the merger rate

of primordial black holes: effects of nearest neighbours distribution and clustering. *JCAP*, 10:043, 2018.

[439] Azadeh Moradinezhad Dizgah, Gabriele Franciolini, and Antonio Riotto. Primordial Black Holes from Broad Spectra: Abundance and Clustering. *JCAP*, 11:001, 2019.

[440] Andrea Caputo, Laura Sberna, Alexandre Toubiana, Stanislav Babak, Enrico Barausse, Sylvain Marsat, and Paolo Pani. Gravitational-wave detection and parameter estimation for accreting black-hole binaries and their electromagnetic counterpart. 2020.

[441] P. C. Peters and J. Mathews. Gravitational radiation from point masses in a Keplerian orbit. *Phys. Rev.*, 131:435–439, 1963.

[442] P. C. Peters. Gravitational Radiation and the Motion of Two Point Masses. *Phys. Rev.*, 136:B1224–B1232, 1964.

[443] Derek Inman and Yacine Ali-Haïmoud. Early structure formation in primordial black hole cosmologies. *Phys. Rev. D*, 100(8):083528, 2019.

[444] Salvatore Vitale. One, No One, and One Hundred Thousand – Inferring the properties of a population in presence of selection effects. 2020.

[445] S. Bhagwat, V. De Luca, G. Franciolini, P. Pani, and A. Riotto. The Importance of Priors on LIGO-Virgo Parameter Estimation: the Case of Primordial Black Holes. 8 2020.

[446] `https://dcc.ligo.org/LIGO-P2000217/public`.

[447] Kaze W.K. Wong, Ken K.Y. Ng, and Emanuele Berti. Gravitational-wave signal-to-noise interpolation via neural networks. 7 2020.

[448] https://dcc.ligo.org/LIGO-P1800370/public.

[449] https://dcc.ligo.org/LIGO-P2000223/public.

[450] A.D. Dolgov, A.G. Kuranov, N.A. Mitichkin, S. Porey, K.A. Postnov, O.S. Sazhina, and I.V. Simkin. On mass distribution of coalescing black holes. 5 2020.

[451] Piero Madau and Mark Dickinson. Cosmic Star Formation History. *Ann. Rev. Astron. Astrophys.*, 52:415–486, 2014.

[452] B.S. Sathyaprakash et al. Extreme Gravity and Fundamental Physics. 3 2019.

[453] Pasquale D. Serpico, Vivian Poulin, Derek Inman, and Kazunori Kohri. Cosmic microwave background bounds on primordial black holes including dark matter halo accretion. *Phys. Rev. Res.*, 2(2):023204, 2020.

[454] Daniele Gaggero, Gianfranco Bertone, Francesca Calore, Riley M. T. Connors, Mark Lovell, Sera Markoff, and Emma Storm. Searching for Primordial Black Holes in the radio and X-ray sky. *Phys. Rev. Lett.*, 118(24):241101, 2017.

[455] Julien Manshanden, Daniele Gaggero, Gianfranco Bertone, Riley M.T. Connors, and Massimo Ricotti. Multi-wavelength astronomical searches for primordial black holes. *JCAP*, 06:026, 2019.

[456] Yoshiyuki Inoue and Alexander Kusenko. New X-ray bound on density of primordial black holes. *JCAP*, 1710:034, 2017.

[457] Philip Lu, Volodymyr Takhistov, Graciela B. Gelmini, Kohei Hayashi, Yoshiyuki Inoue, and Alexander Kusenko. Constraining Primordial Black Holes with Dwarf Galaxy Heating. 7 2020.

[458] R. A. Allsman et al. MACHO project limits on black hole dark matter in the 1-30

solar mass range. *Astrophys. J. Lett.*, 550:L169, 2001.

[459] Masamune Oguri, Jose M. Diego, Nick Kaiser, Patrick L. Kelly, and Tom Broadhurst. Understanding caustic crossings in giant arcs: characteristic scales, event rates, and constraints on compact dark matter. *Phys. Rev.*, D97(2):023518, 2018.

[460] Hiroko Niikura, Masahiro Takada, Shuichiro Yokoyama, Takahiro Sumi, and Shogo Masaki. Constraints on Earth-mass primordial black holes from OGLE 5-year microlensing events. *Phys. Rev. D*, 99(8):083503, 2019.

[461] Zu-Cheng Chen, Chen Yuan, and Qing-Guo Huang. Pulsar Timing Array Constraints on Primordial Black Holes with NANOGrav 11-Year Data Set. *Phys. Rev. Lett.*, 124(25):251101, 2020.

[462] Tomohiro Nakama, Joseph Silk, and Marc Kamionkowski. Stochastic gravitational waves associated with the formation of primordial black holes. *Phys. Rev. D*, 95(4):043511, 2017.

[463] Juan Garcia-Bellido, Marco Peloso, and Caner Unal. Gravitational Wave signatures of inflationary models from Primordial Black Hole Dark Matter. *JCAP*, 09:013, 2017.

[464] Rong-gen Cai, Shi Pi, and Misao Sasaki. Gravitational Waves Induced by non-Gaussian Scalar Perturbations. *Phys. Rev. Lett.*, 122(20):201101, 2019.

[465] Caner Unal. Imprints of Primordial Non-Gaussianity on Gravitational Wave Spectrum. *Phys. Rev. D*, 99(4):041301, 2019.

[466] Rong-Gen Cai, Shi Pi, Shao-Jiang Wang, and Xing-Yu Yang. Pulsar Timing Array Constraints on the Induced Gravitational Waves. *JCAP*, 10:059, 2019.

[467] Zaven Arzoumanian et al. The NANOGrav 12.5-year Data Set: Search For An Isotropic

Stochastic Gravitational-Wave Background. 9 2020.

[468] V. De Luca, G. Franciolini, and A. Riotto. NANOGrav Hints to Primordial Black Holes as Dark Matter. 9 2020.

[469] Ville Vaskonen and Hardi Veermäe. Did NANOGrav see a signal from primordial black hole formation? 9 2020.

[470] Kazunori Kohri and Takahiro Terada. Possible Solar-Mass Primordial Black Holes for NANOGrav Hint of Gravitational Waves. 9 2020.

[471] Guillem Domènech and Shi Pi. NANOGrav Hints on Planet-Mass Primordial Black Holes. 10 2020.

[472] Sunao Sugiyama, Volodymyr Takhistov, Edoardo Vitagliano, Alexander Kusenko, Misao Sasaki, and Masahiro Takada. Testing Stochastic Gravitational Wave Signals from Primordial Black Holes with Optical Telescopes. 10 2020.

[473] Alberto Sesana, Francesco Haardt, Piero Madau, and Marta Volonteri. Low - frequency gravitational radiation from coalescing massive black hole binaries in hierarchical cosmologies. *Astrophys. J.*, 611:623–632, 2004.

[474] Simone Blasi, Vedran Brdar, and Kai Schmitz. Has NANOGrav found first evidence for cosmic strings? 9 2020.

[475] John Ellis and Marek Lewicki. Cosmic String Interpretation of NANOGrav Pulsar Timing Data. 9 2020.

[476] Wilfried Buchmuller, Valerie Domcke, and Kai Schmitz. From NANOGrav to LIGO with metastable cosmic strings. 9 2020.

[477] Rome Samanta and Satyabrata Datta. Gravitational wave complementarity and impact

of NANOGrav data on gravitational leptogenesis: cosmic strings. 9 2020.

[478] Yuichiro Nakai, Motoo Suzuki, Fuminobu Takahashi, and Masaki Yamada. Gravitational Waves and Dark Radiation from Dark Phase Transition: Connecting NANOGrav Pulsar Timing Data and Hubble Tension. 9 2020.

[479] Andrea Addazi, Yi-Fu Cai, Qingyu Gan, Antonino Marciano, and Kaiqiang Zeng. NANOGrav results and Dark First Order Phase Transitions. 9 2020.

[480] Wolfram Ratzinger and Pedro Schwaller. Whispers from the dark side: Confronting light new physics with NANOGrav data. 9 2020.

[481] Ryo Namba and Motoo Suzuki. Implications of Gravitational-wave Production from Dark Photon Resonance to Pulsar-timing Observations and Effective Number of Relativistic Species. 9 2020.

[482] A. Neronov, A. Roper Pol, C. Caprini, and D. Semikoz. NANOGrav signal from MHD turbulence at QCD phase transition in the early universe. 9 2020.

[483] Hao-Hao Li, Gen Ye, and Yun-Song Piao. Is the NANOGrav signal a hint of dS decay during inflation? 9 2020.

[484] Avik Paul, Upala Mukhopadhyay, and Debasish Majumdar. Gravitational Wave Signatures from Domain Wall and Strong First-Order Phase Transitions in a Two Complex Scalar extension of the Standard Model. 10 2020.

[485] Sukannya Bhattacharya, Subhendra Mohanty, and Priyank Parashari. Implications of the NANOGrav result on primordial gravitational waves in nonstandard cosmologies. 10 2020.

[486] Nicola Bellomo, José Luis Bernal, Alvise Raccanelli, and Licia Verde. Primordial Black

Holes as Dark Matter: Converting Constraints from Monochromatic to Extended Mass Distributions. *JCAP*, 01:004, 2018.

[487] Vicente Atal, Judith Cid, Albert Escrivà, and Jaume Garriga. PBH in single field inflation: the effect of shape dispersion and non-Gaussianities. *JCAP*, 05:022, 2020.

[488] Davide Gerosa, Geraint Pratten, and Alberto Vecchio. Gravitational-wave selection effects using neural-network classifiers. 7 2020.

[489] Gianfranco Bertone, Dan Hooper, and Joseph Silk. Particle dark matter: Evidence, candidates and constraints. *Phys. Rept.*, 405:279–390, 2005.

[490] Asimina Arvanitaki, Savas Dimopoulos, Sergei Dubovsky, Nemanja Kaloper, and John March-Russell. String Axiverse. *Phys. Rev. D*, 81:123530, 2010.

[491] David J. E. Marsh. Axion Cosmology. *Phys. Rept.*, 643:1–79, 2016.

[492] Asimina Arvanitaki, Junwu Huang, and Ken Van Tilburg. Searching for dilaton dark matter with atomic clocks. *Phys. Rev. D*, 91(1):015015, 2015.

[493] Hsi-Yu Schive, Tzihong Chiueh, and Tom Broadhurst. Cosmic Structure as the Quantum Interference of a Coherent Dark Wave. *Nature Phys.*, 10:496–499, 2014.

[494] Vitor Cardoso, Óscar J. C. Dias, Gavin S. Hartnett, Matthew Middleton, Paolo Pani, and Jorge E. Santos. Constraining the mass of dark photons and axion-like particles through black-hole superradiance. *JCAP*, 03:043, 2018.

[495] Ya. B. Zel'Dovich. Generation of Waves by a Rotating Body. *Soviet Journal of Experimental and Theoretical Physics Letters*, 14:180, August 1971.

[496] William H. Press and Saul A. Teukolsky. Floating Orbits, Superradiant Scattering and the Black-hole Bomb. *Nature*, 238:211–212, 1972.

[497] Steven L. Detweiler. KLEIN-GORDON EQUATION AND ROTATING BLACK HOLES. *Phys. Rev. D*, 22:2323–2326, 1980.

[498] Asimina Arvanitaki and Sergei Dubovsky. Exploring the String Axiverse with Precision Black Hole Physics. *Phys. Rev. D*, 83:044026, 2011.

[499] Miguel C. Ferreira, Caio F. B. Macedo, and Vitor Cardoso. Orbital fingerprints of ultralight scalar fields around black holes. *Phys. Rev. D*, 96(8):083017, 2017.

[500] Sam R. Dolan. Instability of the massive Klein-Gordon field on the Kerr spacetime. *Phys. Rev. D*, 76:084001, 2007.

[501] Kazunari Eda, Yousuke Itoh, Sachiko Kuroyanagi, and Joseph Silk. New Probe of Dark-Matter Properties: Gravitational Waves from an Intermediate-Mass Black Hole Embedded in a Dark-Matter Minispike. *Phys. Rev. Lett.*, 110(22):221101, 2013.

[502] Farhan Feroz and M. P. Hobson. Multimodal nested sampling: an efficient and robust alternative to MCMC methods for astronomical data analysis. *Mon. Not. Roy. Astron. Soc.*, 384:449, 2008.

[503] F. Feroz, M. P. Hobson, and M. Bridges. MultiNest: an efficient and robust Bayesian inference tool for cosmology and particle physics. *Mon. Not. Roy. Astron. Soc.*, 398:1601–1614, 2009.

[504] F. Feroz, M. P. Hobson, E. Cameron, and A. N. Pettitt. Importance Nested Sampling and the MultiNest Algorithm. *Open J. Astrophys.*, 2(1):10, 2019.

[505] Travis Robson, Neil J. Cornish, and Chang Liu. The construction and use of LISA sensitivity curves. *Class. Quant. Grav.*, 36(10):105011, 2019.

[506] K. G. Arun, Alessandra Buonanno, Guillaume Faye, and Evan Ochsner. Higher-

order spin effects in the amplitude and phase of gravitational waveforms emitted by inspiraling compact binaries: Ready-to-use gravitational waveforms. *Phys. Rev. D*, 79:104023, 2009. [Erratum: Phys.Rev.D 84, 049901 (2011)].

[507] Balazs Mikoczi, Matyas Vasuth, and Laszlo A. Gergely. Self-interaction spin effects in inspiralling compact binaries. *Phys. Rev. D*, 71:124043, 2005.

[508] Alejandro Bohé, Sylvain Marsat, and Luc Blanchet. Next-to-next-to-leading order spin–orbit effects in the gravitational wave flux and orbital phasing of compact binaries. *Class. Quant. Grav.*, 30:135009, 2013.

[509] Piotr Jaranowski, Andrzej Krolak, and Bernard F. Schutz. Data analysis of gravitational - wave signals from spinning neutron stars. 1. The Signal and its detection. *Phys. Rev. D*, 58:063001, 1998.

[510] Bruce Allen, Warren G. Anderson, Patrick R. Brady, Duncan A. Brown, and Jolien D. E. Creighton. FINDCHIRP: An Algorithm for detection of gravitational waves from inspiraling compact binaries. *Phys. Rev. D*, 85:122006, 2012.

[511] Emanuele Berti, Alessandra Buonanno, and Clifford M. Will. Estimating spinning binary parameters and testing alternative theories of gravity with LISA. *Phys. Rev. D*, 71:084025, 2005.

[512] Michele Vallisneri. Testing general relativity with gravitational waves: A reality check. PRD, 86(8):082001, October 2012.

[513] Paolo Gondolo and Joseph Silk. Dark matter annihilation at the galactic center. *Phys. Rev. Lett.*, 83:1719–1722, 1999.

[514] LIGO Scientific Collaboration. LIGO Algorithm Library - LALSuite. free software

(GPL), 2018.

[515] Jonathan R. Gair, Leor Barack, Teviet Creighton, Curt Cutler, Shane L. Larson, E. Sterl Phinney, and Michele Vallisneri. Event rate estimates for LISA extreme mass ratio capture sources. *Class. Quant. Grav.*, 21:S1595–S1606, 2004.

[516] Kazunari Eda, Yousuke Itoh, Sachiko Kuroyanagi, and Joseph Silk. Gravitational waves as a probe of dark matter minispikes. *Phys. Rev. D*, 91(4):044045, 2015.

[517] Asimina Arvanitaki, Masha Baryakhtar, and Xinlu Huang. Discovering the QCD Axion with Black Holes and Gravitational Waves. *Phys. Rev. D*, 91(8):084011, 2015.

[518] Daniel Baumann, Horng Sheng Chia, and Rafael A. Porto. Probing Ultralight Bosons with Binary Black Holes. *Phys. Rev. D*, 99(4):044001, 2019.

[519] Pau Amaro-Seoane. Relativistic dynamics and extreme mass ratio inspirals. *Living Reviews in Relativity*, 21(1):4, May 2018.

[520] Atsushi Nishizawa, Emanuele Berti, Antoine Klein, and Alberto Sesana. eLISA eccentricity measurements as tracers of binary black hole formation. *Phys. Rev. D*, 94(6):064020, 2016.

[521] Carlos A. R. Herdeiro and Eugen Radu. Kerr black holes with scalar hair. *Phys. Rev. Lett.*, 112:221101, 2014.

[522] Stanislav Babak, Hua Fang, Jonathan R. Gair, Kostas Glampedakis, and Scott A. Hughes. 'Kludge' gravitational waveforms for a test-body orbiting a Kerr black hole. *Phys. Rev. D*, 75:024005, 2007. [Erratum: Phys.Rev.D 77, 04990 (2008)].

[523] Alvin J. K. Chua, Christopher J. Moore, and Jonathan R. Gair. Augmented kludge waveforms for detecting extreme-mass-ratio inspirals. *Phys. Rev. D*, 96(4):044005,

2017.

[524] Valeria Ferrari, Emanuele Berti, Marco D'Andrea, and A. Ashtekar. Gravitational Waves Emitted by Extrasolar Planetary Systems. *International Journal of Modern Physics D*, 9(5):495–509, January 2000.

[525] E. Berti and V. Ferrari. Gravitational waves emitted by extrasolar planetary systems. *ICTP Lect. Notes Ser.*, 3:371–383, 2001.

[526] E. Berti and V. Ferrari. Excitation of g-modes of solar-type stars by an orbiting companion. PRD, 63(6):064031, March 2001.

[527] A. Cassan, D. Kubas, J. P. Beaulieu, M. Dominik, K. Horne, J. Greenhill, J. Wambsganss, J. Menzies, A. Williams, U. G. Jørgensen, A. Udalski, D. P. Bennett, M. D. Albrow, V. Batista, S. Brillant, J. A. R. Caldwell, A. Cole, Ch. Coutures, K. H. Cook, S. Dieters, D. Dominis Prester, J. Donatowicz, P. Fouqué, K. Hill, N. Kains, S. Kane, J. B. Marquette, R. Martin, K. R. Pollard, K. C. Sahu, C. Vinter, D. Warren, B. Watson, M. Zub, T. Sumi, M. K. Szymański, M. Kubiak, R. Poleski, I. Soszynski, K. Ulaczyk, G. Pietrzyński, and L. Wyrzykowski. One or more bound planets per Milky Way star from microlensing observations. Nature, 481(7380):167–169, January 2012.

[528] Przemek Mróz, Andrzej Udalski, Jan Skowron, Radoslaw Poleski, Szymon Kozlowski, Michal K. Szymański, Igor Soszyński, Lukasz Wyrzykowski, Pawel Pietrukowicz, Krzysztof Ulaczyk, Dorota Skowron, and Michal Pawlak. No large population of unbound or wide-orbit Jupiter-mass planets. Nature, 548(7666):183–186, August 2017.

[529] Anirban Ain, Shilpa Kastha, and Sanjit Mitra. Stochastic gravitational wave back-

ground from exoplanets. PRD, 91(12):124023, June 2015.

[530] C. J. Moore, R. H. Cole, and C. P. L. Berry. Gravitational-wave sensitivity curves. *Classical and Quantum Gravity*, 32(1):015014, January 2015.

[531] Curt Cutler. Angular resolution of the LISA gravitational wave detector. PRD, 57(12):7089–7102, June 1998.

[532] Emanuele Berti, Alessandra Buonanno, and Clifford M. Will. Estimating spinning binary parameters and testing alternative theories of gravity with LISA. PRD, 71(8):084025, April 2005.

[533] T. Kupfer, V. Korol, S. Shah, G. Nelemans, T. R. Marsh, G. Ramsay, P. J. Groot, D. T. H. Steeghs, and E. M. Rossi. LISA verification binaries with updated distances from Gaia Data Release 2. MNRAS, 480(1):302–309, October 2018.

[534] Arkadiusz Blaut, Stanislav Babak, and Andrzej Królak. Mock LISA data challenge for the Galactic white dwarf binaries. PRD, 81(6):063008, March 2010.

[535] Jeff Crowder and Neil J. Cornish. Extracting galactic binary signals from the first round of Mock LISA Data Challenges. *Classical and Quantum Gravity*, 24(19):S575–S585, October 2007.

[536] Eric Poisson and Clifford M. Will. Gravitational waves from inspiraling compact binaries: Parameter estimation using second-post-Newtonian waveforms. PRD, 52(2):848–855, July 1995.

[537] Seth E. Timpano, Louis J. Rubbo, and Neil J. Cornish. Characterizing the galactic gravitational wave background with LISA. PRD, 73(12):122001, June 2006.

[538] Sweta Shah and Gijs Nelemans. Constraining Parameters of White-dwarf Binaries

Using Gravitational-wave and Electromagnetic Observations. ApJ, 790(2):161, August 2014.

[539] Alberto Sesana. Prospects for Multiband Gravitational-Wave Astronomy after GW150914. PRL, 116(23):231102, June 2016.

[540] Krzysztof Belczynski, Matthew Benacquista, and Tomasz Bulik. Double Compact Objects as Low-frequency Gravitational Wave Sources. ApJ, 725(1):816–823, December 2010.

[541] Katelyn Breivik, Carl L. Rodriguez, Shane L. Larson, Vassiliki Kalogera, and Frederic A. Rasio. Distinguishing between Formation Channels for Binary Black Holes with LISA. ApJ, 830(1):L18, October 2016.

[542] Atsushi Nishizawa, Emanuele Berti, Antoine Klein, and Alberto Sesana. eLISA eccentricity measurements as tracers of binary black hole formation. PRD, 94(6):064020, September 2016.

[543] Atsushi Nishizawa, Alberto Sesana, Emanuele Berti, and Antoine Klein. Constraining stellar binary black hole formation scenarios with eLISA eccentricity measurements. MNRAS, 465(4):4375–4380, March 2017.

[544] Johan Samsing, Daniel J. D'Orazio, Abbas Askar, and Mirek Giersz. Black Hole Mergers from Globular Clusters Observable by LISA and LIGO: Results from post-Newtonian Binary-Single Scatterings. *arXiv e-prints*, page arXiv:1802.08654, February 2018.

[545] Kyle Kremer, Carl L. Rodriguez, Pau Amaro-Seoane, Katelyn Breivik, Sourav Chatterjee, Michael L. Katz, Shane L. Larson, Frederic A. Rasio, Johan Samsing, Claire S.

Ye, and Michael Zevin. Post-Newtonian dynamics in dense star clusters: Binary black holes in the LISA band. PRD, 99(6):063003, March 2019.

[546] Johan Samsing and Daniel J. D'Orazio. How post-Newtonian dynamics shape the distribution of stationary binary black hole LISA sources in nearby globular clusters. PRD, 99(6):063006, March 2019.

[547] Daniel J. D'Orazio and Johan Samsing. Black hole mergers from globular clusters observable by LISA II. Resolved eccentric sources and the gravitational wave background. MNRAS, 481(4):4775–4785, December 2018.

[548] Johan Samsing and Daniel J. D'Orazio. Black Hole Mergers From Globular Clusters Observable by LISA I: Eccentric Sources Originating From Relativistic N-body Dynamics. MNRAS, 481(4):5445–5450, December 2018.

[549] Kyle Kremer, Sourav Chatterjee, Katelyn Breivik, Carl L. Rodriguez, Shane L. Larson, and Frederic A. Rasio. LISA Sources in Milky Way Globular Clusters. PRL, 120(19):191103, May 2018.

[550] Lisa Randall and Zhong-Zhi Xianyu. A Direct Probe of Mass Density near Inspiraling Binary Black Holes. ApJ, 878(2):75, June 2019.

[551] Marcus E. Lower, Eric Thrane, Paul D. Lasky, and Rory Smith. Measuring eccentricity in binary black hole inspirals with gravitational waves. PRD, 98(8):083028, October 2018.

[552] Emanuele Berti, Enrico Barausse, Vitor Cardoso, Leonardo Gualtieri, Paolo Pani, Ulrich Sperhake, Leo C. Stein, Norbert Wex, Kent Yagi, Tessa Baker, C. P. Burgess, Flávio S. Coelho, Daniela Doneva, Antonio De Felice, Pedro G. Ferreira, Paulo C. C.

Freire, James Healy, Carlos Herdeiro, Michael Horbatsch, Burkhard Kleihaus, Antoine Klein, Kostas Kokkotas, Jutta Kunz, Pablo Laguna, Ryan N. Lang, Tjonnie G. F. Li, Tyson Littenberg, Andrew Matas, Saeed Mirshekari, Hirotada Okawa, Eugen Radu, Richard O'Shaughnessy, Bangalore S. Sathyaprakash, Chris Van Den Broeck, Hans A. Winther, Helvi Witek, Mir Emad Aghili, Justin Alsing, Brett Bolen, Luca Bombelli, Sarah Caudill, Liang Chen, Juan Carlos Degollado, Ryuichi Fujita, Caixia Gao, Davide Gerosa, Saeed Kamali, Hector O. Silva, João G. Rosa, Laleh Sadeghian, Marco Sampaio, Hajime Sotani, and Miguel Zilhao. Testing general relativity with present and future astrophysical observations. *Classical and Quantum Gravity*, 32(24):243001, December 2015.

[553] Enrico Barausse, Nicolás Yunes, and Katie Chamberlain. Theory-Agnostic Constraints on Black-Hole Dipole Radiation with Multiband Gravitational-Wave Astrophysics. PRL, 116(24):241104, June 2016.

[554] Koutarou Kyutoku and Naoki Seto. Gravitational-wave cosmography with LISA and the Hubble tension. PRD, 95(8):083525, April 2017.

[555] Walter Del Pozzo, Alberto Sesana, and Antoine Klein. Stellar binary black holes in the LISA band: a new class of standard sirens. MNRAS, 475(3):3485–3492, April 2018.

[556] Rhondale Tso, Davide Gerosa, and Yanbei Chen. Optimizing LIGO with LISA forewarnings to improve black-hole spectroscopy. PRD, 99(12):124043, June 2019.

[557] Salvatore Vitale. Multiband Gravitational-Wave Astronomy: Parameter Estimation and Tests of General Relativity with Space- and Ground-Based Detectors. PRL, 117(5):051102, July 2016.

[558] Kaze W. K. Wong, Ely D. Kovetz, Curt Cutler, and Emanuele Berti. Expanding the LISA Horizon from the Ground. PRL, 121(25):251102, December 2018.

[559] Alberto Mangiagli, Antoine Klein, Alberto Sesana, Enrico Barausse, and Monica Colpi. Post-Newtonian phase accuracy requirements for stellar black hole binaries with LISA. PRD, 99(6):064056, March 2019.

[560] Alberto Sesana. Multi-band gravitational wave astronomy: science with joint space- and ground-based observations of black hole binaries. In *Journal of Physics Conference Series*, volume 840 of *Journal of Physics Conference Series*, page 012018, May 2017.

[561] Koutarou Kyutoku and Naoki Seto. Concise estimate of the expected number of detections for stellar-mass binary black holes by eLISA. MNRAS, 462(2):2177–2183, October 2016.

[562] Vaibhav Tiwari. Estimation of the sensitive volume for gravitational-wave source populations using weighted Monte Carlo integration. *Classical and Quantum Gravity*, 35(14):145009, July 2018.

[563] R. O'Shaughnessy, V. Kalogera, and K. Belczynski. Binary Compact Object Coalescence Rates: The Role of Elliptical Galaxies. ApJ, 716(1):615–633, June 2010.

[564] M. Dominik, E. Berti, R. O'Shaughnessy, I. Mandel, K. Belczynski, C. Fryer, D. E. Holz, T. Bulik, and F. Pannarale. Double Compact Objects III: Gravitational-wave Detection Rates. ApJ, 806(2):263, June 2015.

[565] H.-Y. Chen, D. E. Holz, J. Miller, M. Evans, S. Vitale, and J. Creighton. Distance measures in gravitational-wave astrophysics and cosmology. *arXiv e-prints*, page arXiv:1709.08079, September 2017.

[566] B. P. Abbott, R. Abbott, T. D. Abbott, M. R. Abernathy, K. Ackley, C. Adams, P. Addesso, R. X. Adhikari, V. B. Adya, C. Affeldt, and et al. Exploring the sensitivity of next generation gravitational wave detectors. *Classical and Quantum Gravity*, 34(4):044001, February 2017.

[567] P. C. Peters. Gravitational Radiation and the Motion of Two Point Masses. *Physical Review*, 136(4B):1224–1232, November 1964.

[568] Travis Robson, Neil J. Cornish, and Chang Liu. The construction and use of LISA sensitivity curves. *Classical and Quantum Gravity*, 36(10):105011, May 2019.

[569] P. Ajith, S. Babak, Y. Chen, M. Hewitson, B. Krishnan, J. T. Whelan, B. Brügmann, P. Diener, J. Gonzalez, M. Hannam, S. Husa, M. Koppitz, D. Pollney, L. Rezzolla, L. Santamaría, A. M. Sintes, U. Sperhake, and J. Thornburg. A phenomenological template family for black-hole coalescence waveforms. *Classical and Quantum Gravity*, 24(19):S689–S699, October 2007.

[570] Curt Cutler, Theocharis A. Apostolatos, Lars Bildsten, Lee Smauel Finn, Eanna E. Flanagan, Daniel Kennefick, Dragoljub M. Markovic, Amos Ori, Eric Poisson, Gerald Jay Sussman, and Kip S. Thorne. The last three minutes: Issues in gravitational-wave measurements of coalescing compact binaries. PRL, 70(20):2984–2987, May 1993.

[571] Ilya Mandel and Alison Farmer. Merging stellar-mass binary black holes. *arXiv e-prints*, page arXiv:1806.05820, June 2018.

[572] K. Belczynski, J. Klencki, C. E. Fields, A. Olejak, E. Berti, G. Meynet, C. L. Fryer, D. E. Holz, R. O'Shaughnessy, D. A. Brown, T. Bulik, S. C. Leung, K. Nomoto,

P. Madau, R. Hirschi, E. Kaiser, S. Jones, S. Mondal, M. Chruslinska, P. Drozda, D. Gerosa, Z. Doctor, M. Giersz, S. Ekstrom, C. Georgy, A. Askar, V. Baibhav, D. Wysocki, T. Natan, W. M. Farr, G. Wiktorowicz, M. Coleman Miller, B. Farr, and J. P. Lasota. Evolutionary roads leading to low effective spins, high black hole masses, and O1/O2 rates for LIGO/Virgo binary black holes. A&A, 636:A104, April 2020.

[573] Davide Gerosa, Michael Kesden, Emanuele Berti, Richard O'Shaughnessy, and Ulrich Sperhake. Resonant-plane locking and spin alignment in stellar-mass black-hole binaries: A diagnostic of compact-binary formation. PRD, 87(10):104028, May 2013.

[574] Chris L. Fryer, S. E. Woosley, and Dieter H. Hartmann. Formation Rates of Black Hole Accretion Disk Gamma-Ray Bursts. ApJ, 526(1):152–177, November 1999.

[575] Krzysztof Belczynski, Vassiliki Kalogera, and Tomasz Bulik. A Comprehensive Study of Binary Compact Objects as Gravitational Wave Sources: Evolutionary Channels, Rates, and Physical Properties. ApJ, 572(1):407–431, June 2002.

[576] Krzysztof Belczynski, Daniel E. Holz, Tomasz Bulik, and Richard O'Shaughnessy. The first gravitational-wave source from the isolated evolution of two stars in the 40-100 solar mass range. Nature, 534(7608):512–515, June 2016.

[577] Serena Repetto and Gijs Nelemans. Constraining the formation of black holes in short-period black hole low-mass X-ray binaries. MNRAS, 453(3):3341–3355, November 2015.

[578] Étienne Racine. Analysis of spin precession in binary black hole systems including quadrupole-monopole interaction. PRD, 78(4):044021, August 2008.

[579] Davide Gerosa, Michael Kesden, Ulrich Sperhake, Emanuele Berti, and Richard

O'Shaughnessy. Multi-timescale analysis of phase transitions in precessing black-hole binaries. PRD, 92(6):064016, September 2015.

[580] B. Paczynski. Common Envelope Binaries. In Peter Eggleton, Simon Mitton, and John Whelan, editors, *Structure and Evolution of Close Binary Systems*, volume 73, page 75, January 1976.

[581] N. Ivanova, S. Justham, X. Chen, O. De Marco, C. L. Fryer, E. Gaburov, H. Ge, E. Glebbeek, Z. Han, X. D. Li, G. Lu, T. Marsh, P. Podsiadlowski, A. Potter, N. Soker, R. Taam, T. M. Tauris, E. P. J. van den Heuvel, and R. F. Webbink. Common envelope evolution: where we stand and how we can move forward. A&A Rev., 21:59, February 2013.

[582] Antoine Klein, Enrico Barausse, Alberto Sesana, Antoine Petiteau, Emanuele Berti, Stanislav Babak, Jonathan Gair, Sofiane Aoudia, Ian Hinder, Frank Ohme, and Barry Wardell. Science with the space-based interferometer eLISA: Supermassive black hole binaries. PRD, 93(2):024003, January 2016.

[583] William A. Fowler and F. Hoyle. Neutrino Processes and Pair Formation in Massive Stars and Supernovae. ApJS, 9:201, December 1964.

[584] Z. Barkat, G. Rakavy, and N. Sack. Dynamics of Supernova Explosion Resulting from Pair Formation. PRL, 18(10):379–381, March 1967.

[585] Pablo Marchant, Mathieu Renzo, Robert Farmer, Kaliroe M. W. Pappas, Ronald E. Taam, Selma E. de Mink, and Vassiliki Kalogera. Pulsational Pair-instability Supernovae in Very Close Binaries. ApJ, 882(1):36, September 2019.

[586] Mario Spera and Michela Mapelli. Very massive stars, pair-instability supernovae

and intermediate-mass black holes with the sevn code. MNRAS, 470(4):4739–4749, October 2017.

[587] S. E. Woosley. Pulsational Pair-instability Supernovae. ApJ, 836(2):244, February 2017.

[588] Ely D. Kovetz, Ilias Cholis, Marc Kamionkowski, and Joseph Silk. Limits on runaway growth of intermediate mass black holes from advanced LIGO. PRD, 97(12):123003, June 2018.

[589] Pau Amaro-Seoane and Lucía Santamaría. Detection of IMBHs with Ground-based Gravitational Wave Observatories: A Biography of a Binary of Black Holes, from Birth to Death. ApJ, 722(2):1197–1206, October 2010.

[590] Bence Kocsis and Janna Levin. Repeated bursts from relativistic scattering of compact objects in galactic nuclei. PRD, 85(12):123005, June 2012.

[591] Samantha A. Usman, Alexander H. Nitz, Ian W. Harry, Christopher M. Biwer, Duncan A. Brown, Miriam Cabero, Collin D. Capano, Tito Dal Canton, Thomas Dent, Stephen Fairhurst, Marcel S. Kehl, Drew Keppel, Badri Krishnan, Amber Lenon, Andrew Lundgren, Alex B. Nielsen, Larne P. Pekowsky, Harald P. Pfeiffer, Peter R. Saulson, Matthew West, and Joshua L. Willis. The PyCBC search for gravitational waves from compact binary coalescence. *Classical and Quantum Gravity*, 33(21):215004, November 2016.

[592] A. Lamberts, S. Garrison-Kimmel, P. F. Hopkins, E. Quataert, J. S. Bullock, C. A. Faucher-Giguère, A. Wetzel, D. Kereš, K. Drango, and R. E. Sanderson. Predicting the binary black hole population of the Milky Way with cosmological simulations.

MNRAS, 480(2):2704–2718, October 2018.

[593] Alberto Sesana. Prospects for Multiband Gravitational-Wave Astronomy after GW150914. *Phys. Rev. Lett.*, 116(23):231102, 2016.

[594] Collin Capano, Thomas Dent, Yi-Ming Hu, Martin Hendry, Chris Messenger, and John Veitch. Systematic errors in estimation of gravitational-wave candidate significance. 1 2016.

[595] B.. P.. Abbott et al. GW170608: Observation of a 19-solar-mass Binary Black Hole Coalescence. *Astrophys. J.*, 851(2):L35, 2017.

[596] Ryan Lynch, Michael Coughlin, Salvatore Vitale, Christopher W. Stubbs, and Erik Katsavounidis. Observational implications of lowering the LIGO-Virgo alert threshold. *Astrophys. J. Lett.*, 861(2):L24, 2018.

[597] Walter Del Pozzo, Alberto Sesana, and Antoine Klein. Stellar binary black holes in the LISA band: a new class of standard sirens. *Mon. Not. Roy. Astron. Soc.*, 475(3):3485–3492, 2018.

[598] B. P. Abbott et al. The Rate of Binary Black Hole Mergers Inferred from Advanced LIGO Observations Surrounding GW150914. *Astrophys. J. Lett.*, 833(1):L1, 2016.

[599] Hsin-Yu Chen, Daniel E. Holz, John Miller, Matthew Evans, Salvatore Vitale, and Jolien Creighton. Distance measures in gravitational-wave astrophysics and cosmology. *Class. Quant. Grav.*, 38(5):055010, 2021.

[600] K. Belczynski et al. The Effect of Pair-Instability Mass Loss on Black Hole Mergers. *Astron. Astrophys.*, 594:A97, 2016.

[601] Ely D. Kovetz, Ilias Cholis, Marc Kamionkowski, and Joseph Silk. Limits on Runaway

Growth of Intermediate Mass Black Holes from Advanced LIGO. *Phys. Rev. D*, 97(12):123003, 2018.

[602] Eanna E. Flanagan and Scott A. Hughes. Measuring gravitational waves from binary black hole coalescences: 1. Signal-to-noise for inspiral, merger, and ringdown. *Phys. Rev. D*, 57:4535–4565, 1998.

[603] Curt Cutler and Eanna E. Flanagan. Gravitational waves from merging compact binaries: How accurately can one extract the binary's parameters from the inspiral wave form? *Phys. Rev. D*, 49:2658–2697, 1994.

[604] Tito Dal Canton et al. Implementing a search for aligned-spin neutron star-black hole systems with advanced ground based gravitational wave detectors. *Phys. Rev. D*, 90(8):082004, 2014.

[605] Samantha A. Usman et al. The PyCBC search for gravitational waves from compact binary coalescence. *Class. Quant. Grav.*, 33(21):215004, 2016.

[606] Alexander H. Nitz, Thomas Dent, Tito Dal Canton, Stephen Fairhurst, and Duncan A. Brown. Detecting binary compact-object mergers with gravitational waves: Understanding and Improving the sensitivity of the PyCBC search. *Astrophys. J.*, 849(2):118, 2017.

[607] Marc van der Sluys, Vivien Raymond, Ilya Mandel, Christian Rover, Nelson Christensen, Vicky Kalogera, Renate Meyer, and Alberto Vecchio. Parameter estimation of spinning binary inspirals using Markov-chain Monte Carlo. *Class. Quant. Grav.*, 25:184011, 2008.

[608] `https://lisa-ldc.lal.in2p3.fr/`.

[609] Michalis Agathos, Walter Del Pozzo, Tjonnie G. F. Li, Chris Van Den Broeck, John Veitch, and Salvatore Vitale. TIGER: A data analysis pipeline for testing the strong-field dynamics of general relativity with gravitational wave signals from coalescing compact binaries. *Phys. Rev. D*, 89(8):082001, 2014.

[610] B. P. Abbott et al. Tests of general relativity with GW150914. *Phys. Rev. Lett.*, 116(22):221101, 2016. [Erratum: Phys. Rev. Lett.121,no.12,129902(2018)].

[611] Salvatore Vitale. Multiband Gravitational-Wave Astronomy: Parameter Estimation and Tests of General Relativity with Space- and Ground-Based Detectors. *Phys. Rev. Lett.*, 117(5):051102, 2016.

[612] Enrico Barausse, Nicolás Yunes, and Katie Chamberlain. Theory-Agnostic Constraints on Black-Hole Dipole Radiation with Multiband Gravitational-Wave Astrophysics. *Phys. Rev. Lett.*, 116(24):241104, 2016.

[613] Nicolas Yunes, Kent Yagi, and Frans Pretorius. Theoretical Physics Implications of the Binary Black-Hole Mergers GW150914 and GW151226. *Phys. Rev. D*, 94(8):084002, 2016.

[614] Ilias Cholis, Ely D. Kovetz, Yacine Ali-Haïmoud, Simeon Bird, Marc Kamionkowski, Julian B. Muñoz, and Alvise Raccanelli. Orbital eccentricities in primordial black hole binaries. *Phys. Rev. D*, 94(8):084013, 2016.

[615] Katelyn Breivik, Carl L. Rodriguez, Shane L. Larson, Vassiliki Kalogera, and Frederic A. Rasio. Distinguishing Between Formation Channels for Binary Black Holes with LISA. *Astrophys. J. Lett.*, 830(1):L18, 2016.

[616] Atsushi Nishizawa, Alberto Sesana, Emanuele Berti, and Antoine Klein. Constraining

stellar binary black hole formation scenarios with eLISA eccentricity measurements. *Mon. Not. Roy. Astron. Soc.*, 465(4):4375–4380, 2017.

[617] László Gondán, Bence Kocsis, Péter Raffai, and Zsolt Frei. Accuracy of Estimating Highly Eccentric Binary Black Hole Parameters with Gravitational-Wave Detections. *Astrophys. J.*, 855(1):34, 2018.

[618] Daniel J. D'Orazio and Johan Samsing. Black Hole Mergers From Globular Clusters Observable by LISA II: Resolved Eccentric Sources and the Gravitational Wave Background. *Mon. Not. Roy. Astron. Soc.*, 481(4):4775–4785, 2018.

[619] Kohei Inayoshi, Nicola Tamanini, Chiara Caprini, and Zoltán Haiman. Probing stellar binary black hole formation in galactic nuclei via the imprint of their center of mass acceleration on their gravitational wave signal. *Phys. Rev. D*, 96(6):063014, 2017.

[620] Kyle Kremer, Sourav Chatterjee, Katelyn Breivik, Carl L. Rodriguez, Shane L. Larson, and Frederic A. Rasio. LISA Sources in Milky Way Globular Clusters. *Phys. Rev. Lett.*, 120(19):191103, 2018.

[621] Johan Samsing, Daniel J. D'Orazio, Abbas Askar, and Mirek Giersz. Black Hole Mergers from Globular Clusters Observable by LISA and LIGO: Results from post-Newtonian Binary-Single Scatterings. 2 2018.

[622] M. Miyoshi, J. Moran, J. Herrnstein, L. Greenhill, N. Nakai, P. Diamond, and M. Inoue. Evidence for a black hole from high rotation velocities in a sub-parsec region of NGC4258. Nature, 373:127–129, January 1995.

[623] A. M. Ghez et al. Measuring Distance and Properties of the Milky Way's Central Supermassive Black Hole with Stellar Orbits. *Astrophys. J.*, 689:1044–1062, 2008.

[624] S. Gillessen, F. Eisenhauer, S. Trippe, T. Alexander, R. Genzel, F. Martins, and T. Ott. Monitoring stellar orbits around the Massive Black Hole in the Galactic Center. *Astrophys. J.*, 692:1075–1109, 2009.

[625] Bradley M. Peterson et al. Central masses and broad-line region sizes of active galactic nuclei. II. A Homogeneous analysis of a large reverberation-mapping database. *Astrophys. J.*, 613:682–699, 2004.

[626] F. Özel, D. Psaltis, R. Narayan, and J. E. McClintock. The Black Hole Mass Distribution in the Galaxy. ApJ, 725:1918–1927, December 2010.

[627] D. Steeghs, J. E. McClintock, S. G. Parsons, M. J. Reid, S. Littlefair, and V. S. Dhillon. The not-so-massive black hole in the microquasar GRS1915+105. *Astrophys. J.*, 768:185, 2013.

[628] B. Kızıltan, H. Baumgardt, and A. Loeb. An intermediate-mass black hole in the centre of the globular cluster 47 Tucanae. Nature, 542:203–205, February 2017.

[629] M. Mezcua. Observational evidence for intermediate-mass black holes. *International Journal of Modern Physics D*, 26:1730021, 2017.

[630] Dragoljub Markovic. On the possibility of determining cosmological parameters from measurements of gravitational waves emitted by coalescing, compact binaries. *Phys. Rev.*, D48:4738–4756, 1993.

[631] Nicolas Yunes, M. Coleman Miller, and Jonathan Thornburg. The Effect of Massive Perturbers on Extreme Mass-Ratio Inspiral Waveforms. *Phys. Rev.*, D83:044030, 2011.

[632] Davide Gerosa and Christopher J. Moore. Black hole kicks as new gravitational wave observables. *Phys. Rev. Lett.*, 117(1):011101, 2016.

[633] Yohai Meiron, Bence Kocsis, and Abraham Loeb. Detecting triple systems with gravitational wave observations. *Astrophys. J.*, 834(2):200, 2017.

[634] Lisa Randall and Zhong-Zhi Xianyu. A Direct Probe of Mass Density Near Inspiraling Binary Black Holes. *ArXiv e-prints*, 2018.

[635] Camille Bonvin, Chiara Caprini, Riccardo Sturani, and Nicola Tamanini. Effect of matter structure on the gravitational waveform. *Phys. Rev.*, D95(4):044029, 2017.

[636] Travis Robson, Neil J. Cornish, Nicola Tamanini, and Silvia Toonen. Detecting hierarchical stellar systems with LISA. *Phys. Rev.*, D98(6):064012, 2018.

[637] Naoki Seto. Detecting Planets around Compact Binaries with Gravitational Wave Detectors in Space. *Astrophys. J.*, 677:L55–L58, 2008.

[638] Nicola Tamanini and Camilla Danielski. Listening to the gravitational wave sound of circumbinary exoplanets. *ArXiv e-prints*, 2018.

[639] Jason H. Steffen, Dong-Hong Wu, and Shane L. Larson. Detecting circumbinary exoplanets and hierarchical stellar triples with the LISA gravitational radiation mission. *ArXiv e-prints*, 2018.

[640] Curt Cutler. Angular resolution of the LISA gravitational wave detector. *Phys. Rev.*, D57:7089–7102, 1998.

[641] Katie Chamberlain, Christopher J. Moore, Davide Gerosa, and Nicolas Yunes. Frequency-domain waveform approximants capturing Doppler shifts. *ArXiv e-prints*, 2018.

[642] Lisa Randall and Zhong-Zhi Xianyu. Induced Ellipticity for Inspiraling Binary Systems. *Astrophys. J.*, 853(1):93, 2018.

[643] Lisa Randall and Zhong-Zhi Xianyu. An Analytical Portrait of Binary Mergers in Hierarchical Triple Systems. *Astrophys. J.*, 864(2):134, 2018.

[644] Johan Samsing and Daniel J. D'Orazio. Black Hole Mergers From Globular Clusters Observable by LISA I: Eccentric Sources Originating From Relativistic N-body Dynamics. *Mon. Not. Roy. Astron. Soc.*, 481(4):5445–5450, 2018.

[645] Carl L. Rodriguez, Pau Amaro-Seoane, Sourav Chatterjee, Kyle Kremer, Frederic A. Rasio, Johan Samsing, Claire S. Ye, and Michael Zevin. Post-Newtonian Dynamics in Dense Star Clusters: Formation, Masses, and Merger Rates of Highly-Eccentric Black Hole Binaries. *Phys. Rev.*, D98(12):123005, 2018.

[646] E. Poisson and C. M. Will. *Gravity*. Cambridge University Press, May 2014.

[647] Natalia Ivanova, K. Belczynski, J. M. Fregeau, and F. A. Rasio. The Evolution of binary fractions in globular clusters. *Mon. Not. Roy. Astron. Soc.*, 358:572–584, 2005.

[648] A. Sollima, G. Beccari, F. R. Ferraro, F. Fusi Pecci, and A. Sarajedini. The fraction of binary systems in the core of thirteen low-density Galactic globular clusters. *Mon. Not. Roy. Astron. Soc.*, 380:781, 2007.

[649] Jarrod R. Hurley, Sverre J. Aarseth, and Michael M. Shara. The core binary fractions of star clusters from realistic simulations. *Astrophys. J.*, 665:707–718, 2007.

[650] Michael D. Albrow, Ronald L. Gilliland, Timothy M. Brown, Peter D. Edmonds, Puragra Guhathakurta, and Ata Sarajedini. The frequency of binary stars in the core of 47 tucanae. *Astrophys. J.*, 559:1060, 2001.

[651] M. Hénon. Monte carlo models of star clusters. *Astrophysics and Space Science*, 13(2):284–299, October 1971.

[652] Pau Amaro-Seoane and Rainer Spurzem. The loss-cone problem in dense nuclei. *Mon. Not. Roy. Astron. Soc.*, 327:995, 2001.

[653] John M. Fregeau, P. Cheung, S. F. Portegies Zwart, and F. A. Rasio. Stellar collisions during binary - binary and binary - single star interactions. *Mon. Not. Roy. Astron. Soc.*, 352:1, 2004.

[654] G. Fragione, E. Grishin, N. W. C. Leigh, H. B. Perets, and R. Perna. Black Hole and Neutron Star Mergers in Galactic Nuclei. *ArXiv e-prints*, November 2018.

[655] Charles J. Hailey, Kaya Mori, Franz E. Bauer, Michael E. Berkowitz, Jaesub Hong, and Benjamin J. Hord. A density cusp of quiescent x-ray binaries in the central parsec of the galaxy. *Nature*, 556:70 EP, April 2018.

[656] Warren R. Brown, Margaret J. Geller, Scott J. Kenyon, and Michael J. Kurtz. Discovery of an unbound hyper-velocity star in the Milky Way halo. *Astrophys. J.*, 622:L33–L36, 2005.

[657] Blake D. Sherwin, Abraham Loeb, and Ryan M. O'Leary. Hypervelocity Stars from the Andromeda Galaxy. *Mon. Not. Roy. Astron. Soc.*, 386:1179, 2008.

[658] Jillian M. Bellovary, Mordecai-Mark Mac Low, Barry McKernan, and K. E. Saavik Ford. Migration Traps in Disks Around Supermassive Black Holes. *Astrophys. J.*, 819(2):L17, 2016.

[659] Wen-Biao Han and Xian Chen. Identify binary extreme-mass-ratio inspirals with multi-band gravitational-wave observations. *ArXiv e-prints*, 2018.

[660] Xian Chen and Wen-Biao Han. A New Type of Extreme-mass-ratio Inspirals Produced by Tidal Capture of Binary Black Holes. *Communications Physics*, 1:53, 2018.

[661] Edward J. M. Colbert and Richard F. Mushotzky. The Nature of accreting black holes in nearby galaxy nuclei. *Astrophys. J.*, 519:89–107, 1999.

[662] M. D. Caballero-Garcia, T. Belloni, and L. Zampieri. Quasi-Periodic Oscillations and energy spectra from the two brightest Ultra-Luminous X-ray sources in M82. *Mon. Not. Roy. Astron. Soc.*, 436:3262, 2013.

[663] Dheeraj R. Pasham, Tod E. Strohmayer, and Richard F. Mushotzky. A 400 solar mass black hole in the Ultraluminous X-ray source M82 X-1 accreting close to its Eddington limit. *ArXiv e-prints*, 2015. [Nature513,74(2014)].

[664] I. V. Chilingarian, I. Y. Katkov, I. Y. Zolotukhin, K. A. Grishin, Y. Beletsky, K. Boutsia, and D. J. Osip. A Population of Bona Fide Intermediate-mass Black Holes Identified as Low-luminosity Active Galactic Nuclei. ApJ, 863:1, August 2018.

[665] D. D. Nguyen, A. C. Seth, N. Neumayer, S. Iguchi, M. Cappellari, J. Strader, L. Chomiuk, E. Tremou, F. Pacucci, K. Nakanishi, A. Bahramian, P. M. Nguyen, M. den Brok, C. Ahn, K. T. Voggel, N. Kacharov, T. Tsukui, C. K. Ly, A. Dumont, and R. Pechetti. Improved Dynamical Constraints on the Masses of the Central Black Holes in Nearby Low-mass Early-type Galactic Nuclei And the First Black Hole Determination for NGC 205. *ArXiv e-prints*, January 2019.

[666] Toshikazu Ebisuzaki, Junichiro Makino, Takeshi Go Tsuru, Yoko Funato, Simon F. Portegies Zwart, Piet Hut, Steve McMillan, Satoki Matsushita, Hironori Matsumoto, and Ryohei Kawabe. Missing link found? – the "runaway" path to supermassive black holes. *Astrophys. J.*, 562:L19, 2001.

[667] G. Fragione, I. Ginsburg, and B. Kocsis. Gravitational Waves and Intermediate-mass

Black Hole Retention in Globular Clusters. ApJ, 856:92, April 2018.

[668] G. Fragione, N. W. C. Leigh, I. Ginsburg, and B. Kocsis. Tidal Disruption Events and Gravitational Waves from Intermediate-mass Black Holes in Evolving Globular Clusters across Space and Time. ApJ, 867:119, November 2018.

[669] M. Arca-Sedda and A. Gualandris. Gravitational wave sources from inspiralling globular clusters in the Galactic Centre and similar environments. MNRAS, 477:4423–4442, July 2018.

[670] M. Arca-Sedda and R. Capuzzo-Dolcetta. The MEGaN project II. Gravitational waves from intermediate-mass and binary black holes around a supermassive black hole. MNRAS, 483:152–171, February 2019.

Vita

Kaze, Wang Kei, Wong was born in Hong Kong on December 15, 1995. He became a physics-major undergraduate in The Chinese University of Hong Kong (CUHK) in 2013. In 2015, he received the Summer Undergraduate Research Exchange Program (SURE) scholarship and traveled to Carnegie Mellon University to work on cosmology with Shirley Ho. For his undergraduate final year project, he stayed at CUHK to work on gravitational-wave astrophysics with Tjonnie G. F. Li. He joined the Department of Physics & Astronomy at Johns Hopkins University in 2017 and received a Ph.D. degree in physics in 2021 under the supervision of Prof. Emanuele Berti. After his graduation, he will move to the Center for Computational Astrophysics, Flatiron Institute to continue his research on gravitational waves and deep learning as a research fellow.